Investigation of the scintillating fiber SCSF-38M for the 6m-tagger and measurement of inclusive K_S^0 meson and Λ baryon production in neutral current deep inelastic scattering at HERA

Dissertation
zur Erlangung des Doktorgrades
des Fachbereichs Physik
der Universität Hamburg

vorgelegt von
Arzu Ziegler
aus Hamburg

Hamburg
2003

Gutachter der Dissertation:	Prof. Dr. Wick Prof. Dr. Scobel
Gutachter der Disputation:	Prof. Dr. Wick Prof. Dr. Strohbusch
Datum der Disputation:	14.04.2003
Vorsitzender des Prüfungsausschusses:	Dr. Fretwurst
Vorsitzender des Promotionsausschusses:	Prof. Dr. Huber
Dekan des Fachbereichs Physik:	Prof. Dr. F.-W. Büßer

Zusammenfassung

Die Transmission der SCSF-38M Faser mit einem Durchmesser von $\varnothing$ 0.5 mm wurde vorher, während und nach der Bestrahlung mit einer ^{137}Cs-Quelle gemessen. Zusätzliche Messungen wurden durchgeführt, indem Fasern bis zu einer Temperatur von $T = 68°$C aufgeheizt wurden. Ein beschleunigter Alterungsprozess für $T > 40°$C war zu beobachten, der nicht reversibel war. Die Transmission einer Faser wird gemessen, indem Licht durch die Faser geleitet wird. Dieses Licht hat Einfluss auf den Strahlenschaden der Faser. Je mehr Licht durch die Faser geleitet wird, desto besser ist die Ausheilung. Dieser Effekt kann nicht auf das Szintillationslicht übertragen werden.

Der 6m-tagger, ein Wolfram-Szintillator-Spaghetti-Faser Kalorimeter, wurde November 2001 in das ZEUS Experiment installiert. Bei den Fasern handelt es sich um den Typ SCSF-38M. Ein ^{60}Co-Kontroll-System dient dazu, mechanische Schäden, Alterungseffekte und Strahlenschäden der szintillierdenden Fasern zu untersuchen. Die 6m-tagger-Detektorleistung wurde über einen Zeitraum von 10 Monaten beobachtet. Während dieser Zeit war der Detektor einer Gesamtdosis von 477 Gy ausgesetzt. Der dadurch erzeugte Strahlenschaden änderte die Abschwächlänge der Fasern. Die Synchrotronstrahlung hat einen großen Effekt auf die Fasern, was in den Messungen demonstriert wird.

Die Produktion von Strange-Quarks in tiefunelastischen Streuprozessen wurde am HERA-Speicherring anhand von K^0_S Mesonen und Λ Baryonen untersucht, wo Elektronen mit einer Energie von 27.5 GeV und Protonen mit einer Energie von 920 GeV zur Kollision gebracht werden. Für die Analyse wurden Datensätze des ZEUS Experimentes verwendet, welche einer integrierten Luminosität von 60 pb^{-1} entsprechen. Die K^0_S Mesonen und Λ Baryonen wurden in einem beschränkten kinematischen Bereich von $20 < Q^2 < 500$ GeV^2, $3 \cdot 10^{-4} < x < 10^{-1}$, $0.04 < y < 0.8$, $0.5 < p_T(K^0_S, \Lambda) < 5.0$ GeV und $|\eta(K^0_S, \Lambda)| < 1.5$ gemessen. Der gemessene Gesamtwirkungsquerschnitt für diese Teilchen in diesem beschränkten kinematischen Bereich ist $\sigma(e^+p \to e^+K^0_SX) = 6431 \pm 38(\text{stat.})^{+64}_{-207}(\text{syst.})$ pb, $\sigma(e^+p \to e^+\Lambda X) = 779 \pm 19(\text{stat.})^{+15}_{-36}(\text{syst.})$ pb, $\sigma(e^+p \to e^+\bar{\Lambda}X) = 724 \pm 17(\text{stat.})^{+21}_{-21}(\text{syst.})$ pb, und für Λ und $\bar{\Lambda}$ zusammen ist es $\sigma(\Lambda + \bar{\Lambda}) = 1503 \pm 26(\text{stat.})^{+28}_{-50}(\text{syst.})$ pb. Die differentiellen Wirkungsquerschnitte wurden als Funktion von Q^2, x, p_T und η für K^0_S Mesonen, Λ Baryonen, $\bar{\Lambda}$ Antibaryonen und für Λ und $\bar{\Lambda}$ zusammen gemessen. Zusätzlich wurde das Verhältnis $\sigma(\Lambda + \bar{\Lambda})/\sigma(K^0_S)$ als Funktion von Q^2, x, p_T und η gemessen. Die gemessenen totalen und differentiellen Wirkungsquerschnitte sowie das Verhältnis $\sigma(\Lambda + \bar{\Lambda})/\sigma(K^0_S)$ dieser Teilchen wurde mit dem ARIADNE und HERWIG Monte Carlo verglichen. ARIADNE beschreibt die Kinematik der K^0_S Meson und Λ Baryon Produktion besser als HERWIG. Es wurden zu gleichen Teilen Λ Baryonen und $\bar{\Lambda}$ Antibaryonen produziert.

ARIADNE ist im Großen und Ganzen das bessere Modell als HERWIG, um die Produktion von K^0_S Meson und Λ Baryon zu simulieren.

Abstract

The transmission of the fiber SCSF-38M with a diameter of $\varnothing$ 0.5 mm was measured before, during and after irradiation with a ^{137}Cs source. In addition transmission measurements were performed for a fiber, which was heated up to $T = 68°$C and showed an accelerated ageing phenomenon for $T > 40°$C. The damage due to the high temperature did not recover after reducing the temperature below $40°$C. The transmission of the fiber is measured by sending light through the fiber. This light has an influence on the radiation damage in the fiber. The more light transmits down the fiber, the better is the annealing. It seems that this effect cannot be transfered to the scintillation light, i.e. that at least for continuous illumination the light yield from the scintillation was lower than with an illumination of 42 seconds per hour.

The 6m-tagger, a tungsten-scintillator-spaghetti-fiber calorimeter, has been installed in the ZEUS experiment in November 2001. The fibers which are used are SCSF-38M fibers. A monitor system with a ^{60}Co source is used to monitor mechanical damage, ageing effects and radiation damage of the scintillating fibers. The development of the performance of the 6m-tagger is investigated over a time of 10 months. In this time the detector was exposed to a total dose of 477 Gy. The radiation damage changed the attenuation of the fibers. In addition the synchrotron radiation has a severe effect on the fibers, which is clearly seen by the measurements.

The strange-quark production in neutral current deep-inelastic scattering of 27.5 GeV positrons and 920 GeV protons has been studied at HERA by reconstructing K^0_S mesons and Λ baryons. The data corresponds to an integrated luminosity of 60 pb^{-1}. These particles are measured in a restricted kinematic region of $20 < Q^2 < 500$ GeV^2, $3 \cdot 10^{-4} < x < 10^{-1}, 0.04 < y < 0.8, 0.5 < p_T(K^0_S, \Lambda) < 5.0$ GeV and $|\eta(K^0_S, \Lambda)| < 1.5$. The total cross sections in this restricted kinematic region have been measured to be $\sigma(e^+p \to e^+K^0_SX) = 6431 \pm 38(\text{stat.})^{+64}_{-207}(\text{syst.})$ pb, $\sigma(e^+p \to e^+\Lambda X) = 779 \pm 19(\text{stat.})^{+15}_{-36}(\text{syst.})$ pb, $\sigma(e^+p \to e^+\bar{\Lambda}X) = 724 \pm 17(\text{stat.})^{+21}_{-21}(\text{syst.})$ pb and for both Λ and $\bar{\Lambda}$ together to be $\sigma(\Lambda + \bar{\Lambda}) = 1503 \pm 26(\text{stat.})^{+28}_{-50}(\text{syst.})$ pb. Differential cross sections have been measured as a function of Q^2, x, p_T and η for K^0_S meson, Λ, $\bar{\Lambda}$ and both Λ and $\bar{\Lambda}$ baryons together. In addition the ratio $\sigma(\Lambda + \bar{\Lambda})/\sigma(K^0_S)$ has been measured as a function of Q^2, x, p_T and η. The total and the differential cross sections as well as the ratio of these are compared to ARIADNE and HERWIG Monte Carlo. ARIADNE performs a better description of the kinematics of K^0_S meson and Λ baryon production than HERWIG. An equal number of Λ baryons and $\bar{\Lambda}$ anti-baryons has been measured in total and in bins of Q^2, x, p_T and η.

ARIADNE is the overall better model to simulate the production of K^0_S meson and Λ baryon production than HERWIG.

Contents

Chapter 1

Introduction

The storage ring HERA is the world's first lepton-nucleon collider located in Hamburg, Germany. Electrons are accelerated to an energy of 27.5 GeV and protons to an energy of 920 GeV. The ZEUS experiment investigates high-energy electron-proton scattering that provide information about the processes occurring inside the proton. The 6m-tagger is a ZEUS subsystem which is positioned near the beam-pipe to intercept electrons from the interaction point. It is a very small, $85 \times 24 \times 100$ mm^3, tungsten-scintillator-spaghetti-fiber calorimeter consisting of 85 tungsten plates with $1 \times 24 \times 100$ mm^3. It has an energy resolution of $\sigma(E)/E = 17.0\%/\sqrt{E} \oplus 15.7\%/E$. Since the detector is very close to the beam-pipe the fibers have to withstand high radiation of approximately 10–20 kGy / year which corresponds to a few gray per hour at a constant dose rate. For a longer-term operation the scintillating fibers have to be radiation hard. An investigation [30] proved SCSF-38M to be the suitable fiber. Further investigation of the scintillating SCSF-38M fibers concerning the radiation damage of these fibers are measured in this thesis. Very little is known about the behavior of this fiber at temperatures above 40°C which is important for the 6m-tagger. It is placed inside a quadrupole magnet which can reach temperatures of up to 40°C. Also the effect of light which transmits inside the fiber, could have a supporting effect on the annealing of the fiber which is investigated in detail. A monitor system using a ^{60}Co source has been developed for the 6m-tagger. It is in the situation to check the quality and the status of the 6m-tagger. This method allows one to monitor mechanical damage, ageing effects and radiation damage of the scintillator.

The strange-quark production in inclusive deep-inelastic positron-proton scattering was measured before by ZEUS [44, 43, 10] and H1 [20, 19] using K^0_S, Λ and $\phi(1020)$. These measurements tested the parameters of the Lund string fragmentation as implemented in the Monte Carlo Generator JETSET [3] which has been measured by LEP experiments [2, 14]. Concerning the strangeness suppression factor $\lambda_s = P(s)/P(u)$, which sets the probability of strange quark production $P(s)$ relative to the probability of up and down quark production $P(u) = P(d)$, an indication of a difference was found [10]. Although the fragmentation should be independent of the primary scattering, the experiments at LEP measured a strangeness suppression factor of $\lambda_s = 0.3$ while the measurements at HERA prefer a value close to $\lambda_s = 0.2$. However the statistics of the measurements at HERA [20, 43, 19, 44] where not sufficient to allow a precise measurement, which is possible with the latest data from 1999 and 2000. Recent measurements of Ξ^- and $\Sigma(1385)^{\pm}$ baryons showed [47] that the strangeness suppression factor is not the sole parameter which has to be tuned, but also parameters which have an effect on the probability to create spin 1/2 relative to spin 3/2 baryons in the fragmentation. A precise measurement of the total cross section of K_S^0 meson and Λ baryon production support answering some questions. In addition differential distributions of K_S^0 meson and Λ baryon production can be measured and compared which could answer the question if the kinematics of both processes are simulated properly. Also a measurement of Λ baryons and $\bar{\Lambda}$ anti-baryons could show if an equal number of Λ baryons and $\bar{\Lambda}$ anti-baryons is produced.

The thesis is organized as follows: Chapter 2 describes the HERA collider and the ZEUS detector. In chapter 3, the investigation of scintillating SCSF-38M fibers concerning the radiation damage of these fibers are presented. ^{60}Co scans are performed on the 6m-tagger to monitor the radiation damage on the detector. Chapter 4 discusses the measurement of K_S^0 meson and Λ baryon production in neutral current deep inelastic scattering.

Chapter 2

HERA and ZEUS

2.1 The Hadron-Electron Ring Accelerator

The storage ring HERA is the world's first lepton-nucleon collider located in Hamburg, Germany, and is described elsewhere [25, 40]. The collider consists of two beam-pipes, each of them ~ 6.4 km in length, located 10 to 25 m deep under ground. One of them accelerates electrons to an energy of 27.5 GeV, the other accelerates protons to an energy of 920 GeV. The electron beam is focused by normal conducting magnets with a field of 0.16 T. Magnets of the proton beam need to produce a magnetic field of 4.7 T for bending the high momentum beam in the arcs of the ring. Therefore superconducting magnets have been constructed which operate at a temperature of 4.2 K. Electrons and protons circulate in opposite directions and are grouped in bunches. These bunches cross the interaction point (IP) at zero crossing angle every 96 ns and provide ep interactions for the experiments H1 and ZEUS. Both are used to investigate high-energy electron-proton scattering that provide information about the processes occurring inside the proton.

2.2 The ZEUS Detector

The ZEUS detector is a multipurpose detector to determine the energy, momentum and the nature of single particles and particle jets created in electron-proton scattering. A full description can be found elsewhere [45].

The ZEUS coordinate system is a right-handed orthogonal coordinate system. The X axis is pointing towards the center of HERA, the Y axis points upwards and the Z axis to the proton beam direction. The origin of the coordinate system ($X = Y = Z = 0$) is at the nominal interaction point. The polar angle θ is measured with respect to the $+Z$ axis that is referred to as the forward direction and $-Z$ as the backward direction. The angle θ is usually transferred into a pseudorapidity, η, by the formula $\eta = -\ln(\tan\ \theta/2)$. The azimuthal angle ϕ is measured relatively to the $+X$ axis.

In the following only a brief description of the parts of the ZEUS detector will be given, which are important for this thesis and the measurements which are presented. These are the Central Tracking Detector (CTD), the Uranium Scintillator Calorimeter (CAL), the luminosity monitor and the trigger system.

2.2.1 Central Tracking Detector (CTD)

The inner tracking detectors are designed to measure the tracks of charged particles. They consist of the forward (FTD), central (CTD), rear tracking (RTD) detectors and the transition radiation detector (TRD). A thin superconducting solenoid coil surrounds these chambers producing a magnetic field of 1.43 T in order to determine the trajectories of the charged particles.

The key component of this analysis is the CTD, a cylindrical drift chamber with a total length of 241 cm along the Z axis and an inner radius of 16.2 cm. The active volume has a length of 205 cm along the Z axis and an inner radius of 18.2 cm. The inner structure consists of 72 cylindrical drift chamber layers, arranged into nine superlayers. Each superlayer is subdivided into cells with eight sense wires and a total of 576 drift cells. This results in a total number of 4608 sense wires and 19584 field wires. The signal and potential wires have opposite electrical potentials. When a charged particle traverses the drift cell it ionizes the gas of the chamber. The released atomic electrons drift to the positively charged signal wire while the positively charged ions move more slowly to the field wires. The wires of the odd-numbered superlayers, the so-called axial layers, are stretched parallel to the beam axis. In the even-numbered superlayers, the so-called stereo layers, the sense wires are inclined at angles of about 5° with respect to the beam axis to allow the determination of the Z position of the tracks. Another way to determine the Z position is the Z-by-Timing system. The inner three axial superlayers are equipped with this system. The Z position of the track in the cell is obtained by measuring the difference of the arrival time of the electrons and ions.

The transverse momentum resolution of the CTD for charged tracks is $\sigma(p_T)/p_T = 0.0058p_T \oplus 0.0065 \oplus 0.0014/p_T$ with p_T being the transverse momentum of the track in GeV [21].

2.2.2 Uranium Scintillator Calorimeter (CAL)

The heart of the ZEUS detector is the uranium scintillator calorimeter (CAL) which encloses the CTD. The CAL measures the energy of particles by their absorption in a medium that becomes ionized or excited. It is a sandwich calorimeter consisting of three regions: a forward (FCAL), a barrel (BCAL) and a rear (RCAL) calorimeter. FCAL and RCAL are planar disks in proton and electron direction, respectively, while the BCAL is arranged coaxially with the beam. These calorimeter components are subdivided into two parts: the inner part is the electromagnetic calorimeter (EMC) and the outer part is called the hadronic calorimeter (HAC). FCAL and BCAL own two HAC sections. The three components are organized into modules with depleted uranium plates wrapped in stainless steel foils as absorber material and sheets of plastic scintillator (SCSN-38) as the detector of the deposited energy. The thickness of the absorber and detector plates result in equal electron and hadron response, i.e. in complete compensation. The energy resolutions obtained from test beam measurements were $\sigma(E)/E \approx 18\%/\sqrt{E} \oplus 1\%$ for electrons and $\sigma(E)/E \approx 35\%/\sqrt{E} \oplus 2\%$ for hadrons. Light generated by charged particles traverses the scintillator and is collected by plastic wavelength shifters. They transport the light to photomultipliers (PMT) where it is transformed into electrical signals. A small angle rear tracking detector (SRTD) was installed in 1994 covering the small angle region between the RTD and the beam-pipe. So a precise impact position measurement of the scattered electron and an energy correction in the rear direction is possible.

2.2.3 Luminosity monitor

The luminosity $\mathcal{L}$ is defined by the relation

$$\mathcal{L} = \frac{R}{A \cdot \sigma}$$

where R is the event rate of a process with a cross section σ and A is the acceptance of the detector for this process.

At HERA this process has traditionally been the Bethe-Heitler (BH) process [8], $ep \to e'\gamma p$, where the incoming electron radiates a high energy photon. The cross section of this process is known from QED to an accuracy of 0.5%.

Two luminosity measurement systems will be described which will be referred to as HERA-I that was in use until 2000 and HERA-II that has been in use since 2001.

Luminosity measurement with HERA-I

At about 80 m from the IP the proton beam was bent upwards so that the photons could leave the proton beam-pipe beyond this area through a copper-beryllium window. The photons were detected in the photon detector at Z $=$ 107 m. It was a lead-scintillator sampling calorimeter with an absorber in front made of a $2\ X_0$ thick graphite block to shield against synchrotron radiation. A further component of this photon detector was an air-filled Cerenkov counter to veto charged particles. The bremsstrahlung electrons with a lower energy were bend towards the center of the ring and could leave the electron beam-pipe through exit windows. At a distance of $Z = 35$ m from the IP an electron detector was installed close to the beam-line to measure the scattered electrons at angles $\theta'_e < 6$ mrad. In addition to the electron calorimeter of the luminosity system two small calorimeters located close to the beam-pipe were installed at the distances of $Z = 8$ and 44 m from the IP. They measured scattered electrons in different energy ranges and extended the kinematic range of tagged photoproduction events. Also it has been used for systematic checks of the energy scale in the reconstruction of photoproduction and in the estimation of the photoproduction background corrections in the deep inelastic scattering (DIS) [5].

A detailed description of the luminosity measurement with HERA-I can be found elsewhere [5].

Luminosity measurement with HERA-II

The luminosity measurement with HERA-II is described briefly, a detailed description can be found elsewhere [11, 12].

The luminosity of HERA-I had reached values of $L \simeq 1.4 \cdot 10^{31}$ cm^{-2}s^{-1}, which was close to the design value. The desire for an increase in luminosity was great to put the experiments in a position to do further important measurements. A long shutdown of about one year followed and new superconducting magnets were installed inside the H1 and ZEUS detectors to bend the electrons more strongly than the protons resulting in strong synchrotron radiation. The interaction region was rebuild using new magnets, vacuum pumps and synchrotron absorber systems. Since the synchrotron radiation increased to a level which does not allow a precise measurement of the luminosity with the old system, an improved luminosity monitor was designed. This new system permits an accurate luminosity measurement using two luminosity counters, the photon calorimeter and the spectrometer.

The **photon calorimeter** is a lead-scintillator-sandwich calorimeter which is protected from the high synchrotron radiation flux by two carbon filters of $2X_0$ together. Each filter is followed by an aerogel Cerenkov counter which is read out by phototubes. The calorimeter consists of 48 lead-scintillator-sandwich layers and a position detector. This consists of 16 vertical and 14 horizontal scintillator fingers each read out by a PMT. The luminosity is measured in the same way as described above for HERA-I.

The **spectrometer** determines the luminosity from the rate of the bremsstrahlung process by counting about 10% of the bremsstrahlung photons which convert to e^+e^- pairs in the beampipe window located at 92 m from the IP. A few centimeter behind this window a 60 cm long dipole magnet separates the e^+e^- pair in its bending field. The coincidence rate is measured in the spectrometer which consists of a pair of small detectors placed symmetrically above and below the photon beam.

In order to do cross-checks of the energy calibration and the acceptance for both calorimeters, a so-called **6m-tagger** is used. The detector is located behind a thin exit window for bremsstrahlung electrons (positrons[1]) inside a quadrupole at around Z ≈ -5.3 m from the IP. Thus the measurement of the energy and position of the bremsstrahlung electron (positron) is possible. Due to its position in the magnet, where temperatures up to 40°C are expected, the detector is equipped with a cooling system. The acceptance of the detector is $\sim 100\%$ for electrons (positrons) in the energy range of 5–9 GeV (4–8 GeV) [18].

The energy calibration of the photon calorimeter and spectrometer can be exactly cross-calibrated by coincidences with the 6m-tagger using the beam energy constraint, and vice versa. Since the 6m-tagger has an acceptance of nearly 100% for electrons and positrons in the specified energy range, the acceptance of the spectrometer and photon calorimeter can be measured. So a significant reduction in the systematic error of the luminosity determination is possible.

The 6m-tagger is a very small, $85 \times 24 \times 100$ mm^3, tungsten-scintillator-spaghetti-fiber calorimeter consisting of 85 tungsten plates with $1 \times 24 \times 100$ mm^3 and 1890 SCSF-38M fibers. On both

[1]It depends on the run mode of HERA II if bremsstrahlung electrons or positrons are measured.

faces the plates have semicylindrical grooves of about 0.56 mm diameter. The stacked plates are held together by three 1.5 cm wide steel straps which are fixed at the base (1 cm thickness) of the detector. Several 2 mm thick PVC plates with holes are glued to a strap at the rear side of the detector. The 1890 fibers, each machined with a diamond cutter on both sides, are glued to the PVC masks (Fig. 2.1). The fibers have a length of 1.5 m and a diameter of 0.5 mm. 27 fibers are bundled to one cell which covers a plane of 6×4.68 mm^2. In total the detector has 70 cells. The front face of the detector is painted with white color to improve the light collection efficiency and the uniformity of the signal (see chapter 3.4.2). Each cell is read-out by a R5600U Hamamatsu PMT placed in a metal box fixed below the magnet. Amber colored LEDs are connected by clear lightguide fibers to the PMTs to measure the stability of the light yield with light pulses of ~ 1 kHz.

Since the detector is very close to the beam-pipe the fibers have to withstand a high radiation dose rate of approximately 10–20 kGy / year which corresponds to a few gray per hour at a constant dose rate. For a longer-term operation the scintillating fibers have to be radiation hard. An investigation [30] proved SCSF-38M to be the suitable fiber.

2.2.4 Trigger System

The ZEUS trigger system selects a small fraction of interesting physics events and decreases the total rate of interaction which is about 10–100 MHz to an output rate of ~ 10 Hz. This trigger system has three levels.

The first level trigger (FLT) is a hardware trigger. Each detector component has its own FLT and a store pipeline, sending its decision to the global first level trigger (GFLT). The FLT reduces the input rate below 1 kHz.

The second level trigger (SLT) is a programmable transputer network. This has the advantage of using more sophisticated algorithms for rejecting background events so that the output rate is below 100 Hz.

The third level trigger (TLT) reduces the rate by an additional factor of 10, such that data is written to tape at 10 Hz. The TLT includes a better vertex fitting and track finding than it is possible for the SLT.

In addition, the kinematical parameters like $Q^2$and x are calculated at this level and used in the decision process.

Figure 2.1: Photo of the back-side of the 6m-tagger. Shown are the fibers which are glued to the PVC masks. The PVC masks are glued to the strap which is fixed at the base of the detector.

Chapter 3

Investigations of the scintillating fiber SCSF-38M

3.1 Chemical and Physical Properties of SCSF-38M

Scintillating fibers transform energy in light. This takes place when a particle hits the fiber. The scintillation light is transported through the fiber via total reflection. The fiber is wrapped in a cover to ensure this, the so-called cladding. This cladding surrounds and protects the polystyrene (PS) core of the fiber. The 'M' behind the term SCSF-38 stands for the expression 'multi-cladding'. It consists of a polymethylmethacrylate (PMMA) and a fluorinated polymer (FP) layer [28]. This cladding has a smaller index of refraction than the core (Tab. 3.1). If the flight direction of the photon from the scintillation emission is within a cone with an angle of Θ with respect to the fiber axis then the light will be transported through the fiber (Fig. 3.1). The angle Θ is set by the refraction index of the core and the cladding. Photons outside Θ are lost.

Scintillating fibers are mostly added with dyes to increase the scintillation process. These dyes in very low concentrations absorb the scintillation light to emit it at higher wavelength.

SCSF-38M is a blue scintillating fiber of the Kuraray company[1] with its emission peak at 428 nm. This multi-cladding fiber has 50% higher light yield than a single cladding SCSF-38M fiber would have because of the higher trapping efficiency. Two dyes are added to the PS core: the so-called "1. Fluor" b-PBD and "2. Fluor" BDB. One takes care of the luminescence and the other one shifts the scintillation light to the blue part [48].

The investigated SCSF-38M fibers have a so-called standard type (non-S type). This means that the PS core is of almost no oriented polystyrene chains and is optically isotropic and very transparent. The non-S type fibers have an attenuation length of more than 3 m [28] but the core can crack caused by bending. This point has been taken into consideration while handling the fiber. An overview of some physical and chemical properties of the SCSF-38M fiber are given in Tab. 3.1.

[1]Kuraray Co., Ltd., 8F, Maruzen Building, 3–10, 2-Chome, Nihonbashi, Cho-ku, Tokyo, 103–0027, Japan

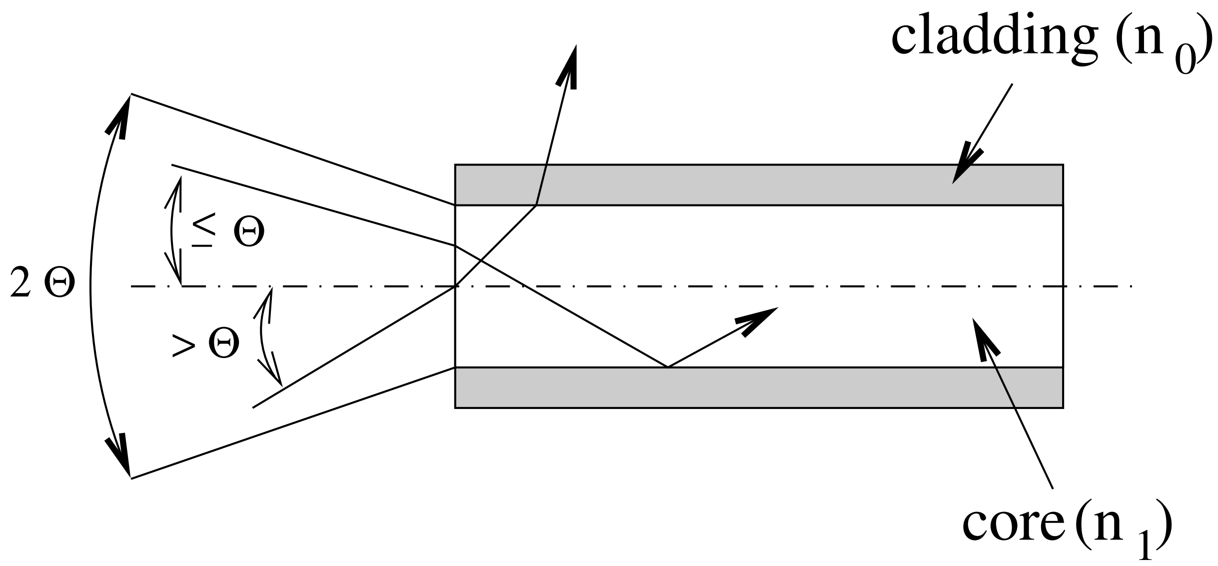

Figure 3.1: Sketch of the light transport in a scintillating fiber. If the flight direction of the photon from the scintillation emission is within a cone with an angle of Θ with respect to the fiber axis (dashed-dotted line), the light will be transported through the fiber. The angle Θ is set by the refraction index n_0 of the cladding and n_1 of the core. The relation $n_0 < n_1$ is necessary to transport the light through the fiber via total reflection.

	Material	Refractive index	Density $\left[\frac{g}{cm^3}\right]$
core	polystyrene (PS)	1.59	1.05
inner cladding	polymethylmethacrylate (PMMA)	1.49	1.19
outer cladding	fluorinated polymer (FP)	1.42	1.43

emission peak	428 nm
attenuation length	> 3.0 m
minimum bending diameter for Ø 0.5 mm fiber	100 mm

Table 3.1: Overview of some physical and chemical properties of the scintillating fiber SCSF-38M. [28]

3.2 Processes in Polymers

It is a well known fact that an optical signal suffers an additional attenuation when transmitted through an optical fiber in a radiation environment. Many parameters affect an optical fibers ability to withstand these conditions, e.g. materials, coatings, operating wavelength, temperature of operation, dose rate and total dose. Attenuation occurs in optical fibers as a result of ionizing radiation generating radicals in the material, the so-called color centers. The color centers are areas in the material that appear opaque to some wavelengths of light and transparent to others.

The damage in polymers created by irradiation is described in detail elsewhere [48]. Here, the main points are mentioned which are important for the measurements in this thesis.

Irradiation

Irradiation forms color centers which can move along the whole material and react depending on their size and movability. If oxygen is dissolved in the polymer an intense and fast reaction with free O_2 molecules will be possible. Consecutive reactions take place so that color centers are reacting through the polymer. The dose rate must be low enough for a fiber to reach an equilibrium. The equilibrium is achieved when the competition between the annealing properties and the generation of the color centers evens out to a steady state attenuation. This behavior is called saturation. Oxygen is very important for consecutive reactions and for damage annealing processes. It can reduce the radiation damage in the fiber.

Dyes in scintillating fibers can also be damaged. In this case the light yield decreases and the emission spectrum changes. The disruption of the dyes results in an improvement in the transmission.

The optical radiation damage draws attention to a change in the wavelength dependent absorption coefficient μ so that $\Delta\mu$ is a measure of the radiation induced damage. The radiation induced absorption coefficient $\Delta\mu$ of the fiber is determined by measuring the transmission before, during and after irradiation applying the formula

$$\Delta\mu = \frac{1}{l} \ln \frac{T_{\text{unirrad}}}{T_{\text{irrad}}}, \tag{3.1}$$

where l is the length of the irradiated fiber and T is the transmission of the fiber before, T_{unirrad}, and after, T_{irrad}, irradiation. Thus $\Delta\mu$ does not depend on the fiber length.

A measurement of the light intensity in the sample channel I_S, in the reference channel I_R and the pedestal I_P is performed to calculate the transmission T

$$T = \frac{I_S - I_P}{I_R - I_P} \cdot normfactor\ .$$

The $normfactor$ is determined before starting the irradiation so that the transmission is set to 1.

Annealing

The fiber anneals when color centers terminate so that the reaction chain described above is interrupted. A defect annealing takes place. No additional color centers are produced any longer.

During irradiation three color centers are generated: short-living, long-living and stable color centers. The short-living color centers decay within a few hours after irradiation. The long-living color centers cause a visible annealing effect. If the annealing is complete so that $\Delta\mu$ is not changing any longer the fiber has reached its **permanent damage**, $\Delta\mu_{\text{perm}}$. The stable color centers are responsible for the permanent damage. The **maximum damage**, $\Delta\mu_{\text{max}}$, of the fiber during a measurement is reached when $\Delta\mu$ obtains its maximum value. If the measurement is finished before reaching the permanent damage, $\Delta\mu$ is called the **final damage**, $\Delta\mu_{\text{final}}$. The permanent damage can be determined by extrapolation. By definition these three radiation induced absorption coefficients are related: $\Delta\mu_{\text{max}} \geq \Delta\mu_{\text{final}} \geq \Delta\mu_{\text{perm}}$.

3.3 In situ measurements of SCSF-38M

The optical transmission of SCSF-38M with a diameter of $\varnothing$ 0.5 mm is measured with two different setups. The fibers are irradiated at a ^{137}Cs source.

3.3.1 Setups and measurement procedures

Each measurement of the optical transmission is performed with an unirradiated SCSF-38M fiber which is wrapped around a cylindrical aluminum device with a diameter of $\varnothing$ 100 mm. This device is placed at a distance of about 50 mm from the ^{137}Cs source in such a way that the fiber has always the same distance to the source. Between the source and directly in front of the fiber a 1.25 mm thick aluminum plate is situated to develop secondary electrons. The mean dose rate $\dot{D}$ is measured with four **T**hermo **L**uminescence **D**osimeters (TLD) to be (0.97 ± 0.11) Gy/h. In this whole aluminum device two heating foils are embedded to expose the fiber to different temperatures. The temperature of this device is measured with three PT-100 temperature sensors. They are fixed at different places on the 1.25 mm thick aluminum plate which points to the ^{137}Cs source. The temperature values which are measured vary up to ± 2°C.

Two setups are used to measure the optical properties of SCSF-38M. Setup L [16] is provided with a three-color LED Nichia NSTM515S with emission peaks at blue (470 nm), green (535 nm) and red (650 nm). Setup M [48] is provided with a monochromator so that a spectral range from $\lambda = 400$ nm to $\lambda = 700$ nm can be scanned. In this case the SCSF-38M scintillating fiber which has its emission peak at 428 nm can be investigated near this wavelength. Both setups and measurement procedures are described in detail:

1. Setup L with a three-color LED
   Setup L (Fig. 3.2) is provided with a three-color LED Nichia NSTM515S with emission

peaks at blue (470 nm), green (535 nm) and red (650 nm) [16]. For a transmission measurement of the fiber the LED is switched on successively and the shutter opens first the sample channel and then the reference channel for each LED color. In the sample channel the LED light traverses first through a lightguide fiber which is connected to the investigated SCSF-38M fiber. The end of the SCSF-38M is connected to another lightguide fiber which reaches the light sensitive device, a Hamamatsu R928 photomultiplier tube (PMT). The reference channel consists only of a lightguide fiber without a reference SCSF-38M fiber. If both channels are closed no light emitted by the LEDs can reach the PMT and the pedestal can be measured. The sample and reference signal are subtracted by the pedestal signal. The changes in the LED or PMT performance are corrected by the reference channel. Each LED color illuminates the fiber for 0.33 seconds. Transmission measurements are done every 5 minutes for the 3 LED lights in Setup L. This corresponds to altogether $(3 \cdot 0.33$ seconds$) \cdot (60$ min$/5$ min$) \approx 12$ seconds of LED light per hour. In a second experiment transmission measurements were repeated every hour. This corresponds to $(3 \cdot 0.33$ seconds$) \approx 1$ second of LED light per hour.

2. Setup M with a Monochromator
   Setup M (Fig. 3.4) is provided with a monochromator and a 35 W xenon lamp as a light source. The reference position of the monochromator can be calibrated with an accuracy of ± 2 nm with a He-Ne laser ($\lambda = 633$ nm). The light is transmitted to two separate channels. In the sample channel the light passes the SCSF-38M fiber which can be irradiated by the γ rays from the ^{137}Cs source. The other channel is used as a reference and contains an identical but undamaged SCSF-38M fiber of the same length as the irradiated fiber. For a transmission measurement of the fiber the shutter opens the sample channel and keeps the reference channel closed and vice versa. This procedure is performed for each adjusted wavelength. Each wavelength illuminates the fibers for 3 seconds. Sample and reference signal are subtracted by the pedestal signal which is obtained while both shutters are closed. Transmission measurements have been performed in two ways:

   (a) The measurement of the transmission starts with a wavelength of $\lambda = 700$ nm. In steps of $\Delta\lambda_{step} = 5$ nm the transmission is measured down to $\lambda = 400$ nm. During one scan from $\lambda = 700$ nm to 400 nm 60 different wavelengths illuminate the fibers for altogether 180 seconds. The pedestal is taken after the measurement of the transmission at $\lambda = 400$ nm. After this scan the monochromator moves back to $\lambda = 700$ nm and the whole measurement procedure starts again. In this case the fibers are continuously illuminated.

   (b) The measurement of the transmission starts with a wavelength of $\lambda = 690$ nm. In steps of $\Delta\lambda_{step} = 20$ nm the transmission is measured down to $\lambda = 410$ nm. During one scan from $\lambda = 690$ nm to 410 nm 14 different wavelengths illuminate the fibers for altogether 42 seconds. The pedestal is taken after each measured wavelength. After measuring the transmission for 14 wavelengths the measurement pauses for 1 hour where the fibers are not illuminated. After this break the monochromator moves to $\lambda = 690$ nm and the whole measurement procedure starts again.

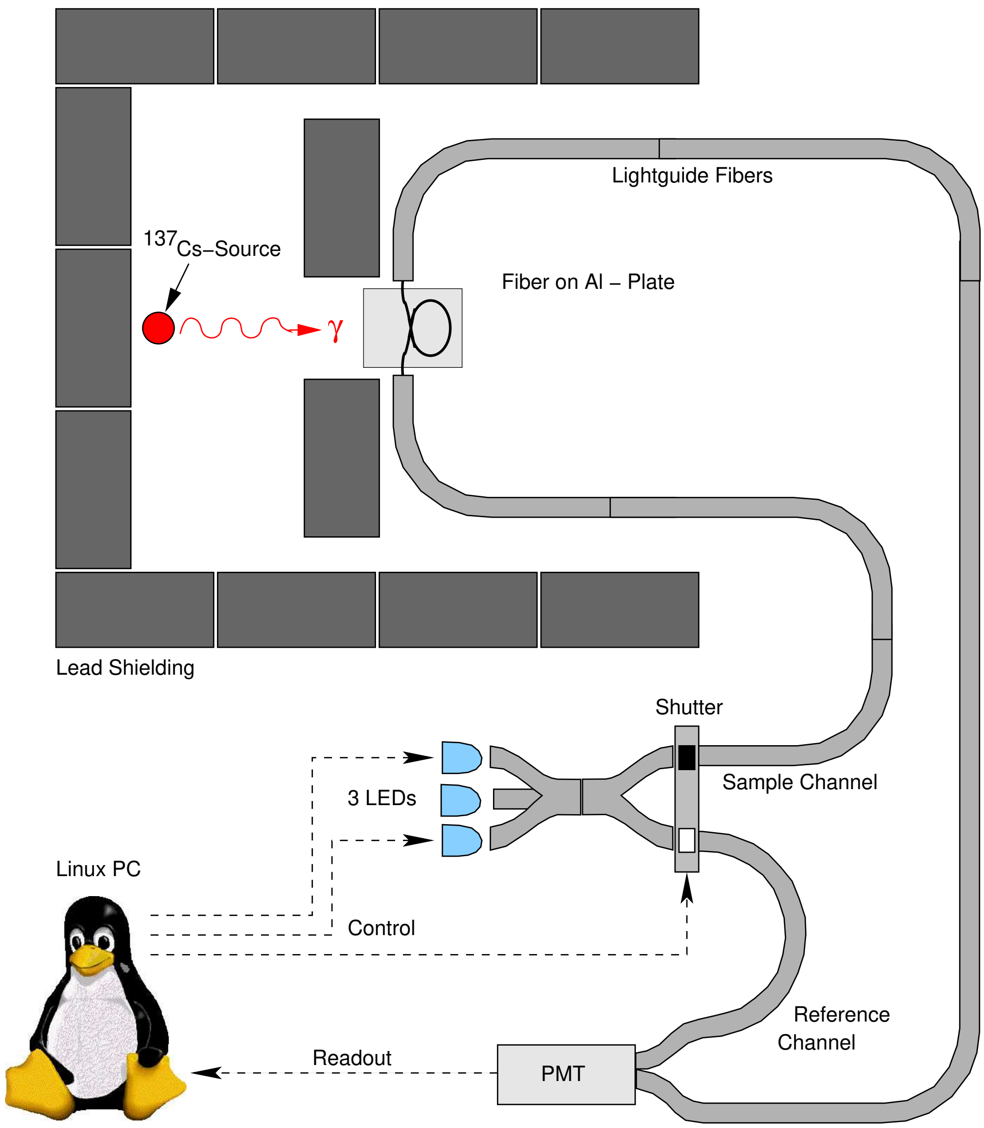

Figure 3.2: Sketch of the Setup L [16]. The ways of light through the reference and the sample channel, which are described in the text, are shown. A Linux PC controls the duration of the LED light and the shutter. The PC reads out the PMT signal via an ADC card. The shutter allows one to open the sample channel and to close the reference channel and vice versa as well as closing both channels. Only in the sample channel a SCSF-38M fiber is included, which is irradiated by the ^{137}Cs source.

In both setups the PMT signal is digitized by an analog-to-digital converter (ADC) plugged into a personal computer which switches the shutter, the LED and controls the monochromator, depending on the setup. The intensity of the LED is considerably higher than the monochromator light.

A non-linearity of the setup is observed for the measurements with Setup M. This non-linearity is investigated [17] and corrected as described in the following part.

The non-linearity can be investigated using the fluorescence light which appears while irradiating the fiber. The time when the irradiation started can exactly be determined from the data because the fluorescence light increases the signal of the pedestal. The light of the fluorescence increases the light yield of the sample and reference channel by a constant number of ADC channels independent of the signal response from the transmitted light from the xenon lamp. If the number of ADC channels in the sample channel measured after starting the irradiation is subtracted by the number of ADC channels in the sample channel measured before starting the irradiation, this difference should be constant for all wavelengths which are measured. The non-linearity of the setup is obvious when plotting the difference between the light yield with and without irradiation of the fiber versus the light yield without irradiation (Fig. 3.3). The difference decreases for a signal with more than 1400 ADC channels. A correction is necessary for all four measurements with Setup M and does only affect a small part of all wavelengths. However the non-linearity for these few points is quite strong thus a small change of the measured light yield changes the correction by a lot. This problem can be solved by a parameterization of the non-linearity. The chosen parameterization is

$$f(x) = \frac{P_1}{e^{\frac{x-P_2}{P_3}} + 1},$$

where P_1, P_2 and P_3 are free parameters of the fit and x is the number of ADC channels which is measured. The data is corrected in such a way that for a signal with more than 1400 ADC channels the parameterization which is fitted to the corresponding data sample is used to increase the signal which is measured. Since the data in the non-linear part is reasonably well described by the parameterization the estimated uncertainty of the correction is much smaller than the uncertainty from the measurement itself.

The SCSF-38M fibers have been irradiated in air. The diameter is $\varnothing\ 0.5$ mm and the total lengths vary between 100 cm and 149 cm. The doses D and dose rates $\dot{D}$ are so low $(D \leq 458$ Gy, $\dot{D} = 0.97$ Gy/h$)$ that the oxygen dissolved in the fiber is not spend during the irradiations [48].

3.3.2 Results of transmission measurements with scintillating SCSF-38M fibers

Different measurements have been performed where the effects of γ rays, fiber temperatures and time of illumination on the transmission, scintillation and induced absorption coefficient $\Delta\mu$ are investigated.

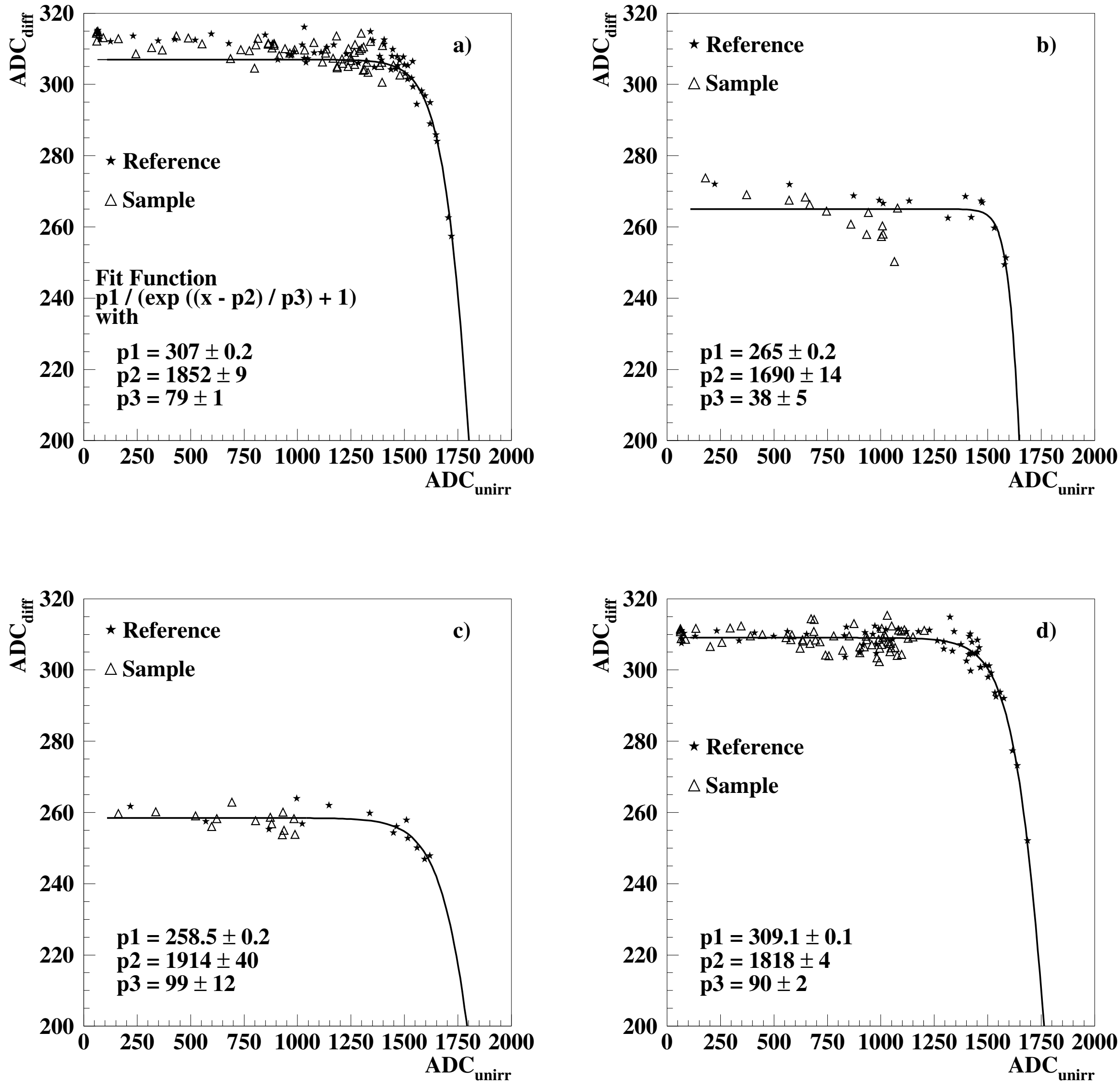

Figure 3.3: The ADC channels in the sample (△) and reference (★) channel after starting the irradiation subtracted by the ADC channels in the sample and reference channel, respectively, before starting the irradiation (ADC_{diff}) versus the number of ADC channels before the irradiation (ADC_{unirr}). The fitted parameterization is shown by a solid line. The plots correspond to the data from Setup M in the file (a) w1020603ar001.dat, (b) w1020614ar003.dat, (c) w1020708ar001.dat and (d) w1020812ar002.dat.

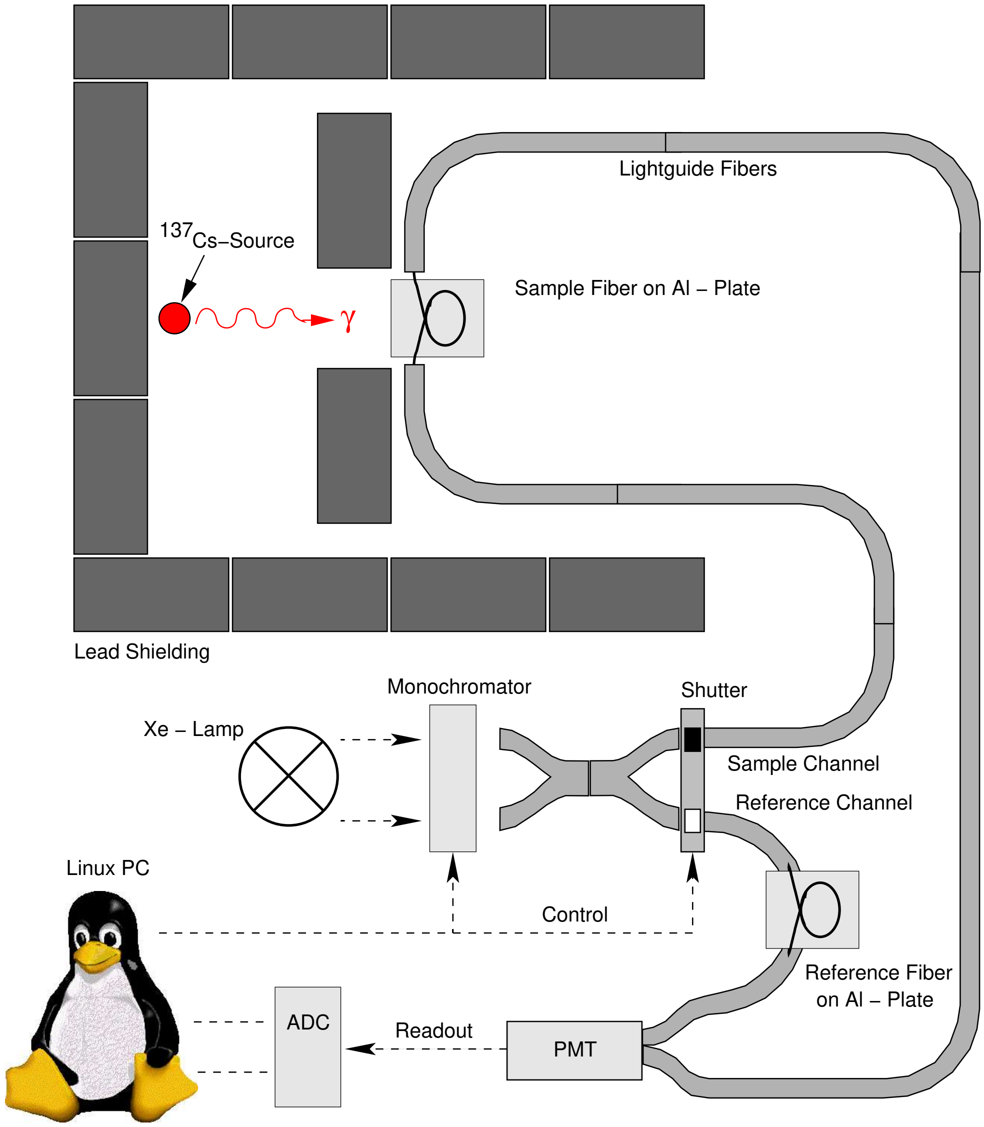

Figure 3.4: Sketch of the Setup M [48]. The ways of light, that comes from a 35 W xenon lamp, through the reference and the sample channel, which are described in the text, are shown. A Linux PC controls the shutter. The PC reads out the PMT signal via an ADC card. The shutter allows one to open the sample channel and to close the reference channel and vice versa as well as closing both channels. In both channels a SCSF-38M fiber is included, whereas the SCSF-38M fiber in the sample channel is irradiated by the ^{137}Cs source.

Irradiation of SCSF-38M

An SCSF-38M fiber with a total length of 1.380 m is investigated with Setup M-a. A length of 1.136 m is irradiated twice to a total dose of D $= 26$ Gy. The temporal development of the induced absorption coefficient $\Delta\mu$ is shown in Fig. 3.5 for the wavelengths $\lambda = 420$ nm, $\lambda = 430$ nm, $\lambda = 450$ nm, $\lambda = 500$ nm, $\lambda = 600$ nm and $\lambda = 700$ nm. The first irradiation starts at $t = 0$ h and ends at $t = 16.4$ h. The second irradiation starts at $t = 26.4$ h and ends at $t = 36.8$ h. The fiber anneals for 10.4 h between these two irradiations. In the range of the maximum fluorescence intensity ($\lambda = 415 - 455$ nm), color centers have a high absorption of light wavelengths in the UV part of the electromagnetic spectrum. This maximum damage at $\lambda = 430$ nm shows less annealing effects (Fig. 3.5(a)) than the maximum damage at $\lambda = 600$ nm (Fig. 3.5(b)) which shows an effect of annealing of 50% within 73 h.

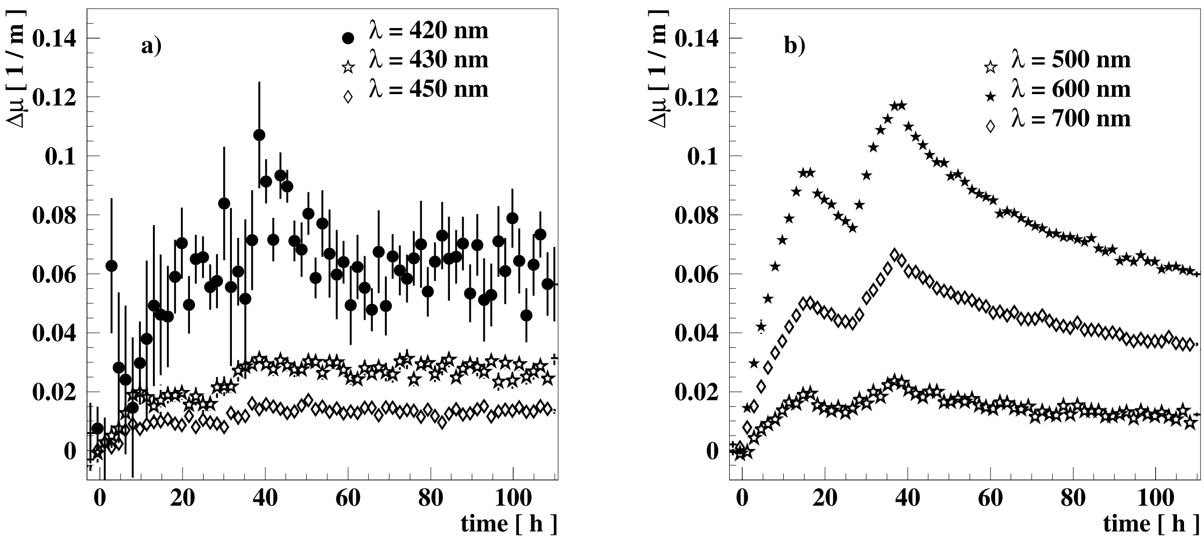

Figure 3.5: Development of the radiation induced absorption coefficient $\Delta\mu$ for the wavelengths λ of $\lambda = 420$ nm, $\lambda = 430$ nm, $\lambda = 450$ nm, $\lambda = 500$ nm, $\lambda = 600$ nm and $\lambda = 700$ nm (Setup M). The fiber was irradiated two times. The first irradiation started at a time, t, of $t = 0$ h and ended at $t = 16.4$ h. The second irradiation started at $t = 26.4$ h and ended at $t = 36.8$ h. The fiber anneals for 10 h between these irradiations. The uncertainty of the measurement is estimated to be $\pm 1\%$.

Another measurement with Setup M-b (Fig. 3.6) shows the same result concerning the radiation damage in the wavelength range of $\lambda = 430 - 470$ nm as shown in Fig. 3.5(a). In this range the color centers have a high absorption of light wavelengths in the UV part of the electromagnetic spectrum.

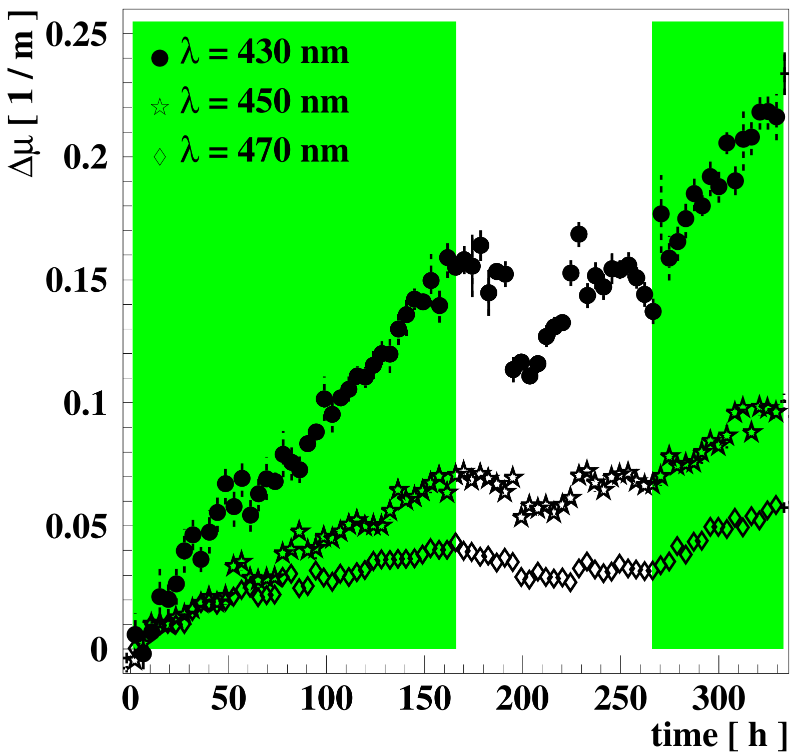

Figure 3.6: Development of the radiation induced absorption coefficient $\Delta\mu$ for the wavelengths λ of $\lambda = 430$ nm, $\lambda = 450$ nm and $\lambda = 470$ nm (Setup M). The fiber was irradiated two times. The first irradiation started at a time, t, of $t = 0$ h and ended at $t = 166$ h. The second irradiation started at $t = 266$ h and ended at $t = 338$ h. The fiber anneals for 100 h between these irradiations.

Another measurement with the same setup (Setup M-a) investigates a SCSF-38M fiber of the length $l = 1.380$ m. The length $l_{irr} = 1.136$ m of the fiber is irradiated. The transmission at a wavelength of $\lambda = 620$ nm and the dependence of the radiation induced absorption coefficient $\Delta\mu$ on wavelengths from $\lambda = 400$ nm to 700 nm in steps of $\Delta\lambda_{step} = 5$ nm are measured (Fig. 3.7). The induced absorption coefficient $\Delta\mu$ depending on the wavelengths is shown for four different times: before the irradiation ($t_1 = 10$ h), shortly after the irradiation ($t_2 = 27$ h), at the end of the irradiation ($t_3 = 165$ h) and at the end of the annealing ($t_4 = 250$ h). The fiber is continuously illuminated. The fiber is irradiated once starting at $t = 20.6$ h and ending at $t = 165$ h. The total dose is $D_1 = 140$ Gy. Two color centers are obvious, one at a wavelength of $\lambda_1 \simeq 420$ nm (C_1) and the other one at $\lambda_2 \simeq 620$ nm (C_2). The color center C_1 develops faster than C_2. During the phase of annealing C_1 is unimproved while C_2 anneals to a level of 80% with respect to the maximum damage. Taking into account, that the transmission is still slightly rising from $t = 0$ h to $t = 20$ h and not constant at 1, the shown $\Delta\mu$ distribution present a conservative measurement. Assuming that the unirradiated transmission would rise linearly, the $\Delta\mu$ would be greater. This fact is indicated by the error bar (Fig. 3.7) which is placed at $\lambda = 620$ nm and $t = 165$ h, and represents the estimated uncertainty for all $\Delta\mu$ distributions. The influence on the annealing of 80% described above could be smaller.

A similar measurement (Fig. 3.8) is performed with Setup M-b and a total and irradiated length of $l = 1.380$ m and $l_{irr} = 1.136$ m, respectively, for wavelengths $\lambda = 430$ nm to 690 nm in steps of $\Delta\lambda_{step} = 20$ nm. The fiber is illuminated for 42 seconds per hour. The fiber is irradiated twice. The first irradiation starts at $t = 66$ h and ends at $t = 233$ h. The second irradiation starts at $t = 338$ h and ends at $t = 409$ h. The total dose is $D_2 = 231$ Gy. The dependence of the radiation induced coefficient $\Delta\mu$ on the wavelengths is shown for four different times: before the irradiation ($t_1 = 65$ h), at the end of the first irradiation ($t_2 = 230$ h), at the end of the annealing ($t_3 = 338$ h) and at the end of the second irradiation ($t_4 = 405$ h). The same color centers C_1 and C_2 as seen in the previous measurement are visible at $\lambda_1 \simeq 430$ nm and $\lambda_2 \simeq 610$ nm, respectively. Again the color center C_1 shows no annealing effects while the color center C_2 befalls an annealing of 60%.

Measurements of SCSF-38M fibers with Setup M using an X-ray source were analyzed before [48]. There SCSF-38M fibers with a diameter of $\varnothing$ 1 mm and a total length of $l = 88$ cm is irradiated to a dose of $D = 0.9$ kGy ($\dot{D} = 33$ Gy/h). The dependence of the radiation induced absorption coefficient $\Delta\mu$ on wavelengths from $\lambda = 400$ nm to 700 nm in steps of $\Delta\lambda_{step} = 5$ nm were measured. Two peaks in the maximum damage were observed at $\lambda = 610$ nm and $\lambda = 655$ nm. After finishing the irradiation the peak at $\lambda = 610$ nm anneals much faster than the peak at $\lambda = 655$ nm. The structure of these two peaks cannot be seen in the measurements using a ^{137}Cs source (Figs. 3.7 and 3.8). This difference could be explained by the lower dose rate of $\dot{D} = 0.97$ Gy/h of the ^{137}Cs source.

The time development of the transmission and the induced absorption coefficient $\Delta\mu$ for a quadruplicate irradiation of the scintillating fiber SCSF-38M at room temperature is shown in Fig. 3.9 for a wavelength of $\lambda = 470$ nm. This measurement has been performed with Setup L.

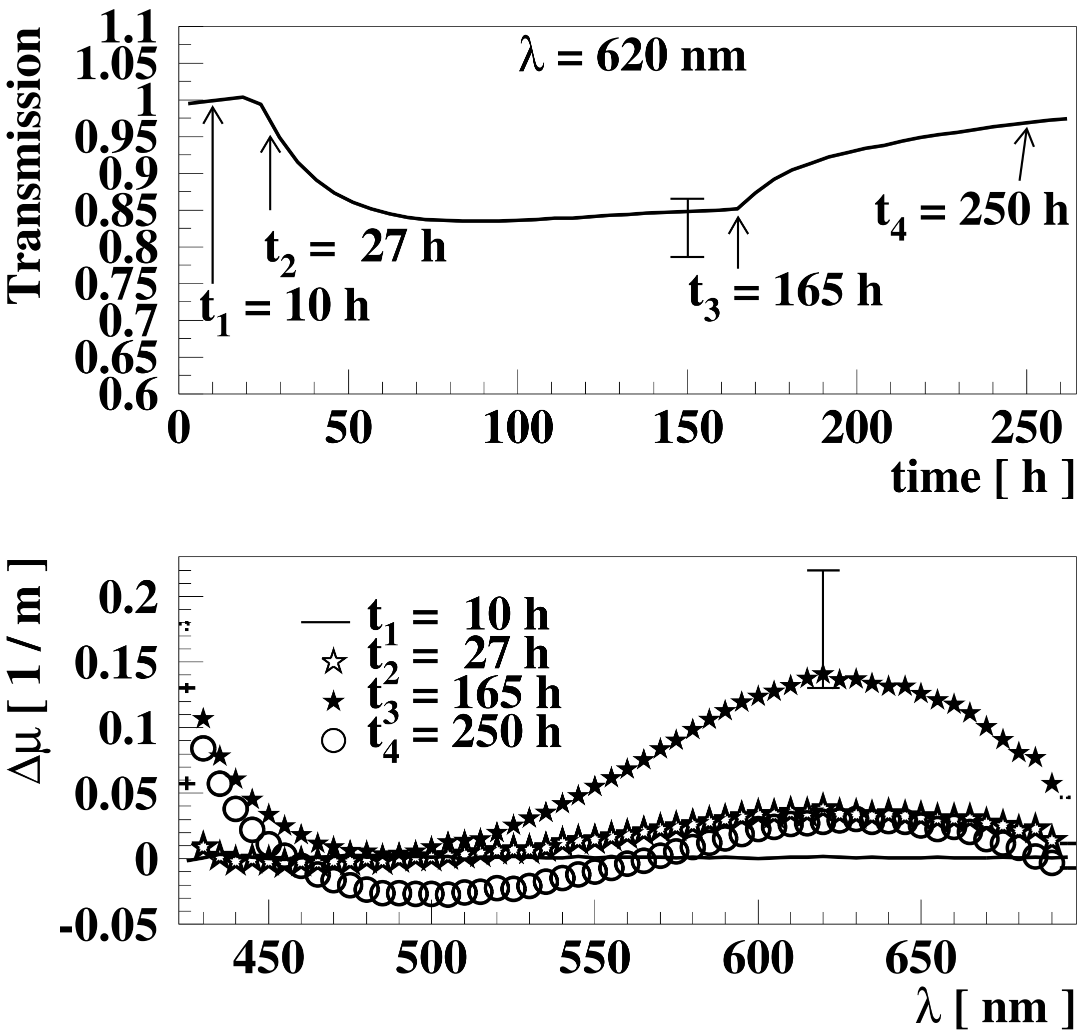

Figure 3.7: Time development of the transmission of a SCSF-38M fiber at a wavelength of $\lambda = 620$ nm (up) and the development of the radiation induced absorption coefficient $\Delta\mu$ for wavelengths from $\lambda = 400$ nm to 700 nm in steps of $\Delta\lambda_{step} = 5$ nm at the times $t_1 = 10$ h, $t_2 = 27$ h, $t_3 = 165$ h and $t_4 = 250$ h (Setup M). The fiber is irradiated once starting at $t = 20.6$ h and ending at $t = 165$ h. The irradiated fiber length is $l_{irr} = 1.136$ m and the total dose at $t_3 = 165$ h is $D = 140$ Gy. The transmission is normalized to 1 at $t = 10$ h. Taking into account, that the transmission is still slightly rising from $t = 0$ h to $t = 20$ h and not constant at 1, the shown $\Delta\mu$ distribution present a conservative measurement. Assuming that the unirradiated transmission would rise linearly (indicated by the error bar at $t = 150$ h), the $\Delta\mu$ would be greater. This fact is indicated by the error bar which is placed at $\lambda = 620$ nm and $t = 165$ h, and represents the estimated uncertainty for all $\Delta\mu$ distributions.

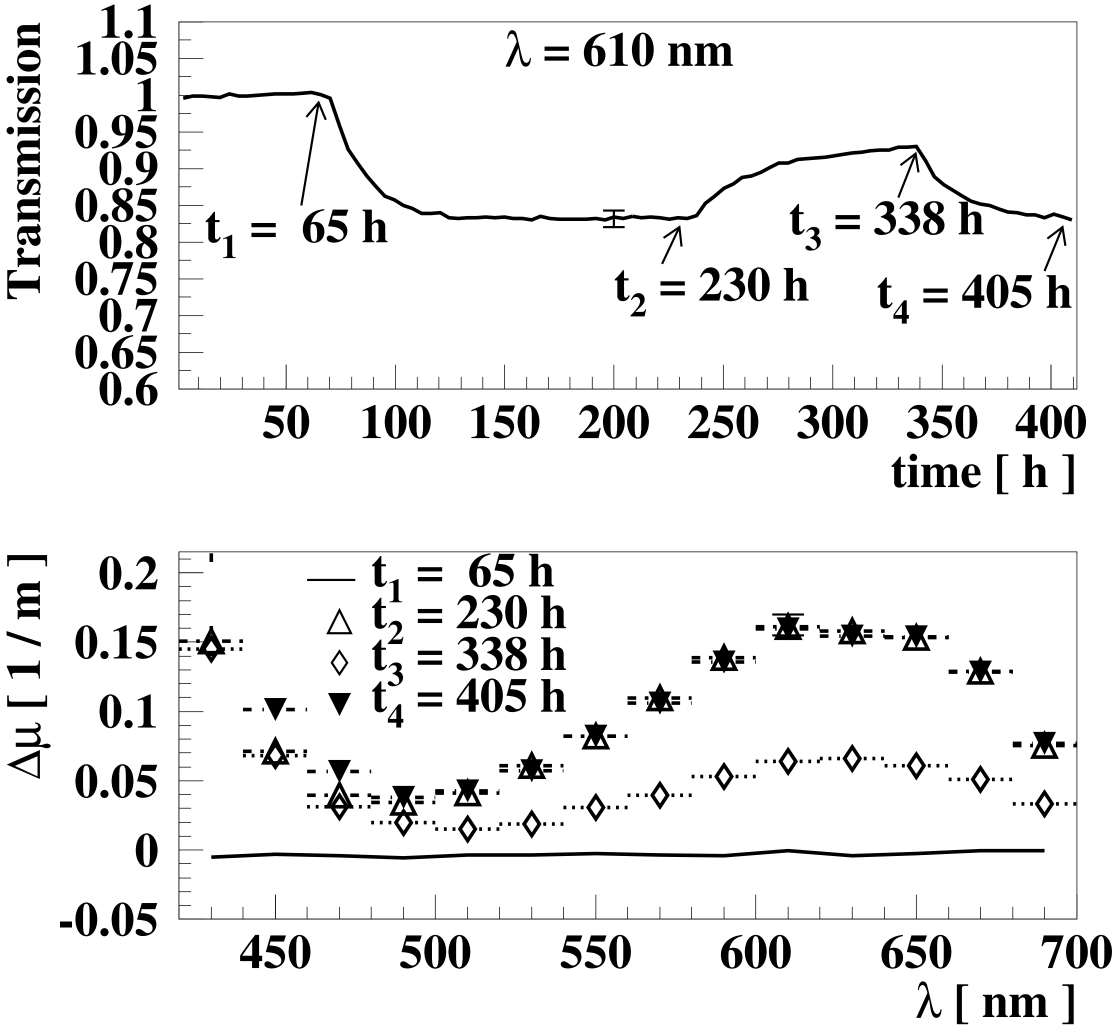

Figure 3.8: Time development of the transmission for $\lambda = 610$ nm and the development of the radiation induced absorption coefficient $\Delta\mu$ of an irradiated SCSF-38M fiber for wavelengths $\lambda = 430 - 690$ nm ($\Delta\lambda_{step} = 20$ nm) for $t_1 = 65$ h, $t_2 = 230$ h, $t_3 = 338$ h and $t_4 = 405$ h (Setup M). The irradiated fiber length is $l_{irr} = 1.136$ m with $D = 231$ Gy. The transmission is normalized to 1 at $t = 50$ h. The uncertainty of the measurement is estimated to be $\pm 1\%$ indicated by the error bars.

The fiber with a length of 1 m is irradiated at a length[2] of $l_{irr} \approx 0.7$ m to a total dose of D $= 458$ Gy. During irradiation two different types of absorption are seen (Fig. 3.9). The first type is the so-called short-living absorption and is characterized by a non-linear increase of $\Delta\mu$ right after starting the irradiation. This type can be seen three times (Fig. 3.9) namely from $t = 60$ h to $t = 95$ h, from $t = 260$ h to $t = 295$ h and from $t = 500$ h to $t = 535$ h. At the end of all these time intervals the non-linear increase changes into a linear increase of $\Delta\mu$, which means that this process of building short-living absorption saturates. The reason for this behavior is due to two processes in the fiber during the irradiation which are antipodal. On the one hand color centers are produced and on the other hand these centers decay, as explained in chapter 3.2. The decay of the color centers depends on the concentration of the participating radicals which changes during irradiation. The second type is the so-called long-living absorption and is characterized by a linear increase of $\Delta\mu$ right after the short-living absorption has saturated. The second type rises linearly with the dose which can be seen from $t = 95$ h to $t = 200$ h, from $t = 295$ h to $t = 380$ h and from $t = 535$ h to $t = 640$ h. The dose rate is so low that the oxygen dissolved in the fiber was not spend during the irradiations so that the recovery is not attributed to the diffusion of oxygen into the fiber [48].

Temperature induced ageing effect

A high temperature of $T > 40°$C is very severe for SCSF-38M fibers [39]. The mechanical properties change. A permanent bending and a permanent shrinkage will occur at temperatures more than $80°$C. Another problem is the accelerated ageing of the fiber which is even more important. The ageing phenomena is supposed to the dyes in the PS core by reacting with oxygen [39]. The gradual increase of absorption loss at short wavelengths decreases the attenuation length, which reduces the light output far from the event. The chemical change of dyes to absorptive inpurity is less than the chemical change of the PS bulk [39]. In spite of improvements concerning the ageing the following is not avoidable. The higher the temperature the more rapid the ageing proceeds.

The time development of the transmission at $\lambda = 470$ nm is measured with Setup L for a multi heating exposure up to $T = 68°$C for a fiber length of $l = 100$ cm whereas a length of $l = 52$ cm is heated (Fig. 3.10). The fiber is heated with five different temperatures and the transmission loss which is measured ($T_{\text{meas. loss}}$) is listed in Tab. 3.2. From measurements done by Kuraray [39] the values for the transmission loss, $T_{\text{loss, Kuraray}}$, of a SCSF-38M fiber with a diameter of $\varnothing$ 1 mm for $\lambda = 500$ nm are listed, too. Kuraray assumes [39] that the values for the measured transmission loss, $T_{\text{meas. loss}}$, for $\lambda = 470$ nm and a diameter of the fiber of $\varnothing$ 0.5 mm will be much higher than for $\lambda = 500$ nm at a diameter of $\varnothing$ 1 mm. This conclusion is in agreement with the measurement. The measurement is performed at room temperature until $t = 175$ h to make sure that the transmission is constant. Then the temperature is increased to $T = 40°$C for 253 hours. No transmission loss is measured at this temperature. For $T \geq 49°$C a transmission loss is observed which has its origin from the temperature. At $T = 68°$C the loss per 30.6 days is

[2]For this measurement the length of the fiber which was irradiated cannot be exactly determined. This length is more or less a guess. Thus the measured $\Delta\mu$ cannot be compared to other measurements.

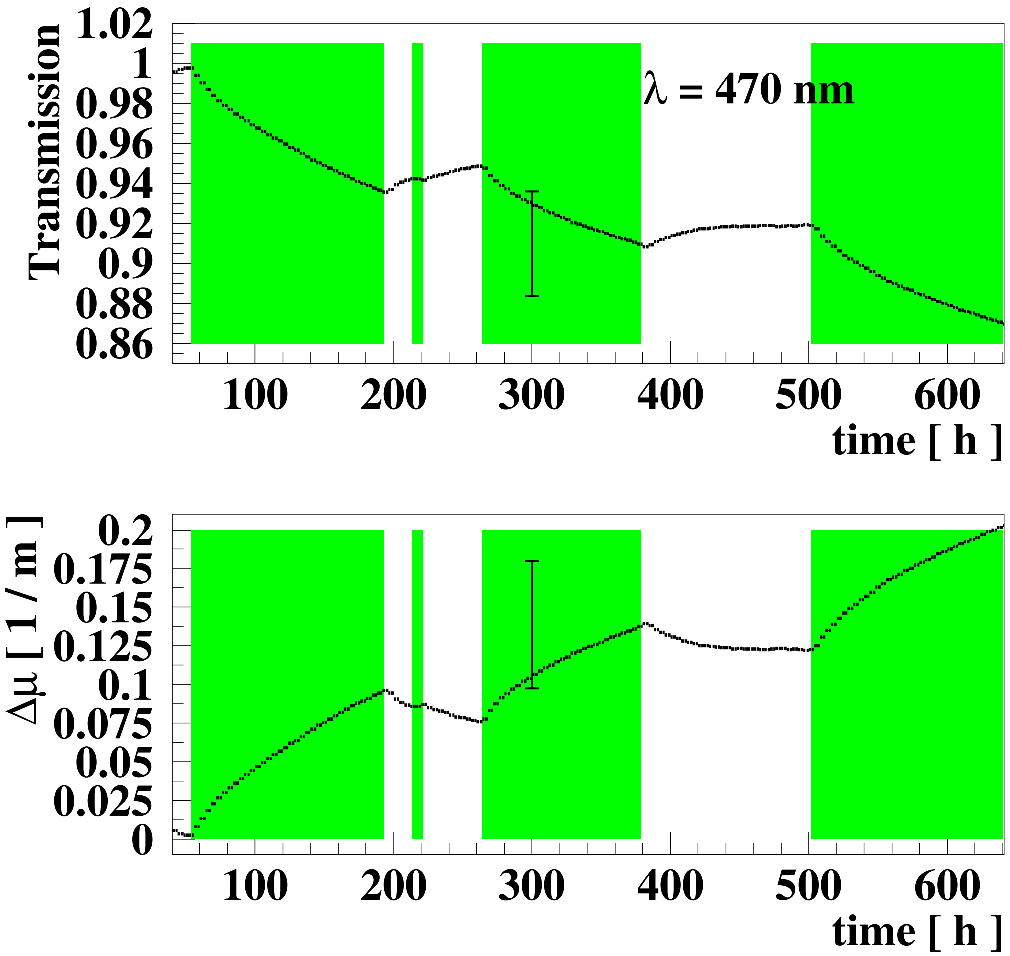

Figure 3.9: Time development of the transmission and the induced absorption coefficient $\Delta\mu$ of a SCSF-38M fiber for $\lambda = 470$ nm with a total dose of $D = 458$ Gy (Setup L). The four irradiation periods (grey boxes) are from $t = 60$ h to $t = 200$ h, from $t = 210$ h to $t = 230$ h, from $t = 260$ h to $t = 380$ h and from $t = 500$ h to $t = 640$ h.The transmission is normalized to 1 at $t = 60$ h. The uncertainty of the transmission measurement is estimated to be $^{+0.4}_{-5}\%$ indicated by the error bars.

T [°C]	d [day]	time interval [h] t_1–t_2	$T_{\text{loss, Kuraray}}$ [%] (for $\lambda = 500$ nm)	$T_{\text{meas. loss}}$ [%] (for $\lambda = 470$ nm)	$\Delta\mu/d$ [10^{-3}/(day·m)]
40	10.5	175–428	—	—	—
49	3	428–500	0.1	0.4 ± 0.1	2.6 ± 0.7
57	10	500–740	1	2.09 ± 0.02	4.06 ± 0.04
37	11.04	740–1005	0.1	-0.2 ± 0.3	-0.3 ± 0.5
60	14.17	1005–1345	1.9	3.02 ± 0.08	4.2 ± 0.1
68	30.6	1345–2080	9.2	15.1 ± 0.1	10.3 ± 0.1

Table 3.2: Transmission measurement with a heated SCSF-38M in air. The temperature, T, the duration at this temperature, d, the time intervals from Fig. 3.10, the transmission loss calculated using data measured by Kuraray, $T_{\text{loss, Kuraray}}$, the measured transmission loss, $T_{\text{meas. loss}}$, and the absorption coefficient per day, $\Delta\mu/d$, are given.

$(15.1 \pm 0.1)\%$ for a heated fiber length of $l = 52$ cm. This accelerated ageing phenomenon due to the temperature is only seen at high temperatures and it never recovers so that the fibers are permanently damaged. This measurement is important for the SCSF-38M fibers which are used in the 6m-tagger (chapter 3.4). The 6m-tagger is exposed to temperatures up to $T = 40$°C [46] and has an active length of 10 cm. The maximum transmission loss which is measured would correspond to a transmission loss of nearly 3% per month for a fiber length of $l = 10$ cm at $T = 68$°C.

Irradiating and heating the SCSF-38M fiber

A combined measurement with irradiation and heating has been performed with a fiber with a total length of $l = 1.49$ m whereas $l = 1.43$ m have been irradiated three times and exposed to four different temperatures (Fig. 3.11). Setup L is used for this measurement. Starting with T_1 = RT (room temperature) the fiber is irradiated from $t = 0$ h to $t = 198$ h. Then the fiber anneals for $t = 345$ h at room temperature until $t = 543$ h. Then the temperature is increased to $T_2 = 54$°C and the fiber anneals for further 120 h. At $t = 663$ h the irradiation of the fiber starts and ends at $t = 970$ h at a temperature of $T_2 = 54$°C and anneals for 248 h. Then the temperature is decreased to $T_3 = 26$°C for the period from $t = 1218$ h to $t = 1405$ h. From $t = 1405$ h on, the annealing continuous for 99 h at a temperature of $T_4 = 40$°C. At this temperature the third irradiation starts at $t = 1504$ h and ends at $t = 1667$ h. The fiber anneals until the rest of the measurement at $T_4 = 40$°C. After increasing the temperature to $T_2 = 54$°C the transmission decreases even without any irradiation as seen in Fig. 3.11, too. However the fluorescence light seems to be not affected by the increased temperature since the light yield of the fluorescence starts at the same level for T_2 as it stopped after the irradiation at T_1. The same is valid for the third irradiation. Also here the fluorescence light yield stays stable although the temperature changed.

The decrease of the fluorescence ($\Delta F \approx 35\%$ at $t \approx 1650$ h) cannot be completely explained by

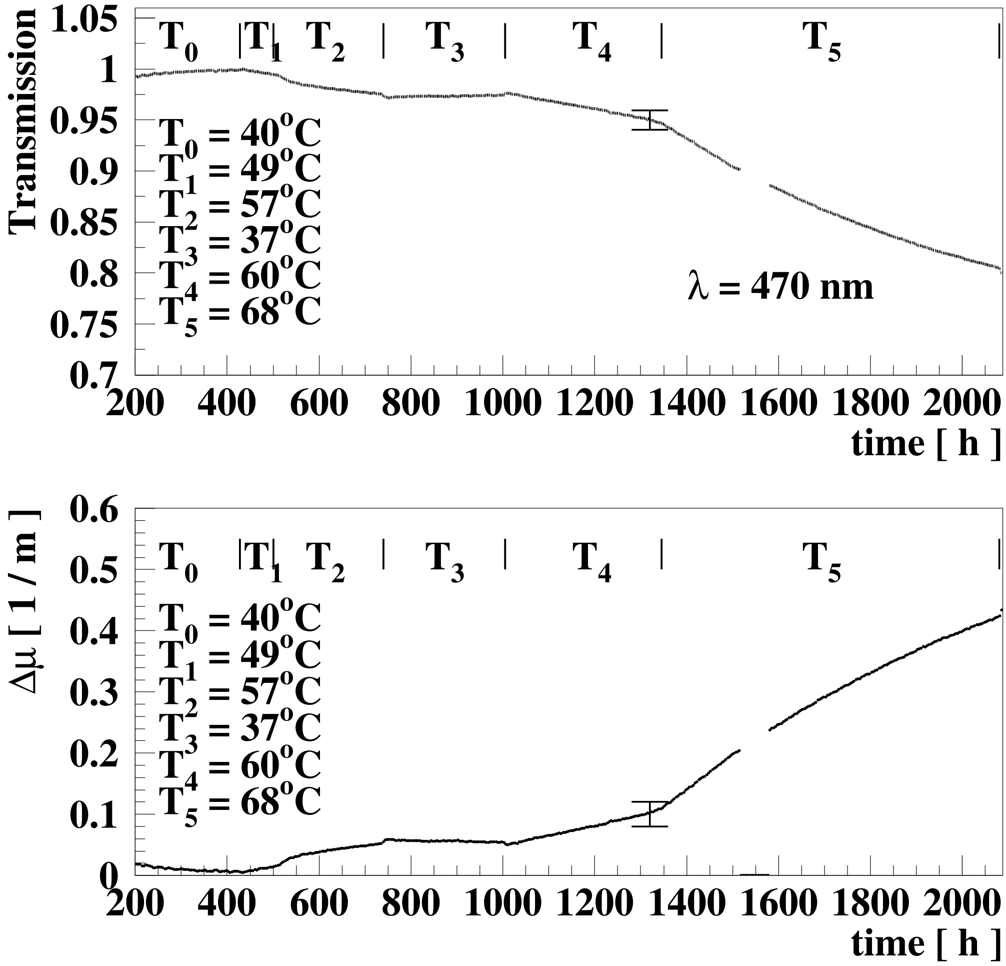

Figure 3.10: Time dependent transmission and radiation induced absorption coefficient, $\Delta\mu$, of a SCSF-38M fiber at different temperatures, T (Setup L, wavelength $\lambda = 470\,\mathrm{nm}$). The measurement started at room temperature, $T \approx 24°$C. The temperature of the SCSF-38M fiber was set to $T_0 = 40°$C, $T_1 = 49°$C, $T_2 = 57°$C, $T_3 = 37°$C, $T_4 = 60°$C and $T_5 = 68°$C. The transmission is normalized to 1 at $t = 400$ h. The uncertainty of the measurement is estimated to be $\pm1\%$ indicated by the error bars.

the increase of the absorption. The decrease of transmission amounts nearly $\Delta T \approx 25\%$ at $t \approx 1650$ h. Assume that the fluorescence light is generated in the center of the fiber then it should apply in a simplified way to $\Delta F \approx \frac{1}{2} \cdot \Delta T$. In this case there is no agreement. A possible reason for this discrepancy could be the different values of the fluorescence light maximum at $\lambda = 428$ nm and the transmission measurement wavelength at $\lambda = 470$ nm.

Temperature effect on the induced absorption coefficient

The induced absorption coefficient $\Delta\mu$ of the scintillating fiber SCSF-38M at room temperature from Fig. 3.9 for a wavelength of $\lambda = 470$ nm is shown in Fig. 3.12(a) for the first, the third and the forth irradiation. The second irradiation was only 20 h long and is not shown. These three distributions are plotted in such a way that all three irradiations start at the same time $t = 0$ h and end at $t = 120$ h. The $\Delta\mu$ distribution of the scintillating fiber SCSF-38M at different temperatures presented in Fig. 3.11 for a wavelength of $\lambda = 470$ nm is shown again in Fig. 3.13(a) for all irradiations. Also here the distributions are plotted in such a way that all three irradiations start at the same time $t = 0$ h and end at $t = 120$ h. Since the irradiated length of the fiber with the measurement at room temperature only (Fig. 3.12(a)) cannot exactly be determined the $\Delta\mu$ distribution with and without heating (Fig. 3.13(a)) cannot directly be compared. However, the effect introduced by the higher temperature can be investigated by measuring the ratio $\Delta\mu/\Delta\mu_1$ of the induced absorption coefficient $\Delta\mu$ to the induced absorption coefficient of the first irradiation $\Delta\mu_1$. Comparing this ratio with (Fig. 3.12(b)) and without (Fig. 3.13(b)) heating the distribution for $T = 54$°C shows a special feature. The ratios for $T \leq 40$°C show, after a fast increase ($t < 30$ h), a nearly constant run of the curve, while at $T = 54$°C the ratio increases nearly linearly from $t \approx 35$ h on. This effect is due to the accelerated ageing of the fiber which is already discussed above.

Photobleaching

A fibers tendency to attenuate is sometimes suppressed by its self healing abilities. The ability of a fiber to heal itself or anneal is aided by the light that transmits down the fiber while in a radiation environment. This self annealing is called photobleaching.

The radiation induced transmission loss reduction of optical fibers has been investigated with respect to the suitability for radiation dosimetry purposes [24]. A strong acceleration of the annealing with increasing light power was observed with fibers with pure SiO_2 core after irradiation at a temperature of $T = 24$°C. So far such an accelerated annealing effect has not been observed in scintillating fibers.

Measurements have been performed with successive illuminations of blue, green and red LED light with Setup L (chapter 3.3.1). Two measurements with different time of illuminations are compared. In one measurement the fiber is illuminated for 1 second per hour, while in a second measurement the fiber is illuminated for 12 seconds per hour (chapter 3.3.1). The time development of the transmission is measured and the induced absorption coefficient $\Delta\mu$ for a wavelength

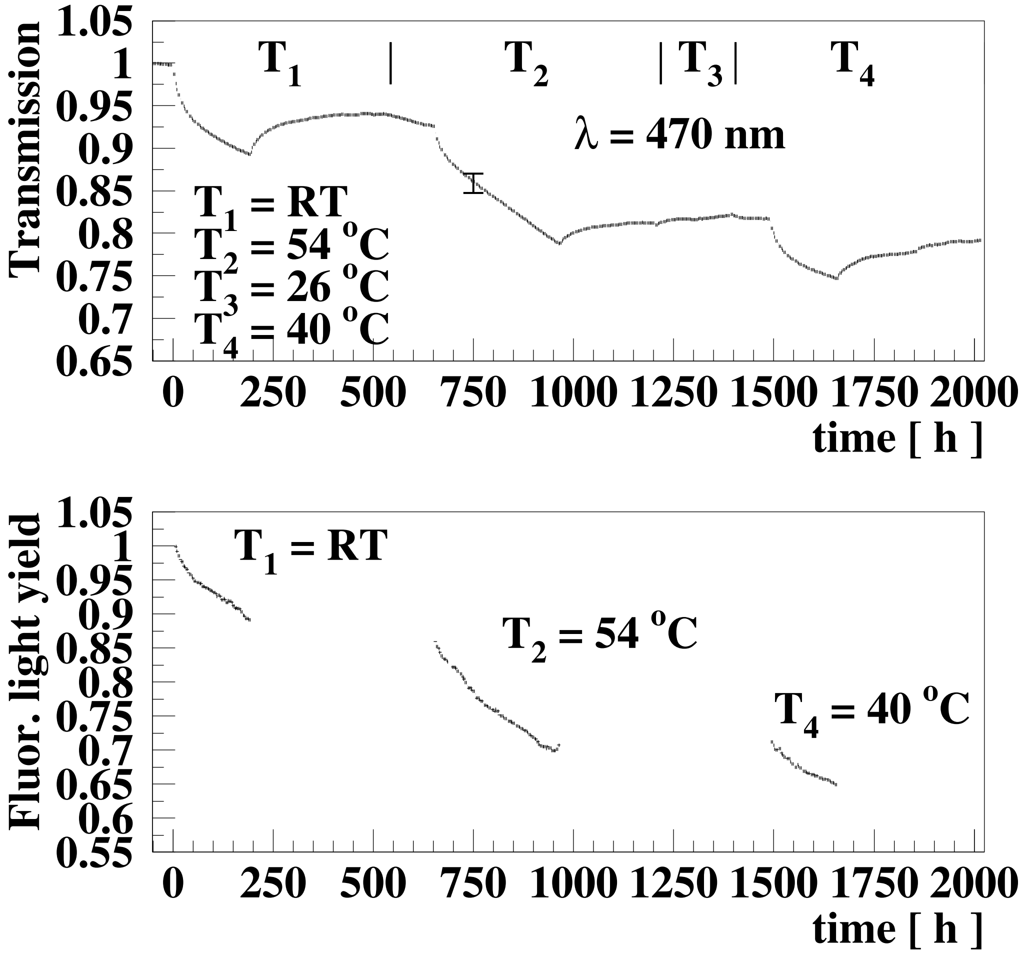

Figure 3.11: Time dependent transmission and light yield of fluorescence of a SCSF-38M fiber which is irradiated three times and exposed to four different temperatures T. The fiber is irradiated from $t = 0$ h to $t = 198$ h at RT, from $t = 663$ h to $t = 970$ h at $T_2 = 54$°C and from $t = 1504$ h to $t = 1667$ h at $T_4 = 40$°C. The transmission and the light yield of the fluorescence are normalized to 1 at $t = 0$ h. The uncertainty of the measurement is estimated to be $\pm 1.5\%$ indicated by the error bar.

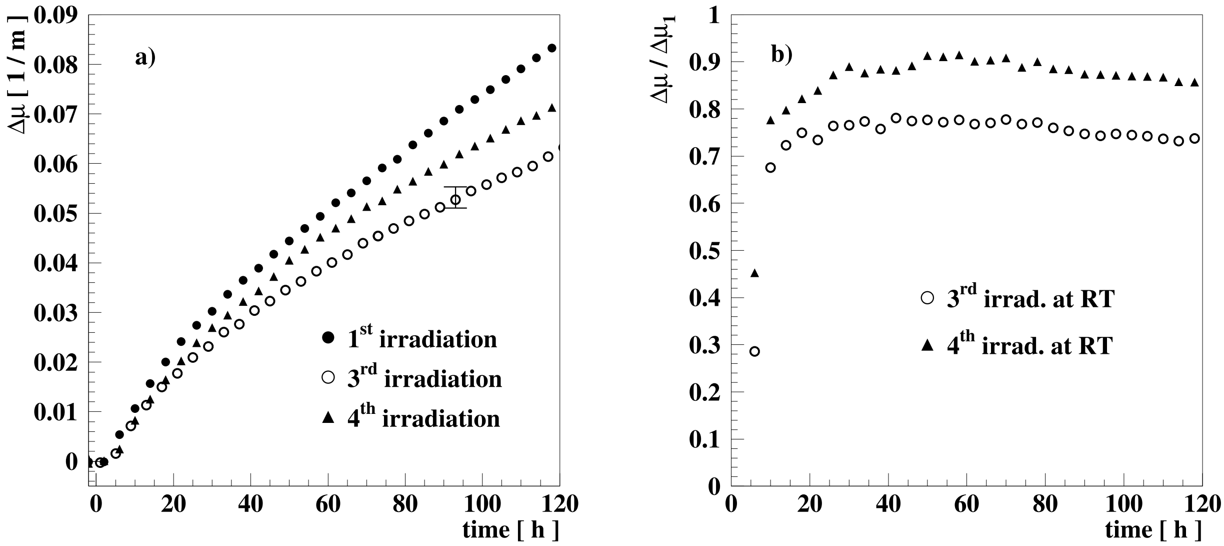

Figure 3.12: (a) The induced absorption coefficient $\Delta\mu$ for a wavelength of $\lambda = 470$ nm. The first, third and forth irradiation at RT (room temperature, see Fig. 3.9) is shown in such a way that all three irradiations start at the same time $t = 0$ h. The second irradiation was only 20 h long and is not shown. The uncertainty of the absorption coefficient is estimated to be $^{+5}_{-0.4}\%$ indicated by the error bar. (b) The ratio $\Delta\mu/\Delta\mu_1$ of the induced absorption coefficient $\Delta\mu$ to the induced absorption coefficient of the first irradiation $\Delta\mu_1$ is presented.

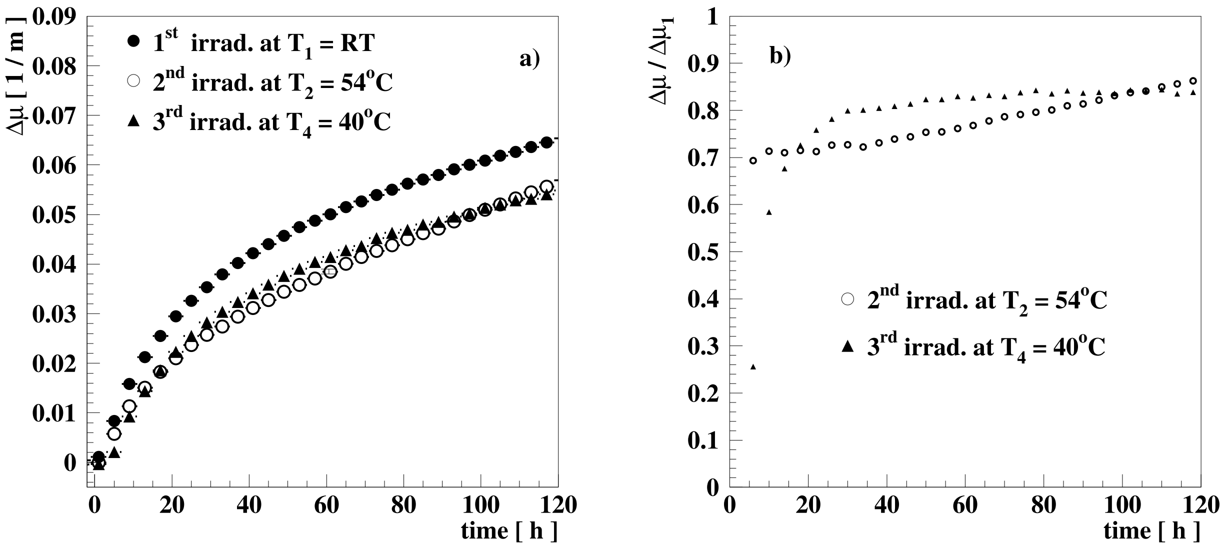

Figure 3.13: (a) The induced absorption coefficient $\Delta\mu$ for a wavelength of $\lambda = 470$ nm. The first, second and third irradiation at different temperatures (see Fig. 3.11) is shown in such a way that all three irradiations start at the same time $t = 0$ h. The uncertainty of the absorption coefficient is estimated to be $\pm 1.5\%$ indicated by the error bar. (b) The ratio $\Delta\mu/\Delta\mu_1$ of the induced absorption coefficient $\Delta\mu$ to the induced absorption coefficient of the first irradiation $\Delta\mu_1$ is presented.

λ of $\lambda = 470$ nm is shown for both measurements (Fig. 3.14). At the beginning of the irradiation $(t \leq 15$ h$)$ color centers are produced equally in both measurements. After $t = 96$ h which corresponds to a dose D of $D = 93$ Gy the more illuminated fiber has a smaller induced absorption coefficient than the less illuminated one. With 11 seconds more LED light per hour the induced absorption coefficient is 40% lower than for the other measurement at the same time $t = 96$ h. At $t = 235$ h the time of illumination of the fiber which has been illuminated with 1 second of LED light per hour is increased to 12 seconds of light per hour. At this time the fiber has annealed for $\Delta t = 139$ h. This change supports an extra and faster annealing than with 1 second of light per hour only. The recovery in the blue part of the absorption spectrum is observed to be higher with more illumination. Consequently the permanent induced absorption coefficient per absorbed dose $\Delta\mu_{perm}/D$ differ roughly by a factor of 4 for the two curves at the end of both measurements.

This photobleaching effect is confirmed with measurements with Setup M. In Setup M the total illumination with light is set to 42 seconds per hour and continuous illumination (chapter 3.3.1). Combined with the measurements from Setup L a clear dependence of the induced absorption coefficient on the illumination with light is obvious (Fig. 3.15). At a dose of $D = 93$ Gy the induced absorption coefficient is reduced by 60% for 42 seconds of light per hour with respect to the Setup L measurement with 1 second of LED light per hour whereas the induced absorption coefficient is reduced by 90% with continuous illumination.

At this stage it is not sure whether the blue, green or red LED light is responsible for this photobleaching effect.

The illumination has an effect on the scintillation, too, as can be seen from Fig. 3.16. There the time development of the fluorescence light is shown for the four measurements described above (Fig. 3.15). More light, up to 42 seconds of light per hour, results in an improved light yield of the scintillation. However, for continuous illumination the light yield of the scintillation is degraded with respect to the measurement with 42 seconds of light per hour. Therefore the positive effect of photobleaching in the induced absorption coefficient is not visible in the fluorescence light yield measured with Setup M. This behavior cannot be explained. The real fluorescence reduction is estimated by the difference of the actual fluorescence reduction and the uncertainty of the setup. The uncertainty is indicated by the error bars.

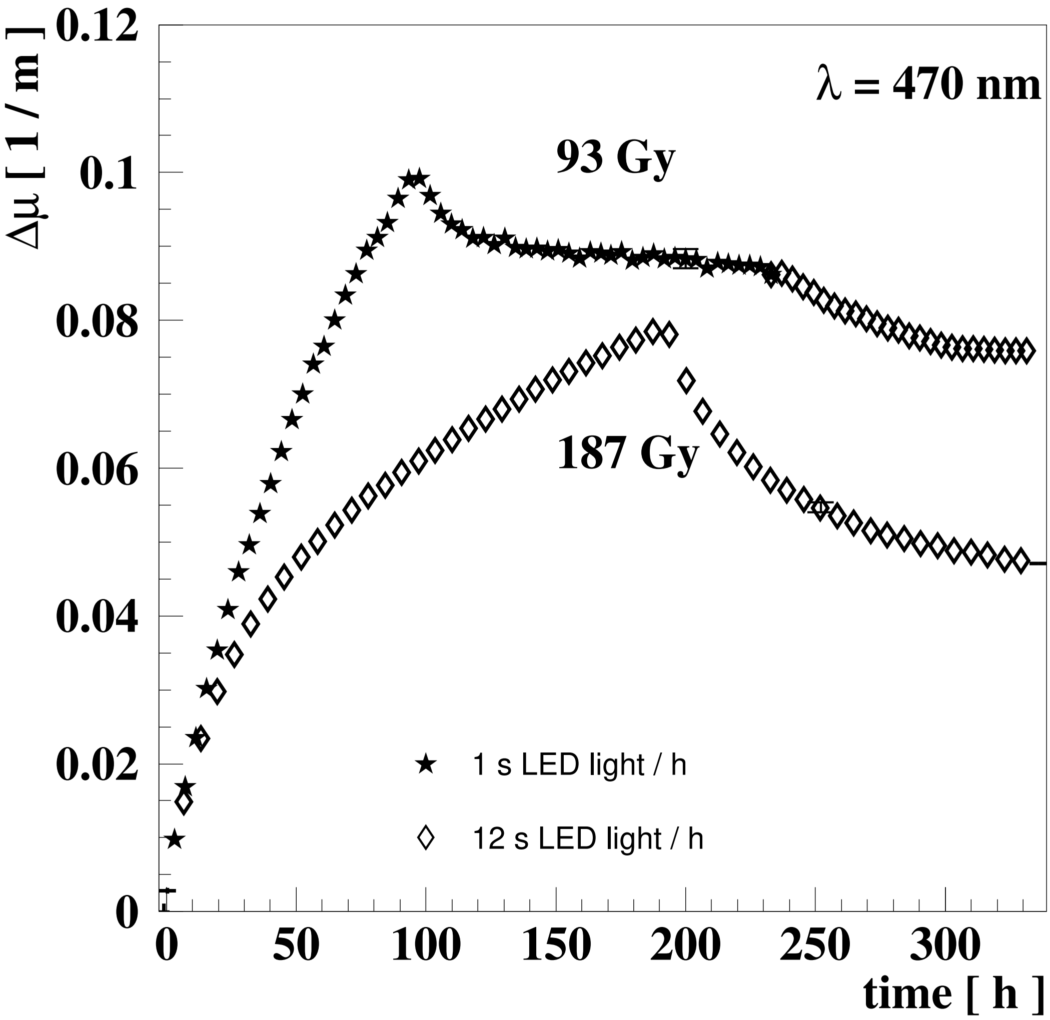

Figure 3.14: Time dependent radiation induced absorption coefficient $\Delta\mu$ of SCSF-38M measured with Setup L for $\lambda = 470$ nm. The measurement with 1 second of LED light per hour ($\star$) is irradiated until $t = 96$ h which corresponds to a dose of $D = 93$ Gy. The measurement with 12 seconds of LED light per hour ($\diamondsuit$) is irradiated until $t = 193$ h which corresponds to a dose of $D = 187$ Gy. The uncertainty of both measurements is estimated to be $\pm 1.5\%$ indicated by the error bars.

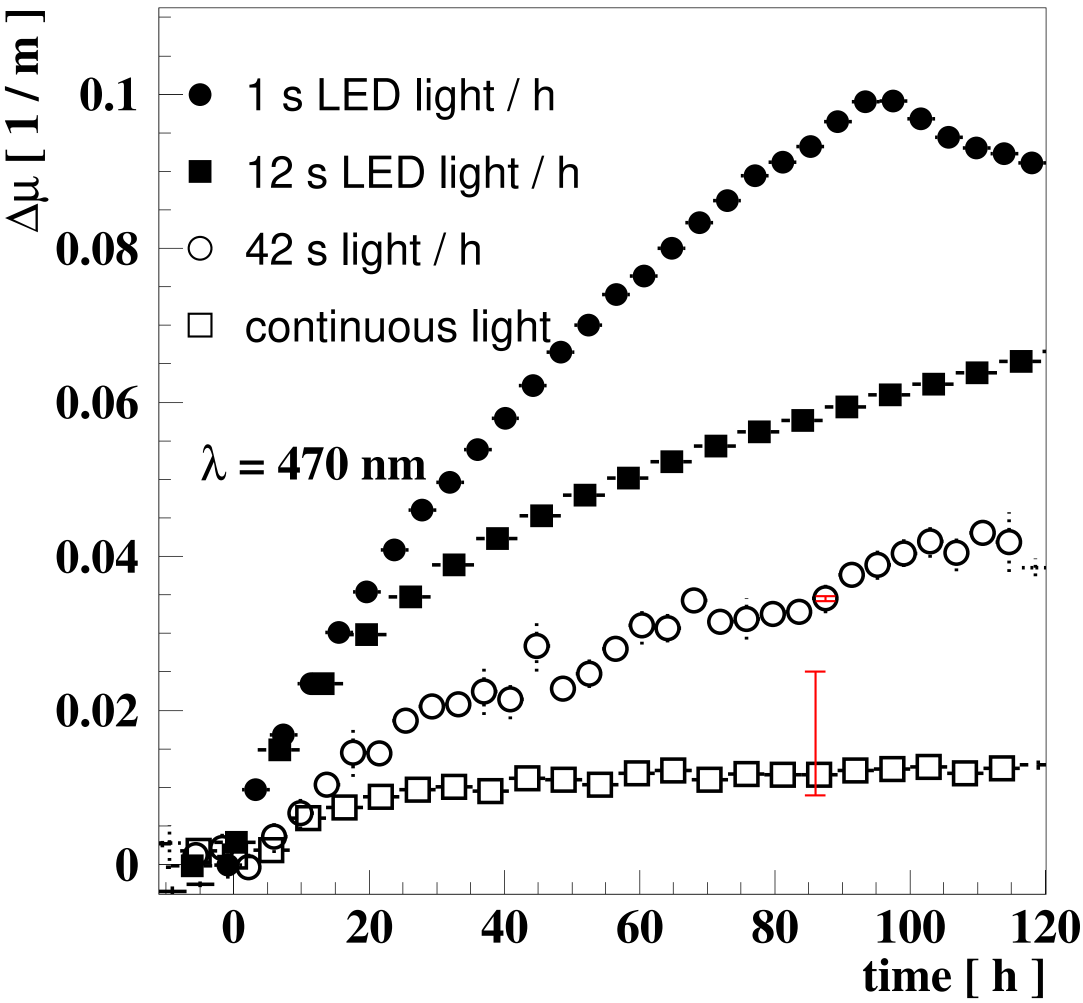

Figure 3.15: Time dependent radiation induced absorption coefficient $\Delta\mu$ of SCSF-38M measured with Setup L and M for $\lambda = 470$ nm. Measurements with Setup L (• and ■) are from Fig. 3.14. The uncertainty of these measurements is estimated to be $\pm 1.5\%$ indicated by the error bars. The measurement with 1 second of LED light per hour (•) is irradiated until $t = 96$ h which corresponds to a dose of $D = 93$ Gy. The measurement with 12 seconds of LED light per hour (■) is irradiated longer than plotted. The measurements, taken with Setup M, are illuminated with 42 seconds of light per hour ($\circ$) and with continuous light ($\square$) and are irradiated for more than 120 hours. The uncertainty of these measurements is estimated to be $\pm 1\%$ and $^{+2.5}_{-0.4}\%$, respectively, indicated by the error bars.

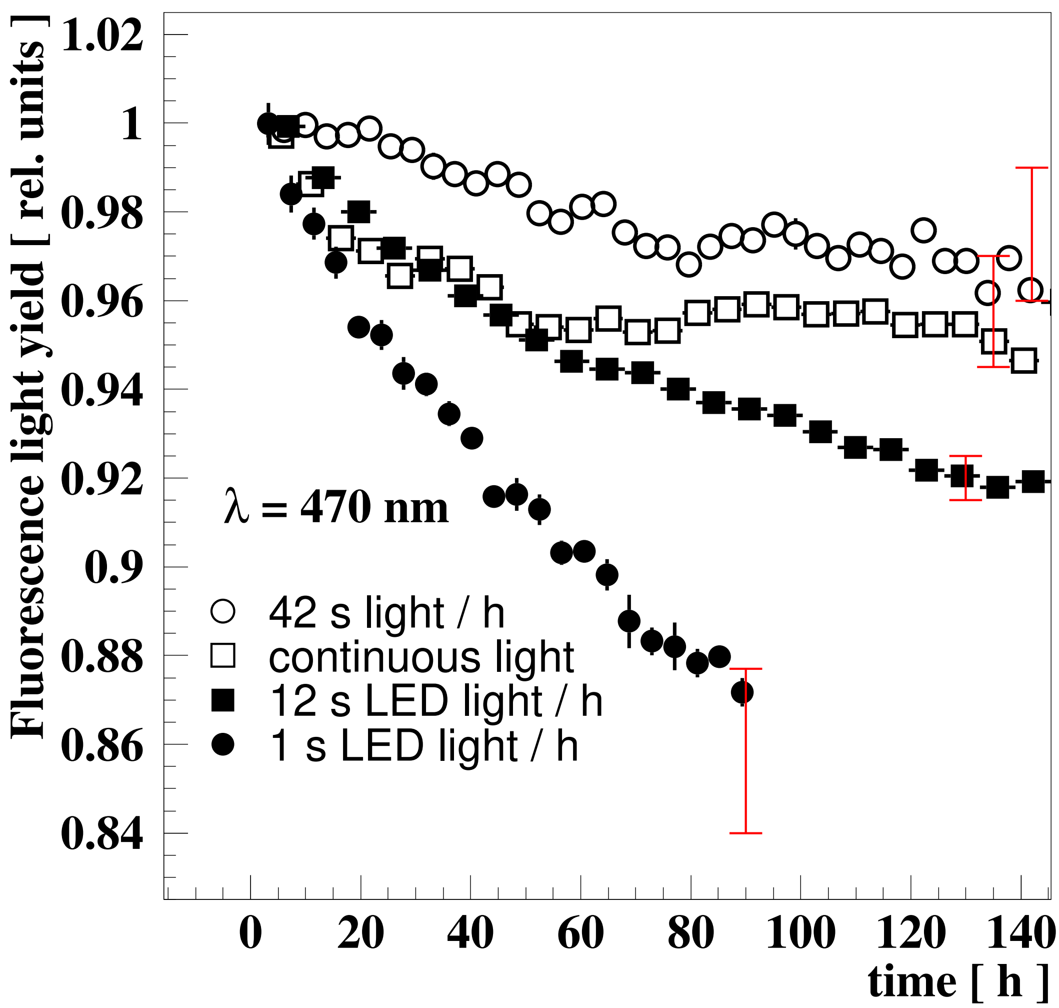

Figure 3.16: Time dependent light yield of fluorescence of SCSF-38M measured with Setup L and M. Measurements with Setup L (• and ■) the same as shown in Fig. 3.14 (the fluorescence reduction is estimated to be -7.5% and -8.4%, respectively). The measurement with 1 second of LED light per hour (•) is irradiated until $t = 96$ h which corresponds to a dose of $D = 93$ Gy. The measurement with 12 seconds of LED light per hour (■) is irradiated longer than plotted. The measurements, taken with Setup M, are illuminated with 42 seconds of light per hour (○) and with continuous light (□) and are irradiated for more than 120 hours (the fluorescence reduction is estimated to be -1% and -3%, respectively).

3.4 Measurements with the 6m-tagger and a ^{60}Co source

A monitor system using a ^{60}Co source has been used for the 6m-tagger. It allows the detection of changes in the performance of the scintillators as well as the drifts in the gain of the PMTs.

The 6m-tagger was calibrated during a test-beam with electrons in May 2001. There it was ensured that all 70 cells of the calorimeter produce the same signal response if hit by electrons of the same energy. The calibration was performed with 5 GeV electrons and is described elsewhere [27]. The energy resolution was measured to be $\sigma(E)/E = 17.0\%/\sqrt{E} \oplus 15.7\%/E$. In order to transport the electron calibration from the test-beam to the ZEUS experiment a relative cell-to-cell calibration was done with a ^{60}Co source. The source was used in different ways to produce scintillation light in the fibers which are read-out. The ^{60}Co monitor system is described in detail elsewhere [7]. It is in the situation to check the quality and the status of the 6m-tagger. This method allows one to monitor mechanical damage, ageing effects and radiation damage of the scintillator.

3.4.1 ^{60}Co setup

A 2 mCi point-like ^{60}Co source is attached to the tip of a steel wire. The wire and the source are enclosed inside a stainless-steel tube. This source wire is guided through brass tubes which run parallel to the scintillating fibers. Altogether 8 brass tubes, which are labeled as scan tubes, are located above and below the 6m-tagger at defined positions and 2 brass tubes, which are labeled as calibration tubes, are placed at the base of the detector. The calibration tubes jut out of the front-side of the detector, so that the end of these tubes is 14 cm in front of the detector while the scan tubes end at the front side of the detector (Fig. 3.17). The end of all tubes are sealed thus the source is at a defined position when starting the measurement.

A PC-controlled motor withdraws the ^{60}Co source wire starting at the sealed side of the brass tubes which are mounted parallel to the scintillating fibers of the 6m-tagger. The wire is moved in steps of 3 mm and the radiation causes a local energy deposition in the fibers. This creates a signal response depending on the position of the source. The pedestal is determined by moving the source inside a lead ball. This pedestal is subtracted from the signal response. Only pedestal subtracted signals are shown.

3.4.2 Measurements with a 5 cell 6m-tagger model and a ^{60}Co source

First measurements have been performed on a small 6m-tagger model consisting of 5 cells and 1 source guide tube embedded in an aluminum device. Compared with Fig. 3.17 this model consists of the cells 1D to 5D only.

With this model of the 6m-tagger the signal responses and a possible improvement of the light yield and the optimal calibration distance have been investigated. For this model only one tube was mounted in such a way that the tube ended at the rear side of the detector (Fig. 3.18). The

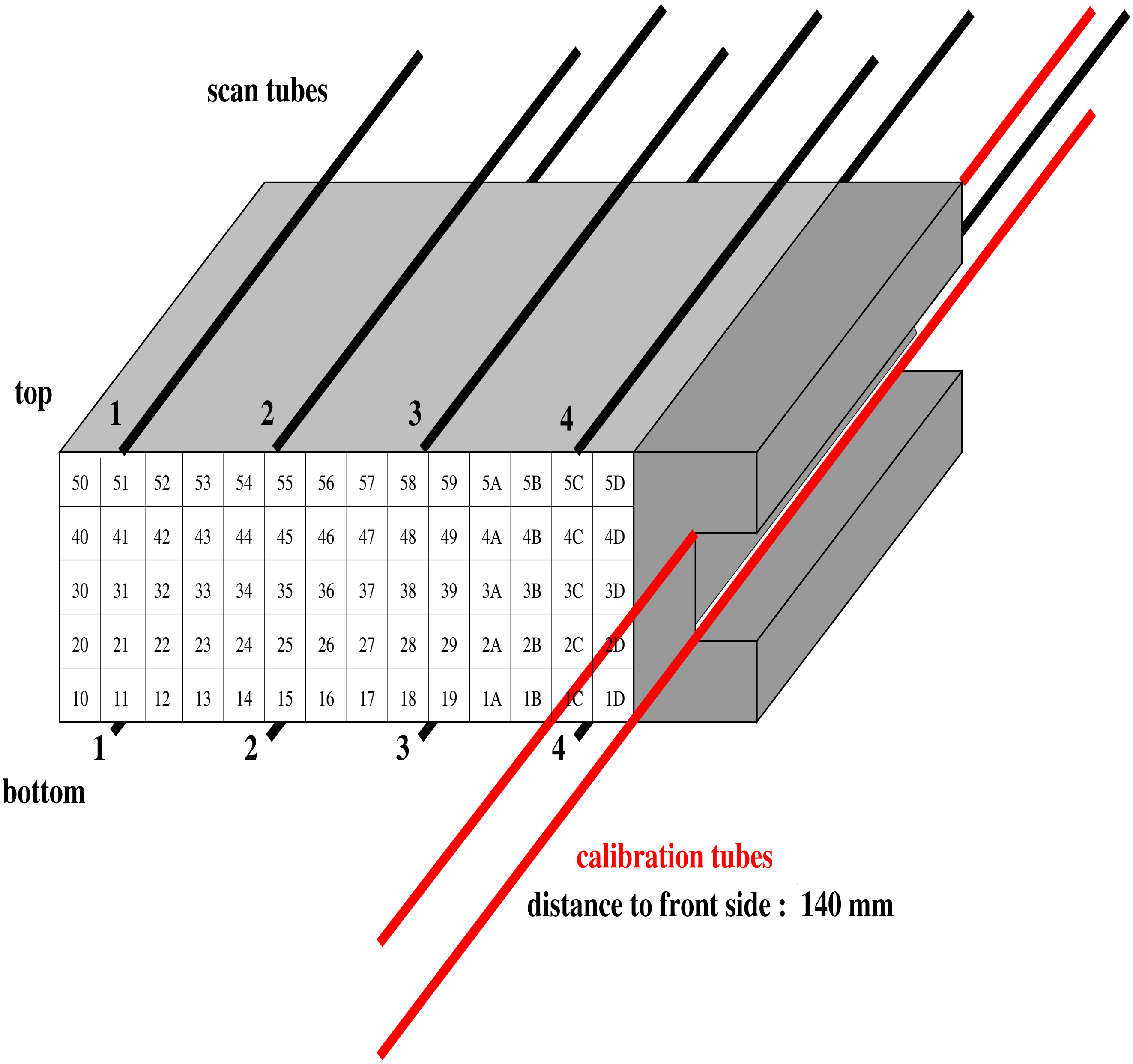

Figure 3.17: Sketch of the 6m-tagger. The front-side of the calorimeter is shown, which means that the fibers start at this side. The scan tubes are mounted parallel to the fibers and end directly at the front side. The calibration tubes are mounted parallel to the fibers, too, but end 140 mm in front of the detector.

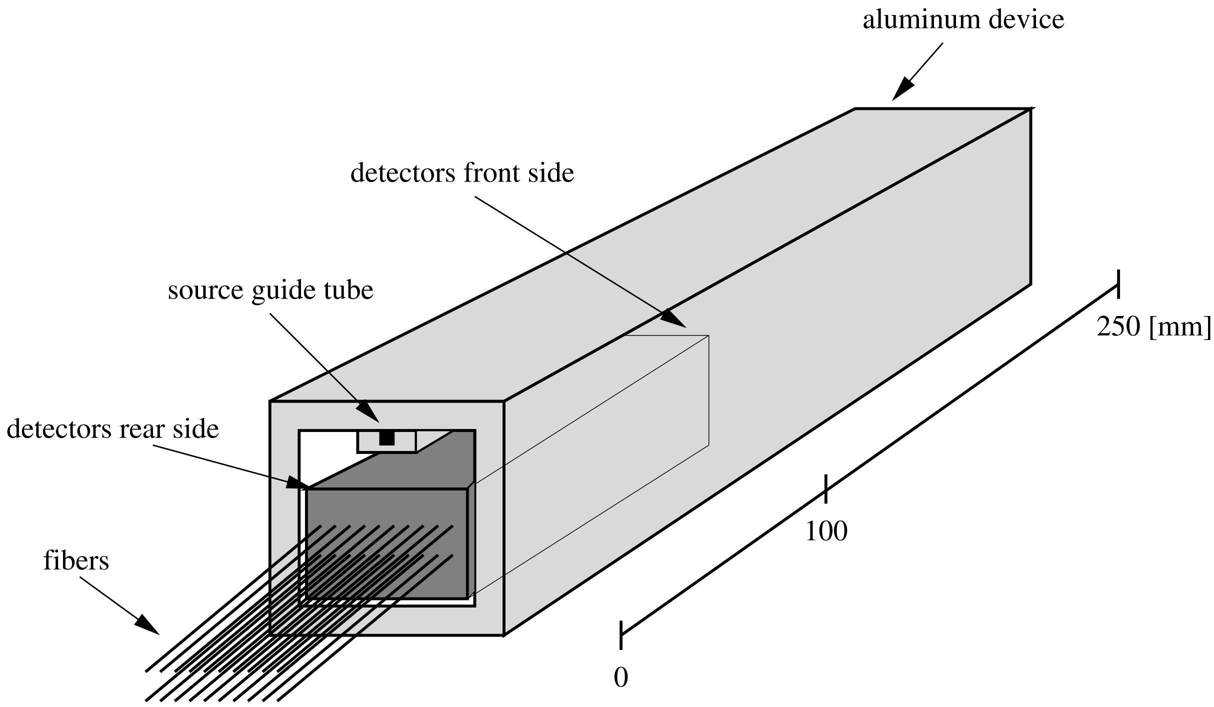

Figure 3.18: Sketch of the five cell 6m-tagger model. This detector is fixed inside an aluminum device. The scan tube is mounted above the detector and parallel to the fibers. The detector has a total length of 10 cm. The scan of the detector starts at the rear side of the detector and ends at an overall distance of 25 cm.

PC-controlled motor withdrew the ^{60}Co source wire starting at the rear side of the tube parallel to the scintillating fibers. A distance of 25 cm was scanned, which means that the measurement passed the front side of the detector at the position of 10 *cm*. Then the end of the fibers which belong to 3 of the 5 cells, i.e. $3 \cdot 27 = 81$ fibers, were painted with a white color[3]. The scan was repeated and the light yield can be compared between both setups (Fig. 3.19(a)). The light yield is higher and more uniform for the cells with the white paint. The ratio, $\text{scan}_2/\text{scan}_1$, of the signal after, scan_2, to the signal before, scan_1, painting the end of the fibers shows (Fig. 3.19(b)) that the light yield increased by $30 - 35\%$ across the tagger and up to 50% near the front side. This ratio is shown for a cell which was whitened and for a cell which was not whitened. The cell which remained unchanged shows that the second measurement was consistent with the first one. A slight increase of the light yield of $\approx 5\%$ at the front side is measured but the effect which is seen for the whitened cell is much higher. Due to this positive result all 70 cells of the final detector were whitened.

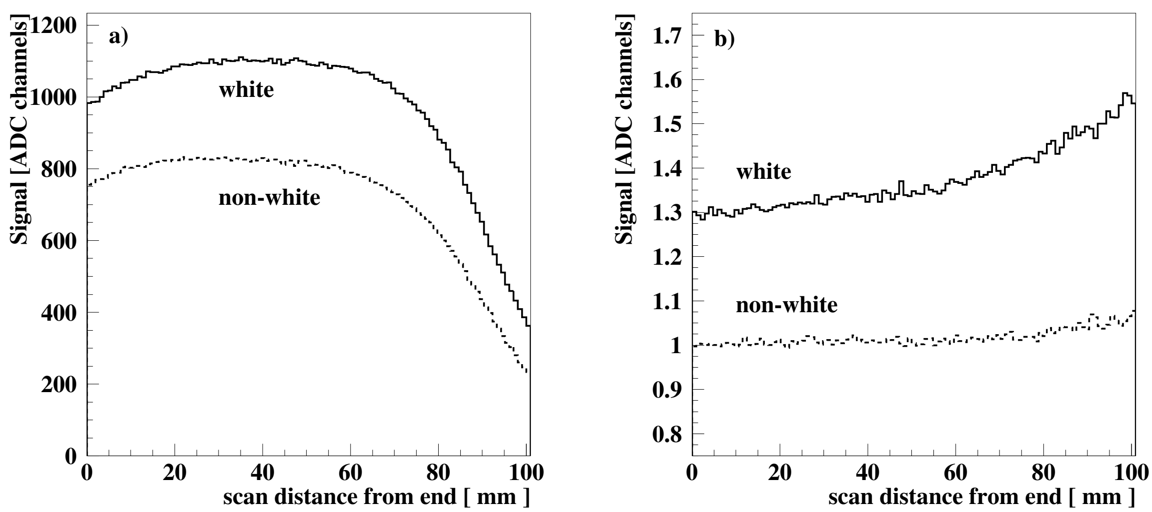

Figure 3.19: (a) Signal of a scan with a Co^{60} source starting at the rear side of the 6m-tagger model (Fig. 3.18). The same cell was measured before (dashed line) and after (solid line) painting the front side of this cell with white color. (b) Signal ratio, $\text{scan}_2/\text{scan}_1$, of the scan for two different cells with a Co^{60} source starting at the front side of the 6m-tagger. For one cell (solid line) the front side was whitened after the first scan, while for an other cell (dashed line) the front side remained as before.

[3]Ernst Diegel GmbH, covering white color FT 37, number 9-05197 HV/Z

3.4.3 Measurement of the relative cell-to-cell calibration of the 6m-tagger with a ^{60}Co source

Measurements with the ^{60}Co source were made in May 2001 during the electron test-beam, in February 2002 after mounting the detector in the magnet near the main ZEUS detector, and then during almost every month ^{60}Co measurements are performed to check the performance and the calibration of the 6m-tagger.

For calibration purposes the ^{60}Co source is moved to the end of the two brass tubes, which end 14 cm in front of the detector, so that the whole front side of the detector is homogeneously illuminated without moving the source. This measurement allows one to determine a relative cell-to-cell calibration. This cell-to-cell calibration is defined to be the ratio S_x/S_{36} of the signal response of a cell x, S_x, to the signal response of the cell 36, S_{36}, which is the central cell of the total detector (Fig. 3.17). This ratio should be nearly the same for electron and ^{60}Co calibration if the signal response created by electrons from the test-beam is compared to the signal response created by the ^{60}Co source. Thus the ratio $(S_x/S_{36})^{e^-}/(S_x/S_{36})^{^{60}Co}$ of the ratios determined from the measurement with electrons (superscript e^-) and with the ^{60}Co source (superscript ^{60}Co) should have a value equal to 1. For the ratio $(S_x/S_{36})^{e^-}$ the calibration constants from the test-beam [27] are taken to be the signal S. The signal S in the ^{60}Co measurements are determined in the following way. The ^{60}Co source is moved to the end of the calibration brass tube which ends in front of the 6m-tagger (Fig. 3.17). Then the signal of all 70 channels is measured[4]. Then the ^{60}Co source is moved into a lead ball and the pedestal of the signal for all 70 channels is measured with the same settings. The signal subtracted by the pedestal is taken to be the signal S. The ratio $(S_x/S_{36})^{e^-}/(S_x/S_{36})^{^{60}Co}$ with the ^{60}Co measurement during the setup at the test-beam facility is close to 1 for all 70 cells x (Tab. 3.3). Only the cells in column C and D show a strange behavior which cannot be explained. The ratio $(S_x/S_{36})^{e^-}/(S_x/S_{36})^{^{60}Co}$ with the ^{60}Co measurements in February 2002 is listed for all active cells[5] (Tab. 3.4). For this measurement the electrical noise, which disturbed the measurement in the ZEUS hall, was filtered in a special way by correcting the data. Since the noise on the signal has the same size on all channels of the ADC cards [15], the cell 10 is taken to measure the noise and used to correct all other cells. The correction was done in a certain order: first the mean on the signal in cell 10 is measured. Then the time dependent change of the ADC channels around this mean is taken to correct the data for all other cells. If the mean of all other cells is fitted with a Gaussian before and after correction, the mean does only change within its uncertainty, while the spread of the signal becomes smaller. Thus the signal itself does not change, only the Gaussian distribution becomes smaller. Cell 10 is chosen for correction because the PMT of this cell changed with respect to the test-beam. This results in a ratio $(S_x/S_{36})^{e^-}/(S_x/S_{36})^{^{60}Co}$ (Tab. 3.4) which is not in agreement with the measurement from May 2001 (Tab. 3.3). For all other cells the relative cell-to-cell calibration remained nearly unchanged. The features in column C and D did not appear again in February 2002 (Tab. 3.4).

[4]The mean of 100 single measurements in a row is taken to be the signal response. This measurement is repeated 750 times.

[5]In February 2002 the two cells 51 and 21 were out of order.

	x0	x1	x2	x3	x4	x5	x6
5x	0.911±0.003	0.889±0.003	0.935±0.003	0.996±0.003	1.139±0.003	1.145±0.003	1.128±0.003
4x	0.886±0.004	0.823±0.003	0.816±0.004	0.972±0.003	1.185±0.003	0.820±0.003	0.970±0.003
3x	0.853±0.003	0.840±0.003	0.888±0.009	0.923±0.004	0.912±0.004	0.940±0.003	1
2x	0.864±0.003	0.788±0.004	0.818±0.003	0.890±0.003	0.924±0.003	0.939±0.003	1.186±0.003
1x	0.947±0.004	0.942±0.001	0.978±0.004	0.990±0.005	1.029±0.003	1.076±0.003	1.090±0.003

	x7	x8	x9	xA	xB	xC	xD
5x	1.259±0.003	1.223±0.002	1.117±0.002	1.150±0.003	1.190±0.003	0.557±0.005	0.35±0.01
4x	1.005±0.003	1.025±0.003	1.065±0.003	1.077±0.002	0.968±0.004	0.502±0.005	1.090±0.003
3x	1.068±0.003	1.036±0.003	1.060±0.002	1.091±0.002	1.087±0.003	0.510±0.006	0.30±0.02
2x	1.069±0.003	0.937±0.003	1.081±0.003	1.007±0.003	1.142±0.003	0.525±0.005	1.080±0.002
1x	1.360±0.003	1.244±0.002	1.178±0.003	1.242±0.002	1.210±0.003	0.585±0.005	0.32±0.01

Table 3.3: The ratio $(S_x/S_{36})^{e^-}/(S_x/S_{36})^{^{60}Co}$ determined as described in the text for all 70 cells in May 2001. The labeling of the cells is consistent with figure 3.17.

	x0	x1	x2	x3	x4	x5	x6
5x	—	0.92±0.01	1.08±0.02	1.01±0.07	1.01±0.08	1.19±0.02	1.13±0.02
4x	1.23±0.02	0.80±0.02	0.86±0.02	0.92±0.08	1.03±0.07	0.76±0.03	1.00±0.02
3x	0.80±0.02	0.81±0.01	0.88±0.05	0.87±0.07	0.72±0.30	0.88±0.02	1
2x	—	0.77±0.01	0.83±0.02	0.88±0.04	0.88±0.10	0.89±0.02	1.16±0.02
1x	1±2	0.85±0.01	1.05±0.02	1.05±0.02	1.05±0.09	1.15±0.11	1.10±0.02

	x7	x8	x9	xA	xB	xC	xD
5x	1.21±0.02	1.29±0.03	1.21±0.04	1.22±0.01	0.93±0.03	1.08±0.02	1.05±0.08
4x	1.03±0.02	1.12±0.03	1.01±0.04	0.96±0.02	1.01±0.02	0.94±0.02	0.93±0.11
3x	1.06±0.02	1.01±0.03	1.07±0.04	1.07±0.01	1.09±0.01	0.94±0.02	1.07±0.08
2x	1.10±0.02	0.90±0.04	1.07±0.04	1.08±0.01	1.13±0.01	0.99±0.02	1.06±0.08
1x	1.41±0.02	1.30±0.01	1.21±0.05	1.17±0.14	1.18±0.01	1.14±0.02	1.19±0.02

Table 3.4: The ratio $(S_x/S_{36})^{e^-}/(S_x/S_{36})^{^{60}Co}$ determined as described in the text for all active cells in February 2002. The labeling of the cells is consistent with figure 3.17. The cells are corrected as described in the text by using cell 10. The cells 20 and 50 were broken.

The distance between the ^{60}Co source and the front side of the detector was 114 mm during the setup at the test-beam facility. To complicate matters all following measurements, after mounting the detector in the magnet near the main ZEUS detector, used a longer brass tube for the calibration which placed the ^{60}Co source 140 mm in front of the detector. The distance of the ^{60}Co source from the front side of the detector could be measured with a high accuracy if this tube is used as a scan tube, which means that the source is pulled by a certain distance, then the signal for all 70 cells is measured and then this procedure is repeated until the source reaches the final position. If the dependence of the signal on the position of the source is plotted (Fig. 3.20) the distribution shows a significant feature for all cells which are not next to the brass tubes. Since the tungsten shields the ^{60}Co radiation the signal shows a dip at the position where the ^{60}Co source passes the front side. This dip allows one to measure the distance which the source was pulled. In Fig. 3.20 two scan measurements performed in the calibration brass tubes are shown for the same cell at different dates. One measurement was taken in May 2001 after the calibration of the detector with the electron test-beam. The other measurement was taken in August 2002 after the 6m-tagger was irradiated with about ~ 266 Gy due to its position near the main ZEUS detector and close to the beam-pipe. Since the distance of the ^{60}Co source to the front side is different for these two measurements the measurement from May is corrected in such a way that both measurements have the front side of the detector at a position of 140 mm. The position corrected signals are overlaid (Fig. 3.20) and show that the signal at the front side (140 mm) from August is nearly 60% lower than it was in May. In the following it is discussed in detail how such a damage of the fibers occurred.

3.4.4 Investigation of the radiation damage of the SCSF-38M fibers in the 6m-tagger with a ^{60}Co source

The investigation of the scans with a ^{60}Co source in February, May, July, August, October, November and December 2002 shows the influence of the radiation of the beams on the 6m-tagger. To keep the overview only 9 cells of all 70 are chosen to be presented here. These 9 cells are selected from 3 columns which have a scan brass tube directly above and below. Always the two outer cells and the cell in the middle are taken. The signal as a function of the distance of the ^{60}Co source from the front-side of the detector is shown for the selected cells 51, 31, 11, 55, 35, 15 (Fig. 3.21) and 5C, 3C, 1C (Fig. 3.22). These plots show the signal as a function of the position of the ^{60}Co source in the corresponding top brass tube for the cells $5x$ and $3x$ and as a function of the position of the ^{60}Co source in the corresponding bottom tube for the cells $1x$, where x stands for 1, 5 and C. The cells $3x$ are in the middle between the top and the bottom tube. The signal of cell $3x$ created by a scan in the top and the bottom tube were superimposed and showed that the setup is perfectly symmetric. The signal of the scan in the top tube is shown for all $3x$. Figures 3.21 and 3.22 show that the signal response decreased from the reference scan in February to the scans in May, July and August. To remove the geometrical dependence which is folded into the signal the ratio of the measured signal in May, July and August to the measured reference signal in February is calculated (Fig. 3.23 and 3.24). The ratio as a function of the position of the ^{60}Co source shows that from February to May not only the light yield decreased

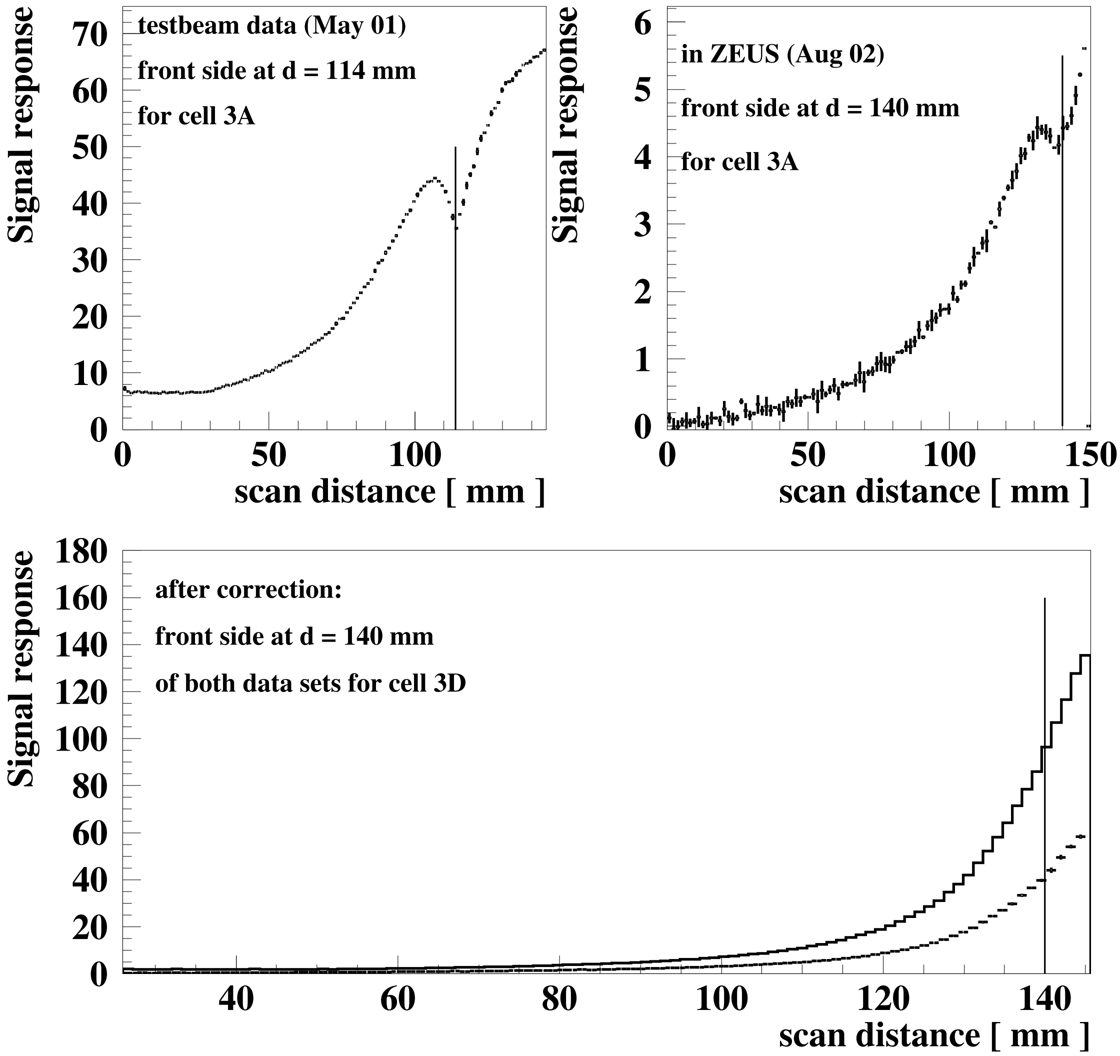

Figure 3.20: Signal response of scans with a ^{60}Co source starting at the end of the calibration tube in front of the detector. The upper plots show the signal response of cell 3A (Fig. 3.17) in dependence of the distance from the end of the calibration tube. At the position where the source reaches the plane of the front side, the signal in cell 3A decreases due to the tungsten in between. In May 2001 and in August 2002, the source had a different maximum distance to the front side of the detector. Using the information of the distance from the upper two plots, the signal response from May 2001 and August 2002 of cell 3D can be shown in dependence of the distance from the front side of the detector. The front side of the 6m-tagger is always presented by the vertical solid line.

but also the shape changed, which is a clear sign that the attenuation changed. However the shape is still nearly linear up to 80 mm. Behind this position (>80 mm) the ratio shows a strange behavior which can be explained by the fibers which come out of the detector at 100 mm. The fibers outside of the detector are not always at the same position because they are not fixed since they have to guide the light to the photomultipliers (PMTs). However from May to July this linear shape changed in the range of the first 10 mm and show a higher decrease of the light yield there. During this time HERA increased the beam currents and started to study the synchrotron radiation in the collider since this created a high background for any measurement with the ZEUS detector. The decrease in the first 10 mm is a clear evidence that synchrotron radiation, which has an energy of about 100 keV and does not penetrate the detector deeply, damaged the first few millimeters of the fibers. Since the light yield was increased by painting the end of the fibers with white color (chapter 3.4.2), this radiation damage is quite severe. The damage in this region has a big effect on the light yield in the first few millimeters. Right after the ^{60}Co measurement in August 2002, a 2 mm thick lead plate was glued in front of the 6m-tagger to shield it from the synchrotron radiation. In figures 3.25–3.26 and 3.27–3.28 the signal and ratio, respectively, for the following measurements are shown for the same cells as mentioned above. It can be clearly seen that the lead shielding and nearly no radiation from August to October helped to increase the light yield in the upper and lower cells ($5x$ and $1x$) but nearly no change was measured in the central cells $(3x)$. The two main sources of radiation for the 6m-tagger are the synchrotron radiation and the bremsstrahlung electrons which have to be tagged by the detector. The bremsstrahlung electrons are bend in the magnetic field in such a way that they mainly hit the central cells $(3x)$. Thus the radiation damage which has been measured in the upper and lower cells ($5x$ and $1x$ respectively) has its origin in the synchrotron radiation which can be shielded with the lead plate. This explains why the upper and lower cells show a very steep rise in the ratio for the first 10 mm while the central cells show a rise which is not so steep and is even deeper (up to 25 mm). The radiation damage in the first 10 mm has its reason in the synchrotron radiation, while the deeper radiation damage has its source in the bremsstrahlung electron which penetrate the 6m-tagger up to 60 mm [27].

The cell 15 seems to behave different concerning the radiation damage in the first 10 mm. The ratio (Fig. 3.23) for cell 15 does not show a steep rise in this range. The reason for this behavior is unclear. However the behavior in the remaining scan range (> 10 mm) is similar to the measurement of the other lower cells ($1x$): the ratio (Fig. 3.23) falls to a value of about 0.65 in May, then to about 0.58 in July and August. Also the changes in the following scans are compatible with the other lower cells ($1x$).

From October to November a high dose of radiation was deposited in the alanine dosimeter (Tab. 3.5). However, the upper and lower cells show a decrease of the light yield but not so intense as seen before. It can be concluded that the lead shielding covers the detector from synchrotron radiation. The central cells do not show any obvious change in the light yield. Since the lead plate has been mounted in front of the detector, the light yield close to the front side of the detector has not changed a lot.

For cell 3A the scans along the calibration tube are compared for the measurements in August, October, November and December (Fig. 3.29). Since the lead shielding has been mounted the light yield in the first 5 mm of the fibers behind the front side has not changed at all. Also this measurement supports that the lead protects from further synchrotron radiation.

3.4.5 Measurement of the deposited dose near the 6m-tagger

The deposited dose of the radiation at the position of the 6m-tagger was measured with 10 glass dosimeters, a string of alanine with a length of about 24 cm and thermo-luminescence-dosimeters (TLD). These dosimeters are placed on-top of the 6m-tagger close to the beam-pipe because this is the only available space. The cells which are close to the dosimeters are the cells 50 and 51.

The deposited dose in the glass dosimeters is measured by the radio photo luminescence effect of phosphorus [34]. The phosphorus in the glass dosimeter becomes excited when it is irradiated. If the phosphorus is illuminated with UV light it will emit fluorescence light at a higher wavelength than the UV light. The light yield of the emitted light can be measured and is proportional to the deposited dose. The maximum value of the glass dosimeter measurements is given in Tab. 3.5. The dose is measured with an uncertainty of about 15% [26].

The string with alanine is divided in 8 parts which are measured separately. The dose deposited in the alanine is measured using the electron-spin-resonance (ESR) spectroscopy [48]. The measuring method makes use of the fact that absorption of radiation leads to the formation of free radicals of alanine, an amino acid existing in crystalline form. The concentration of the free radicals formed in a volume is proportional to the dose rate in this volume. The concentration of the free radicals is determined on the basis of ESR spectroscopy [48]. The maximum value of all these measurements is taken to be the deposited dose. The dose in this case is measured with an uncertainty of about 10% [34].

For TLDs the absorbed dose is measured by the radio thermo luminescence of lithium crystals. The absorbed dose is proportional to the emitted light of the lithium crystal which is emitted when heating the TLD. TLDs allow an accurate measurement up to 10 Gy and the dose is measured with an uncertainty of about 5% [34].

Since the dose for one month exceeds 30 Gy the TLDs were only used for the first time period. The glass dosimeters are sensitive to synchrotron radiation which adulterates the dosimetry. Therefore the alanine measurements are the values to hold to [34].

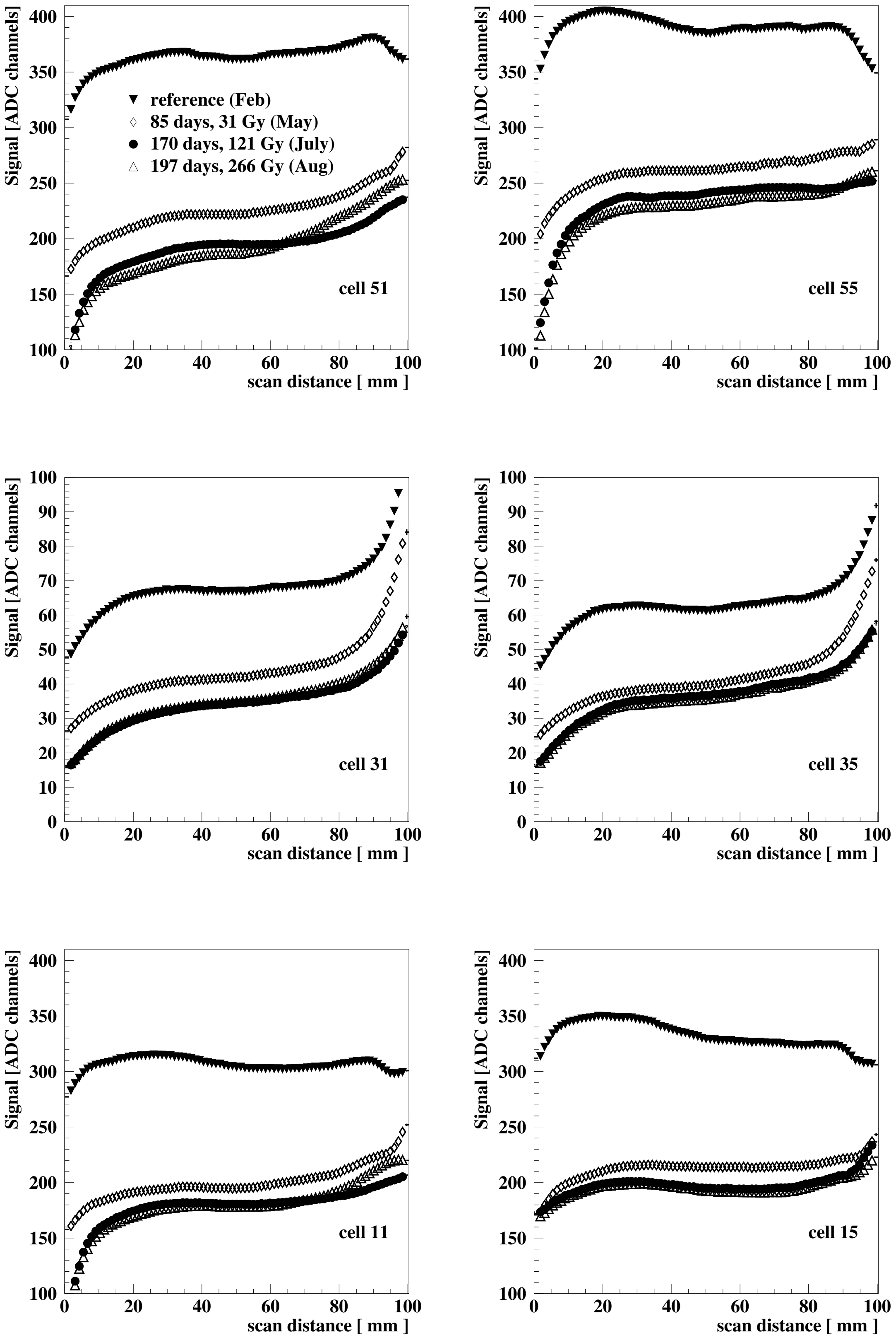

Figure 3.21: Signal response of scans with a ^{60}Co source starting at the front side of the detector. The scans for different cells (Fig. 3.17) have been measured without any irradiation (▼) and after an irradiation of the detector with an accumulated dose of 31 Gy (◇), 121 Gy (•) and 266 Gy (△).

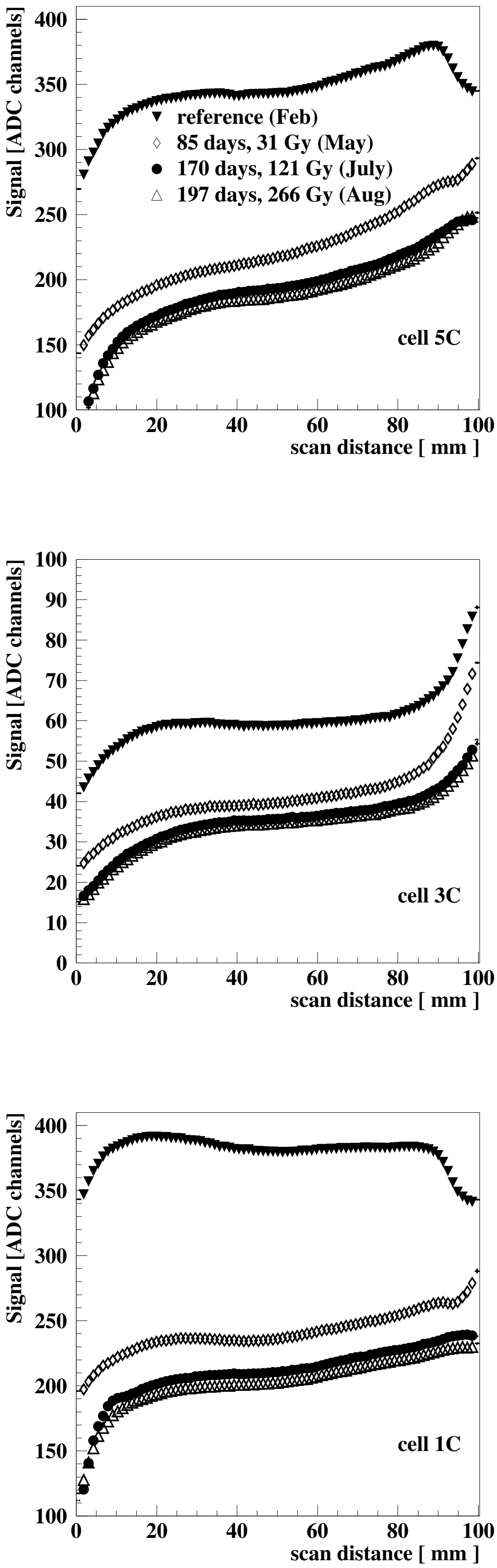

Figure 3.22: Signal response of scans with a ^{60}Co source starting at the front side of the detector. The scans for different cells (Fig. 3.17) have been measured without any irradiation (▼) and after an irradiation of the detector with an accumulated dose of 31 Gy (◊), 121 Gy (•) and 266 Gy (△).

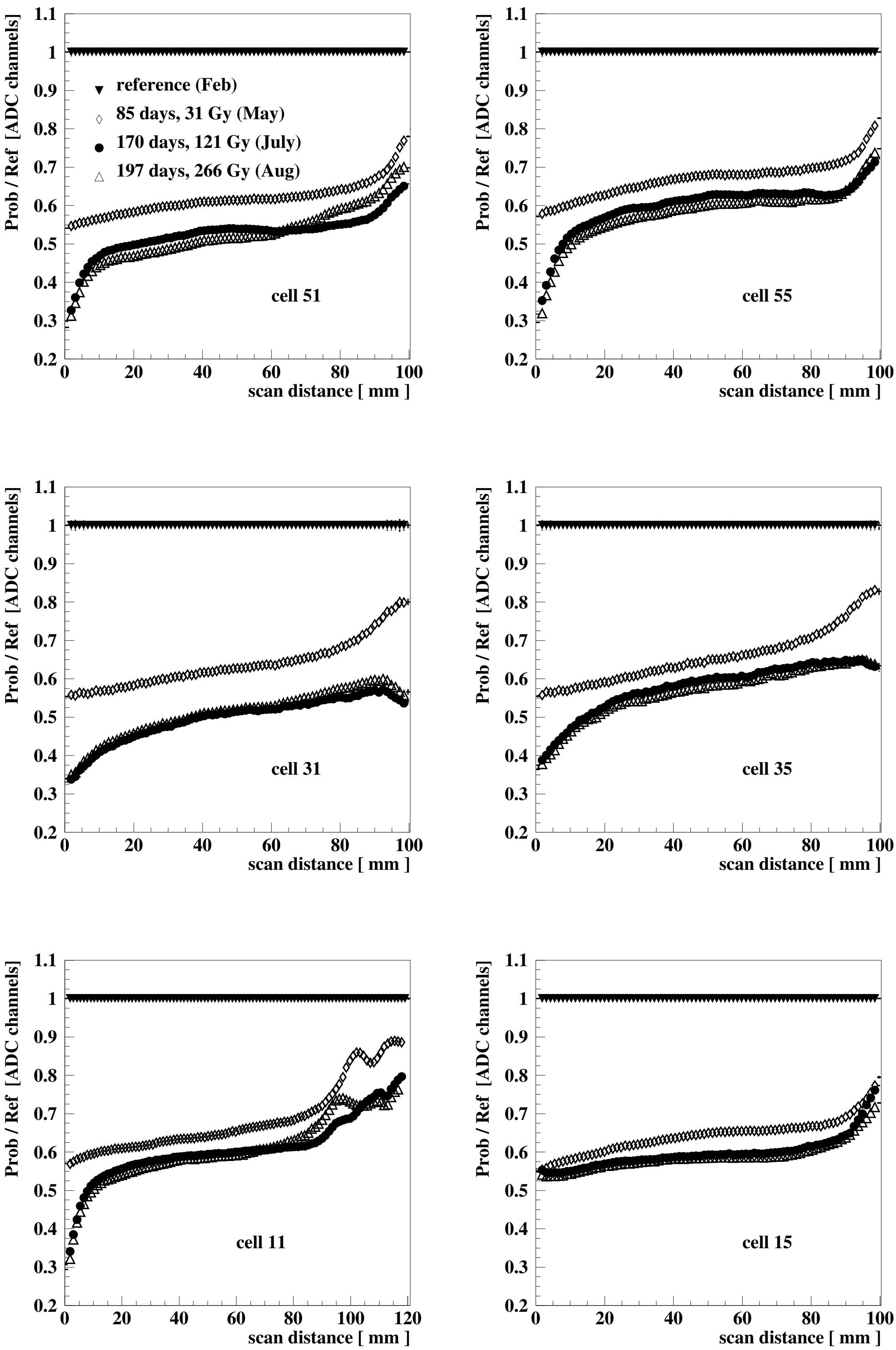

Figure 3.23: Ratio, Prob/Ref, of the signal response of scans with a ^{60}Co source in May, July and August (Prob) to February (Ref) starting at the front side of the detector. This ratio for different cells (Fig. 3.17) of the signal at a certain distance from the front-side is shown for an accumulated dose of 31 Gy ($\Diamond$), 121 Gy ($\bullet$) and 266 Gy ($\triangle$). These plots are related to Fig. 3.21.

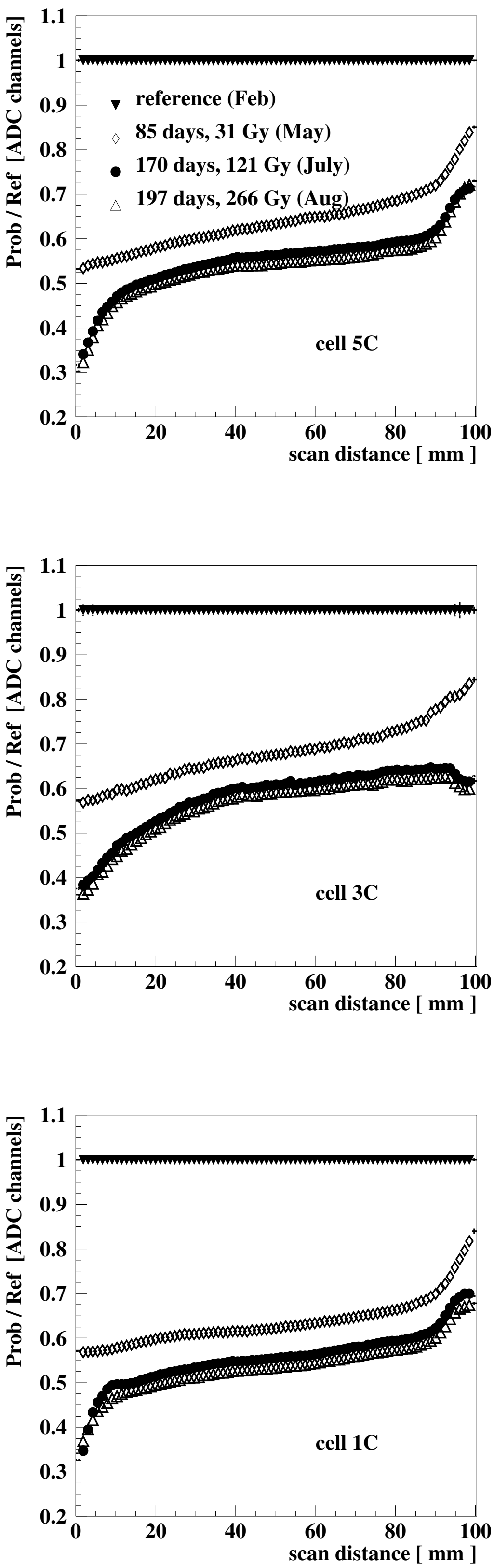

Figure 3.24: Ratio, Prob/Ref, of the signal response of scans with a ^{60}Co source in May, July and August (Prob) to February (Ref) starting at the front side of the detector. This ratio for different cells (Fig. 3.17) of the signal at a certain distance from the front-side is shown for an accumulated dose of 31 Gy ($\Diamond$), 121 Gy ($\bullet$) and 266 Gy ($\triangle$).These plots are related to Fig. 3.22.

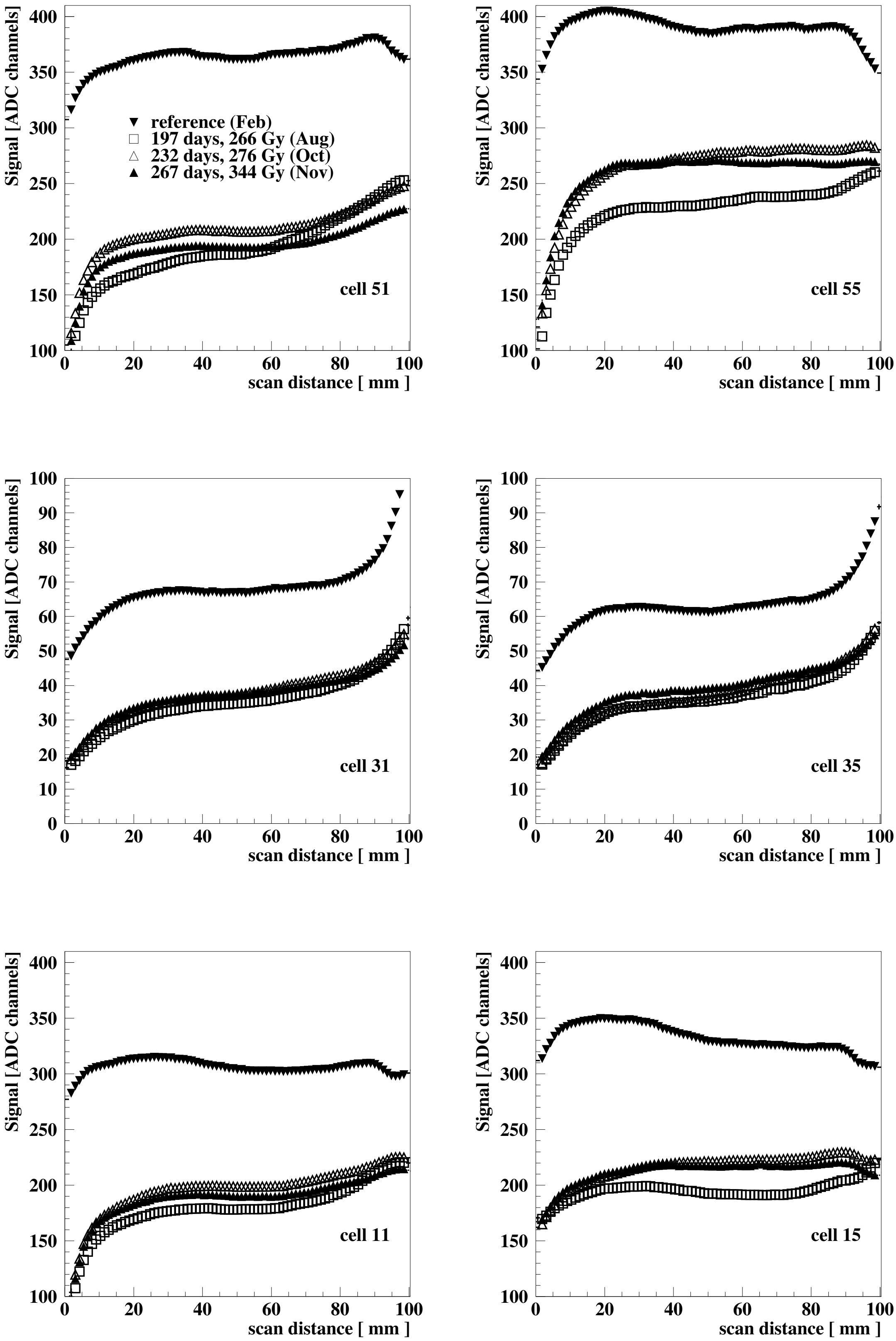

Figure 3.25: Signal response of scans with a ^{60}Co source starting at the front side of the detector. The scans for different cells (Fig. 3.17) have been measured without any irradiation (▼) and after an irradiation of the detector with an accumulated dose of 266 Gy (□), 276 Gy (△) and 344 Gy (▲).

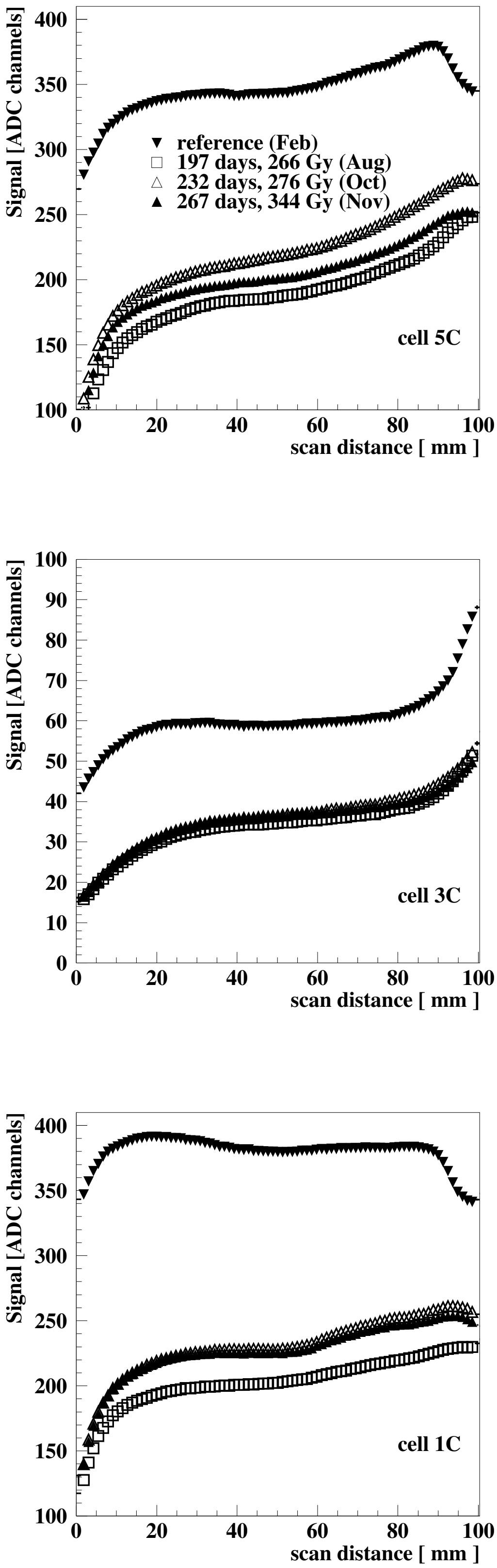

Figure 3.26: Signal response of scans with a ^{60}Co source starting at the front side of the detector. The scans for different cells (Fig. 3.17) have been measured without any irradiation (▼) and after an irradiation of the detector with an accumulated dose of 266 Gy (□), 276 Gy (△) and 344 Gy (▲).

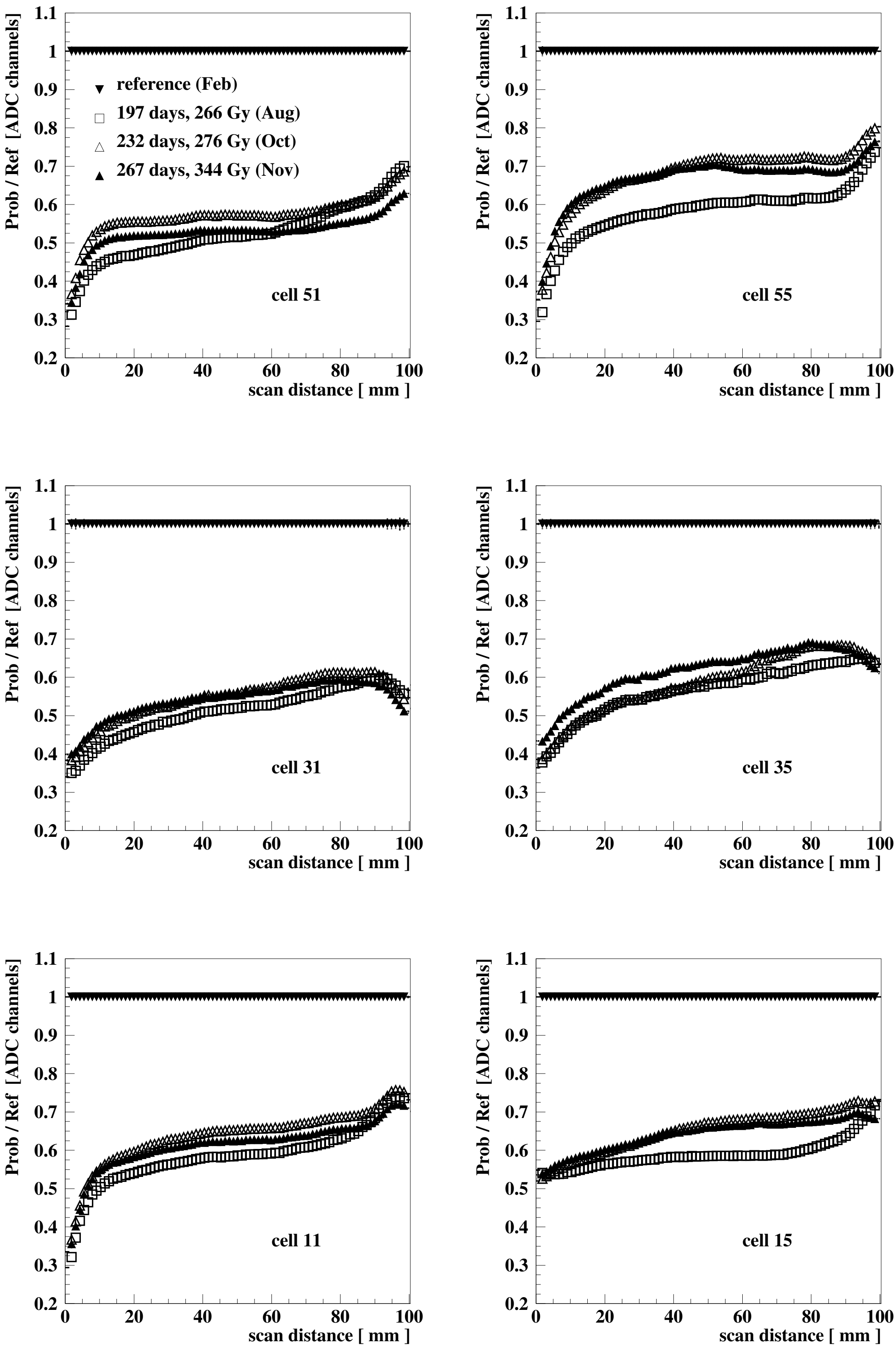

Figure 3.27: Ratio, Prob/Ref, of the signal response of scans with a ^{60}Co source in August, October and November (Prob) to February (Ref) starting at the front side of the detector. This ratio for different cells (Fig. 3.17) of the signal at a certain distance from the front-side is shown for an accumulated dose of 266 Gy (□), 276 Gy (△) and 344 Gy (▲). These plots are related to Fig. 3.25.

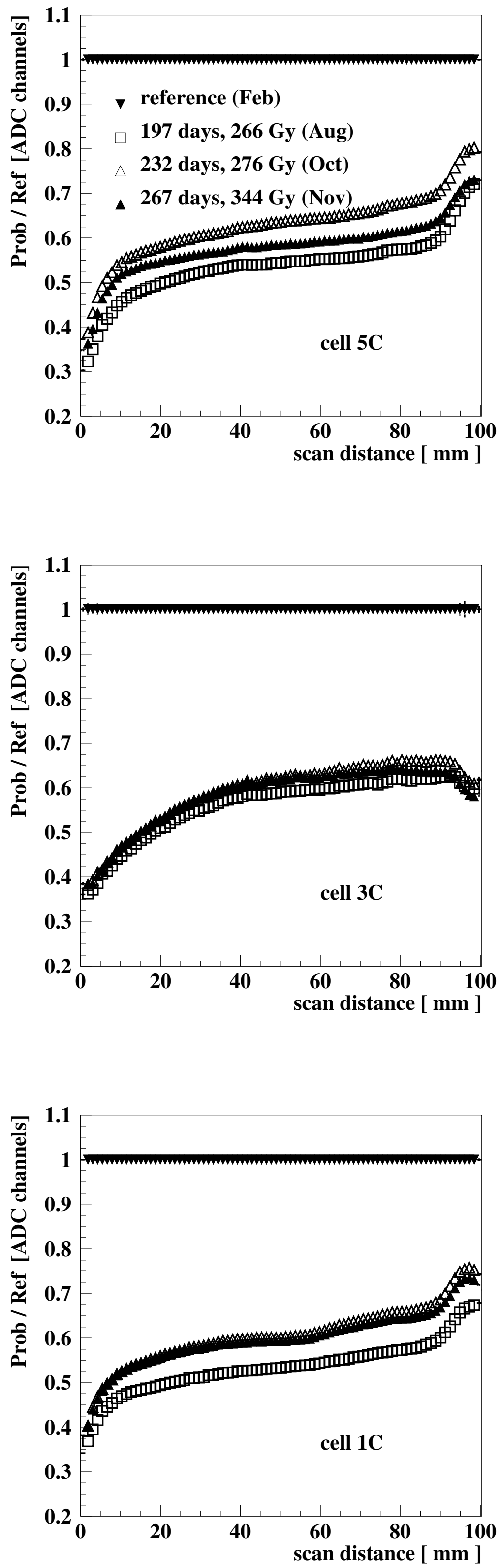

Figure 3.28: Ratio, Prob/Ref, of the signal response of scans with a ^{60}Co source in August, October and November (Prob) to February (Ref) starting at the front side of the detector. This ratio for different cells (Fig. 3.17) of the signal at a certain distance from the front-side is shown for an accumulated dose of 266 Gy (□), 276 Gy (△) and 344 Gy (▲). These plots are related to Fig. 3.26.

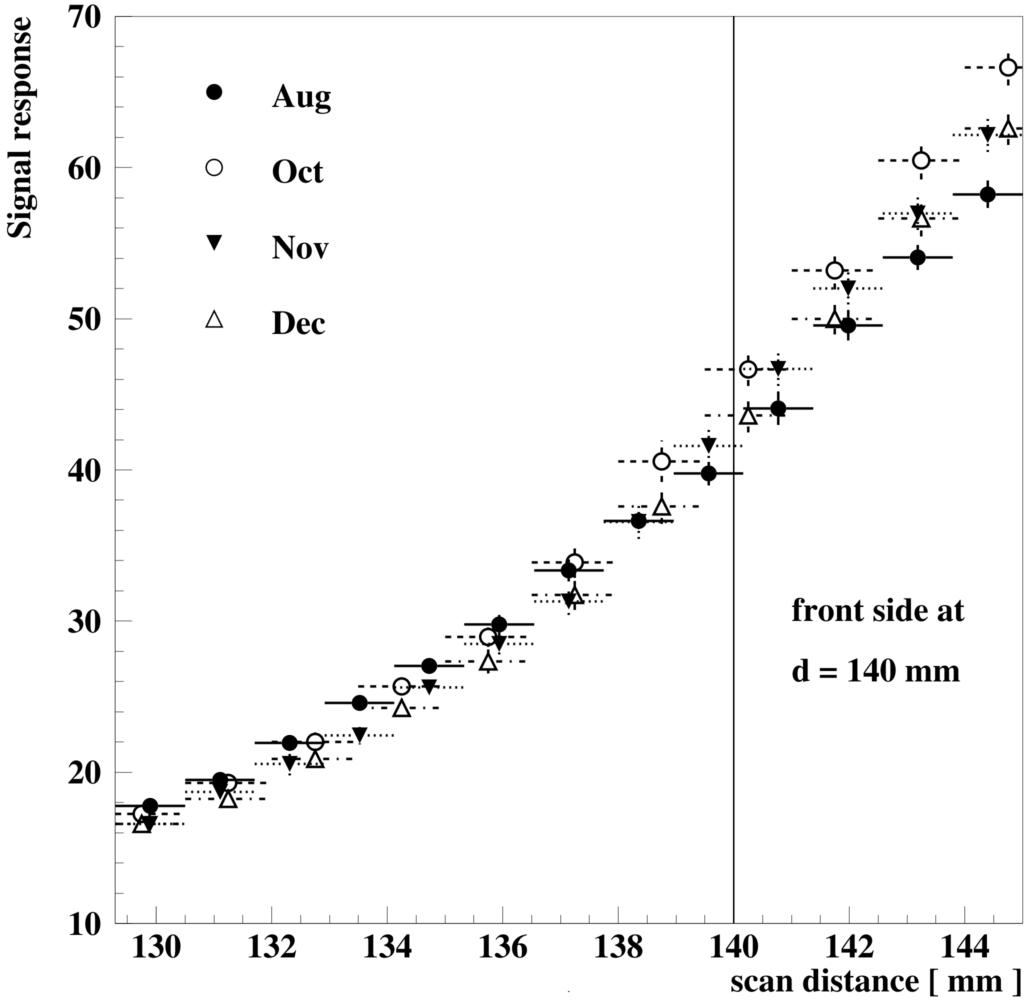

Figure 3.29: Signal response of scans with a ^{60}Co source starting at the end of the calibration tube in front of the detector. Only a part of the total scan around the front-side of the 6m-tagger is shown. The front side of the 6m-tagger is presented by a vertical solid line at a distance d from the end of the tube of $d = 140$ mm. The signal response of cell 3D is shown for the measurements in August (•), October (○), November (▼) and December (△). After the measurement in August the lead plate was installed.

irradiation period	label in figures	glass dosimeter	alanine	TLD
11.02.–**07.05.**	May	∼30 Gy	∼31 Gy	∼39 Gy
07.05.–**05.06.**	Jun	—	∼90 Gy	—
05.06.–**31.07.**	Jul	∼60 Gy		—
31.07.–**27.08.**	Aug	∼40 Gy	∼ 145 Gy	—
27.08.–**01.10.**	Oct	∼6 Gy	≤10 Gy	—
01.10.–**05.11.**	Nov	∼80 Gy	∼ 68 Gy	—
05.11.–**03.12.**	Dec	∼96 Gy	∼ 133 Gy	—
total dose		—	∼477 Gy	—

Table 3.5: Measured radiation dose for each time period. The radiation dose was measured with glass dosimeter, alanine and thermo-luminescence-dosimeter (TLD). The bold date indicates the day when the dosimeter were removed.

Chapter 4

Measurement of K_S^0 meson and Λ baryon production in neutral current deep inelastic scattering at HERA

4.1 Electron-proton scattering

When the point-like electron collides with a proton, it penetrates the proton and encounters one of the quarks of the proton which is explained in the quark-parton-model (QPM) [36]. The quark is knocked out of the proton and transformed into new particles that are scattered in all directions along with the electron and the fragments of the proton. These particles allows one to make conclusions about the structure of the proton. The higher the energy of the colliding particles, the more details are revealed.

The electron-proton scattering can be described by the exchange of a boson. Depending on the charge of this boson, two classes of electron-proton scattering exist. In a neutral current (NC) event a photon γ or a Z^0 boson is exchanged. In a charged current (CC) event a $W^{\pm}$ boson is exchanged. The kinematics of all events can be described by variables that are invariant under Lorentz transformations:

- $\sqrt{s}$ is the center-of-mass energy of the electron-proton system and is given by

  $$s = (p_p + p_e)^2$$

  where p_p and p_e are the four-vectors of the incoming proton and electron, respectively.

- Q^2 is the negative square of the momentum transfer q and is defined by

  $$Q^2 = -q^2 = -\left(p_e - p_{e'}\right)^2 ,$$

  where $p_{e'}$ is the four-vector of the scattered electron.

- The so-called Bjorken scaling variable x is given by

$$x = \frac{Q^2}{2 \cdot p_p \cdot q} .$$

In the QPM it can be interpreted as the fraction of the proton momentum which is carried by the scattered quark.

- y is the fraction of the initial electron energy which is transferred between the electron and the hadronic system in the proton rest frame and is defined by

$$y = \frac{p_p \cdot q}{p_p \cdot p_e} .$$

The variables mentioned so far are correlated such that

$$Q^2 = x \cdot y \cdot s$$

if the masses of the quarks are neglected. The maximal value for Q^2 is $Q^2_{max} \approx s$.

The electron-proton scattering can be separated into two regions: $Q^2 \approx 0$ corresponds to real photon-proton scattering and is called *photoproduction.* The other region is called *deep inelastic scattering (DIS)* including all events with $Q^2 \gg 1$ GeV^2.

In this thesis DIS events are selected. Therefore the kinematics and processes in DIS will be described in more detail.

4.1.1 Strange quark production in DIS

Feynman used the term parton to refer to the constituents of hadrons. These constituents are quarks, antiquarks and gluons. Valence quarks determine the external properties of a hadron. In addition to the valence quarks every hadron contains a fluctuating population of $q\bar{q}$ pairs, mainly $u\bar{u}$ and $d\bar{d}$. These are the sea quarks. They are generated by quarks emitting gluons which in turn become $q\bar{q}$ pairs. The reverse steps lead to a loss of the pairs and an equilibrium is established which, on a very short time scale, is represented by a fluctuating number of pairs.

The aim of this analysis is the measurement of the strange meson K_S^0 and the strange baryon Λ. The observation of strangeness in the final state of neutral current DIS raises the question of its origin. Possible sources are:

- *Flavor excitation.* After a fluctuation of a gluon, $g \rightarrow s\bar{s}$, one of the strange quarks receives a large momentum transfer by the exchanged virtual photon, so that a recombination of the pair is not possible. The hit quark leaves the proton and the other one remains roughly collinear with the proton remnant (Fig. 4.1(a)).

- *Boson-gluon fusion (BGF).* The virtual photon couples with a gluon of the proton via a virtual strange-antistrange quarkpair (Fig. 4.1(b)).

- *Decays of heavier quarks.* Strange quarks in the final state can result from decays of charm quarks. These charm quarks can come from a decayed beauty quark. But charm and beauty quarks are heavier and produced less frequently [10] so their contribution to the production of strange quarks is small.

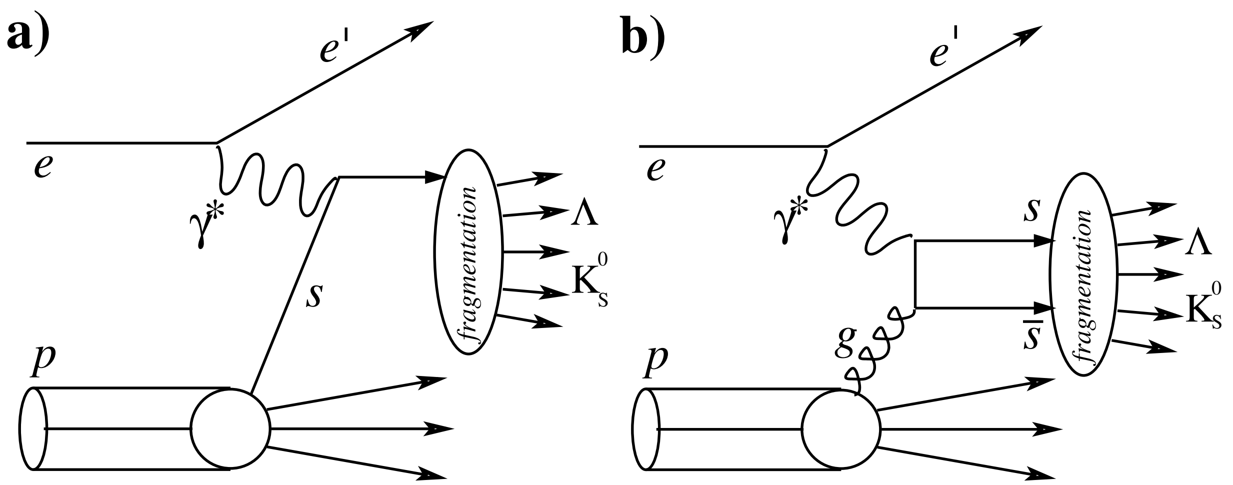

Figure 4.1: Origin of strange quarks in the final state of neutral current DIS events. (a) Flavor excitation: a strange quark, s, of the quark sea of the proton receives a large momentum transfer by the exchanged photon γ^*. (b) BGF: the virtual photon γ^* couples with a gluon, g, of the proton via a strange-antistrange quarkpair.

In addition strange quarks can be produced in fragmentation which is explained in the following section.

4.1.2 Fragmentation of quarks to hadrons

The fragmentation [41] of quarks to hadrons can be characterized by the *Lund model* which is described in detail elsewhere [3]. The main points of the model are reviewed here.

A gluon field conveys color between the quarks and is sometimes called the color flux tube. This tube is a store of energy in the same way as a stretched spring contains energy [41]. Increasing the $q\bar{q}$ separation means increasing the stored energy by doing work against the force tending to contract the spring. As the pair separate after production, the spring joining the pair will stretch and as it stretches it stores increasing energy until it becomes energetically possible for it to break. A new q is attached to the end of the spring on the one side of the break and a $\bar{q}$ of the same flavor at the other side of the break. If the invariant mass of either of the two segments of the spring is large enough, further breaks can occur. When breaking stops several spring segments, each joining a q and a $\bar{q}$, not necessarily of the same flavor, exist. Overall flavor must be conserved. Such segments consist of a q and a $\bar{q}$ with a binding field and are called mesons.

In order to produce the $q\bar{q}$ pair leading to spring breaks, the Lund model [3] invokes the idea of quantum mechanical tunneling. In this model a suppression of heavy-quark production is implied so that $P(u) : P(d) : P(s) : P(c) \approx 1 : 1 : 0.3 : 10^{-11}$ where $P(q)$ is the probability to produce a $q\bar{q}$ pair in the color field. For this reason charm and heavier quarks are not expected to be produced in soft fragmentation. The ratio of the probability $P(s)$ to $P(u) = P(d)$ is parameterized by a phenomenological parameter $\lambda_s = P(s)/P(u)$, which is called the strangeness suppression factor. The strangeness suppression factor is by default $\lambda_s = 0.3$.

Two different scenarios exist for modeling baryon production: the diquark and the popcorn model. The *diquark model* (Figs. 4.2(a) and 4.3(a)) sees a spring break producing not a $q\bar{q}$ pair but a diquark pair, that is a qq on one side of the break and a $\bar{q}\bar{q}$ at the other. When the spring breaks, the forces acting on the mesons will be along the same direction and these mesons will therefore also be produced tending to move along that direction: the resulting hadrons are produced in two back-to-back jets of particles. In the *popcorn model* (Figs. 4.2(b) and 4.3(b)), where diquarks do not exist, several $q\bar{q}$ pairs are produced. Assume that the original q is red r and the $\bar{q}$ is $\bar{r}$. A new $q_1\bar{q}_1$ pair produced in the field would also be $r\bar{r}$, so that two separate color-singlet systems $q\bar{q}_1$ and $q_1\bar{q}$ are formed. Occasionally, the $q_1\bar{q}_1$ pair can be a green $g\bar{g}$. In this case there is no net color charge acting on either q_1 or $\bar{q}_1$. Now the pair cannot gain energy from the field and only exists as a fluctuation. But if q_1 moves towards q and $\bar{q}_1$ towards $\bar{q}$, the net field remaining between q_1 and $\bar{q}_1$ is $b\bar{b}$. An additional $q_2\bar{q}_2$ pair can be created now in this central field. q_2 is now pulled towards qq_1 and $\bar{q}_2$ towards $\bar{q}\bar{q}_1$, with no net color field between q_2 and $\bar{q}_2$. The baryon B will be formed out of $q,\ q_1$ and q_2 and $\bar{B}$ of $\bar{q}$, $\bar{q}_1$ and $\bar{q}_2$.

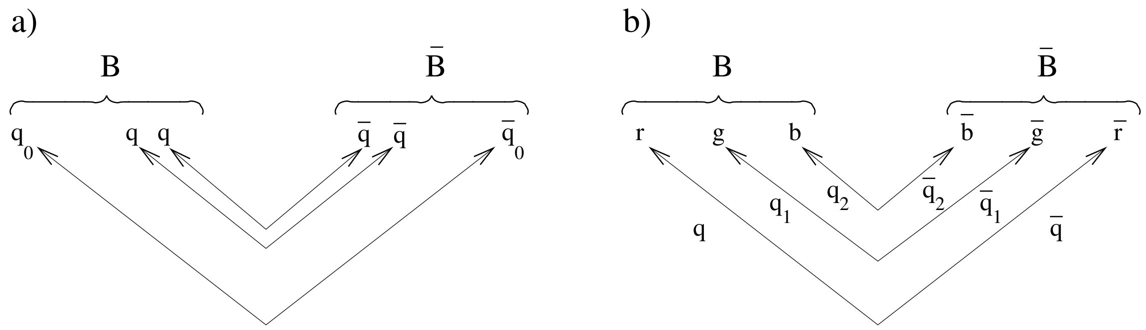

Figure 4.2: Schematic representation of baryon (B) production mechanisms in the (a) diquark and (b) popcorn model. The produced quark-antiquark pairs $(q, \bar{q})$ and their colors (r, g, b), which have the same origin, are connected with a line.

A MC program which simulates the fragmentation based on the Lund String model is JETSET [3]. In JETSET both scenarios of baryon production are implemented.

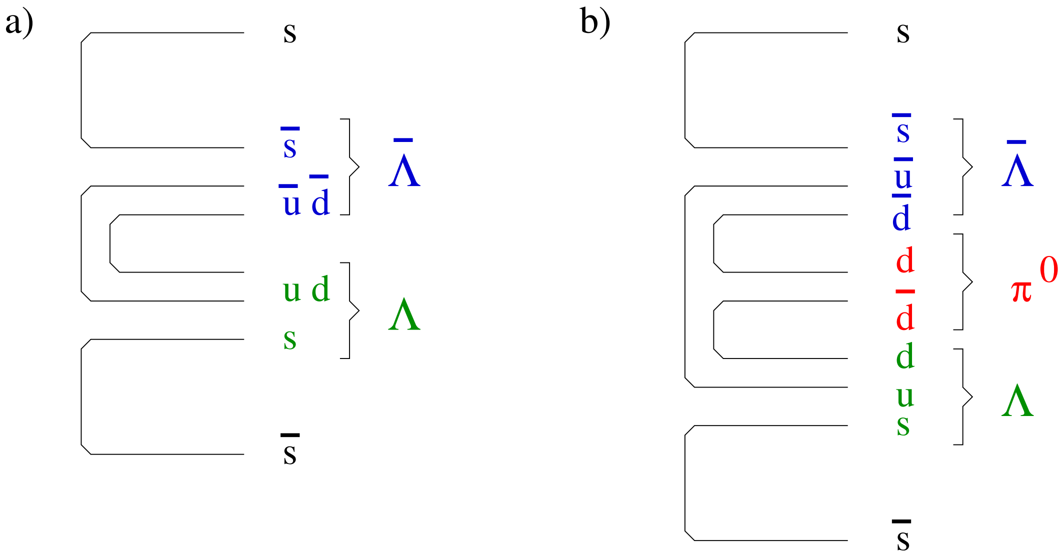

Figure 4.3: Examples of different Λ baryon production models in the Lund string model [3]: (a) the diquark model and (b) the popcorn model.

4.1.3 Simulation of DIS electron-proton scattering

The Monte Carlo (MC) simulation of physics data is an essential tool to compare measurements with theoretical models. Also it is the only way to determine the acceptance of the ZEUS detector.

The measurement is compared to leading-order MC models which generate the entire hadronic final state in neutral current DIS events. These models are based on the parton-cascade approach followed by a fragmentation to hadrons (Fig. 4.4 and 4.5). MC events are generated with HERWIG 6.1 [32, 13] and DJANGOH [37] using ARIADNE [31].

DJANGOH is an interface to the event generator HERACLES [29] to include first-order electroweak corrections. The events generated by HERWIG and ARIADNE are passed through a full simulation of the detector using GEANT 3.13 and processed with the same reconstruction program as that used for the experimental data. The detector-level MC samples are then selected in the same way as the data.

The *Color Dipole Model* (CDM) [4], as implemented in ARIADNE, makes use of the fact that a color dipole is formed between the struck quark and the proton remnant which can radiate gluons (Fig. 4.5). These in turn form additional dipoles which radiate gluons. This shower process is terminated after the participating quarks and gluons reach a certain minimum momentum.

The fragmentation for the events generated with ARIADNE is performed using the Lund String fragmentation, as implemented in JETSET 7.4 [3]. This model is described in chapter 4.1.2 and a sketch of the simulation of an event is shown in Fig. 4.4. In HERWIG the fragmentation into hadrons is modeled in a different way using a Cluster Fragmentation Model [32].

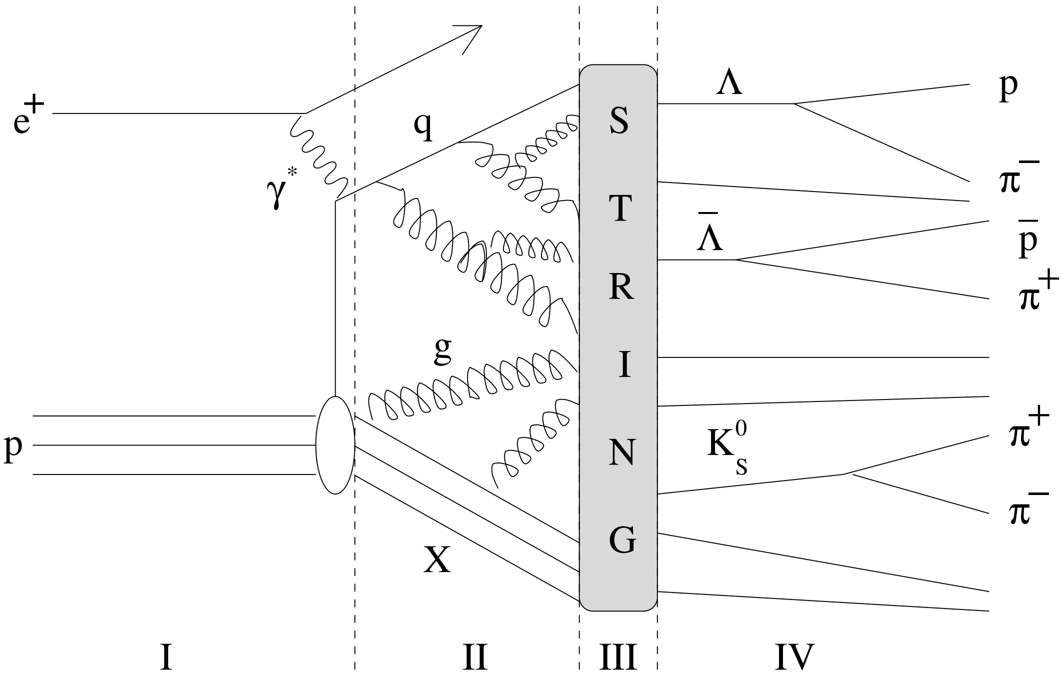

Figure 4.4: Schematic diagram of an event generated by ARIADNE [31] and JETSET [3]. (I) The virtual photon γ^* is scattering a quark out of the proton. (II) The QCD cascade is modeled by gluon emissions as described by the CDM [4]. (III) The parton-cascade fragments to hadrons using the Lund String model. (IV) The hadrons in the final state can be reconstructed.

In the *Cluster Fragmentation Model* (CFM) [32] the final state gluons are split non-perturbatively in $q\bar{q}$ pairs (Fig. 4.5). An object q is then combined with an adjacent object $\bar{q}$ to form a color-singlet cluster. If this cluster is too light to decay into two hadrons, it produces the lightest hadron with its flavor content. If its mass does not have the appropriate value, it is shifted exchanging momentum with an adjacent cluster in the jet. For a $q_1\bar{q}_2$ cluster a $q_3\bar{q}_3$ pair is chosen for instance. A q can be a quark or an antidiquark and $\bar{q}$ stands for an antiquark or a diquark. The resulting decay products are $q_1\bar{q}_3$ and $\bar{q}_2 q_3$. The flavor q_3 is chosen among the possibilities $u,\ d,\ s,\ c,\ \bar{u}\bar{u},\ \bar{u}\bar{d},\ \bar{u}\bar{s},\ \bar{d}\bar{d},\ \bar{d}\bar{s}$ and $\bar{s}\bar{s}$. Choices that would result in a diquark-antidiquark particle are rejected. The pairs $q_1\bar{q}_3$ and $\bar{q}_2 q_3$ are associated with hadrons of this flavor content.

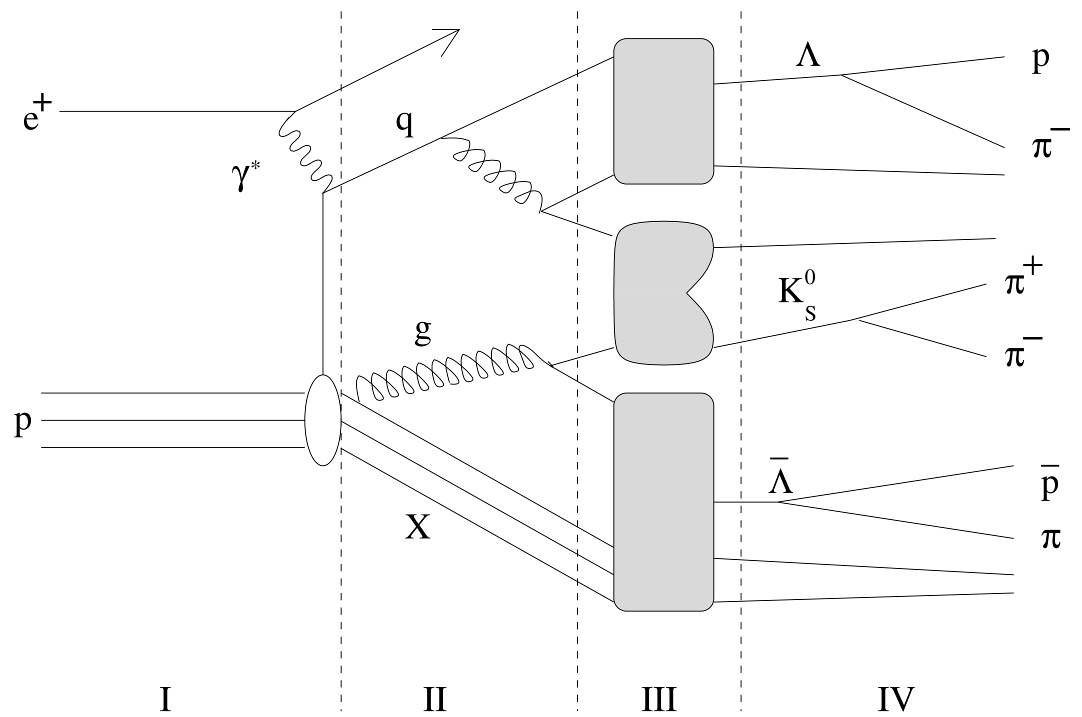

Figure 4.5: Schematic diagram of an event generated by HERWIG [32]. (I) The γ^* is scattering a quark out of the proton. (II) $q\bar{q}$ pairs are created from the break up of color dipoles. (III) The parton-cascade fragments to hadrons using the Cluster Fragmentation model. (IV) The hadrons in the final state can be reconstructed.

4.2 Reconstruction of the kinematic quantities

Several reconstruction methods exist to reconstruct the kinematic variables Q^2, x and y. Three different methods are presented here.

Electron Method

This method uses information from the scattered electron only. The angle θ and the energy $E_{e'}$ of the scattered electron are required. The quantities are given as

$$Q_e^2 = 2E_eE_{e'}(1+\cos\theta)\ ,$$

$$x_e = \frac{E_e}{E_p}\frac{E_{e'}(1+\cos\theta)}{2E_e - E_{e'}(1-\cos\theta)}$$

and

$$y_e = 1 - \frac{E_{e'}}{2E_e}(1-\cos\theta)\ .$$

The x resolution is degraded at small y. At large y the resolution is very good [35].

Double Angle (DA) Method

This method relies on the angle θ of the scattered positron and the angle γ which characterizes the hadronic final state. γ is defined as

$$\cos\gamma = \frac{\left(\sum_h p_{xh}\right)^2 + \left(\sum_h p_{yh}\right)^2 - \left[\sum_h (E_h - p_{zh})\right]^2}{\left(\sum_h p_{xh}\right)^2 + \left(\sum_h p_{yh}\right)^2 + \left[\sum_h (E_h - p_{zh})\right]^2}$$

The quantities are given as

$$Q_{DA}^2 = 4E_e^2\frac{\sin\gamma(1+\cos\theta)}{\sin\gamma + \sin\theta - \sin(\theta+\gamma)}\ ,$$

$$x_{DA} = \frac{E_e}{E_p}\frac{\sin\gamma + \sin\theta + \sin(\theta+\gamma)}{\sin\gamma + \sin\theta - \sin(\theta+\gamma)}$$

and

$$y_{DA} = \frac{\sin\theta(1-\cos\gamma)}{\sin\gamma + \sin\theta - \sin(\theta+\gamma)}\ .$$

Hadron Method or Jacquet-Blondel Method

This method, proposed by Jacquet and Blondel [9], relies entirely on the hadronic system to reconstruct the kinematic variable. The quantity y_{JB} is given as

$$y_{JB} = \frac{\sum_h (E_h - p_{zh})}{2E_e}\ .$$

The sum $\sum_h$ runs over all final state hadrons. For low values of $y_{JB} < 0.05$, the resolution is much better than that with the electron method. The Q_{JB}^2 and x_{JB} resolution is always worse than $Q_e^2,\ Q_{DA}^2$ and $x_e,\ x_{DA}$, respectively, [47] so that Q_{JB}^2 and x_{JB} are not used in this analysis.

4.3 Event selection

In this section the selection of the DIS events used for this analysis is outlined. Trigger conditions and offline cuts will be explained. For the characteristic signature of a DIS event is the scattered electron which is detected in the uranium scintillator calorimeter.

The analysis is performed with the positron-proton data taken in 1999 and 2000 with the ZEUS detector. The data corresponds to a total integrated luminosity of $\mathcal{L} = 60 \pm 1$ pb^{-1}.

4.3.1 Trigger conditions

In section 2.2.4 the ZEUS trigger system was introduced. Different physics filters are used at each trigger level.

For DIS events, the first level trigger (FLT) requires some energy conditions in the calorimeter and a track in the CTD as listed [38] below:

- the total energy in the calorimeter exceeds 14.968 GeV excluding the three innermost towers surrounding the beam-pipe of the FCAL and one tower surrounding the beam-pipe of the BCAL;
- OR the total EMC energy exceeds 10.068 GeV excluding the areas as above;
- OR the total Barrel EMC exceeds 3.404 GeV;
- OR the total RCAL EMC energy exceeds 2.032 GeV excluding one innermost tower surrounding the beam-pipe of RCAL;
- AND a good CTD FLT track from the nominal interaction region.

The second level trigger (SLT) rejects proton beam-gas events by using the times measured in the calorimeter cells.

The third level trigger (TLT) has the full event information. DST bits 9 and 11 are required for this analysis which means that an electron finder reconstructed a positron with an energy $E_{e'}$ of $E_{e'} > 4$ GeV. The DIS event candidates are selected by calculating:

$$E - p_z = \sum_i \; [E_i \; \cdot \; (1 - \cos\theta_i)] - 2 \cdot E_\gamma > 30 \text{ GeV} \; ,$$

where E_i and θ_i are the energy and the polar angle of the energy deposits in the calorimeter cell i. E_γ is the energy measured in the photon calorimeter of the luminosity monitor. The summation runs over all energy deposits in the calorimeter cells. For fully contained DIS events the following relation is valid: $E - p_z \; = \; 2 \cdot E_e = 55$ GeV. Photoproduction events have a lower value of $E - p_z$ compared to DIS events because the scattered electron escapes in the beam-pipe hole of the rear calorimeter.

The selection so far was done by A. Ziegler for his analysis [47]. These events with at least one reconstructed secondary vertex and an impact point of the scattered positron outside a ring centered on $X = Y = 0$ with a radius of 36 cm were written out on disk. Any selection from here on was performed by the author of this thesis.

4.3.2 Offline event selection

SINISTRA [1], a neural network electron finder, identifies an electron candidate with a probability p_{Si} by using the pattern of energy deposition in the calorimeter cells. The following criteria are used to select a sample of DIS events:

- $E_{e',\,corr} > 10$ GeV, being the corrected energy of the scattered positron in the calorimeter. The neural network electrom finder SINISTRA has been shown to be almost 100% efficient for electron energies above 10 GeV. For lower electron energies the efficiency drops to 50% which is not exactly reproduced in the Monte Carlo. Therefore a minimum energy of 10 GeV is required;
- $y_e < 0.8$, to reduce the photoproduction background;
- $y_{JB} > 0.04$, to give sufficient accuracy for DA reconstruction;
- 20 GeV^2 $< Q^2 < 500$ GeV^2, to restrict the measurement to a range with sufficient statistics for differential cross sections;
- probability $p_{Si} > 0.9$;
- $3 \cdot 10^{-4} < x < 10^{-1}$, is related to the Q^2 and y cut by the equation $Q^2 = x \cdot y \cdot s$;
- 40 GeV $\leq\ E - p_z\ \leq\ 60$ GeV, where $E - p_z = \sum_i\ E_i\ \cdot\ (1 - \cos\theta_i)$, E_i is the energy and θ_i the polar angle of the ith calorimeter cell and the sum runs over all cells. Hard initial-state radiation or photoproduction events are suppressed;
- a primary vertex position, determined from the tracks fitted to the vertex, in the range $|Z_{vertex}| < 50$ cm. The reconstructed vertex is required to be close to the nominal interaction point. This requirement rejects beam-gas and cosmic ray events. It ensures tracks to be reconstructed with high efficiency;
- $r_{el}\ >\ 36$ cm: the impact point $(X,\ Y)$ of the scattered positron in the calorimeter must lie outside a ring centered on $X = Y = 0$ with a radius of 36 cm. The DIS trigger chain which is not prescaled requires $r_{el} > 35$ cm. Monte Carlo studies showed that $r_{el} > 36$ cm is the lowest well simulated cut.

4.4 Reconstruction of K_S^0 mesons and Λ baryons

4.4.1 Track reconstruction

The track recognition program VCTRACK [22, 23] is used to identify charged particles in the CTD. The track finding algorithm first considers hits in the axial superlayers only, constructing a track candidate in the XY-plane. Each track candidate begins as a track seed of three hits in the outer superlayers where the hit densities are lower and proceeds inwards from there by adding a virtual hit at $X = Y = 0$. A circle arc is formed in the XY-plane, gathering additional axial hits on the way as the trajectory parameters are updated. In order to reconstruct the Z-coordinate of the trajectory information from axial and stereo superlayers are needed. The Z-by-Timing (ZbT) measurement provides a coarse first estimation of the trajectory in 3D with a resolution of $\sigma_{ZbT} \approx 4.4$ cm [6]. This system limits the region which must be searched for stereo hits. With this configuration the Z-position of a track can be reconstructed with an accuracy of approximately 2 mm.

The whole procedure is repeated until all track seeds in the outermost superlayer are used, at which point it continues with the next inner superlayer. So the longest tracks are found first, and the shortest tracks last.

The reconstructed tracks are used for fitting secondary vertices and a primary vertex, which is done in three steps:

1. Tracks that are incompatible with the beam-line are removed from the fit.
2. Tracks that contribute too much to the overall χ^2 are discarded one by one.
3. The remaining tracks determine the secondary vertices and primary vertex and constrain the tracks to it.

The reconstructed secondary vertices are used to identify K_S^0 mesons and Λ baryons[1].

4.4.2 Reconstruction of K_S^0 mesons

The K_S^0 mesons are identified through the decay $K_S^0 \to \pi^+\pi^-$. The pions leave ionized tracks in the CTD which are reconstructed as described above. Only well measured tracks which left hits in the inner three superlayers and with a transverse momentum $p_T > 0.15$ GeV and a pseudorapidity η of $|\eta| < 1.75$ are considered. The requirements for the reconstructed K_S^0 candidates are $0.5 < p_T\ (K_S^0) < 5.0$ GeV and $|\eta(K_S^0)| < 1.5$. Figure 4.6 shows the invariant mass distribution $m(\pi, \pi)$ of the selected K_S^0 candidates, which is calculated by assigning the mass $m_\pi = (139.5707 \pm 0.0004)$ MeV [33] to the tracks from the secondary vertex.

[1]In the following when a baryon is mentioned, the anti-baryon is also ment if not explicitly stated.

The selection includes mainly K_S^0 candidates but also has some contribution from $\Lambda \to p\,\pi^-$ candidates. The contribution of Λ candidates in the K_S^0 selection can be reduced by calculating the invariant mass $m(p,\pi)$ of these K_S^0 candidates. Therefore the track from the secondary vertex candidate with the higher momentum is considered to be the proton with a mass of $m_p = (938.271998 \pm 0.000038)$ MeV [33], the other one with the lower momentum is the pion with $m_\pi = (139.5707 \pm 0.0004)$ MeV [33]. Only K_S^0 candidates with a mass hypothesis $m(p,\pi) > 1.12$ GeV are kept which eliminates nearly all Λ contamination of the K_S^0 signal.

The number of K_S^0 mesons is obtained by fitting a parameterization to the invariant mass distribution $m(\pi,\pi)$. This parameterization consists of two Gaussians[2] normalized to one for the K_S^0 signal plus a term describing the background:

$$P(m) = \underbrace{N \cdot \left[\, r \;\cdot G_{1,m_{K_S^0},\sigma_1} + (1-r) \;\cdot G_{2,m_{K_S^0},\sigma_2} \right]}_{Signal} + \underbrace{A \cdot \frac{B\cdot(m-0.45)+1}{\int_{0.484\text{ GeV}}^{0.51\text{ GeV}} [B\cdot(m-0.45)+1]\,dm}}_{Background} \;,$$

where G_1 (G_2) is a Gaussian with the width σ_1 (σ_2) and a common mass $m_{K_S^0}$ as parameters of the fit. The parameter r is a free parameter of the fit and the fit parameter N is the normalization of the signal while A and B are free parameters of the fit of the background. A determines the number of background events in the mass window of $0.484 < m(\pi,\pi) < 0.51$ GeV. The number of K_S^0 mesons $N_{K_S^0}$ is calculated by counting the number of entries in the mass distribution in the mass window $0.484 < m(\pi,\pi) < 0.51$ GeV subtracted by the parameter A from the fit.

The results of the fit to the experimental data and MC mass distribution for K_S^0 candidates is shown in Figs. 4.6(a)–(b). The fitted mass $m_{K_S^0}$ for data and MC is measured to be $m_{K_S^0} = (497.94 \pm 0.03)$ MeV and $m_{K_S^0} = (498.18 \pm 0.02)$ MeV, respectively. These values are close together and close to the current world average quoted by the Particle Data Group (PDG) [33], namely $m_{K_S^0}^{PDG} = (497.672 \pm 0.031)$ MeV. The number of K_S^0 mesons after background subtraction is 49824 ± 605 and 93404 ± 784 for data and MC, respectively. The MC model gives a reasonable description of the general features of the data. However the MC predicts a width of the signal which is slightly smaller than found in the experimental data. This difference is obvious when comparing both background subtracted signals in Fig. 4.6(c). The effect of this small difference on the measurement is taken into account as a systematic uncertainty (chapter 4.4.4).

Several distributions measured in the data are compared to the predicted distributions by the MC (Fig. 4.7, 4.8 and 4.9). The entries in the distribution have at least one K_S^0 meson candidate with a mass in the mass window of $0.484 < m(\pi,\pi) < 0.51$ GeV. The distributions which are compared are the reconstructed corrected energy $E_{e',\,corr}$, $E - p_z$, $\log_{10} x_{DA}$, Q^2_{DA}, y_{el} and y_{JB} (Fig. 4.7). The coordinates X, Y and Z of the reconstructed primary vertex are shown for data and MC in Fig. 4.8. The transverse momentum p_T for the π^+ and π^- from the K_S^0 decay, the

[2]One Gaussian does not describe the shape of the signal sufficiently, but already two Gaussians are able to parameterize the signal.

pseudorapidity η for the π^+ and π^- from the K_S^0 decay, the transverse momentum and pseudorapidity of the K_S^0 candidate are shown in Fig. 4.9. All distributions show a reasonable agreement between data and MC. Only the reconstructed corrected energy shows a small difference in the shape and the $E - p_z$ distributions in the MC is shifted with respect to the distribution in the data. However these systematic differences are taken into account as a systematic uncertainty for the measurement (chapter 4.4.4).

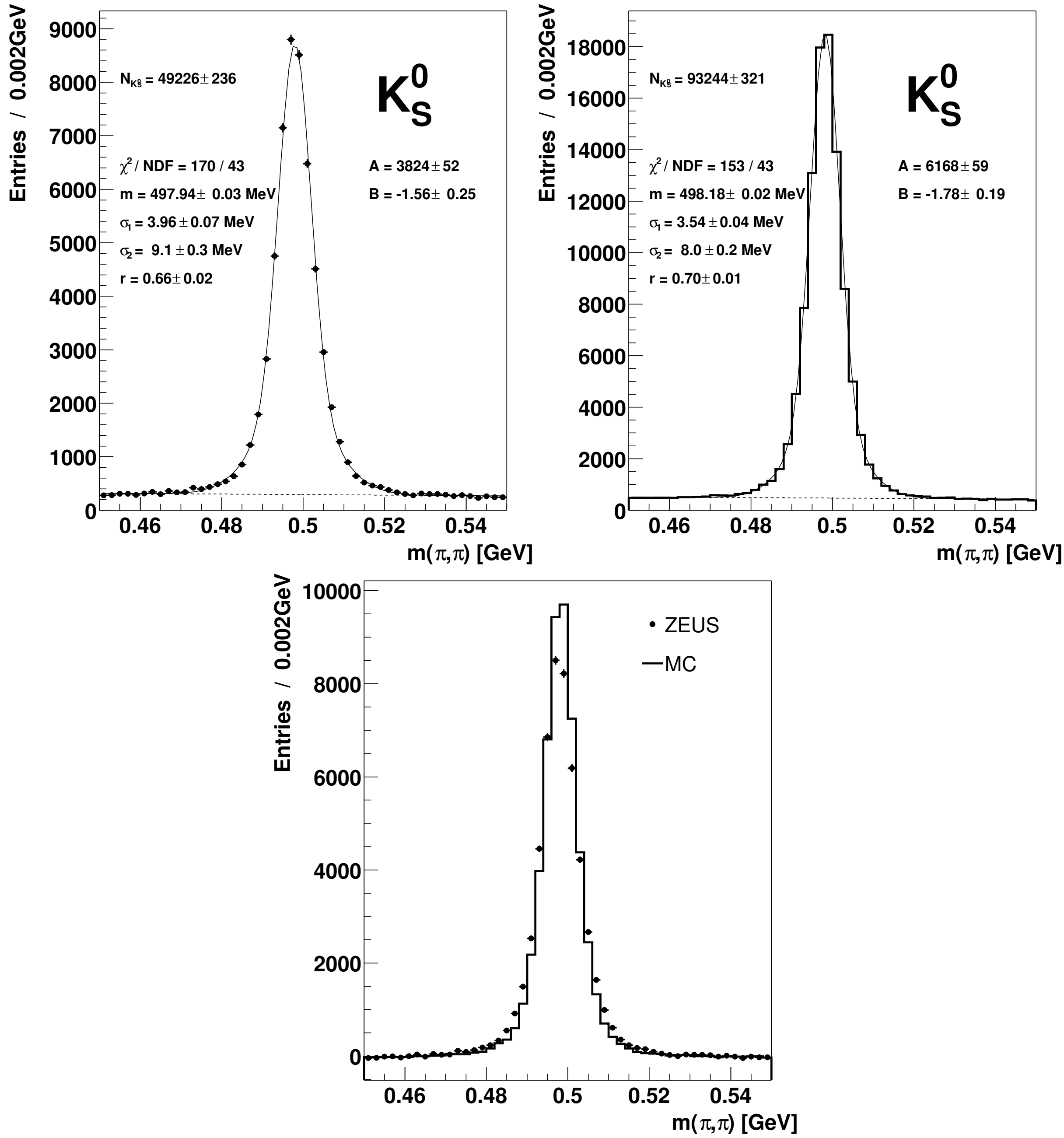

Figure 4.6: Pion-pion mass distribution $m(\pi, \pi)$ for K_S^0 candidates in data (upper left) and MC (upper right) in the restricted kinematic region of 20 GeV^2 $< Q^2 < 500$ GeV^2, $3 \cdot 10^{-4} < x < 10^{-1}$ and $0.04 < y < 0.8$, $0.5 < p_T\ (K_S^0) < 5.0$ GeV and $|\eta(K_S^0)| < 1.5$ following the selection procedure described in the text. The solid line in the plots represents the fit to the distribution as described in the text. The dashed line shows the parameterization of the background only. The lower graph shows the background subtracted signal for data (•) and ARIADNE Monte Carlo (solid histogram). The MC distribution is normalized to the area below the distribution of the data.

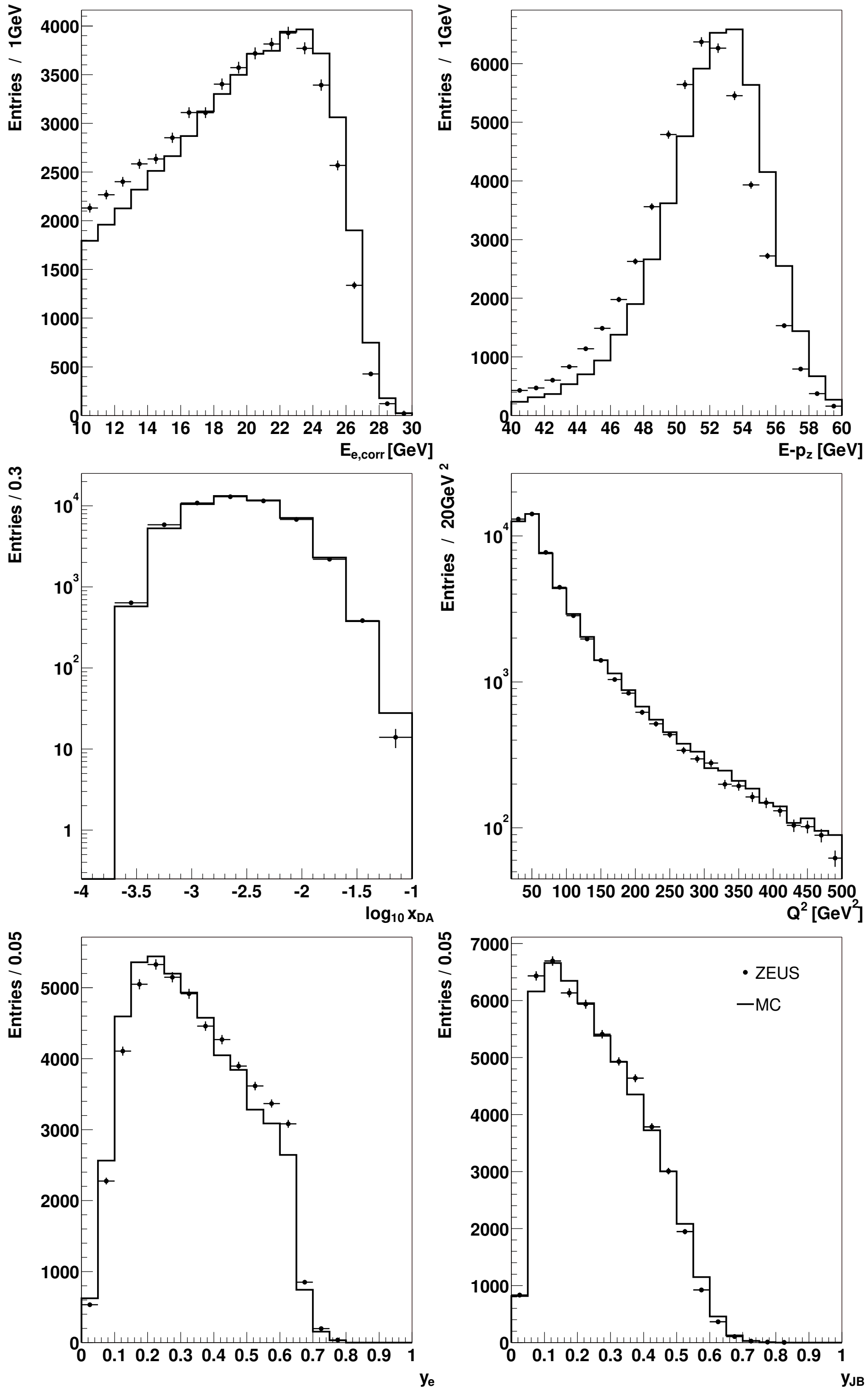

Figure 4.7: Comparison at detector level between data (•) and the ARIADNE Monte Carlo (solid line) for events which have at least one K_S^0 candidate with an invariant mass in the mass window of $0.484 < m(\pi, \pi) < 0.51$ GeV. The distributions of some kinematic variables are shown: the corrected energy of the electron, $E_{e',\,corr}$, the $E - p_z$ distribution, the logarithm of the Bjorken x reconstructed with the double angle method, $\log_{10} x_{DA}$, the squared four momentum transfer reconstructed with the double angle method, Q^2_{DA}, the inelasticity reconstructed with the electron method, y_e and with the Jacquet-Blondel method, y_{JB}. The MC distribution is always scaled to the number of entries in the distribution of the data, thus the shape of the distributions can be compared.

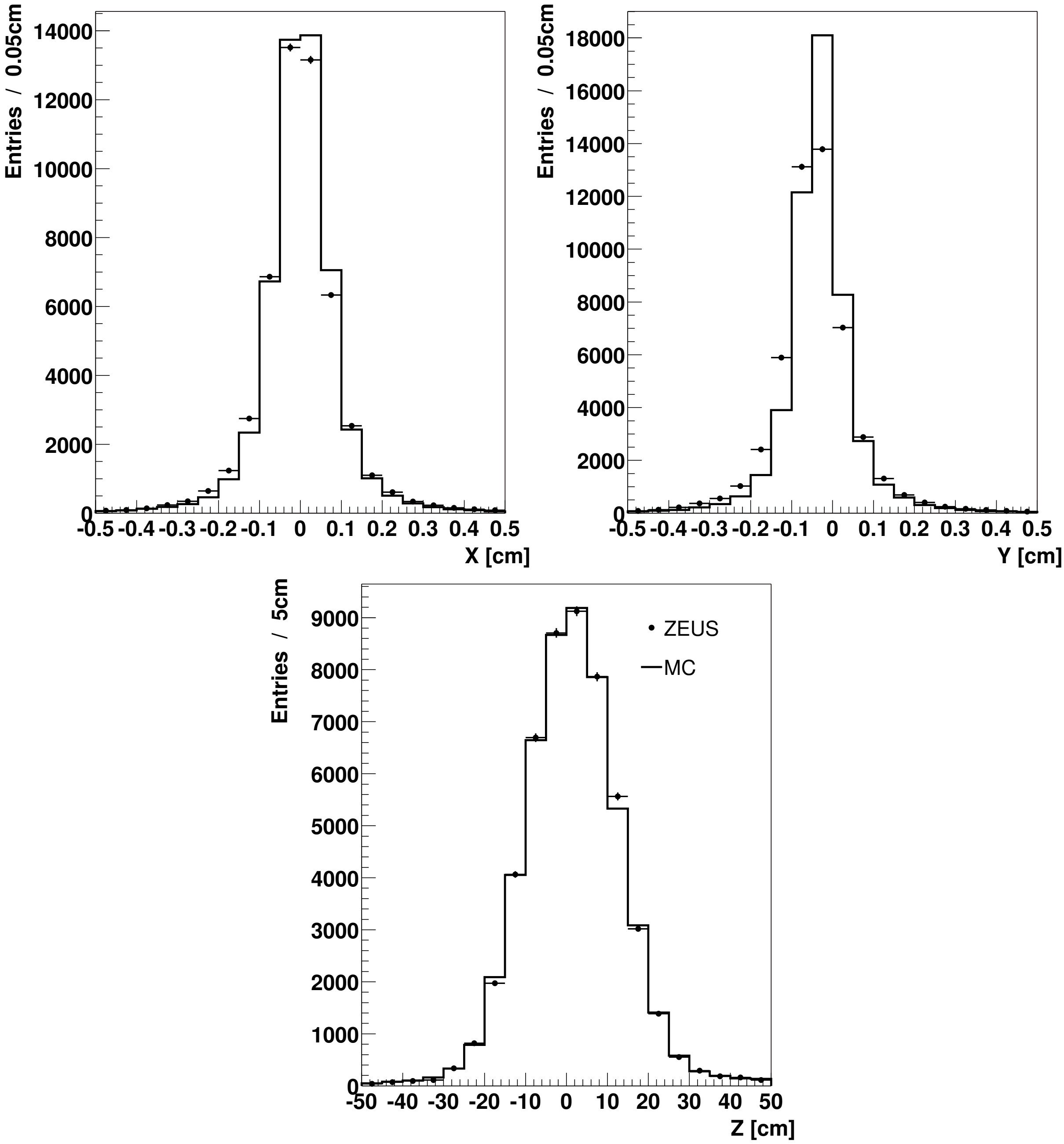

Figure 4.8: Comparison at detector level between data (•) and the ARIADNE Monte Carlo (solid line) for events which have at least one K_S^0 candidate with an invariant mass in the mass window of $0.484 < m(\pi, \pi) < 0.51$ GeV. The X, Y and Z position of the primary event vertex is shown. The MC distribution is always normalized to the area below the distribution of the data.

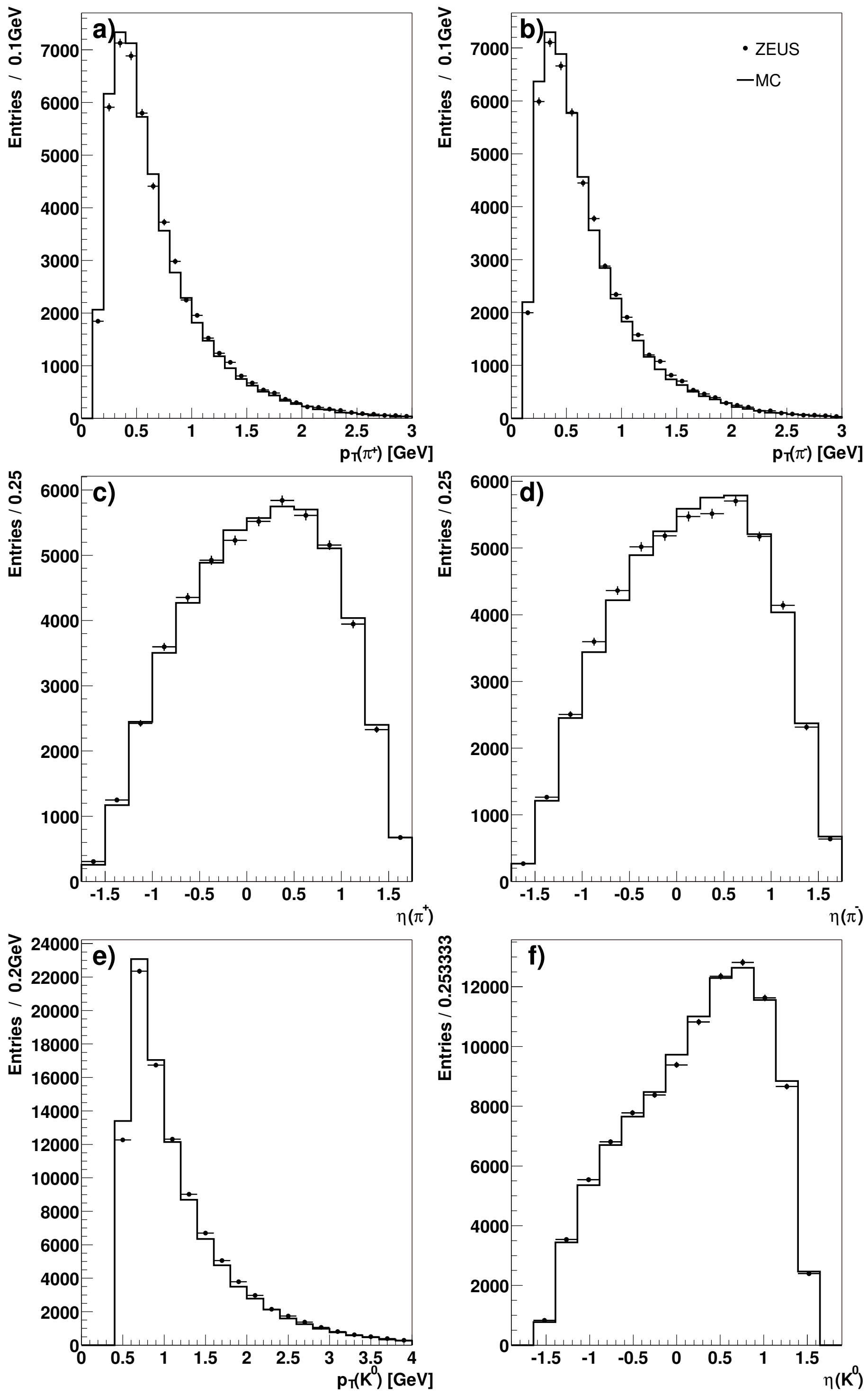

Figure 4.9: Comparison at detector level between data (•) and the ARIADNE Monte Carlo (solid line) for events which have at least one Λ or $\bar{\Lambda}$ candidate with an invariant mass in the mass window of $0.484 < m(\pi, \pi) < 0.51$ GeV. The distributions of some kinematic variables are shown: the transverse momentum p_T for the (a) π^+ and (b) π^- from the K_S^0 decay, the pseudorapidity η for the (c) π^+ and (d) π^- from the K_S^0 decay, (e) the transverse momentum and (f) pseudorapidity of the K_S^0 candidate. The MC distribution is always scaled to the number of entries in the distribution of the data, thus the shape of the distributions can be compared.

4.4.3 Reconstruction of Λ baryons

The Λ baryons are identified through the decay $\Lambda \to p\,\pi^-$. The proton and the pion leave ionized tracks in the CTD which are reconstructed as described above. The track from the secondary vertex candidate with the higher momentum is considered to be the proton with a mass of $m_p = (938.271998 \pm 0.000038)$ MeV [33], the other one with the lower momentum is the pion with $m_\pi = (139.5707 \pm 0.0004)$ MeV [33]. Only well measured tracks which left hits in the inner three superlayers and with a transverse momentum $p_T > 0.15$ GeV and a pseudorapidity η of $|\eta| < 1.75$ are considered. The requirements for the reconstructed Λ candidates are $0.5 < p_T\,(\Lambda) < 5.0$ GeV and $|\eta(\Lambda)| < 1.5$. Figure 4.10 shows the invariant mass distribution $m(p,\pi)$ of the selected Λ candidates.

The number of Λ baryons is obtained by fitting a parameterization to the invariant mass distribution $m(p,\pi)$. This parameterization consists of two Gaussians[3] normalized to one for the Λ signal plus a term describing the background:

$$P(m) = \underbrace{N \cdot [\, r\; G_{1,m_\Lambda,\sigma_1}(m) + (1-r)\; G_{2,m_\Lambda,\sigma_2}(m)\,]}_{Signal} + \underbrace{A \cdot \frac{[m - (m_p + m_{\pi^-})]^B}{\int_{1.1114\text{ GeV}}^{1.1198\text{ GeV}} [m - (m_p + m_{\pi^-})]^B\, dm}}_{Background}\;,$$

where G_1 (G_2) is a Gaussian with the width σ_1 (σ_2) and a common mass m_Λ as parameters of the fit. The parameter r is a free parameter of the fit and the fit parameter N is the normalization of the signal while A and B are free parameters of the fit of the background. A determines the number of background events in the mass window of $1.1114 < m(p,\pi) < 1.1198$ GeV. The number of Λ baryons N_Λ is calculated by counting the number of entries in the mass distribution in the mass window $1.1114 < m(p,\pi) < 1.1198$ GeV subtracted by the parameter A from the fit.

The results of the fit to the experimental data and MC mass distribution for Λ, $\bar\Lambda$ and both $\Lambda + \bar\Lambda$ candidates is shown in Fig. 4.10, 4.11 and 4.12, respectively. The fitted mass m_Λ for data and MC is the same within the uncertainty for Λ, $\bar\Lambda$ and both together. For the combined signal the mass m_Λ for data and MC is measured (Fig. 4.12) to be $m_\Lambda = (1116.23 \pm 0.02)$ MeV and $m_\Lambda = (1116.16 \pm 0.02)$ MeV, respectively. These values are close together and close to the current world average quoted by the PDG [33], namely $m_\Lambda^{PDG} = (1115.683 \pm 0.006)$ MeV. For experimental data the number of Λ, $\bar\Lambda$ and both $\Lambda + \bar\Lambda$ baryons after background subtraction is $N_\Lambda = 4407 \pm 85$, $N_{\bar\Lambda} = 4090 \pm 81$ and $N_{\Lambda+\bar\Lambda} = 8471 \pm 117$, respectively. For MC the values are $N_\Lambda = 7816 \pm 112$, $N_{\bar\Lambda} = 7848 \pm 112$ and $N_{\Lambda+\bar\Lambda} = 15608 \pm 156$, respectively. The MC model gives a reasonable description of the general features of the data. However the MC predicts a width of the signal which is slightly smaller than found in the experimental data. This difference is obvious for Λ, $\bar\Lambda$ and both $\Lambda + \bar\Lambda$ when comparing the background subtracted signals of MC and data (Figs. 4.10, 4.11, 4.12). The effect of this small difference on the measurement is taken into account as a systematic uncertainty (chapter 4.4.4).

[3] One Gaussian does not describe the shape of the signal sufficiently, but already two Gaussians are able to parameterize the signal.

Several distributions measured in the data are compared to the predicted distributions by the MC (Fig. 4.13 and 4.14). The entries in the distribution have at least one $\Lambda, \bar{\Lambda}$ baryon candidate with a mass in the mass window of $1.1126 < m(p, \pi) < 1.1198$ GeV. The distributions which are compared are the reconstructed corrected energy $E_{e',\,corr}$, $E - p_z$, $\log_{10} x_{DA}$, Q^2_{DA}, y_e and y_{JB} (Fig. 4.13). The coordinates X, Y and Z of the reconstructed primary vertex are shown for data and MC in Fig. 4.14. The transverse momentum p_T for the proton and pion from the Λ decay, the pseudorapidity η for the proton and pion from the Λ decay, the transverse momentum and pseudorapidity of the Λ candidates are shown in Fig. 4.15. All distributions show a reasonable agreement between data and MC. Only the reconstructed corrected energy shows a small difference in the shape and the $E - p_z$ distributions in the MC is shifted with respect to the distribution in the data. However these systematic differences are taken into account as a systematic uncertainty for the measurement (chapter 4.4.4).

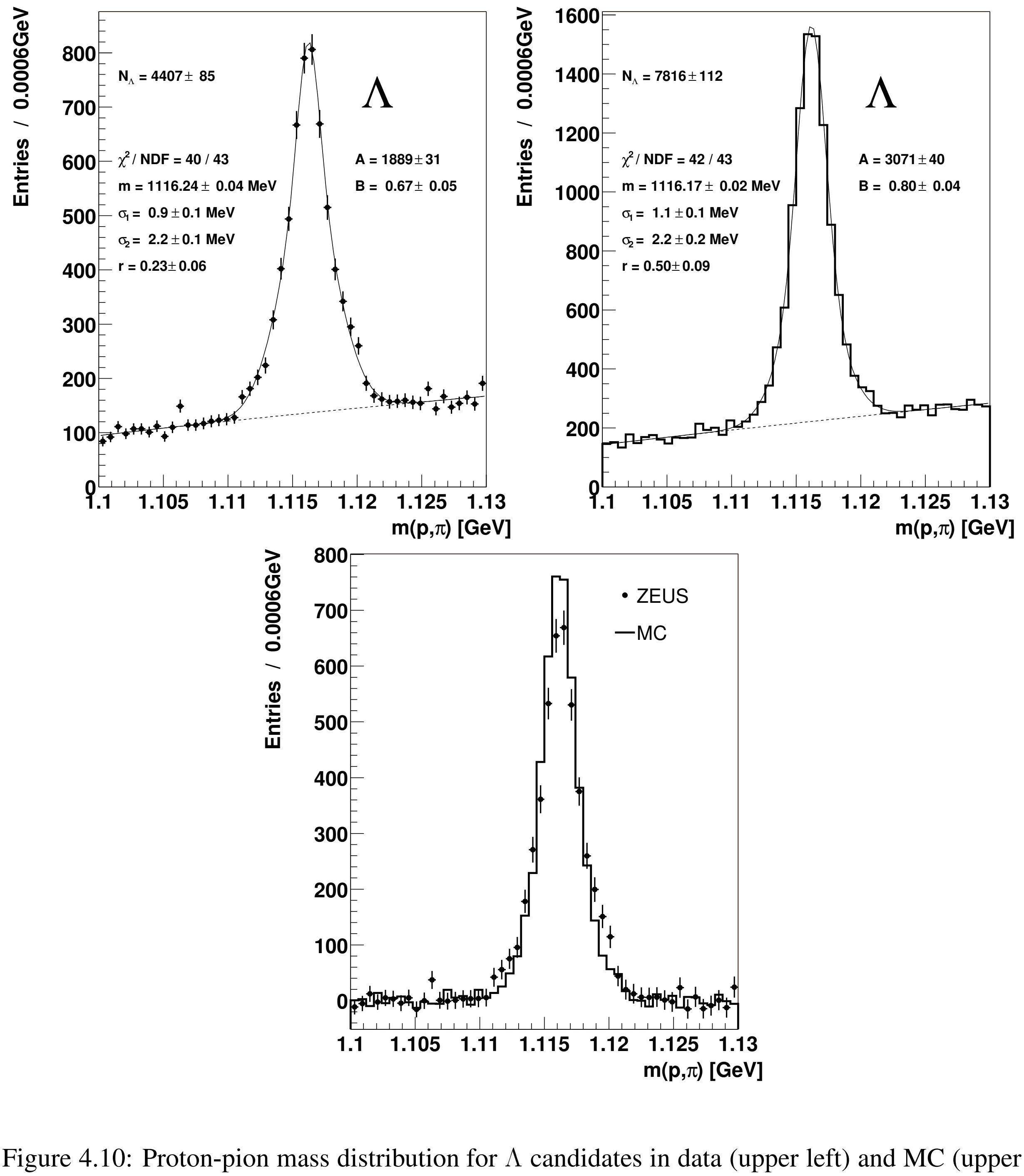

Figure 4.10: Proton-pion mass distribution for Λ candidates in data (upper left) and MC (upper right) in the restricted kinematic region of $20\ \mathrm{GeV}^2 < Q^2 < 500\ \mathrm{GeV}^2$, $3 \cdot 10^{-4} < x < 10^{-1}$ and $0.04 < y < 0.8$, $0.5 < p_T\,(\Lambda) < 5.0$ GeV and $|\eta(\Lambda)| < 1.5$ following the selection procedure described in the text. The solid line in the plots represents the fit to the distribution as described in the text. The dashed line shows the parameterization of the background only. The lower graph shows the background subtracted signal for data (•) and ARIADNE Monte Carlo (solid histogram). The MC distribution is normalized to the area below the distribution of the data.

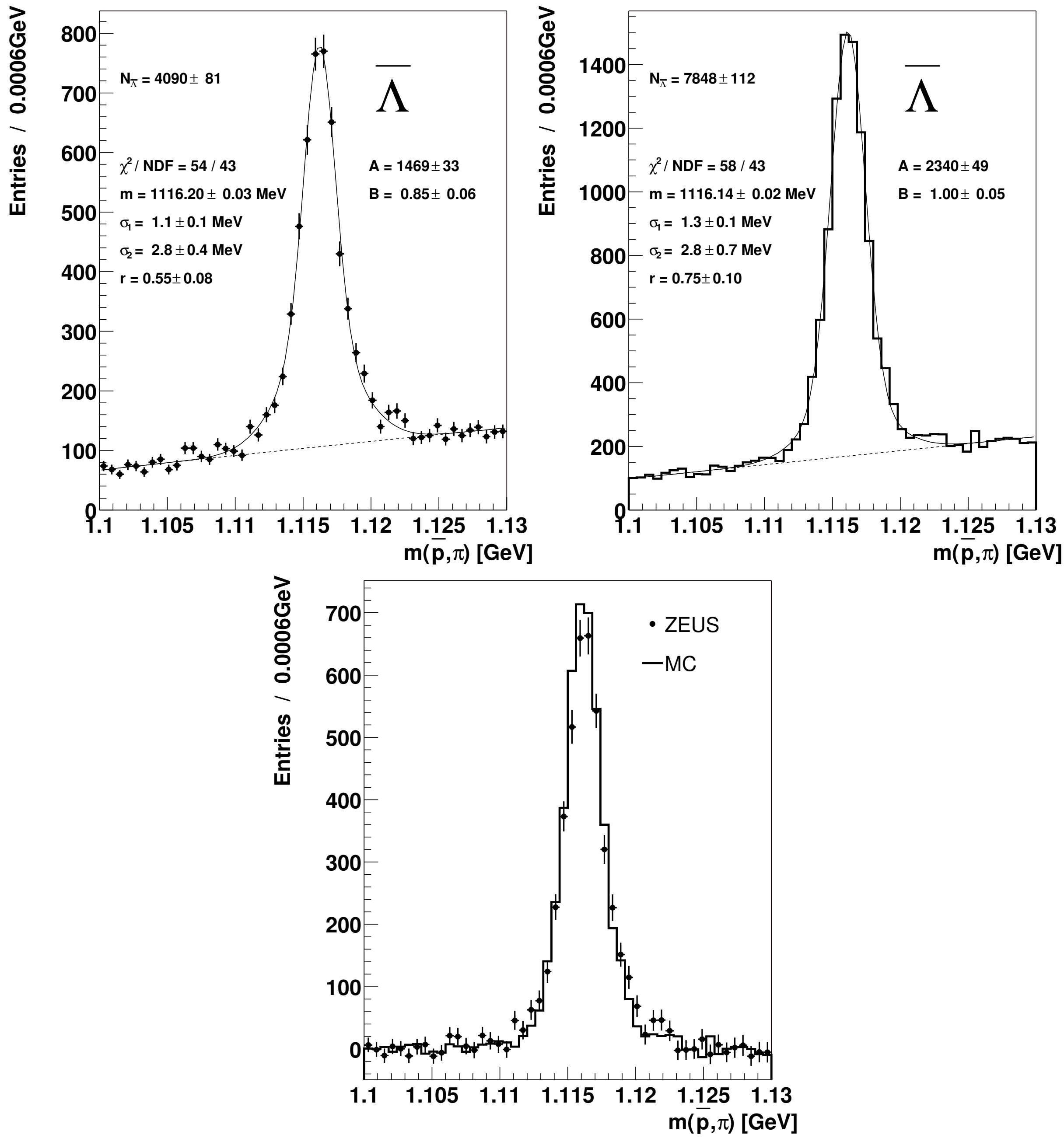

Figure 4.11: Antiproton-pion mass mass distribution for $\bar{\Lambda}$ candidates in data (upper left) and MC (upper right) in the restricted kinematic region of 20 GeV^2 $< Q^2 < 500$ GeV^2, $3 \cdot 10^{-4} < x < 10^{-1}$ and $0.04 < y < 0.8$, $0.5 < p_T\ (\bar{\Lambda}) < 5.0$ GeV and $|\eta(\bar{\Lambda})| < 1.5$ following the selection procedure described in the text. The solid line in the plots represents the fit to the distribution as described in the text. The dashed line shows the parameterization of the background only. The lower graph shows the background subtracted signal for data (•) and ARIADNE Monte Carlo (solid histogram). The MC distribution is normalized to the area below the distribution of the data.

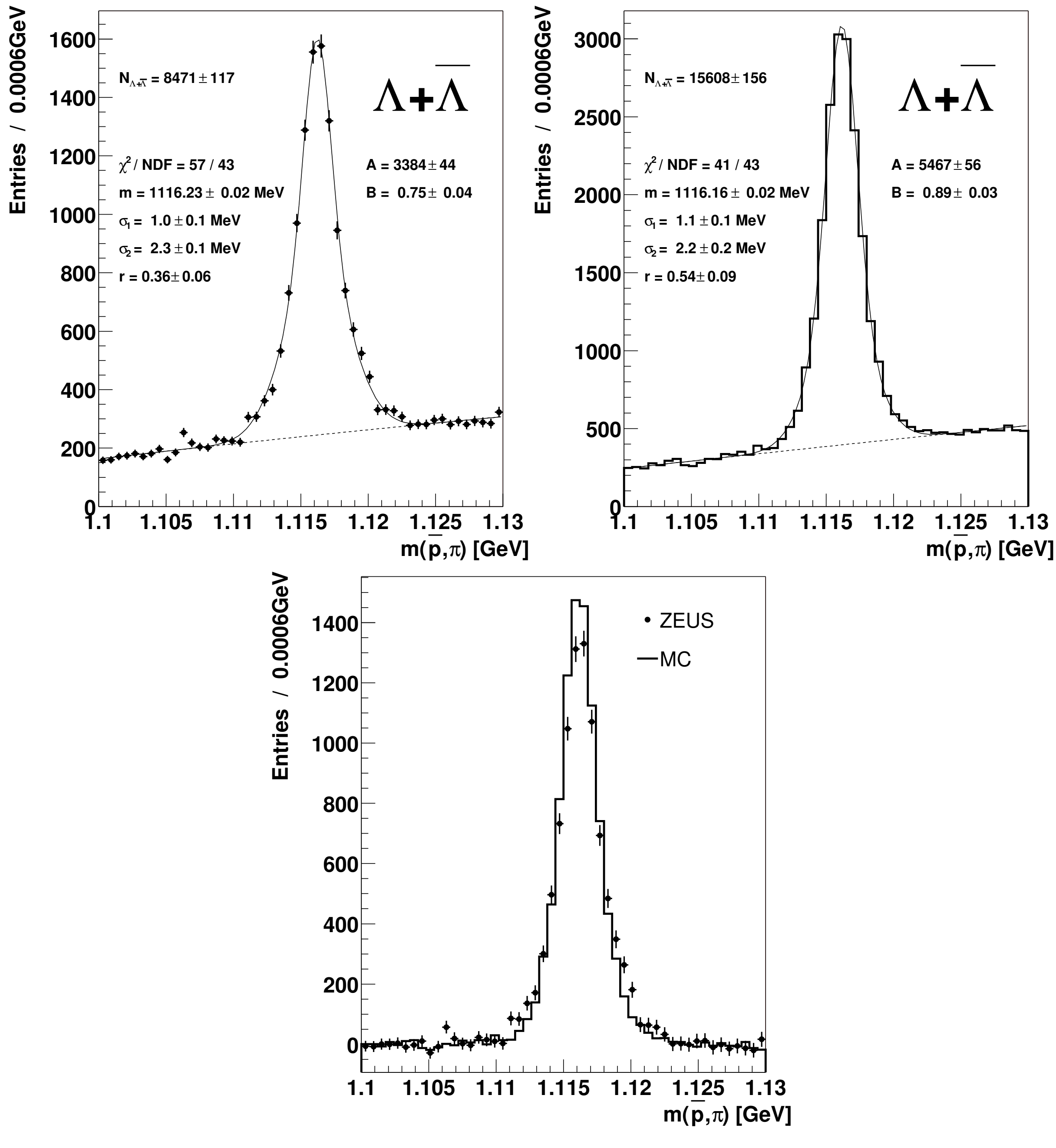

Figure 4.12: Antiproton-pion mass mass distribution for $\Lambda+\bar{\Lambda}$ candidates in data (upper left) and MC (upper right) in the restricted kinematic region of 20 GeV^2 $< Q^2 < 500$ GeV^2, $3 \cdot 10^{-4} < x < 10^{-1}$ and $0.04 < y < 0.8$, $0.5 < p_T\ (\Lambda + \bar{\Lambda}) < 5.0$ GeV and $|\eta(\Lambda + \bar{\Lambda})| < 1.5$ following the selection procedure described in the text. The solid line in the plots represents the fit to the distribution as described in the text. The dashed line shows the parameterization of the background only. The lower graph shows the background subtracted signal for data (•) and ARIADNE Monte Carlo (solid histogram). The MC distribution is normalized to the area below the distribution of the data.

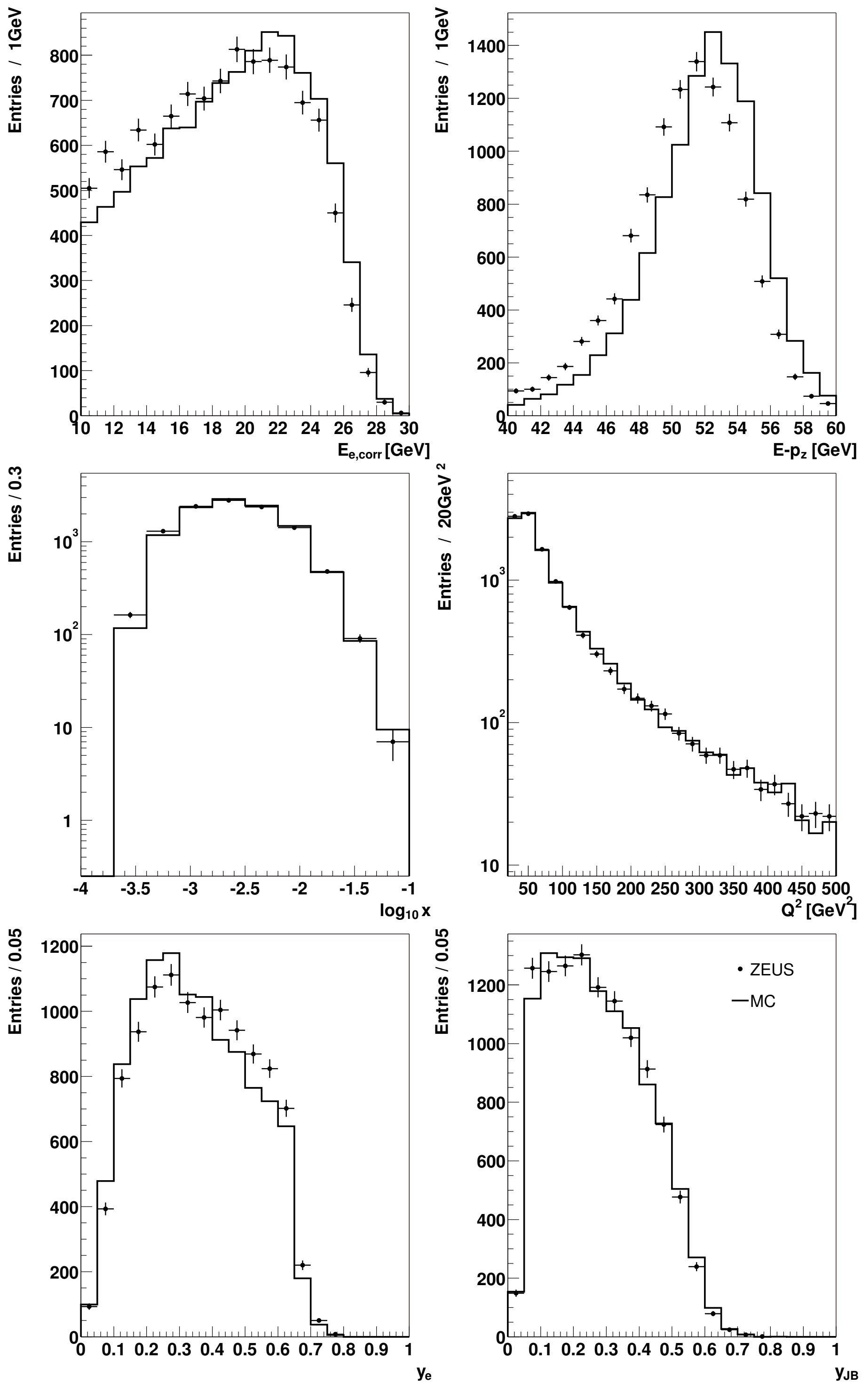

Figure 4.13: Comparison at detector level between data (•) and the ARIADNE Monte Carlo (solid line) for events which have at least one Λ or $\bar{\Lambda}$ candidate with an invariant mass in the mass window of $1.1126 < m(p, \pi) < 1.1198$ GeV. The distributions of some kinematic variables are shown: the corrected energy of the electron, $E_{e',\,corr}$, the hadronic $E - p_z$, the logarithm of the Bjorken x reconstructed with the double angle method, $\log_{10} x_{DA}$, the squared four momentum transfer reconstructed with the double angle method, Q^2_{DA}, the inelasticity reconstructed with the electron method, y_e and with the Jacquet-Blondel method, y_{JB}. The MC distribution is always scaled to the number of entries in the distribution of the data, thus the shape of the distributions can be compared.

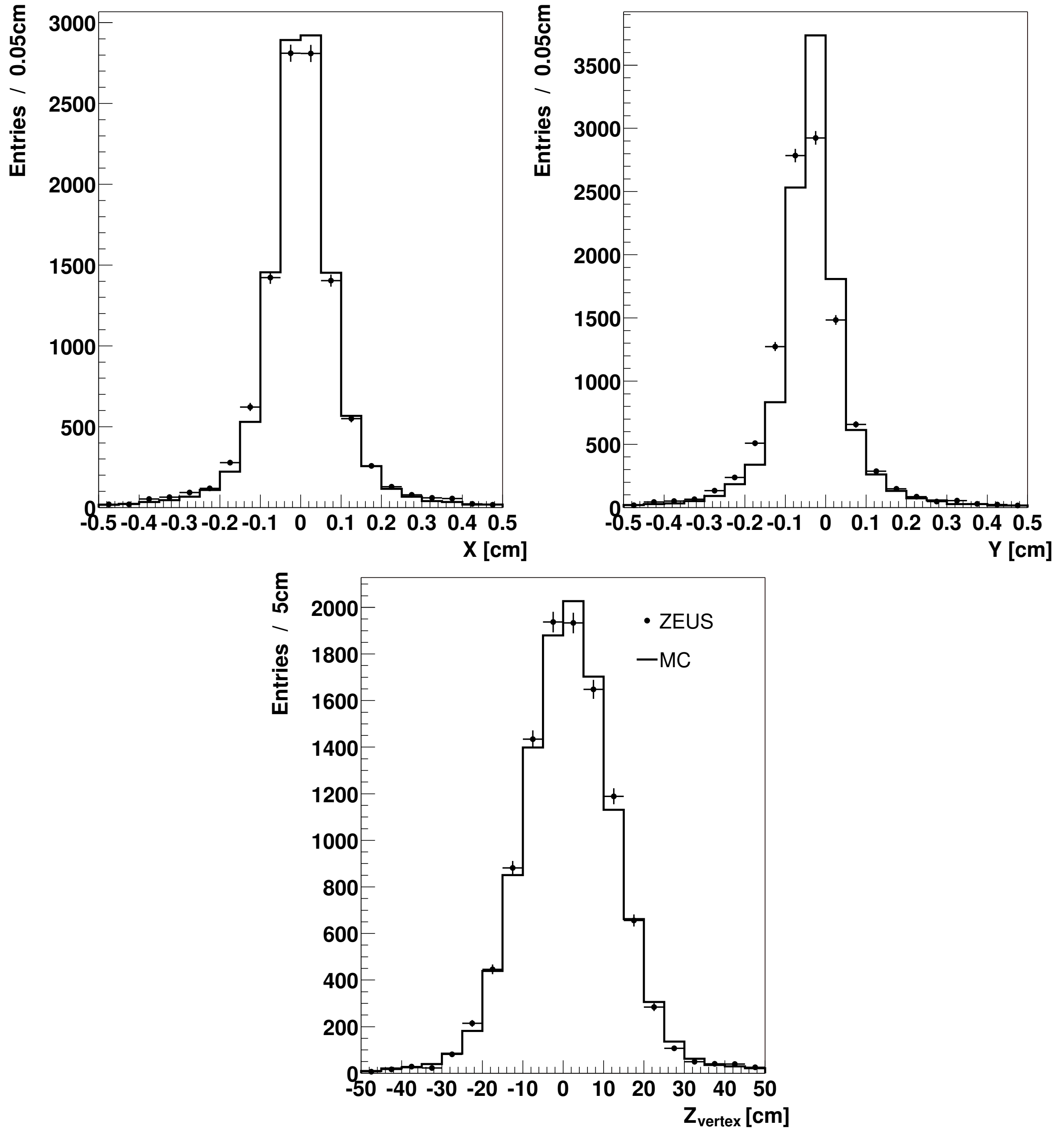

Figure 4.14: Comparison at detector level between data (•) and the ARIADNE Monte Carlo (solid line) for events which have at least one Λ or $\bar{\Lambda}$ candidate with an invariant mass in the mass window of $1.1126 < m(p, \pi) < 1.1198$ GeV. The X, Y and the Z position of the primary event vertex is shown. The MC distribution is always normalized to the area below the distribution of the data. The shape of the vertex distributions is well reproduced by the Monte Carlo, however there is a slight shift in the Y vertex.

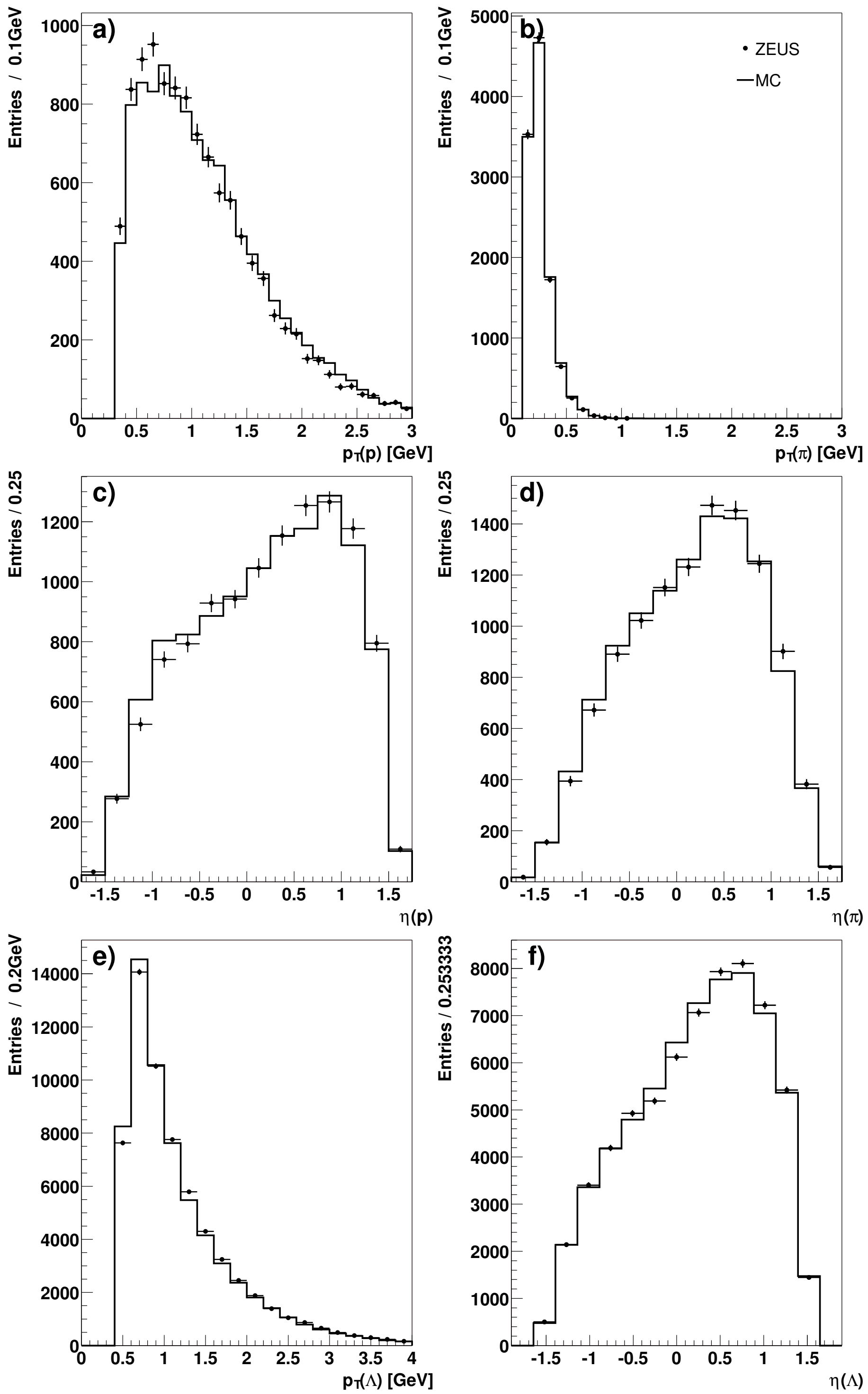

Figure 4.15: Comparison at detector level between data (•) and the ARIADNE Monte Carlo (solid line) for events which have at least one Λ or $\bar{\Lambda}$ candidate with an invariant mass in the mass window of $1.1126 < m(p,\pi) < 1.1198$ GeV. The distributions of some kinematic variables are shown: the transverse momentum p_T for the (a) proton and (b) pion from the Λ decay, the pseudorapidity η for the (c) proton and (d) pion from the Λ decay, (e) the transverse momentum and (f) pseudorapidity of the Λ candidate. The MC distribution is always scaled to the number of entries in the distribution of the data, thus the shape of the distributions can be compared.

4.4.4 Definition of the cross section and systematic uncertainties

The cross section for a given observable Y is determined by

$$\frac{d\sigma}{dY} = \frac{N}{A \cdot \mathcal{L} \cdot B \cdot \Delta Y},$$

where N is the number of events with a K_S^0 meson or a Λ baryon candidate determined from the fits described above in a bin of the size ΔY, $\mathcal{L}$ is the integrated luminosity and A is the acceptance. The acceptance is defined by the number of reconstructed K_S^0 and Λ in a certain bin ΔY divided by the number of generated K_S^0 and Λ for that bin. If the MC simulation provides a good description of the hadronic final state, the acceptance takes into account migrations, efficiencies and radiative effects for that bin. The branching ratio, B, for the decay channels $K_S^0 \to \pi^+\pi^-$and $\Lambda \ \to \ p\,\pi^-$ is taken to be $(68.60\pm0.27)\%$ and $(63.9\pm0.5)\%$ [33], respectively.

The systematic uncertainties on the measured cross sections for K_S^0 mesons and Λ baryons are estimated from the following changes of the cuts:

1. Event reconstruction and selection. Systematic checks are performed by varying the cuts on y_e, y_{JB}, $E - p_z$, $|Z_{vertex}|$, $E_{e',\,corr}$ and r_{el}. The values are varied to $y_e < 0.75$, $y_{JB} > 0.05$, $42 < E - p_z < 58$ GeV and $|Z_{vertex}| < 45$ cm. The cut on the corrected energy of the scattered positron in the calorimeter is increased by 1 GeV to $E_{e',\,corr} > 11$ GeV. The radius cut for the positron position in the calorimeter is raised by 1 cm to $r_{el} > 37$ cm.

2. The electron method is used to reconstruct the kinematic quantities x and Q^2 instead of the double angle method.

3. The transverse momentum p_T for the reconstructed tracks is raised to be $p_T > 0.17$ GeV. Also the systematic uncertainty on the pseudorapidity of the tracks is checked by changing η to be $|\eta| < 1.7$.

4. The mass window which is used to determine the number of K_S^0 and Λ is raised in its width. The selected regions to determine the systematic uncertainty for the K_S^0 reconstruction are $0.486 < m(\pi,\pi) < 0.508$ and $0.480 < m(\pi,\pi) < 0.514$, while the selected regions for the Λ reconstruction are $1.1120 < m(p,\pi) < 1.1192$ and $1.1102 < m(p,\pi) < 1.1210$.

5. The cut on the invariant mass hypothesis $m(p,\pi)$ of K_S^0 candidates which is used to eliminate the Λ contamination of the K_S^0 signal is raised from $m(p,\pi) > 1.12$ GeV to $m(p,\pi) > 1.125$ GeV.

6. HERWIG is used to determine the acceptance instead of ARIADNE. Since HERWIG does not simulate the data properly this systematic is not included in the total systematic uncertainty. For example the p_T distribution of the pions from the K_S^0 decay in data and HERWIG MC are shown (Fig. 4.16). Also disagreements are obvious for the η and p_T distributions of the proton and pion from the Λ decay, which is not shown.

The overall systematic uncertainty was determined by adding the above uncertainties in quadrature. The normalization uncertainties due to the luminosity measurement error, and those due to the branching ratio of 0.27% and 0.5% for $K_S^0 \to \pi^+\pi^-$and $\Lambda \to p\,\pi^-$, respectively, were not included in the systematic uncertainties. The contribution of these changes on the measured cross section is summarized in Tab. 4.1.

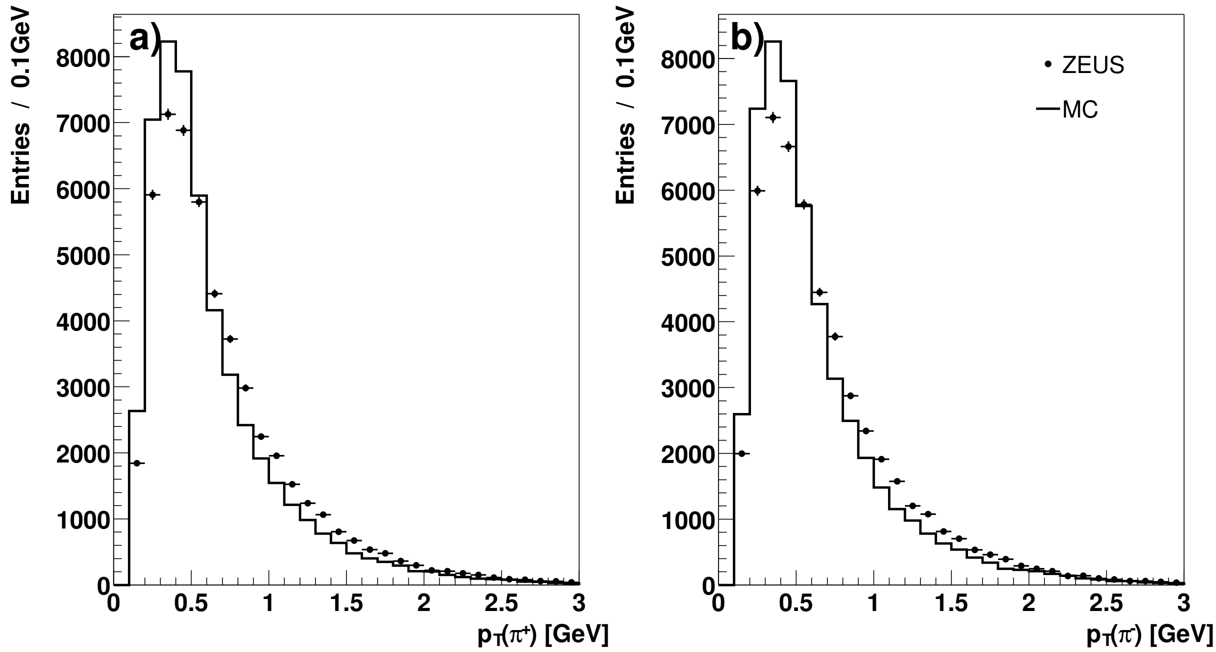

Figure 4.16: Comparison at detector level between data (•) and the HERWIG Monte Carlo (solid line) for events which have at least one K_S^0 candidate with an invariant mass in the mass window of $0.484 < m(\pi, \pi) < 0.51$ GeV. The p_T distribution for the pion with positive and negative charge from the K_S^0 decay are shown. The MC distribution is normalized to the area below the distribution of the data.

cut varied to	K_S^0	$\Lambda + \bar{\Lambda}$
$y_e < 0.75$	-2.1%	-2.4%
$y_{JB} > 0.05$	-2.7%	-1.1%
$42 < E - p_z < 58$ GeV	$+0.03\%$	$+0.3\%$
$\|Z_{vertex}\| < 45$ cm	$+0.1\%$	-0.1%
$r_{el} > 37$ cm	$+0.3\%$	$+0.2\%$
$E_{e',\,corr} > 11$ GeV	-0.7%	-0.8%
electron method	-0.5%	-0.4%
$p_T(\pi, p) > 0.17$ GeV	$+0.3\%$	-0.3%
$\|\eta(\pi, p)\| < 1.7$	$+0.1\%$	-0.05%
mass window narrower	-1.2%	-1.8%
mass window wider	$+1.1\%$	$+1.8\%$
$m(p, \pi) > 1.125$ GeV	$+0.5\%$	—
HERWIG instead of ARIADNE	$(+6.9\%)$	$(+6.6\%)$
total systematic uncertainty	$^{+1.3\%}_{-3.7\%}$	$^{+1.8\%}_{-2.4\%}$

Table 4.1: List of the systematic uncertainties of the total cross section in the restricted kinematic region by varying several cuts as described in the text. The systematic uncertainty contributed by HERWIG is not included in the total systematic uncertainty.

4.4.5 Total cross sections of K^0_S meson and Λ baryon production

The overall K^0_S meson acceptance for $20\,\text{GeV}^2 < Q^2 < 500\,\text{GeV}^2$, $3 \cdot 10^{-4} < x < 10^{-1}$, $0.04 < y < 0.8$, $0.5 < p_T\ (K^0_S) < 5.0$ GeV and $|\eta(K^0_S)| < 1.5$, estimated with DJANGOH using ARIADNE is $18.6 \pm 0.2\%$. Since DJANGOH using ARIADNE provides the best description of the final state in DIS [42] and the K^0_S reconstruction, it is used to calculate the cross section. The total K^0_S meson cross section measured in this restricted kinematic region is

$$\sigma(e^+p \to e^+K^0_S X) = 6431 \pm 38(\text{stat.})^{+64}_{-207}(\text{syst.})\ \text{pb}.$$

This cross section is underestimated by HERWIG which predicts a total cross section of 4836 pb. The ARIADNE model with a strangeness suppression factor λ_s of $\lambda_s = 0.3$ overestimates the measured cross section (7144 pb) while the lower strangeness suppression factor $\lambda_s = 0.2$ underestimates the total measured cross section (5889 pb). Both predictions by ARIADNE are not in agreement with the measurement within the uncertainty of the measurement.

The overall Λ baryon acceptance for the same restricted kinematic region $20\,\text{GeV}^2 < Q^2 < 500\,\text{GeV}^2$, $3 \cdot 10^{-4} < x < 10^{-1}$, $0.04 < y < 0.8$, $0.5 < p_T\ (K^0_S) < 5.0$ GeV and $|\eta(K^0_S)| < 1.5$ is found to be $14.8 \pm 0.2\%$ with DJANGOH using ARIADNE. The total Λ baryon cross section measured in this restricted kinematic region is

$$\sigma(e^+p \to e^+\Lambda X) = 779 \pm 19(\text{stat.})^{+15}_{-36}(\text{syst.})\ \text{pb}.$$

This cross section is overestimated by HERWIG which predicts a total cross section of 1837 pb. The ARIADNE model with a strangeness suppression factor λ_s of $\lambda_s = 0.3$ overestimates the measured cross section (803 pb) while the lower strangeness suppression factor $\lambda_s = 0.2$ underestimates the total measured cross section (641 pb). The prediction with $\lambda_s = 0.3$ is in agreement with the measurement within the uncertainty while the prediction with $\lambda_s = 0.2$ is outside.

The overall $\bar{\Lambda}$ anti-baryon acceptance for the restricted kinematic region $20\,\text{GeV}^2 < Q^2 < 500\,\text{GeV}^2$, $3 \cdot 10^{-4} < x < 10^{-1}$, $0.04 < y < 0.8$, $0.5 < p_T\ (K^0_S) < 5.0$ GeV and $|\eta(K^0_S)| < 1.5$ is found to be $14.7 \pm 0.2\%$ with DJANGOH using ARIADNE. The total $\bar{\Lambda}$ anti-baryon cross section measured in this restricted kinematic region is

$$\sigma(e^+p \to e^+\bar{\Lambda} X) = 724 \pm 17(\text{stat.})^{+21}_{-21}(\text{syst.})\ \text{pb}.$$

This cross section is overestimated by HERWIG which predicts a total cross section of 1842 pb. The ARIADNE model with a strangeness suppression factor λ_s of $\lambda_s = 0.3$ overestimates the measured cross section (803 pb) while the lower strangeness suppression factor $\lambda_s = 0.2$ underestimates the total measured cross section (649 pb). The prediction with $\lambda_s = 0.3$ is in agreement with the measurement within the uncertainty while the prediction with $\lambda_s = 0.2$ is outside.

The overall Λ baryon and $\bar{\Lambda}$ anti-baryon acceptance for the restricted kinematic region $20\,\text{GeV}^2 < Q^2 < 500\,\text{GeV}^2$, $3 \cdot 10^{-4} < x < 10^{-1}$, $0.04 < y < 0.8$, $0.5 < p_T\ (K^0_S) < 5.0$ GeV and

$|\eta(K_S^0)| < 1.5$ is found to be $14.7 \pm 0.2\%$ with DJANGOH using ARIADNE. The total Λ baryon and $\bar{\Lambda}$ anti-baryon cross section, $\sigma(\Lambda + \bar{\Lambda})$, measured in this restricted kinematic region is

$$\sigma(\Lambda + \bar{\Lambda}) = 1503 \pm 26(\text{stat.})^{+28}_{-50}(\text{syst.})\ \text{pb}.$$

Also this cross section is overestimated by HERWIG which predicts a total cross section of 3679 pb. The ARIADNE model with a strangeness suppression factor λ_s of $\lambda_s = 0.3$ overestimates the measured cross section (1606 pb) while the lower strangeness suppression factor $\lambda_s = 0.2$ underestimates the total measured cross section (1209 pb). The prediction with $\lambda_s = 0.3$ is in agreement with the measurement within the uncertainty while the prediction with $\lambda_s = 0.2$ is outside.

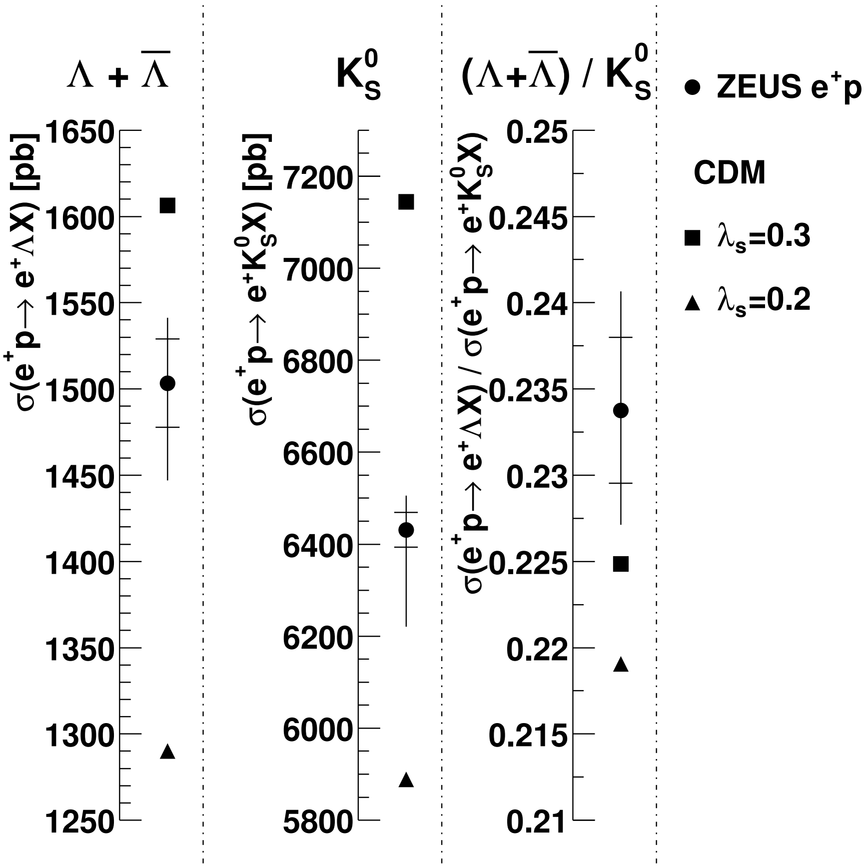

Figure 4.17: Total measured cross sections of K_S^0 meson, $\Lambda + \bar{\Lambda}$ baryon production and the ratio of the cross sections, $\sigma(\Lambda + \bar{\Lambda})/\sigma(K_S^0)$, in a restricted kinematic range ($20 < Q^2 < 500$ GeV^2, $3 \cdot 10^{-4} < x < 10^{-1}$, $0.04 < y < 0.8$, $0.5 < p_T(K_S^0, \Lambda, \bar{\Lambda}) < 5$ GeV and $|\eta(K_S^0, \Lambda, \bar{\Lambda})| < 1.5$). The cross sections predicted by ARIADNE (CDM) with strangeness suppression factor $\lambda_s = 0.3$ and $\lambda_s = 0.2$ are shown, too.

The ratio of Λ baryon to $\bar{\Lambda}$ anti-baryon production in the restricted kinematic range of 20 GeV^2 $<$ $Q^2 < 500$ GeV^2, $3 \cdot 10^{-4} < x < 10^{-1}$ and $0.04 < y < 0.8$, $0.5 < p_T\ (\Lambda, \bar{\Lambda}) < 5.0$ GeV and

	$\sigma(K^0_S)$ [pb]	$\sigma(\Lambda+\bar{\Lambda})$ [pb]	$\sigma(\Lambda+\bar{\Lambda})/\sigma(K^0_S)$
ZEUS	$6431 \pm 38^{+64}_{-207}$	$1503 \pm 26^{+28}_{-50}$	$0.231 \pm 0.005^{+0.006}_{-0.005}$
CDM			
$\lambda_s = 0.3$	7144	1606	0.225
$\lambda_s = 0.2$	5889	1290	0.219
HERWIG	4836	3679	0.761

	$\sigma(\Lambda)$ [pb]	$\sigma(\bar{\Lambda})$ [pb]	$\sigma(\Lambda)/\sigma(\bar{\Lambda})$
ZEUS	$779 \pm 19^{+15}_{-36}$	$724 \pm 17^{+21}_{-21}$	$1.08 \pm 0.04^{+0.003}_{-0.05}$
CDM			
$\lambda_s = 0.3$	803	803	1.00
$\lambda_s = 0.2$	641	649	0.988
HERWIG	1837	1842	0.997

Table 4.2: Total measured cross sections of K^0_S meson, Λ baryon, $\bar{\Lambda}$ baryon and $\Lambda+\bar{\Lambda}$ baryon production and the ratio of the cross sections, $\sigma(\Lambda+\bar{\Lambda})/\sigma(K^0_S)$ and $\sigma(\Lambda)/\sigma(\bar{\Lambda})$, in a restricted kinematic range ($20 < Q^2 < 500\,\text{GeV}^2$, $3 \cdot 10^{-4} < x < 10^{-1}$, $0.04 < y < 0.8$, $0.5 < p_T(K^0_S, \Lambda, \bar{\Lambda}) < 5$ GeV and $|\eta(K^0_S, \Lambda, \bar{\Lambda})| < 1.5$). The cross sections predicted by ARIADNE (CDM) with strangeness suppression factor $\lambda_s = 0.3$ and $\lambda_s = 0.2$ and HERWIG are shown too.

$|\eta(\Lambda, \bar{\Lambda})| < 1.5$ is measured to be $\sigma(\Lambda)/\sigma(\bar{\Lambda}) = 1.08 \pm 0.04^{+0.003}_{-0.05}$. This measurement is in agreement with the predictions of ARIADNE with $\lambda_s = 0.3$ and $\lambda_s = 0.2$ and HERWIG, which forecast an equal production of baryons and anti-baryons.

All cross sections which are measured and the ratios of Λ baryon to $\bar{\Lambda}$ anti-baryon production $\sigma(\Lambda)/\sigma(\bar{\Lambda})$ and of $\sigma(\Lambda+\bar{\Lambda})/\sigma(K^0_S)$ are compiled in Tab. 4.2. The predictions of HERWIG and ARIADNE with strangeness suppression factor $\lambda_s = 0.3$ and $\lambda_s = 0.2$ are listed too. The measurements of $\sigma(\Lambda+\bar{\Lambda})$, $\sigma(K^0_S)$ and $\sigma(\Lambda+\bar{\Lambda})/\sigma(K^0_S)$ and the prediction of ARIADNE with $\lambda_s = 0.3$ and $\lambda_s = 0.2$ are shown in Fig. 4.17.

This measurement shows that the HERWIG model is not able to describe the total cross sections of Λ baryon and K^0_S meson production and the relative ratio $\sigma(\Lambda+\bar{\Lambda})/\sigma(K^0_S)$. However, it predicts an equal production of Λ baryons and $\bar{\Lambda}$ anti-baryons. The ARIADNE MC gives a reasonable description of the total cross section of K^0_S, Λ and $\bar{\Lambda}$ production and of the ratio $\sigma(\Lambda+\bar{\Lambda})/\sigma(K^0_S)$ and $\sigma(\Lambda)/\sigma(\bar{\Lambda})$. This measurement, with its statistics, allows one to say that both strangeness suppression factors are not able to describe the total cross section within the uncertainty. Recent measurements [47] show that the production of heavier baryons is not well simulated, either, and that more parameters of JETSET need to be tuned. The suggested tuning in this thesis [47] has an effect on the prediction of Λ production and therefore it does not make sense to find an optimal strangeness suppression factor with the measurement of K^0_S meson and Λ baryon only.

The total cross section of K^0_S meson and Λ baryon production is much better predicted by ARI-

ADNE with JETSET than by HERWIG. A symmetric production of Λ baryon and $\bar{\Lambda}$ anti-baryon is measured as predicted by all MC models.

4.5 Measurement of K_S^0 meson and Λ baryon production in bins of Q^2, x, p_T and η

The cross section of K_S^0 mesons and Λ baryons are measured in bins of Q^2, x, p_T and η in the restricted kinematic range of $20\,\text{GeV}^2 < Q^2 < 500\,\text{GeV}^2$, $3 \cdot 10^{-4} < x < 10^{-1}$ and $0.04 < y < 0.8$, $0.5 < p_T\ (K_S^0) < 5.0$ GeV and $|\eta(K_S^0)| < 1.5$. The differential cross sections are shown as a function of Q^2, x, $p_T(K_S^0, \Lambda)$ and $\eta(K_S^0, \Lambda)$ and are compared to the Monte Carlo models HERWIG and ARIADNE. The latter Monte Carlo is generated with $\lambda_s = 0.2$ and $\lambda_s = 0.3$ (default value). The HERWIG Monte Carlo model is always scaled to the area below the data points to compare the shapes of the differential cross sections because the HERWIG MC fails to predict the correct total cross section (chapter 4.4). Since the ARIADNE MC model predicts a total cross section close to the measured one, these distributions are not changed in the normalization.

In Fig. 4.18 the cross sections of K_S^0 meson production in bins of Q^2, x, $p_T(K_S^0)$ and $\eta(K_S^0)$ are shown with the MC predictions. The shape of the Q^2 distribution is well reproduced by all Monte Carlo models. For the x distribution the situation is similar, although it seems to be that the measured x distribution falls more rapidly than for the MCs. The shape of the $p_T(K_S^0)$ distribution predicted by HERWIG is not in agreement with the measurement. Comparing with ARIADNE it is clear that the measurement prefers the prediction with $\lambda_s = 0.2$ for $p_T(K_S^0) < 1.2$ GeV. For $p_T(K_S^0) > 1.2$ GeV the difference between the prediction with $\lambda_s = 0.2$ and $\lambda_s = 0.3$ vanishes. However the optimal parameter of λ_s has to be between these values to agree with this distribution. The shape of the measured $\eta(K_S^0)$ distribution is well reproduced by HERWIG. The difference between ARIADNE with $\lambda_s = 0.2$ and $\lambda_s = 0.3$ increases in forward direction. However the measurement prefers $\lambda_s = 0.2$ for $\eta(K_S^0) < 0.5$ and is between $\lambda_s = 0.2$ and $\lambda_s = 0.3$ for $\eta(K_S^0) > 0.5$. Also this distribution should be better described by a parameter λ_s with $0.2 < \lambda_s < 0.3$. The biggest contribution to the systematic uncertainty for the highest x and $\eta(K_S^0)$ bins comes from the change of the reconstruction of the kinematic quantities from the DA method to the electron method.

Comparing the differential cross section of Λ (Fig. 4.19) and $\bar{\Lambda}$ (Fig. 4.20) in bins of Q^2, x, $p_T(\Lambda, \bar{\Lambda})$ and $\eta(\Lambda, \bar{\Lambda})$ it is clear that these behave similarly for both measurement and predictions. The only exception from this agreement is the lowest bin in p_T. The measurement for $p_T(\Lambda) < 1.2$ GeV is in agreement with the prediction by ARIADNE with $\lambda_s = 0.3$, while for $p_T(\bar{\Lambda}) < 1.2$ GeV the measurement is between $\lambda_s = 0.2$ and $\lambda_s = 0.3$. However, both measurements are consistent within 2 standard deviations. Since this agreement exists, only the combined differential cross sections of both Λ and $\bar{\Lambda}$ production $(\Lambda + \bar{\Lambda})$ in bins of Q^2, x, $p_T(\Lambda + \bar{\Lambda})$ and $\eta(\Lambda + \bar{\Lambda})$ are discussed in detail.

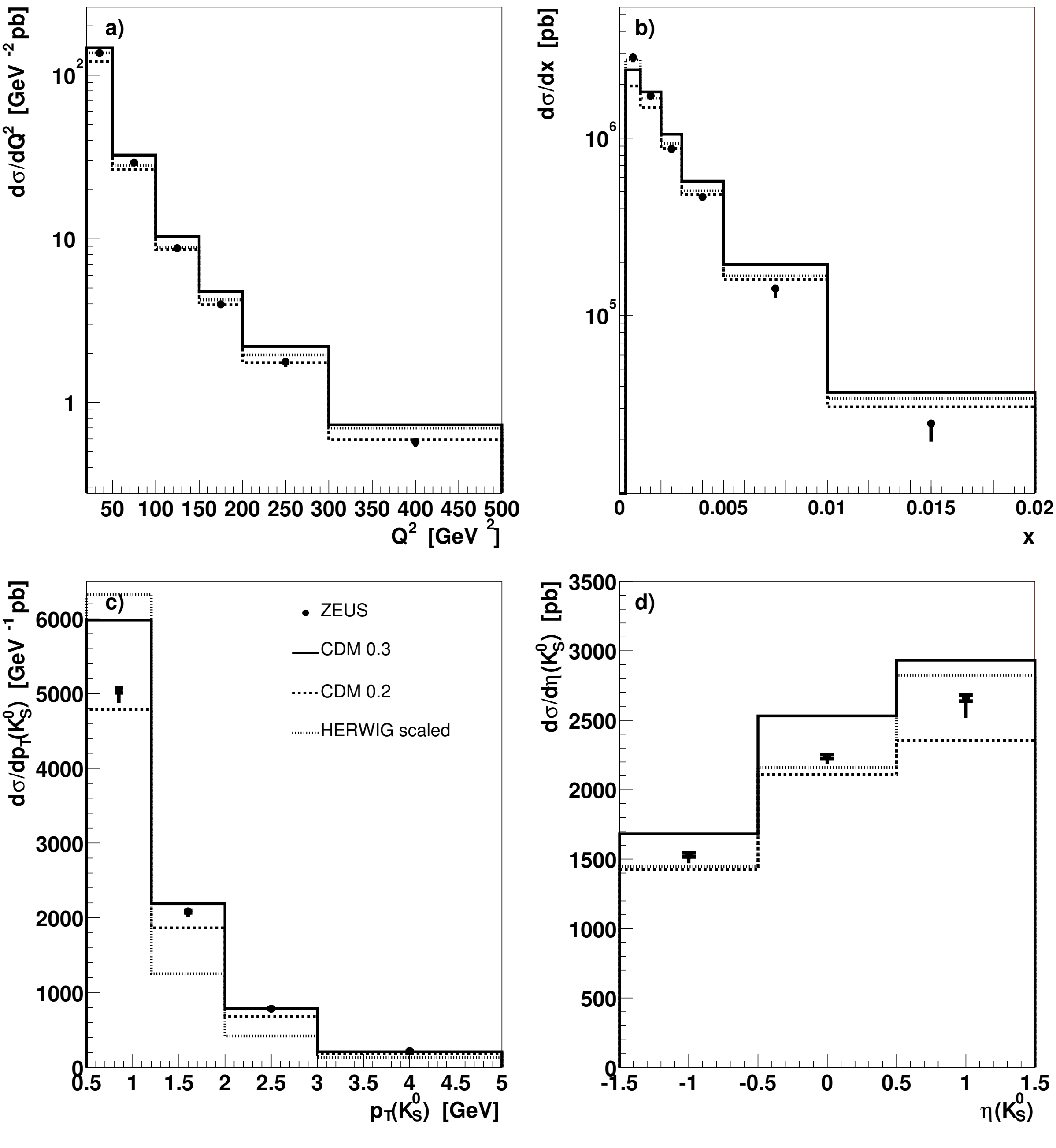

Figure 4.18: Measured differential K^0_S meson cross sections (•) as functions of Q^2, x, $p_T(K^0_S)$ and $\eta(K^0_S)$, compared to the Monte Carlo models HERWIG (dotted line) and ARIADNE with strangeness suppression factor $\lambda_s = 0.3$ (solid line) and $\lambda_s = 0.2$ (dashed line). The full error bars include the systematic uncertainties. HERWIG is scaled to the area below the experimental data.

Q^2 range [GeV^2]	$N_{K_S^0}$	$d\sigma(K_S^0)/dQ^2$ [pb/GeV^2]
$20-50$	20469 ± 150	$136 \pm 1^{+2}_{-5}$
$50-100$	17632 ± 140	$29.2 \pm 0.2^{+0.3}_{-1.0}$
$100-150$	5334 ± 77	$8.8 \pm 0.1^{+0.1}_{-0.3}$
$150-200$	2411 ± 52	$3.97 \pm 0.09^{+0.05}_{-0.17}$
$200-300$	2095 ± 49	$1.77 \pm 0.04^{+0.02}_{-0.12}$
$300-500$	1346 ± 40	$0.57 \pm 0.02^{+0.01}_{-0.04}$

x range	$N_{K_S^0}$	$d\sigma(K_S^0)/dx[10^4$pb]
$0.0003-0.001$	9348 ± 102	$285 \pm 3^{+4}_{-17}$
$0.001-0.002$	11879 ± 114	$173 \pm 2^{+3}_{-4}$
$0.002-0.003$	7368 ± 90	$87 \pm 1^{+3}_{-1}$
$0.003-0.005$	8682 ± 98	$46.6 \pm 0.5^{+0.5}_{-1.6}$
$0.005-0.01$	8276 ± 97	$14.2 \pm 0.2^{+0.2}_{-1.6}$
$0.01-0.02$	3181 ± 61	$2.47 \pm 0.05^{+0.03}_{-0.51}$

$p_T(K_S^0)$ range [GeV]	$N_{K_S^0}$	$d\sigma(K_S^0)/dp_T(K_S^0)$[pb/GeV]
$0.5-1.2$	25421 ± 172	$5044 \pm 34^{+47}_{-168}$
$1.2-2$	15331 ± 128	$2085 \pm 17^{+26}_{-70}$
$2-3$	6318 ± 82	$785 \pm 10^{+6}_{-26}$
$3-5$	2171 ± 48	$218 \pm 5^{+2}_{-6}$

$\eta(K_S^0)$ range	$N_{K_S^0}$	$d\sigma(K_S^0)/d\eta(K_S^0)$[pb]
$-1.5 - -0.5$	11830 ± 113	$1530 \pm 15^{+15}_{-59}$
$-0.5 - 0.5$	20099 ± 149	$2237 \pm 17^{+24}_{-48}$
$0.5 - 1.5$	17317 ± 141	$2660 \pm 22^{+27}_{-140}$

Table 4.3: Measured differential K_S^0 meson cross sections as a function of Q^2, x, $p_T(K_S^0)$ and $\eta(K_S^0)$.

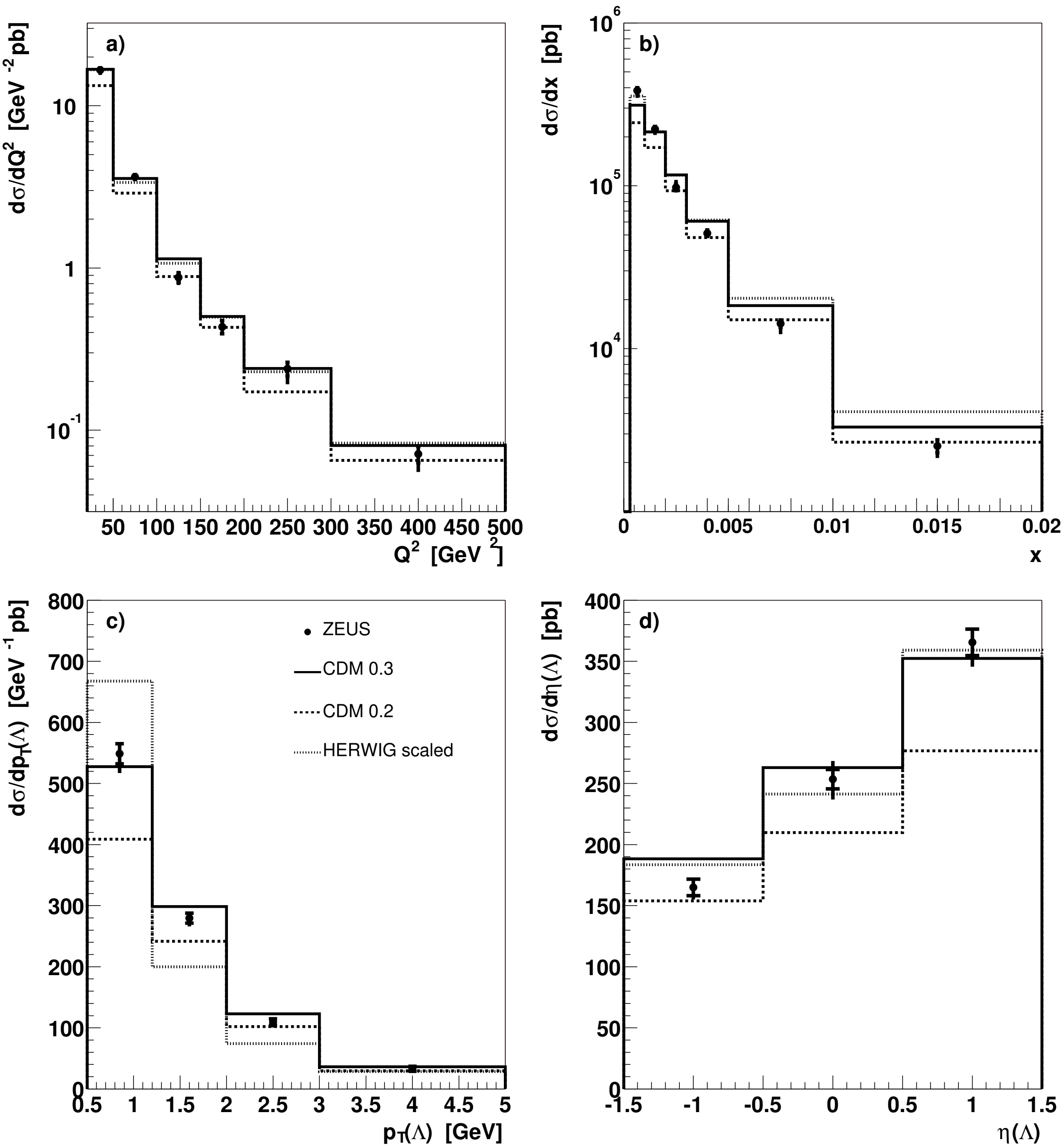

Figure 4.19: Measured differential Λ baryon cross sections ($\bullet$) as functions of Q^2, x, $p_T(\Lambda)$ and $\eta(\Lambda)$, compared to Monte Carlo models HERWIG and ARIADNE (solid and dashed line). The latter Monte Carlo is generated with $\lambda_s = 0.2$ and $\lambda_s = 0.3$. The full error bars include the systematic uncertainties. HERWIG is scaled to the area below the experimental data.

Q^2 range [GeV^2]	N_Λ	$d\sigma(\Lambda)/dQ^2$ [pb/GeV^2]
$20-50$	1874 ± 53	$16.6 \pm 0.5^{+0.5}_{-1.1}$
$50-100$	1622 ± 50	$3.6 \pm 0.1^{+0.1}_{-0.2}$
$100-150$	407 ± 27	$0.87 \pm 0.06^{+0.06}_{-0.07}$
$150-200$	203 ± 19	$0.43 \pm 0.04^{+0.01}_{-0.03}$
$200-300$	193 ± 19	$0.24 \pm 0.02^{+0.005}_{-0.04}$
$300-500$	139 ± 16	$0.071 \pm 0.008^{+0.001}_{-0.014}$

x range	N_Λ	$d\sigma(\Lambda)/dx$ [10^4pb]
$0.0003-0.001$	939 ± 37	$38 \pm 2^{+1}_{-3}$
$0.001-0.002$	1164 ± 41	$22.3 \pm 0.8^{+0.6}_{-1.6}$
$0.002-0.003$	647 ± 31	$9.8 \pm 0.5^{+1.0}_{-0.4}$
$0.003-0.005$	757 ± 34	$5.1 \pm 0.2^{+0.1}_{-0.2}$
$0.005-0.01$	647 ± 34	$1.43 \pm 0.007^{+0.02}_{-0.18}$
$0.01-0.02$	258 ± 23	$0.25 \pm 0.02^{+0.003}_{-0.03}$

$p_T(\Lambda)$ range [GeV]	N_Λ	$d\sigma(\Lambda)/dp_T(\Lambda)$ [pb/GeV]
$0.5-1.2$	2086 ± 62	$549 \pm 16^{+10}_{-27}$
$1.2-2$	1672 ± 48	$280 \pm 8^{+5}_{-11}$
$2-3$	571 ± 28	$109 \pm 5^{+3}_{-7}$
$3-5$	106 ± 13	$33 \pm 4^{+2}_{-1}$

$\eta(\Lambda)$ range	N_Λ	$d\sigma(\Lambda)/d\eta(\Lambda)$ [pb]
$-1.5 - -0.5$	941 ± 38	$165 \pm 7^{+2}_{-7}$
$-0.5-0.5$	1666 ± 52	$254 \pm 8^{+12}_{-15}$
$0.5-1.5$	1828 ± 54	$365 \pm 11^{+4}_{-17}$

Table 4.4: Measured differential Λ baryon cross sections as a function of Q^2, x, $p_T(\Lambda)$ and $\eta(\Lambda)$.

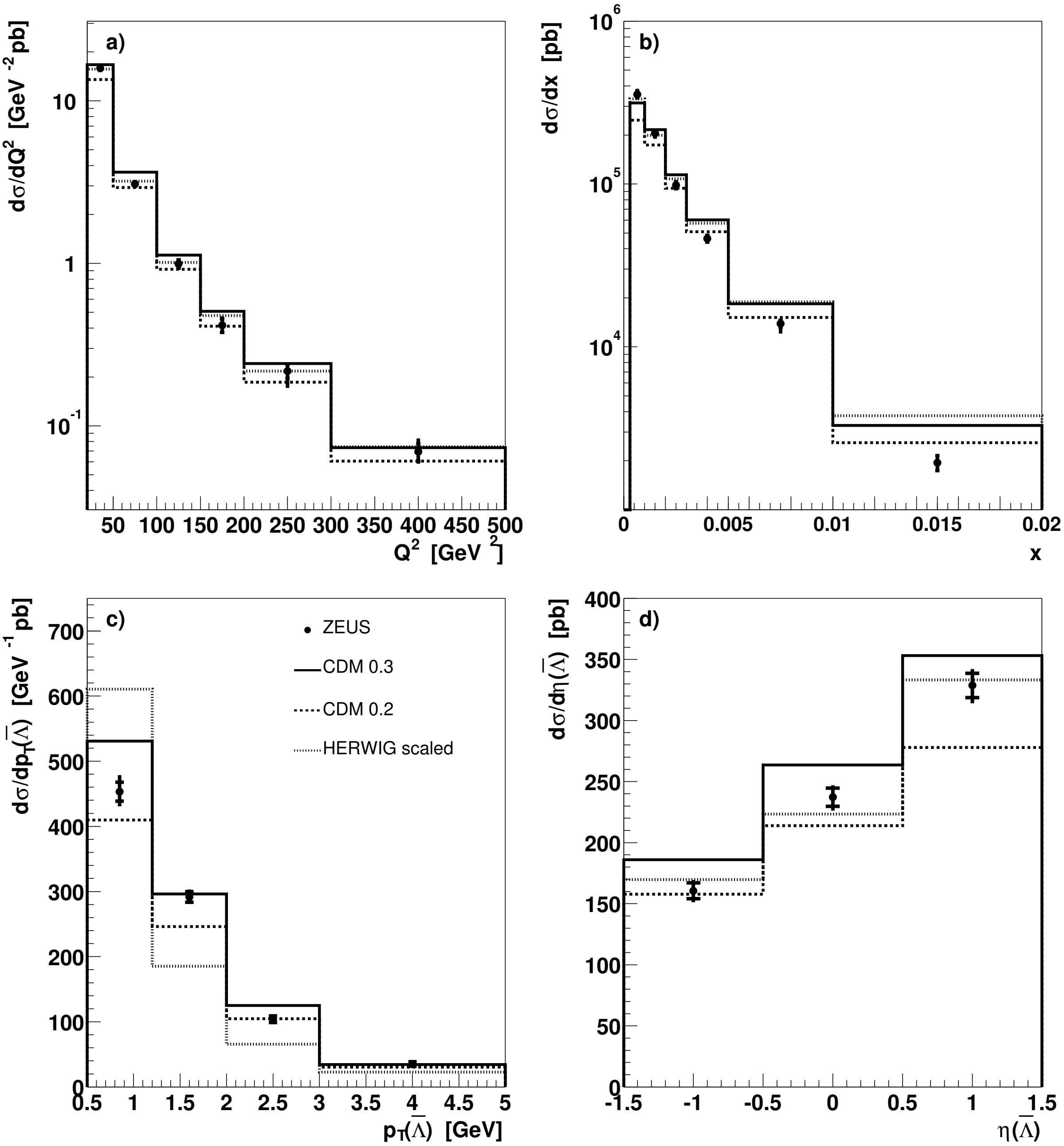

Figure 4.20: Measured differential $\bar{\Lambda}$ baryon cross sections (•) as functions of Q^2, x, $p_T(\bar{\Lambda})$ and $\eta(\bar{\Lambda})$, compared to Monte Carlo models HERWIG and ARIADNE (solid and dashed line). The latter Monte Carlo is generated with $\lambda_s = 0.2$ and $\lambda_s = 0.3$. The full error bars include the systematic uncertainties. HERWIG is scaled to the area below the experimental data.

Q^2 range [GeV^2]	$N_{\bar{\Lambda}}$	$d\sigma(\bar{\Lambda})/dQ^2$ [pb/GeV^2]
$20-50$	1732 ± 50	$15.9 \pm 0.5^{+0.5}_{-0.5}$
$50-100$	1397 ± 46	$3.1 \pm 0.1^{+0.2}_{-0.1}$
$100-150$	482 ± 28	$0.99 \pm 0.06^{+0.05}_{-0.06}$
$150-200$	186 ± 18	$0.41 \pm 0.04^{+0.04}_{-0.02}$
$200-300$	192 ± 18	$0.22 \pm 0.02^{+0.01}_{-0.04}$
$300-500$	126 ± 15	$0.068 \pm 0.008^{+0.012}_{-0.007}$

x range	$N_{\bar{\Lambda}}$	$d\sigma(\bar{\Lambda})/dx$ [10^4pb]
$0.0003-0.001$	799 ± 34	$35 \pm 2^{+3}_{-2}$
$0.001-0.002$	1078 ± 39	$20.5 \pm 0.7^{+0.8}_{-1.4}$
$0.002-0.003$	639 ± 31	$9.8 \pm 0.5^{+0.6}_{-0.3}$
$0.003-0.005$	688 ± 33	$4.6 \pm 0.2^{+0.2}_{-0.1}$
$0.005-0.01$	671 ± 32	$1.39 \pm 0.07^{+0.04}_{-0.17}$
$0.01-0.02$	199 ± 21	$0.19 \pm 0.02^{+0.006}_{-0.01}$

$p_T(\bar{\Lambda})$ range [GeV]	$N_{\bar{\Lambda}}$	$d\sigma(\bar{\Lambda})/dp_T(\bar{\Lambda})$ [pb/GeV]
$0.5-1.2$	1680 ± 55	$453 \pm 15^{+21}_{-17}$
$1.2-2$	1710 ± 48	$292 \pm 8^{+8}_{-7}$
$2-3$	585 ± 29	$103 \pm 5^{+3}_{-4}$
$3-5$	140 ± 14	$35 \pm 3^{+0.8}_{-2}$

$\eta(\bar{\Lambda})$ range	$N_{\bar{\Lambda}}$	$d\sigma(\bar{\Lambda})/d\eta(\bar{\Lambda})$ [pb]
$-1.5 - -0.5$	913 ± 37	$161 \pm 6^{+6}_{-7}$
$-0.5 - 0.5$	1520 ± 48	$237 \pm 7^{+6}_{-8}$
$0.5 - 1.5$	1689 ± 51	$329 \pm 10^{+9}_{-11}$

Table 4.5: Measured differential $\bar{\Lambda}$ anti-baryon cross sections as a function of Q^2, x, $p_T(\bar{\Lambda})$ and $\eta(\bar{\Lambda})$.

The differential cross section of $\Lambda + \bar{\Lambda}$ production in bins of Q^2 is well reproduced by all MC models. The differential distribution of $\Lambda + \bar{\Lambda}$ production, as for K_S^0, in bins of x seems to fall steeper than predicted by the MC models. The measured cross section as a function of $p_T(\Lambda + \bar{\Lambda})$ is not in agreement with the prediction by HERWIG. The shape is more similar to the prediction by ARIADNE with $\lambda_s = 0.3$, which is mainly due to the first two bins with $p_T(\Lambda + \bar{\Lambda}) < 2.0$ GeV. The shape of the differential cross section in bins of $\eta(\Lambda + \bar{\Lambda})$ is well reproduced by HERWIG and ARIADNE with $\lambda_s = 0.3$, while ARIADNE with $\lambda_s = 0.2$ does not simulate the increased production in forward direction correctly.

Q^2 range [GeV^2]	$N_{\Lambda+\bar{\Lambda}}$	$d\sigma(\Lambda+\bar{\Lambda})/dQ^2$ [pb/GeV^2]
$20 - 50$	3593 ± 73	$32.5 \pm 0.7^{+0.9}_{-1.3}$
$50 - 100$	2994 ± 68	$6.7 \pm 0.2^{+0.2}_{-0.2}$
$100 - 150$	885 ± 39	$1.88 \pm 0.08^{+0.03}_{-0.07}$
$150 - 200$	387 ± 26	$0.83 \pm 0.06^{+0.04}_{-0.03}$
$200 - 300$	386 ± 26	$0.45 \pm 0.03^{+0.003}_{-0.08}$
$300 - 500$	263 ± 22	$0.14 \pm 0.01^{+0.01}_{-0.02}$

x range	$N_{\Lambda+\bar{\Lambda}}$	$d\sigma(\Lambda+\bar{\Lambda})/dx$ [10^4pb]
$0.0003 - 0.001$	1741 ± 50	$75 \pm 2^{+3}_{-5}$
$0.001 - 0.002$	2222 ± 57	$43 \pm 1^{+1}_{-3}$
$0.002 - 0.003$	1285 ± 44	$19.9 \pm 0.7^{+0.8}_{-0.4}$
$0.003 - 0.005$	1444 ± 47	$9.8 \pm 0.3^{+0.3}_{-0.2}$
$0.005 - 0.01$	1297 ± 47	$2.8 \pm 0.1^{+0.06}_{-0.3}$
$0.01 - 0.02$	467 ± 31	$0.46 \pm 0.03^{+0.006}_{-0.08}$

$p_T(\Lambda+\bar{\Lambda})$ range [GeV]	$N_{\Lambda+\bar{\Lambda}}$	$d\sigma(\Lambda+\bar{\Lambda})/dp_T(\Lambda+\bar{\Lambda})$[pb/GeV]
$0.5 - 1.2$	3744 ± 82	$1002 \pm 22^{+23}_{-36}$
$1.2 - 2$	3366 ± 67	$572 \pm 11^{+10}_{-17}$
$2 - 3$	1162 ± 40	$215 \pm 7^{+6}_{-10}$
$3 - 5$	248 ± 19	$68 \pm 5^{+2}_{-3}$

$\eta(\Lambda+\bar{\Lambda})$ range	$N_{\Lambda+\bar{\Lambda}}$	$d\sigma(\Lambda+\bar{\Lambda})/d\eta(\Lambda+\bar{\Lambda})$[pb]
$-1.5 - -0.5$	1833 ± 53	$325 \pm 9^{+8}_{-13}$
$-0.5 - 0.5$	3173 ± 71	$491 \pm 11^{+17}_{-20}$
$0.5 - 1.5$	3499 ± 74	$694 \pm 15^{+6}_{-25}$

Table 4.6: Measured differential $\Lambda + \bar{\Lambda}$ baryon cross sections as a function of Q^2, x, $p_T(\Lambda + \bar{\Lambda})$ and $\eta(\Lambda + \bar{\Lambda})$.

The question whether an asymmetric production of Λ and $\bar{\Lambda}$ exists somewhere in the selected phase space can be investigated by measuring the ratio $\sigma(\Lambda)/\sigma(\bar{\Lambda}) - 1$ as a function of Q^2, x, $p_T(\Lambda, \bar{\Lambda})$ and $\eta(\Lambda, \bar{\Lambda})$. All MC models predict a symmetric production of Λ and $\bar{\Lambda}$ which is in agreement with the measurement (Fig. 4.22).

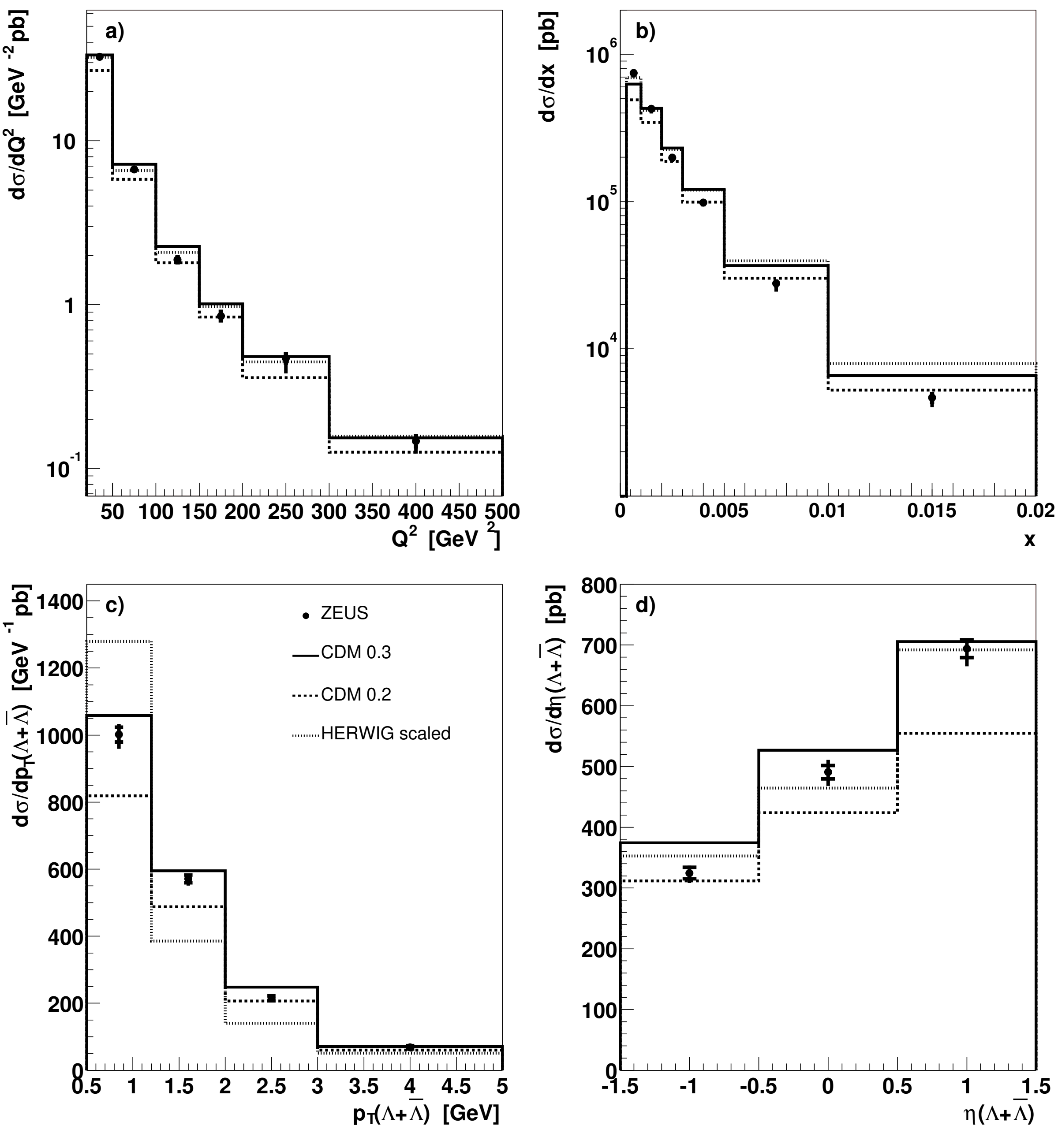

Figure 4.21: Measured differential $\Lambda + \bar{\Lambda}$ baryon cross sections (•) as a function of Q^2, x, $p_T(\Lambda, \bar{\Lambda})$ and $\eta(\Lambda, \bar{\Lambda})$, compared to Monte Carlo models HERWIG and ARIADNE (solid and dashed line). The latter Monte Carlo is generated with $\lambda_s = 0.2$ and $\lambda_s = 0.3$. The full error bars include the systematic uncertainties. HERWIG is scaled to the area below the experimental data.

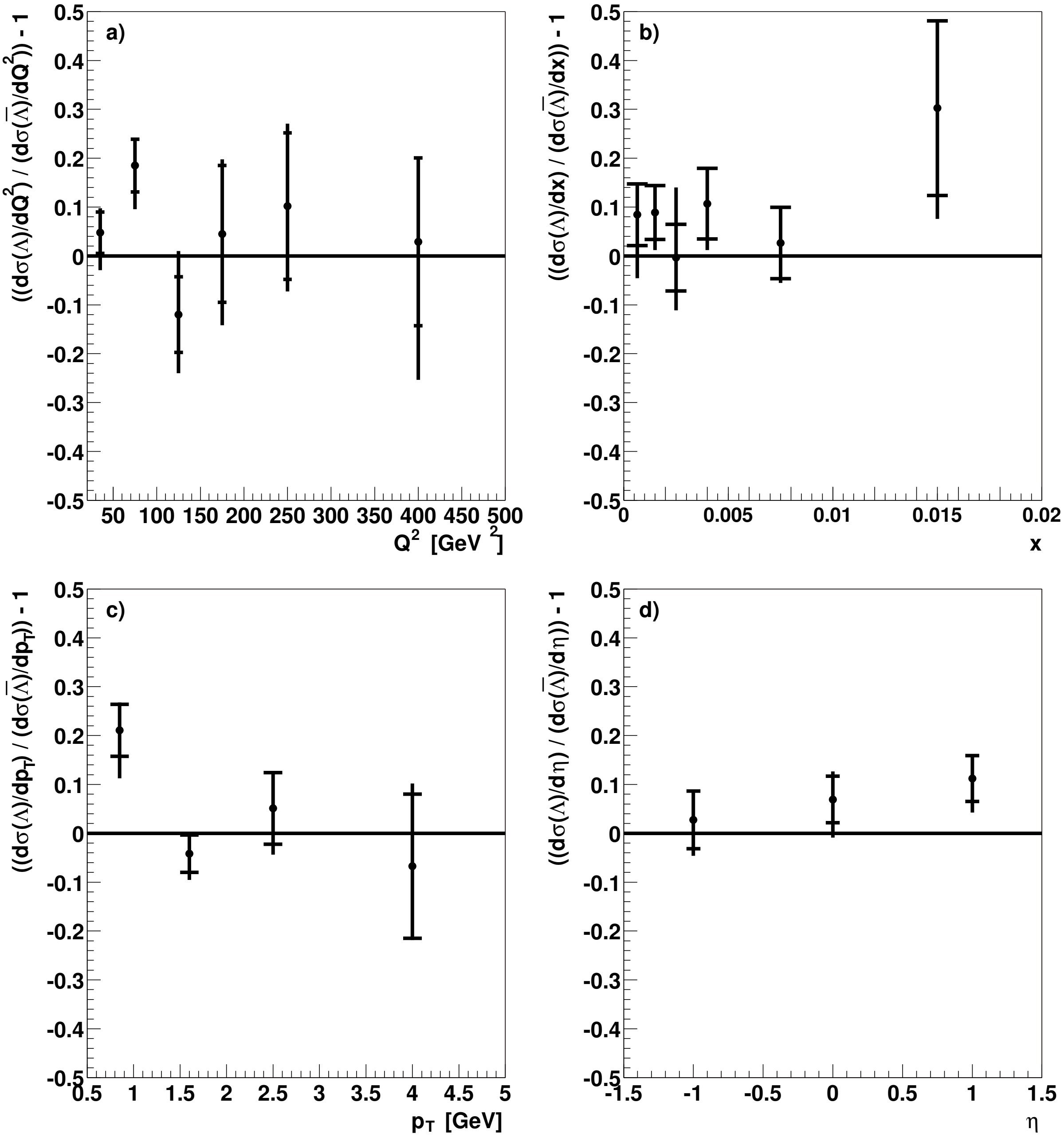

Figure 4.22: Measured differential ratio $\sigma(\Lambda)/\sigma(\bar{\Lambda}) - 1$ of the cross section of Λ baryon to $\bar{\Lambda}$ anti-baryon production as a function of Q^2, x, $p_T(\Lambda, \bar{\Lambda})$ and $\eta(\Lambda, \bar{\Lambda})$. The full error bars include the systematic uncertainties.

The measurement of $\Lambda+\bar{\Lambda}$ baryon and K_S^0 meson production has been compared to the prediction of HERWIG and ARIADNE and has shown that, for example, the measured differential cross section of both K_S^0 and $\Lambda+\bar{\Lambda}$ in bins of x falls steeper for the measurement than for the MC predictions. However, it could be that the ratio $\sigma(\Lambda+\bar{\Lambda})/\sigma(K_S^0)$ is well modeled by the MCs. Thus the ratios of the differential cross sections of Λ baryon to K_S^0 meson production is measured as a function of Q^2 (Fig. 4.23(a)), x (Fig. 4.23(b)), p_T (Fig. 4.23(c)) and η (Fig. 4.23(d)). They are compared to the HERWIG and ARIADNE Monte Carlo model. For Q^2 the measured distribution shows no dependence on Q^2 which is in agreement with all MC models. The measured ratio in bins of x is in agreement with ARIADNE and HERWIG. The HERWIG Monte Carlo shows a rather flat distribution compared to ARIADNE but the data does not allow one to distinguish between the two models and to decide which one describes the data better. The predicted ratio in bins of p_T is similar with the MC models. The measurement has a shape which is slightly flatter than the prediction and is in agreement with it within about 3 standard deviations only. The shape of the ratio as a function of η does not agree with the MC models. However the difference between measurement and prediction for low p_T $(0.5 < p_T < 1.2)$ GeV and high η could be related because higher production of Λ baryons relative to K_S^0 mesons at low p_T could explain the more forward direction of Λ production relative to K_S^0 production. Also low Q^2 events could be related to particles which are produced with a low p_T and in forward direction. This effect is investigated by measuring the η and Q^2 dependence of the cross sections $\sigma(K_S^0)$ and $\sigma(\Lambda+\bar{\Lambda})$ and the ratio $\sigma(\Lambda+\bar{\Lambda})/\sigma(K_S^0)$ for the two intervals in p_T of $1.2 < p_T < 5.0$ GeV (Fig. 4.24) and $0.5 < p_T < 1.2$ GeV (Fig. 4.25). Also it is analyzed by measuring the η and p_T dependence of the cross section $\sigma(K_S^0)$ and $\sigma(\Lambda+\bar{\Lambda})$ and the ratio $\sigma(\Lambda+\bar{\Lambda})/\sigma(K_S^0)$ for the two intervals in Q^2 of $20 < Q^2 < 100\,\mathrm{GeV}^2$ (Fig. 4.27) and $100 < Q^2 < 500\,\mathrm{GeV}^2$ (Fig. 4.26). For the phase space with $1.2 < p_T < 5.0$ GeV (Fig. 4.24) the differential K_S^0 meson and $\Lambda+\bar{\Lambda}$ baryon cross sections as a function of η and Q^2 looks similar to the measurement before (Fig. 4.23). The ratio $\sigma(\Lambda+\bar{\Lambda})/\sigma(K_S^0)$ in bins of η shows a more forward production than simulated by the Monte Carlo models. For the phase space with $0.5 < p_T < 1.2$ GeV, the differential K_S^0 meson and $\Lambda+\bar{\Lambda}$ baryon cross sections and, in particular, the ratio $\sigma(\Lambda+\bar{\Lambda})/\sigma(K_S^0)$ shows a disagreement between measurement and simulation also (Fig. 4.23). The high Q^2 phase space $(100 < Q^2 < 500\ \mathrm{GeV}^2)$ shows the best agreement between data and ARIADNE MC. The shape of the differential K_S^0 meson and $\Lambda+\bar{\Lambda}$ baryon cross section in bins of p_T and η and the ratio of these is well reproduced by the ARIADNE MC independent of the strangeness suppression factor. The HERWIG MC clearly fails to reproduce the shape of the differential K_S^0 meson and $\Lambda+\bar{\Lambda}$ baryon cross section in bin of p_T, but the ratio of these and the shape of all η distribution are in agreement with the measurement. The kinematics in η are well reproduced by HERWIG. The low Q^2 phase space $(20 < Q^2 < 100\,\mathrm{GeV}^2)$ shows a disagreement between the measurement and the prediction in the shape of the differential K_S^0 meson and $\Lambda+\bar{\Lambda}$ baryon cross section in bins of η and p_T. This disagreement becomes obvious when looking at the ratio of these. All MCs do not simulate the high cross section in forward direction properly. For the shapes of the differential cross sections in bins of p_T, the same is valid for the high Q^2 range. ARIADNE provides a good description of the shape of the cross sections and the ratio. HERWIG provides a good description of the ratio but fails to reproduce the shape of the differential cross sections of K_S^0 meson and $\Lambda+\bar{\Lambda}$ baryon production in bins of p_T. Since the disagreement between measurement and prediction of the differential cross section and the ratio in bins of η is obvious for low Q^2, correlated with a low p_T of the particles, the differential cross sections in bins of η are measured in the phase space with $0.5 < p_T < 1.2$ GeV and $20 < Q^2 < 100$ GeV^2 (Fig. 4.28). It is clear that all MCs fail to simulate the correct shape of the $\Lambda + \bar{\Lambda}$ cross section and the ratio in bins of η and are not in agreement with the measurement for this phase space. However, the shape of the differential cross sections of K_S^0 meson production in bins of η is well reproduced by ARIADNE but not by HERWIG.

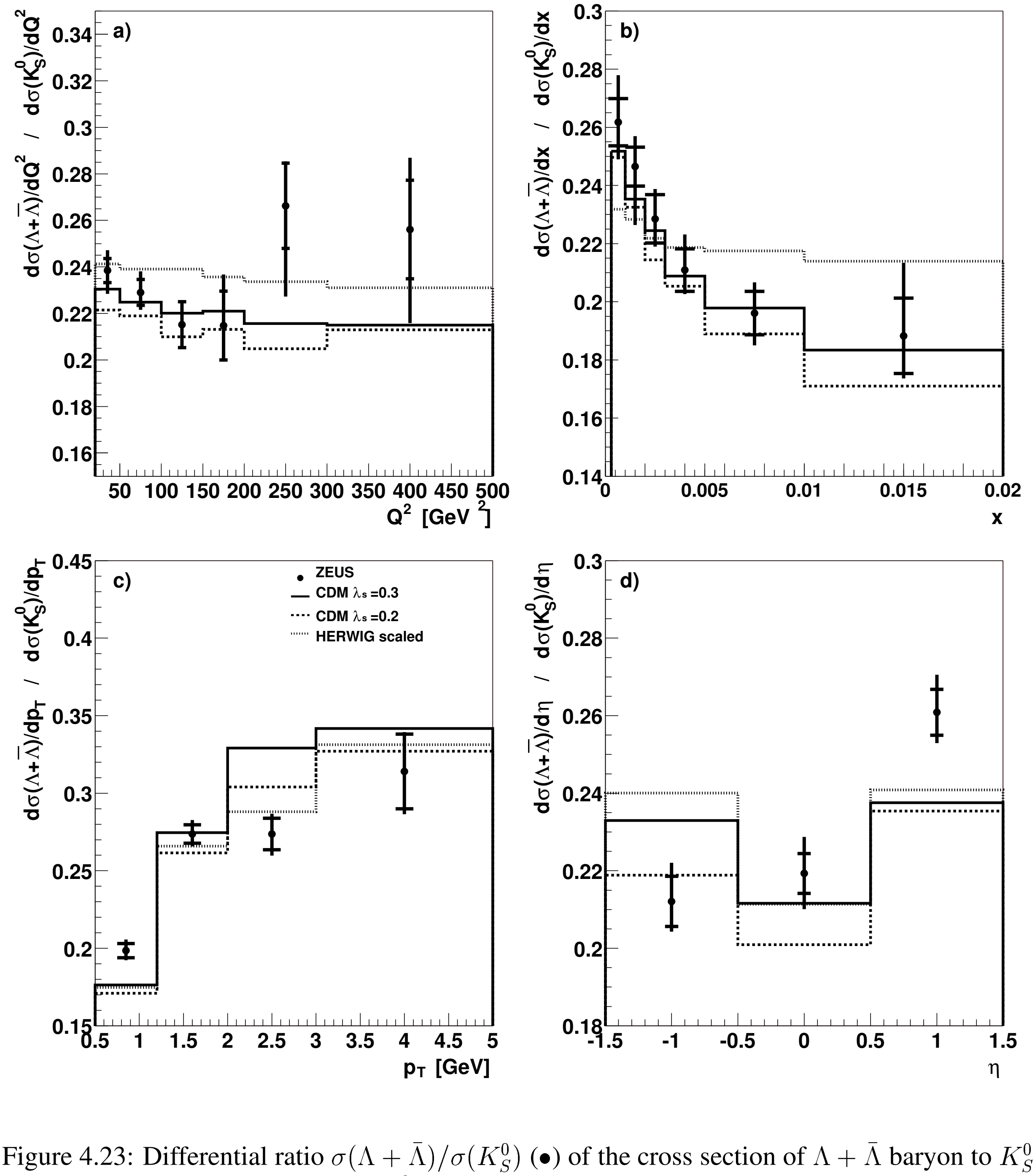

Figure 4.23: Differential ratio $\sigma(\Lambda+\bar{\Lambda})/\sigma(K_S^0)$ (•) of the cross section of $\Lambda+\bar{\Lambda}$ baryon to K_S^0 meson production as a function of Q^2, x, p_T and η, compared to the MC models HERWIG and ARIADNE. HERWIG is scaled to the area below the experimental data.

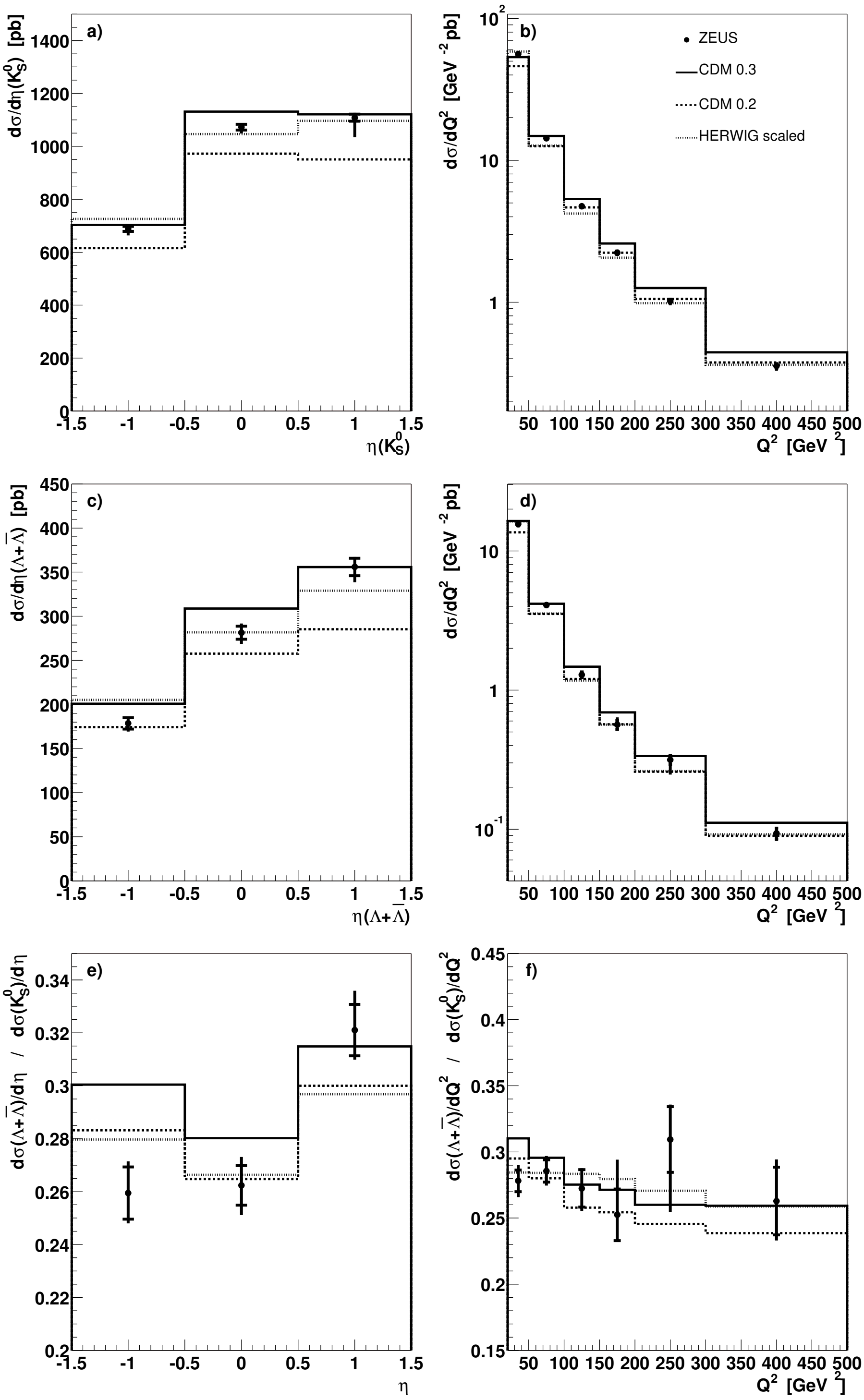

Figure 4.24: The differential cross section $\sigma(K^0_S)$, $\sigma(\Lambda + \bar{\Lambda})$ and the ratio $\sigma(\Lambda + \bar{\Lambda})/\sigma(K^0_S)$ for $1.2 < p_T(K^0_S, \Lambda, \bar{\Lambda}) < 5.0$ GeV as a function of η and Q^2, compared to the MC models HERWIG and ARIADNE. HERWIG is scaled to the area below the experimental data.

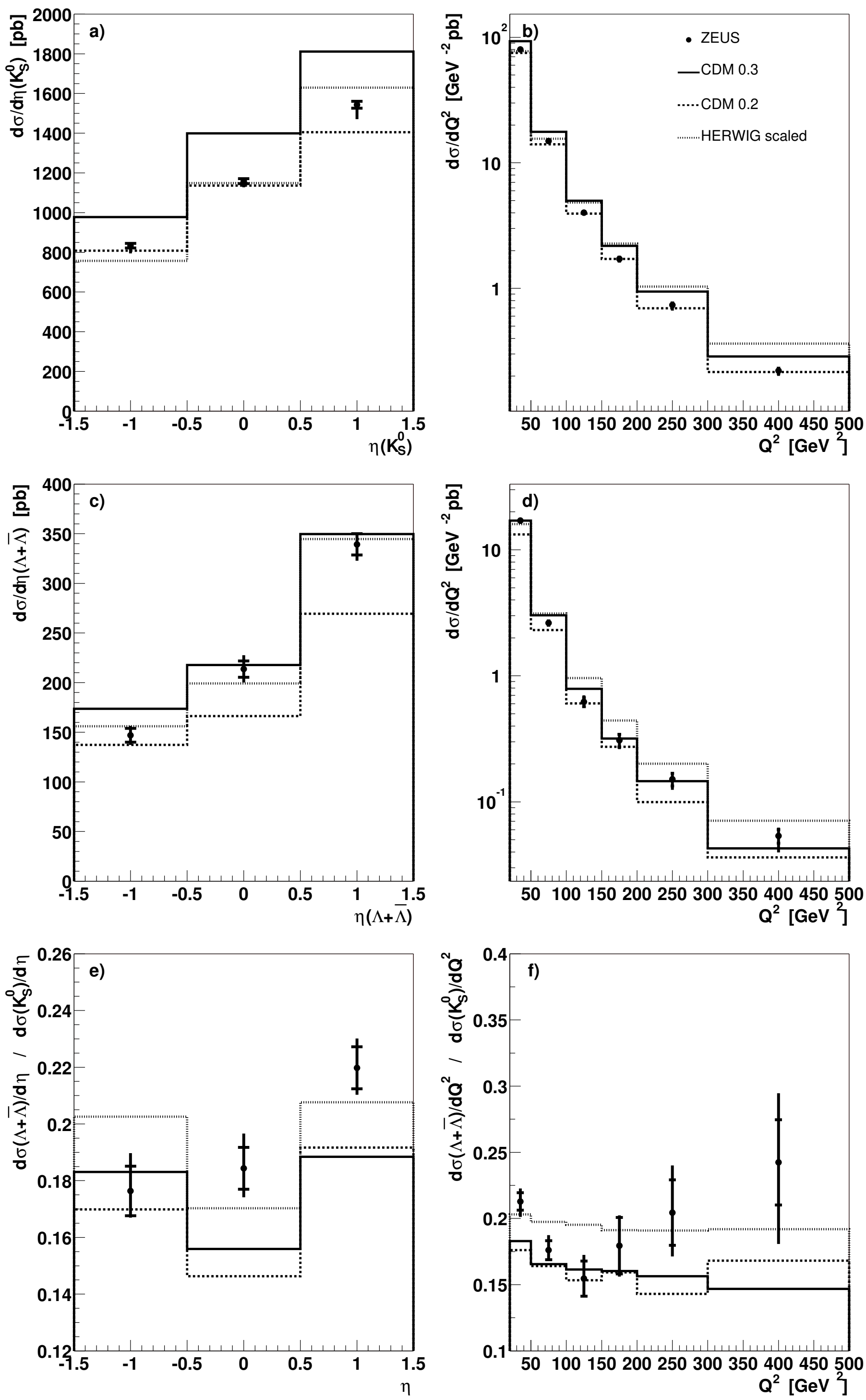

Figure 4.25: The differential cross section $\sigma(K_S^0)$, $\sigma(\Lambda + \bar{\Lambda})$ and the ratio $\sigma(\Lambda + \bar{\Lambda})/\sigma(K_S^0)$ for $0.5 < p_T(K_S^0, \Lambda, \bar{\Lambda}) < 1.2$ GeV as a function of η and Q^2, compared to the MC models HERWIG and ARIADNE. HERWIG is scaled to the area below the experimental data.

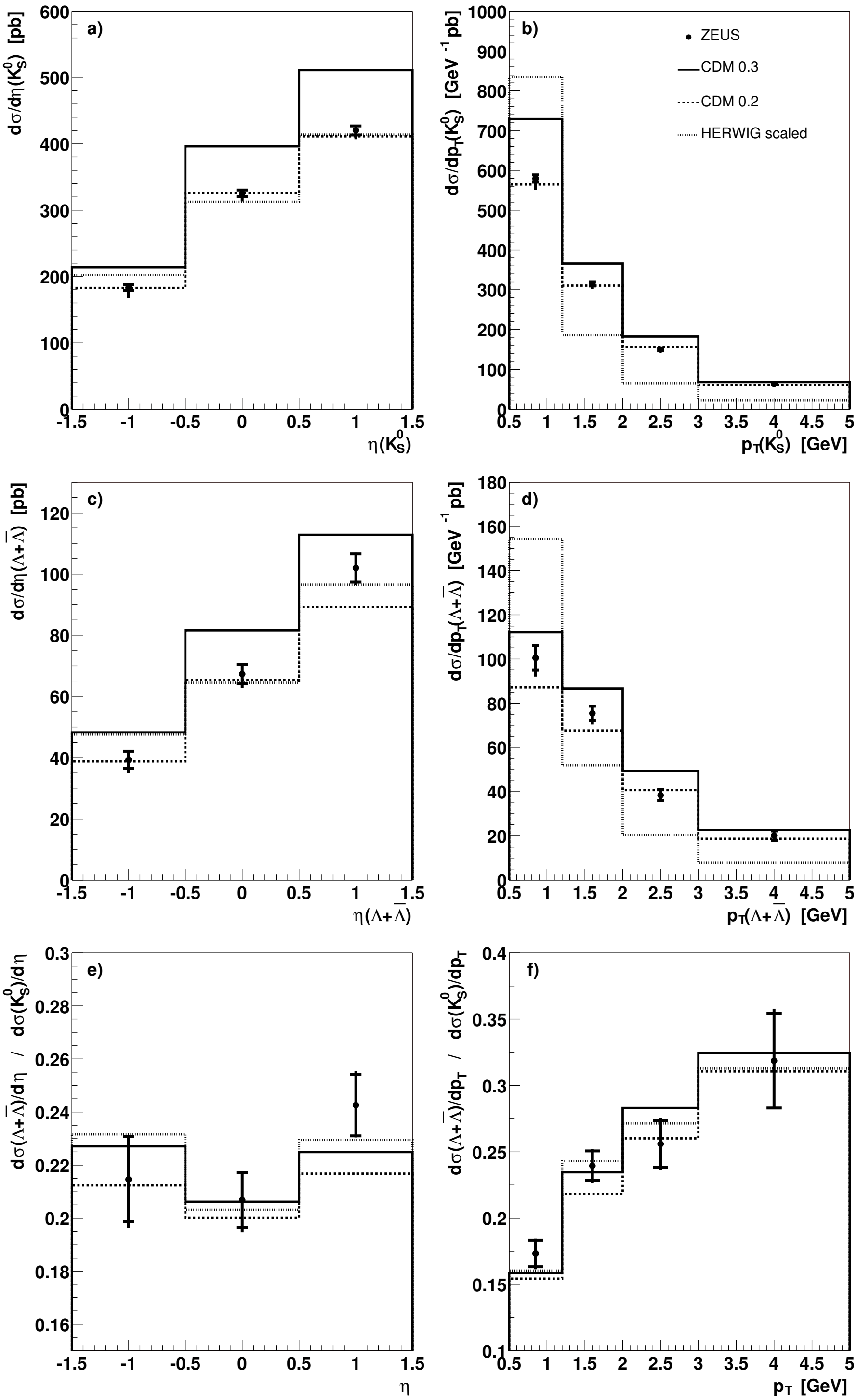

Figure 4.26: The differential cross section $\sigma(K_S^0)$, $\sigma(\Lambda+\bar{\Lambda})$ and the ratio $\sigma(\Lambda+\bar{\Lambda})/\sigma(K_S^0)$ for $100 < Q^2(K_S^0, \Lambda, \bar{\Lambda}) < 500\,\mathrm{GeV}^2$ as a function of η and p_T, compared to the MC models HERWIG and ARIADNE. HERWIG is scaled to the area below the experimental data.

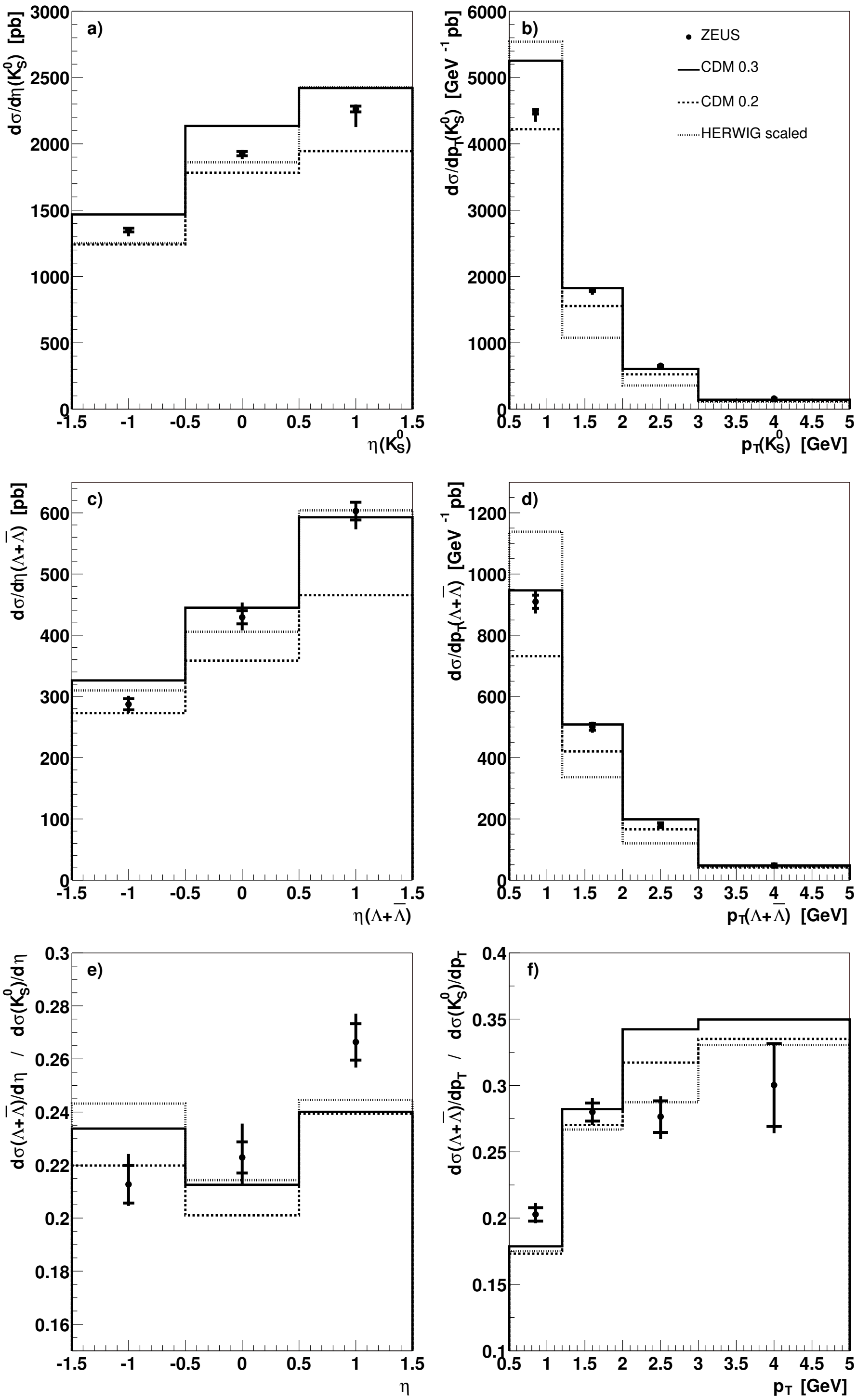

Figure 4.27: The differential cross section $\sigma(K_S^0)$, $\sigma(\Lambda+\bar{\Lambda})$ and the ratio $\sigma(\Lambda+\bar{\Lambda})/\sigma(K_S^0)$ for $20 < Q^2(K_S^0, \Lambda, \bar{\Lambda}) < 100\,\mathrm{GeV}^2$ as a function of η and p_T, compared to the MC models HERWIG and ARIADNE. HERWIG is scaled to the area below the experimental data.

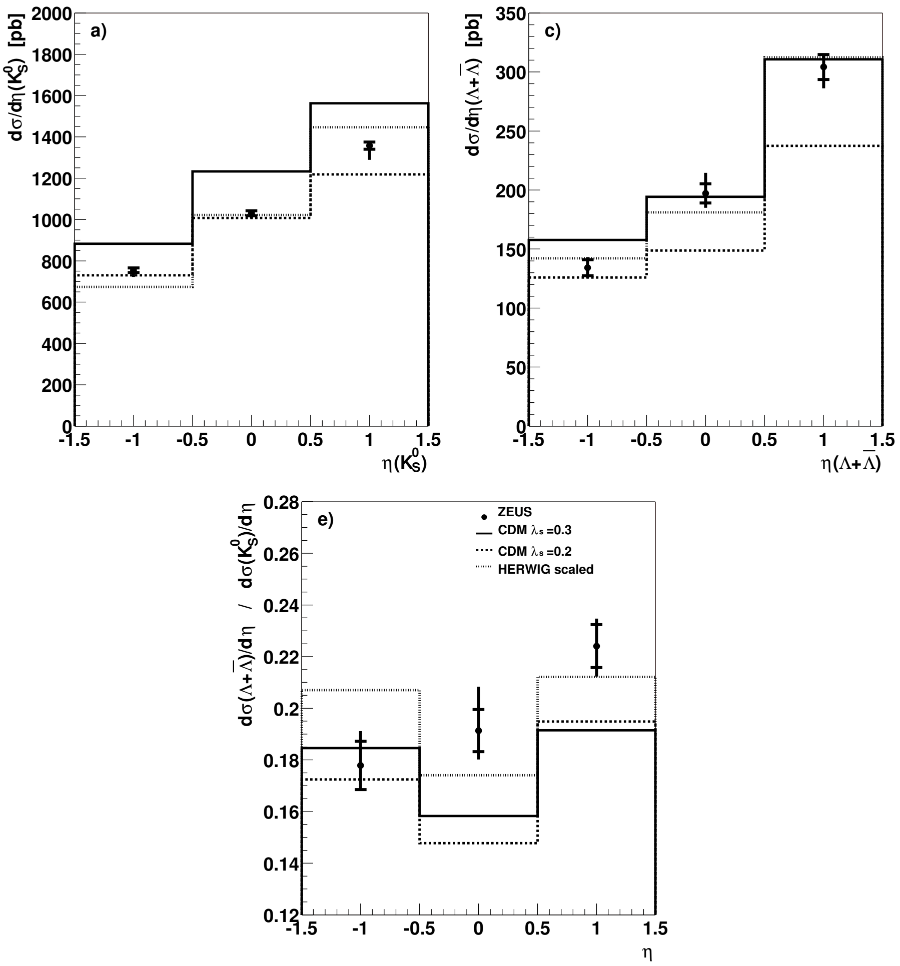

Figure 4.28: The differential cross section $\sigma(K_S^0)$, $\sigma(\Lambda + \bar{\Lambda})$ and the ratio $\sigma(\Lambda + \bar{\Lambda})/\sigma(K_S^0)$ for $0.5 < p_T(K_S^0, \Lambda, \bar{\Lambda}) < 1.2$ GeV and $20 < Q^2(K_S^0, \Lambda, \bar{\Lambda}) < 100\,\mathrm{GeV}^2$ as a function of η, compared to the MC models HERWIG and ARIADNE. HERWIG is scaled to the area below the experimental data.

Chapter 5

Summary and conclusions

Measurements have been performed concerning the properties of the scintillating SCSF-38M fiber. The effects of γ rays from a ^{137}Cs source, different fiber temperatures and different duration of illumination on the transmission, scintillation and induced absorption coefficient $\Delta\mu$ are investigated. Two setups are used which have different light sources. Setup L is equipped with a three-color LED with emission peaks at blue (470 nm), green (535 nm) and red (650 nm) and Setup M with a monochromator so that a wide spectral range can be scanned ($\lambda = 400-700$ nm). The duration of the illumination of the fiber, which is necessary for transmission measurements, is varied so that the fiber is illuminated from 1 second to continuous light per hour.

Measurements with Setup M show that two color centers are developed while irradiating the fiber. One is at a wavelength of $\lambda_1 \simeq 420$ nm (C_1) and the other one is at $\lambda_2 \simeq 620$ nm (C_2). During the phase of annealing C_1 is unimproved while C_2 anneals for the most part. These effects are in agreement with a previous measurement [48].

With Setup L the effect of a higher temperature than the room temperature on the SCSF-38M fiber is investigated. A temperature of $T > 40°$C causes an accelerated ageing of the fiber which is supposed to the dyes in the polystyrene core by reacting with oxygen [39]. At $T = 68°$C the transmission loss per 30.6 days is $(15.1 \pm 0.1)\%$ for a heated fiber length of $l = 52$ cm. This accelerated ageing phenomenon due to the temperature does not recover so that the fibers are permanently damaged. Another measurement shows that the fluorescence light seems to be not affected by the increased temperature. The fluorescence light yield stayed stable although the temperature changed. The ratio $\Delta\mu/\Delta\mu_{RT}$ of the induced absorption coefficient for a SCSF-38M fiber at a temperature higher than room temperature $\Delta\mu$ to the induced absorption coefficient at room temperature $\Delta\mu_{RT}$ of the scintillating fiber SCSF-38M shows an effect which can be attributed to the temperature. After a fast increase of $\Delta\mu/\Delta\mu_{RT}$ which is nearly independent of the temperature of the fiber a nearly constant run of the curve is observed for a fiber at a temperature of $T < 40°$C while for a temperature of $T = 54°$C the ratio increases nearly linearly. Also this effect is due to the accelerated ageing of the fiber.

The photobleaching effect of SCSF-38M fibers is investigated with both setups. The total illumination of SCSF-38M fibers is varied from 1 second to continuous light per hour. The more light transmits down the fiber the lower is the induced absorption coefficient. The illumination has also an effect on the scintillation. The light yield of the fluorescence light increases with increasing illumination of the fiber up to 42 s of light per hour. The continuously illumination does not improve the situation any longer, in contrary the light yield of the fluorescence light is reduced with respect to the illumination with 42 s per hour. This behavior cannot be explained.

After the upgrade of the HERA collider and ZEUS detector a W/Scintillator-spaghetti-calorimeter (6m-tagger) was installed in February 2001. The performance of the detector and its evolution in the following moths near the beam-pipe and interaction point was monitored with a setup using a ^{60}Co source. Due to the upgrade of the collider a lot of synchrotron radiation created a high background for any measurement with the ZEUS detector. This synchrotron radiation damaged the first few millimeters of the fibers in the 6m-tagger which was discovered with measurements with the ^{60}Co source. Also the light yield of the whole detector decreased and the attenuation length along the fibers in the detector changed. To shield the detector from the synchrotron radiation a 2 mm thick lead plate was glued in front of the 6m-tagger in August 2002. Since the lead shielding has been mounted the ^{60}Co measurements showed that the light yield in the first 5 mm of the fibers behind the front side has not changed at all but through the whole detector the light yield decreased.

Inclusive K_S^0 meson and Λ baryon cross sections in a restricted kinematic region have been measured for $20\,\text{GeV}^2 < Q^2 < 500\,\text{GeV}^2$, $3 \cdot 10^{-4} < x < 10^{-1}$, $0.04 < y < 0.8$, $0.5 < p_T\ (K_S^0, \Lambda) < 5.0$ GeV and $|\eta(K_S^0, \Lambda)| < 1.5$ with the ZEUS detector at HERA.

The measurements of the total cross section of K_S^0 mesons, $\sigma(K_S^0)$, Λ baryon, $\sigma(\Lambda)$, $\bar{\Lambda}$ anti-baryon, $\sigma(\bar{\Lambda})$, and both Λ and $\bar{\Lambda}$ production, $\sigma(\Lambda + \bar{\Lambda})$, have been compared to the MC models HERWIG and ARIADNE generated with strangeness suppression factor λ_s of $\lambda_s = 0.3$ (default) and $\lambda_s = 0.2$. HERWIG is not able to describe either the total cross sections which are measured or the ratio of $\sigma(\Lambda + \bar{\Lambda})/\sigma(K_S^0)$. The total K_S^0 cross section is overestimated, while the total Λ cross section is underestimated. The HERWIG MC model predicts a production of Λ baryons relative to K_S^0 mesons which is about 3.5 times higher than measured. The ARIADNE MC model performs a much better description of the total cross sections which are measured. The two sets of strangeness suppression factor predict cross sections which are slightly below and above the measurements. A strangeness suppression factor of $\lambda_s = 0.3$ is too high to accommodate the measurement of $\sigma(K_S^0)$ and $\sigma(\Lambda + \bar{\Lambda})$ while $\lambda_s = 0.2$ is too low to be in agreement with the measurement. The ratio $\sigma(\Lambda + \bar{\Lambda})/\sigma(K_S^0)$ which is predicted by ARIADNE with $\lambda_s = 0.3$ and $\lambda_s = 0.2$ is lower than the measurement, but in agreement with it within an uncertainty of 2 standard deviations. ARIADNE provides a much better description of the total cross section and the ratio $\sigma(\Lambda + \bar{\Lambda})/\sigma(K_S^0)$ than HERWIG.

An equal production of Λ and $\bar{\Lambda}$ baryons is measured in total and in bins of Q^2, x, $p_T(\Lambda, \bar{\Lambda})$ and $\eta(\Lambda, \bar{\Lambda})$ which is in agreement with ARIADNE and HERWIG.

The measurement of the cross section $\sigma(K_S^0)$ and $\sigma(\Lambda + \bar{\Lambda})$ in bins of Q^2, x, p_T and η shows that for high Q^2 ($100 < Q^2 < 500\,\text{GeV}^2$), the shape of the ratio $\sigma(\Lambda + \bar{\Lambda})/\sigma(K_S^0)$ in bins of η is well simulated by HERWIG and ARIADNE with $\lambda_s = 0.3$ and $\lambda_s = 0.2$. For the low Q^2 ($20 < Q^2 < 100\,\text{GeV}^2$) and low p_T ($0.5 < p_T < 1.2$ GeV) phase space the shape of the ratio

$\sigma(\Lambda + \bar{\Lambda})/\sigma(K_S^0)$ in bins of η shows a discrepancy in the forward direction: the MC models underestimate the $\Lambda + \bar{\Lambda}$ production with respect to the K_S^0 meson production. The shape of the Q^2 and x distribution differ slightly between measurement and MCs for both K_S^0 meson and Λ production, but the ratio is well simulated. The shape of the p_T distribution is well reproduced by ARIADNE for K_S^0 and $\Lambda + \bar{\Lambda}$ production, in particular, for the ratio $\sigma(\Lambda + \bar{\Lambda})/\sigma(K_S^0)$. HERWIG fails to reproduce the shape of the differential cross section of both K_S^0 and $\Lambda + \bar{\Lambda}$ production as a function of p_T, but described the ratio $\sigma(\Lambda + \bar{\Lambda})/\sigma(K_S^0)$ much better.

Based on the above measurements, one can conclude that, overall, ARIADNE is a better model to simulate the production of K_S^0 meson and Λ baryon production than HERWIG.

Acknowledgments

I would like to thank Prof. Dr. Klaus Wick and Dr. Uwe Holm for the opportunity to work on the 6m-tagger and to investigate the SCSF-38M fibers.

Many thanks to the people who were involved in the measurement of the fibers and building the 6m-tagger, as there are Dr. N. Gendner, T. Gosau, Dr. R. Graciani, S. Göb, R. Hornung, H. Krause, N. Krumnack, N. Latuske, Dr. R. Wichmann, Dr. T. Zoufal, the mechanical and the electronics workshop.

I also want to thank the members of the QCD group, as there are M. Barbi, S. Chekanov, S. Paganis, A. Raval, M. R. Sutton and A. Ziegler for the great opportunity to work on particle physics.

Special thanks to the ^{60}Co-group as there are R. P. Feller, E. A. Möller and H. Prause for making the 6m-tagger measurements enjoyable.

I would also like to thank the radiation group for the opportunity of irradiations at the DESY Cs source and for dosimeter analysis as there are K. U. Hartz, C. Jordan and B. Racky.

I also want to thank the caretaker W. Weppner for making the car of the institute available for me. Many thanks go to J. Hauk, the technical director of the medical internship, for the amusing support.

I never considered it possible to find a friend at DESY: thank you Amita for your encouragement in the “strange” things of life, for doing the second analysis, for reading the whole draft and for just being there.

A big thanks to my parents for the support and love they gave me. They always gave me plenty of rope so that I could do things my way. I thank my parents-in-law for the support and love and for “giving” me their lovingly son, Andy.

And finally a special thanks to my lovely husband Dr. Andy Ziegler for his patience during the last 15 months which were not easy for me. He is always there when I need him most. He cheers me up when I am sad and motivates me when I am at the end of my tether. I love you and I always will.

Appendix A

Data samples for the SCSF-38M analysis

The analysis of the in-situ measurement of the SCSF-38M fibers in this theses bases on the data samples quoted in Tab. A.1. Measurements from number 1 to 6 are taken with Setup L, the remaining data files are taken with Setup M. The total dose, the overall and processed (irradiated/heated) length, the number of the figures in which the data are presented and in addition comments about the measurement procedure are listed in Tab. A.1, too.

no.	file name suffix .dat	dose [Gy]	overall fiber length [m]	processed fiber length [m]	fig.	comment
1	w800829ar001	458	1.00	≈ 0.7	3.9 3.12	only irradiation 12 s LED light per hour
2	w801210ar001	—	1.00	0.52	3.10	only heating 12 s LED light per hour
3	w810831ar001	93	1.49	1.43		1 s LED light per hour
4	w810913ar001	—				12 s LED light per hour
5	w37-38				3.14 3.15 3.16	this file combines the data samples #3 and #4
6	w810401ar001	187	1.49	1.43	3.11 3.13 3.14 3.15 3.16	irradiation and irradiation+heating 12 s LED light per hour
7	w1020603ar001	140	1.380	1.065	3.3 (a) 3.7 3.15 3.16	spectral range: 400–700 nm continuous light
8	w1020614ar003	231	1.380	1.136	3.3 (b) 3.6 3.8	spectral range: 430–690 nm 42 s light per hour
9	w1020708ar001	163	1.380	1.136	3.3 (c) 3.15 3.16	spectral range: 430–690 nm 42 s light per hour
10	w1020812ar002	26	1.380	1.136	3.3 (d) 3.5	spectral range: 400–700 nm continuous light

Table A.1: List of the data samples which are used and presented in this thesis. The raw data of the in-situ measurements with the SCSF-38M fibers are stored on `lara.desy.de` at `/home/arzu/paw/frodo/dat` and `/home/arzu/paw/bilbo/dat` with the file name which is listed. The maximum dose which was accumulated by the fiber, the overall and the precessed (irradiated/heated) length of the fiber and the number of the figures where these data are presented are listed. The comment describes e.g. how the fiber was treated (irradiated/heated) and the time of illumination per hour.

Appendix B

Mass distributions in bins of Q^2, x, p_T and η

The invariant mass distributions for reconstructed K_S^0 and Λ candidates in bins of Q^2, x, $p_T(K_S^0)$ and $\eta(K_S^0)$ are shown for data and ARIADNE MC. The number of K_S^0 and Λ obtained from these invariant mass distributions are used to determine the differential cross section in bins of Q^2, x, p_T and η.

B.1 Mass distributions of K_S^0 in bins of Q^2, x, $p_T(K_S^0)$ and $\eta(K_S^0)$

The invariant mass distributions $m(\pi\pi)$ in bins of Q^2 (Figs. B.1–B.2), x (Figs. B.3–B.5), $p_T(K_S^0)$ (Figs. B.6–B.7) and $\eta(K_S^0)$ (Fig. B.8) are shown for data and ARIADNE MC. The number of K_S^0 obtained from these invariant mass distributions are used to determine the differential cross section in bins of Q^2, x, $p_T(K_S^0)$ and $\eta(K_S^0)$. If the number of entries in the last four bins is below 48 a Maximum-Likelihood fit is performed on the data instead of an χ-fit. The widths of the two Gaussians which are used to parameterize the signal are fixed to the value determined by the fit to the total signal (Fig. 4.6).

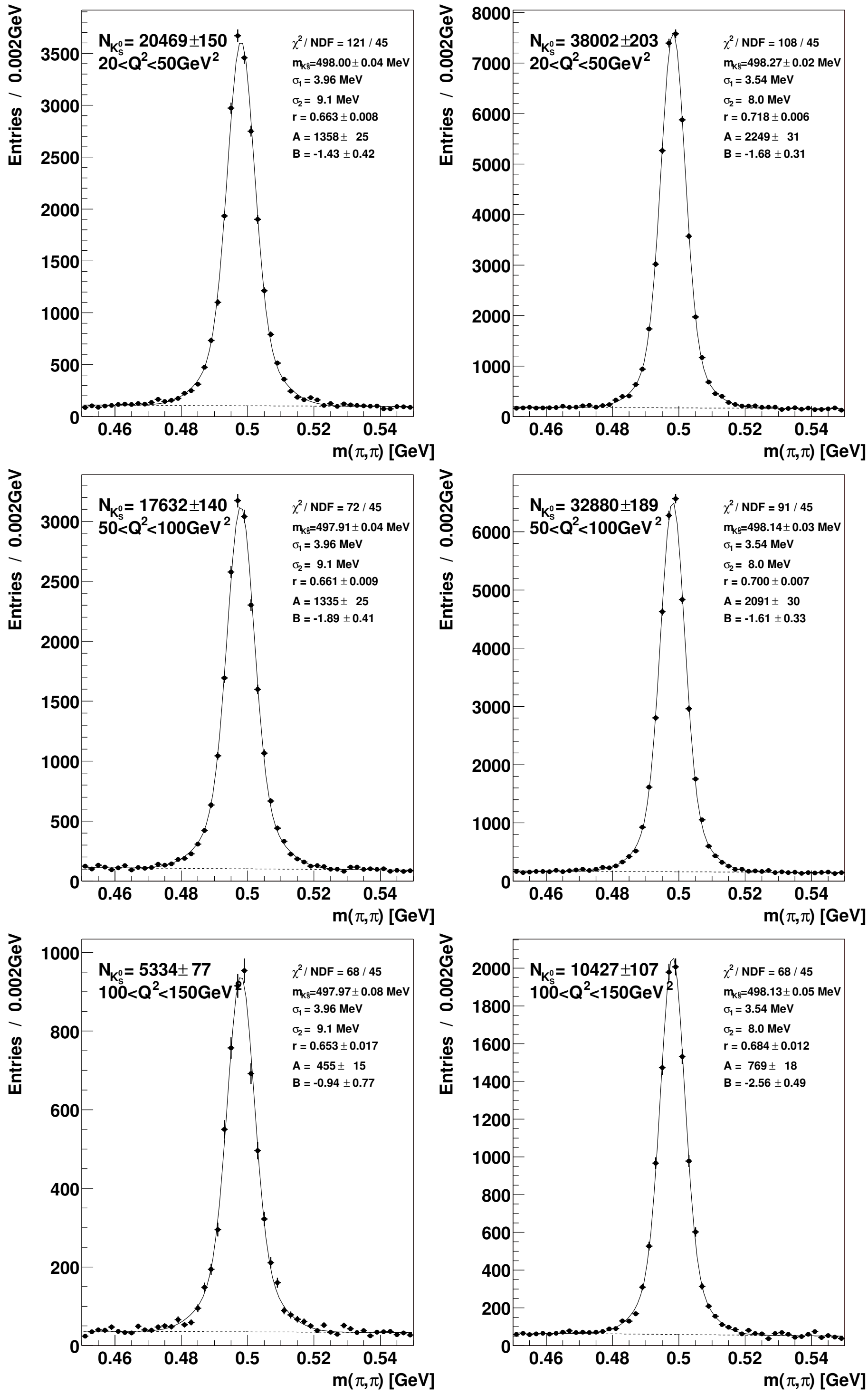

Figure B.1: Invariant mass $m(\pi, \pi)$ in bins of Q^2 for data (left) and ARIADNE MC (right) in the restricted kinematic region described in the text.

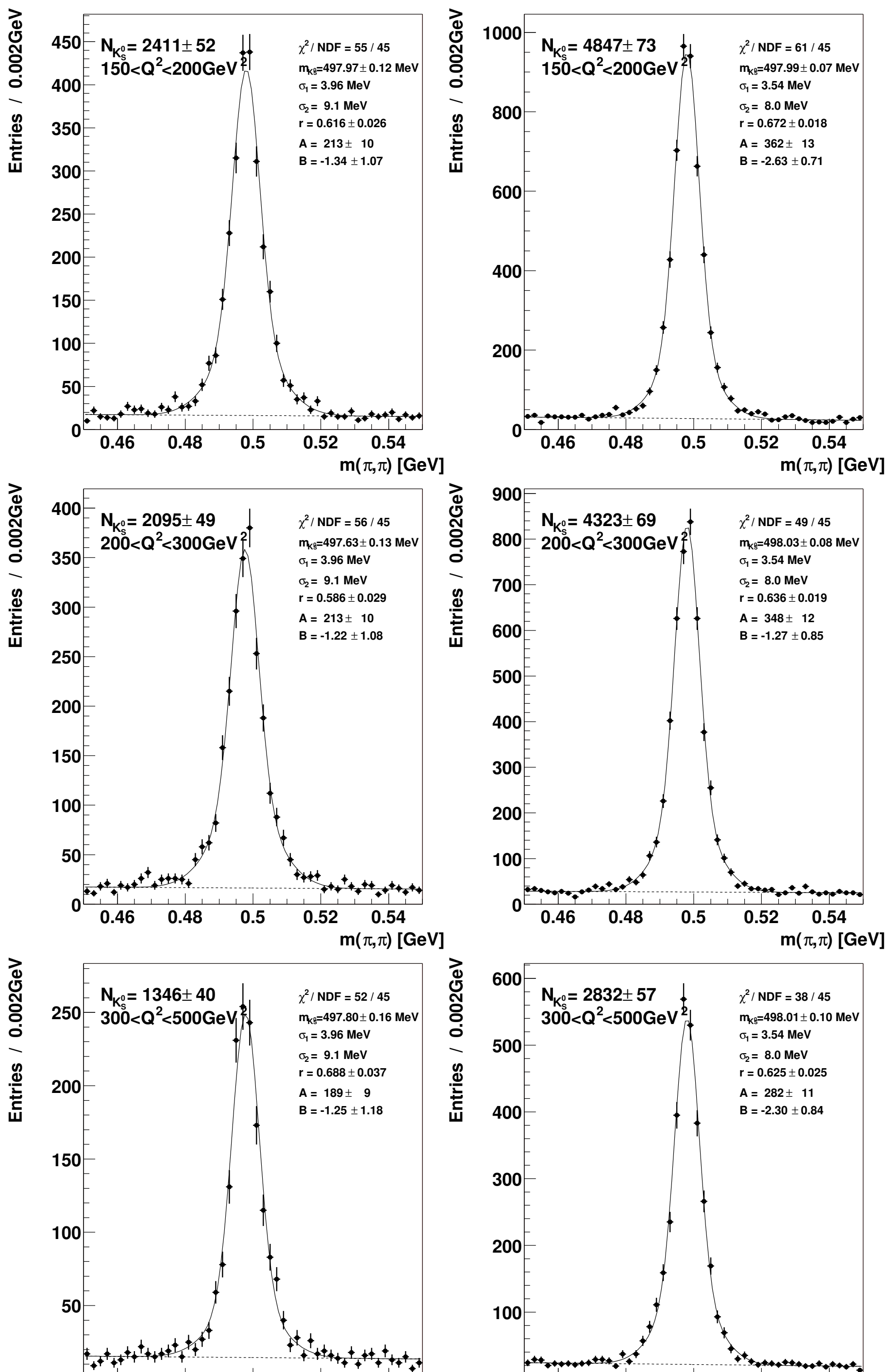

Figure B.2: Invariant mass $m(\pi, \pi)$ in bins of Q^2 for data (left) and ARIADNE MC (right) in the restricted kinematic region described in the text.

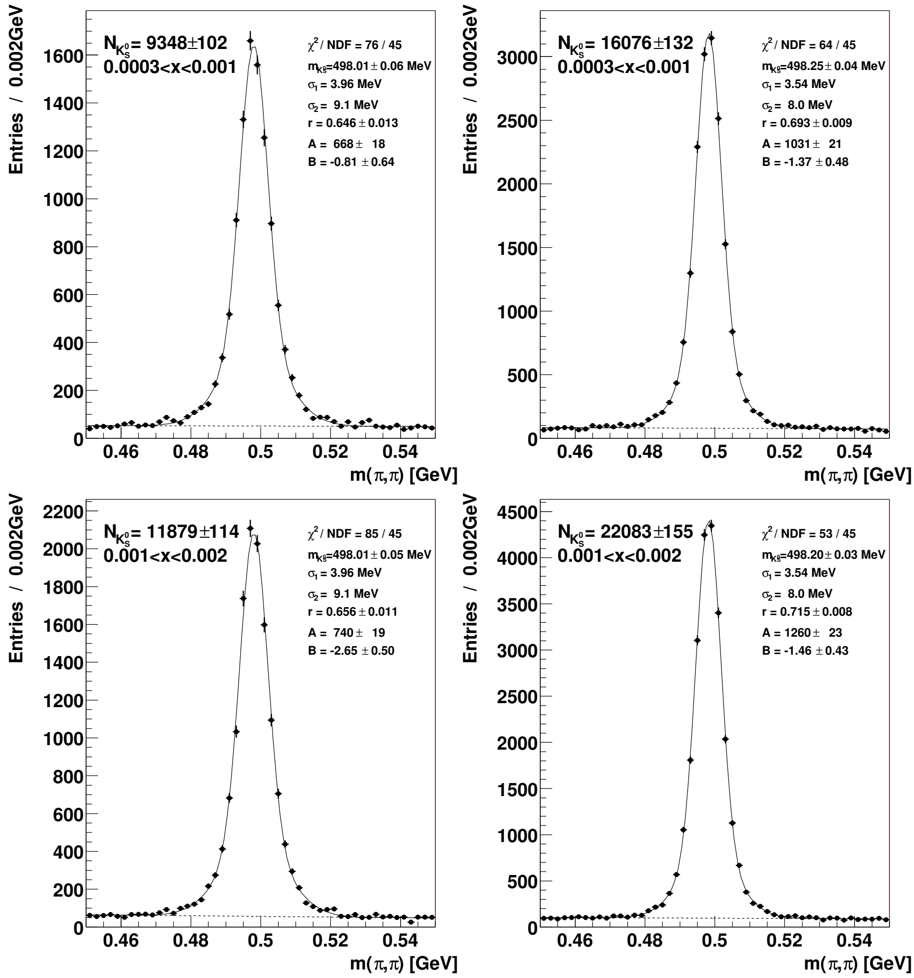

Figure B.3: Invariant mass $m(\pi, \pi)$ in bins of x for data (left) and ARIADNE MC (right) in the restricted kinematic region described in the text.

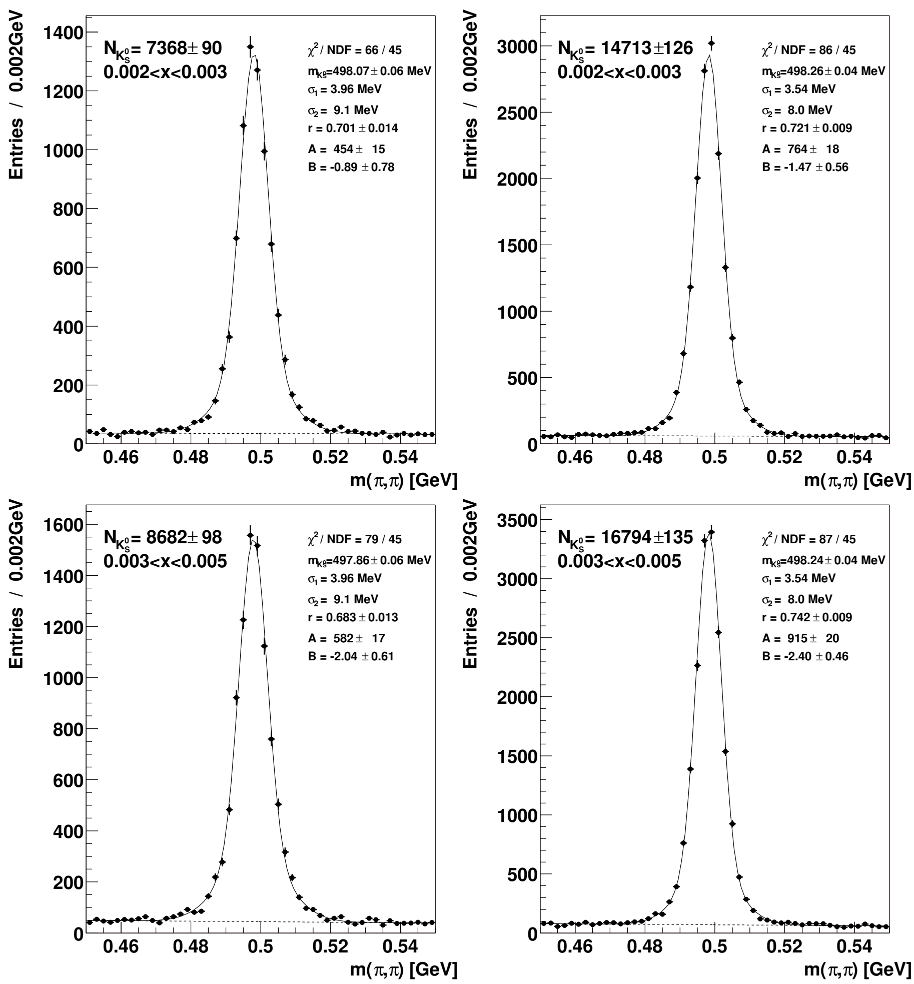

Figure B.4: Invariant mass $m(\pi,\pi)$ in bins of x for data (left) and ARIADNE MC (right) in the restricted kinematic region described in the text.

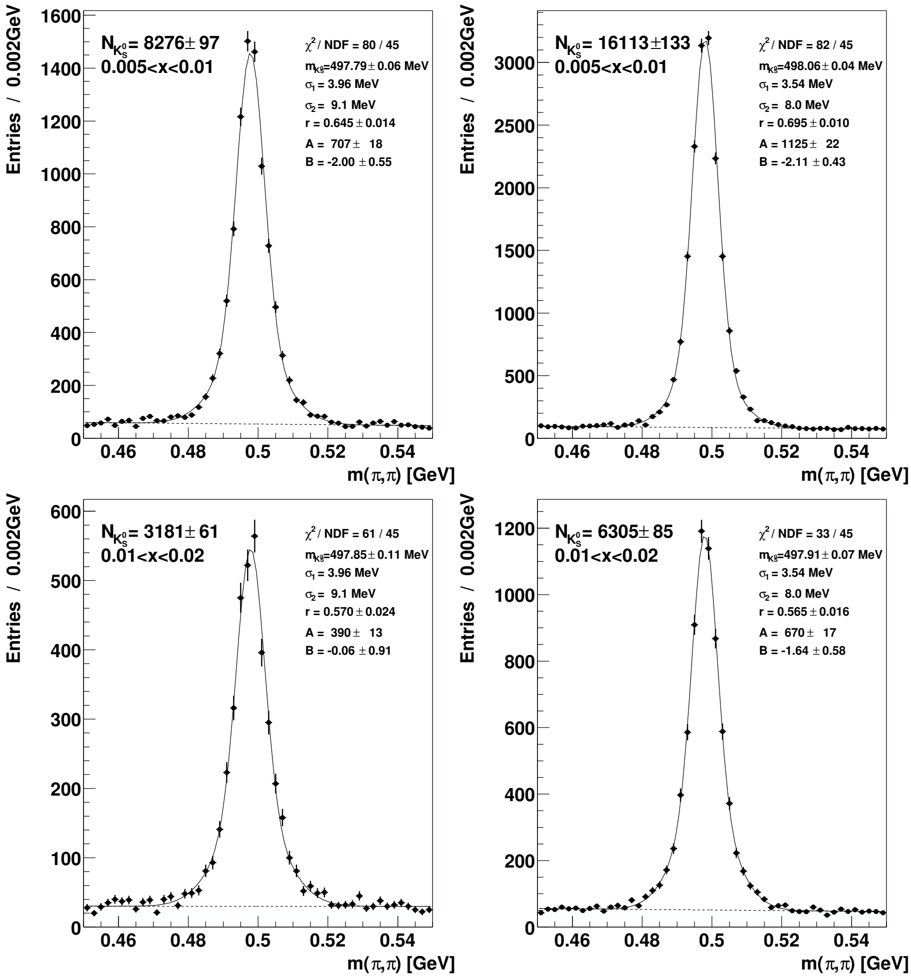

Figure B.5: Invariant mass $m(\pi, \pi)$ in bins of x for data (left) and ARIADNE MC (right) in the restricted kinematic region described in the text.

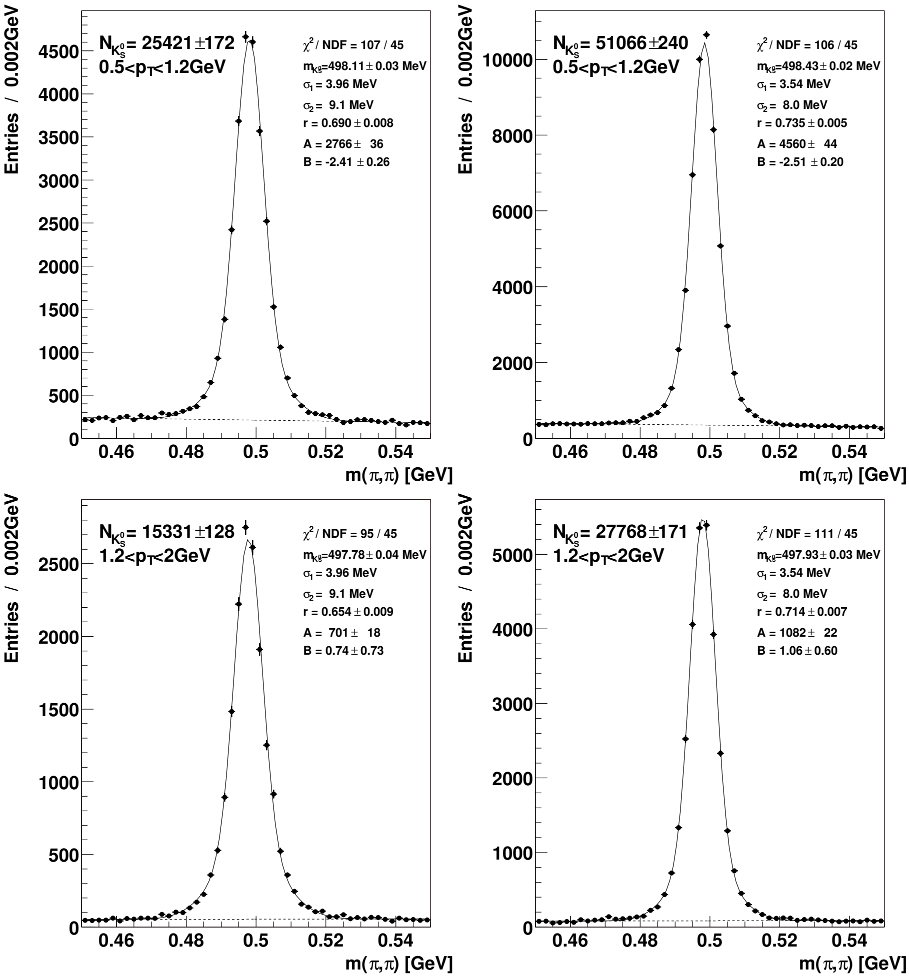

Figure B.6: Invariant mass $m(\pi, \pi)$ in bins of p_T for data (left) and ARIADNE MC (right) in the restricted kinematic region described in the text.

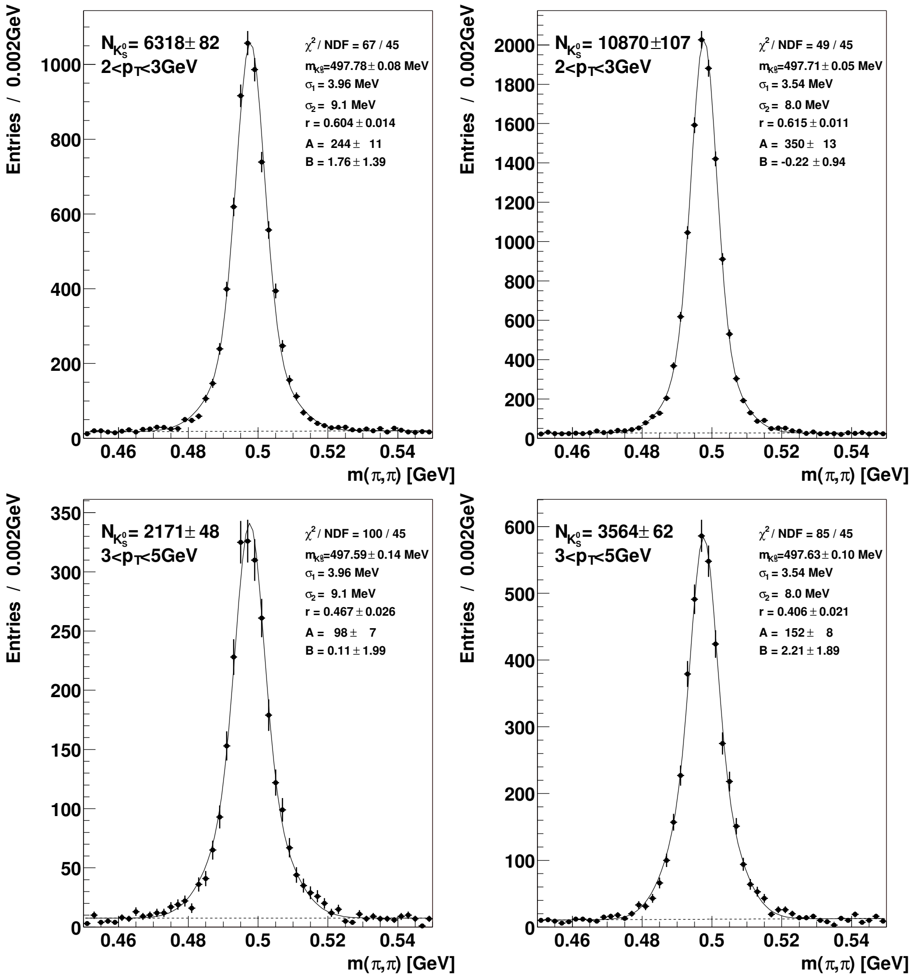

Figure B.7: Invariant mass $m(\pi, \pi)$ in bins of p_T for data (left) and ARIADNE MC (right) in the restricted kinematic region described in the text.

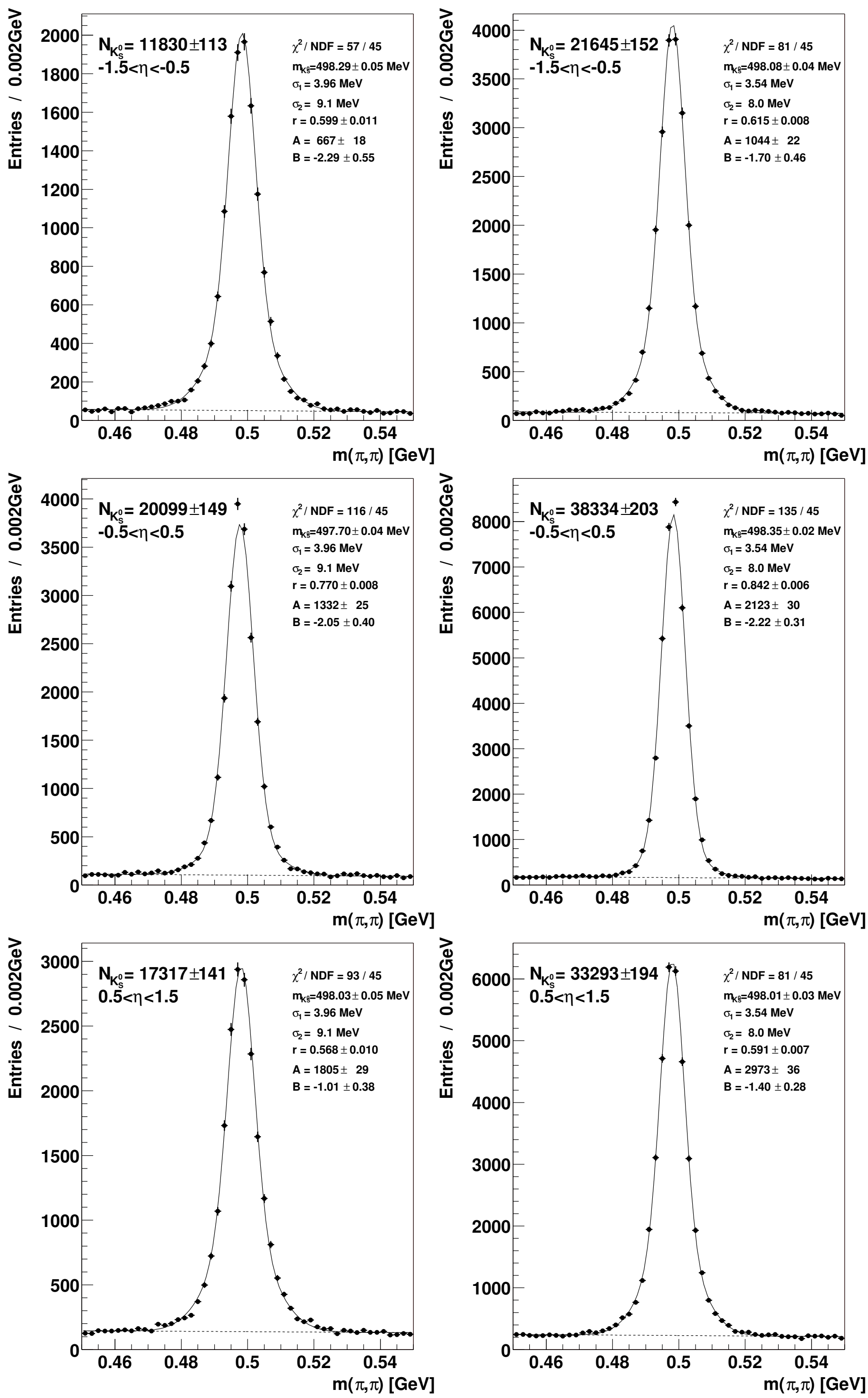

Figure B.8: Invariant mass $m(\pi,\pi)$ in bins of η for data (left) and ARIADNE MC (right) in the restricted kinematic region described in the text.

B.2 Mass distributions of Λ in bins of Q^2, x, $p_T(\Lambda)$ and $\eta(\Lambda)$

The invariant mass distributions $m(p\pi^-)$ in bins of Q^2 (Figs. B.9–B.10), x (Figs. B.11–B.13), $p_T(\Lambda)$ (Figs. B.14–B.15) and $\eta(\Lambda)$ (Fig. B.16) are shown for data and ARIADNE MC. The number of Λ obtained from these invariant mass distribution are used to determine the differential cross section in bins of Q^2, x, $p_T(\Lambda)$ and $\eta(\Lambda)$. If the number of entries in the first four bins is below 48 a Maximum-Likelihood fit is performed on the data instead of an χ-fit. The widths of the two Gaussians which are used to parameterize the signal are fixed to the value determined by the fit to the total signal (Fig. 4.10).

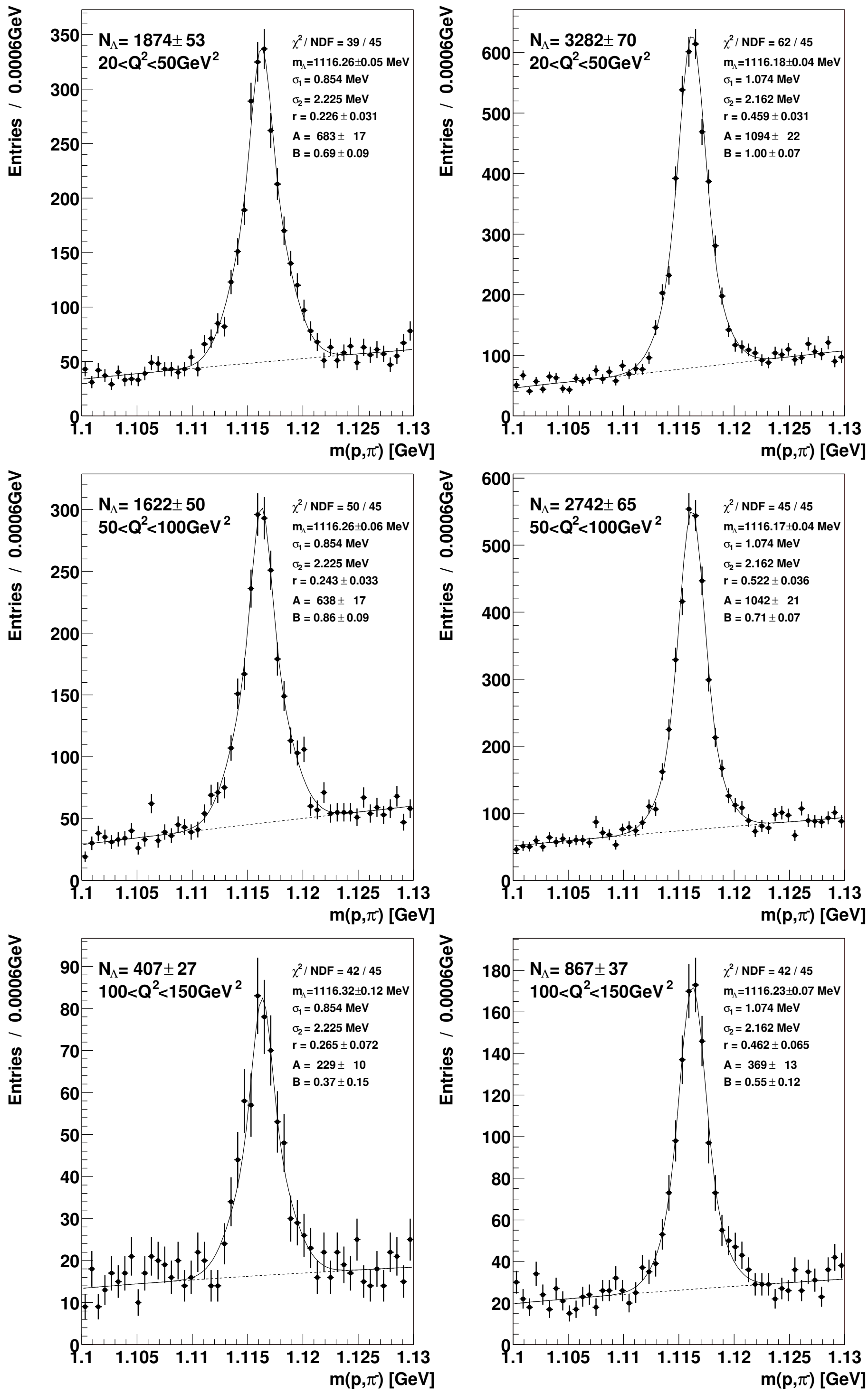

Figure B.9: Invariant mass $m(p, \pi^-)$ in bins of Q^2 for data (left) and ARIADNE MC (right) in the restricted kinematic region described in the text.

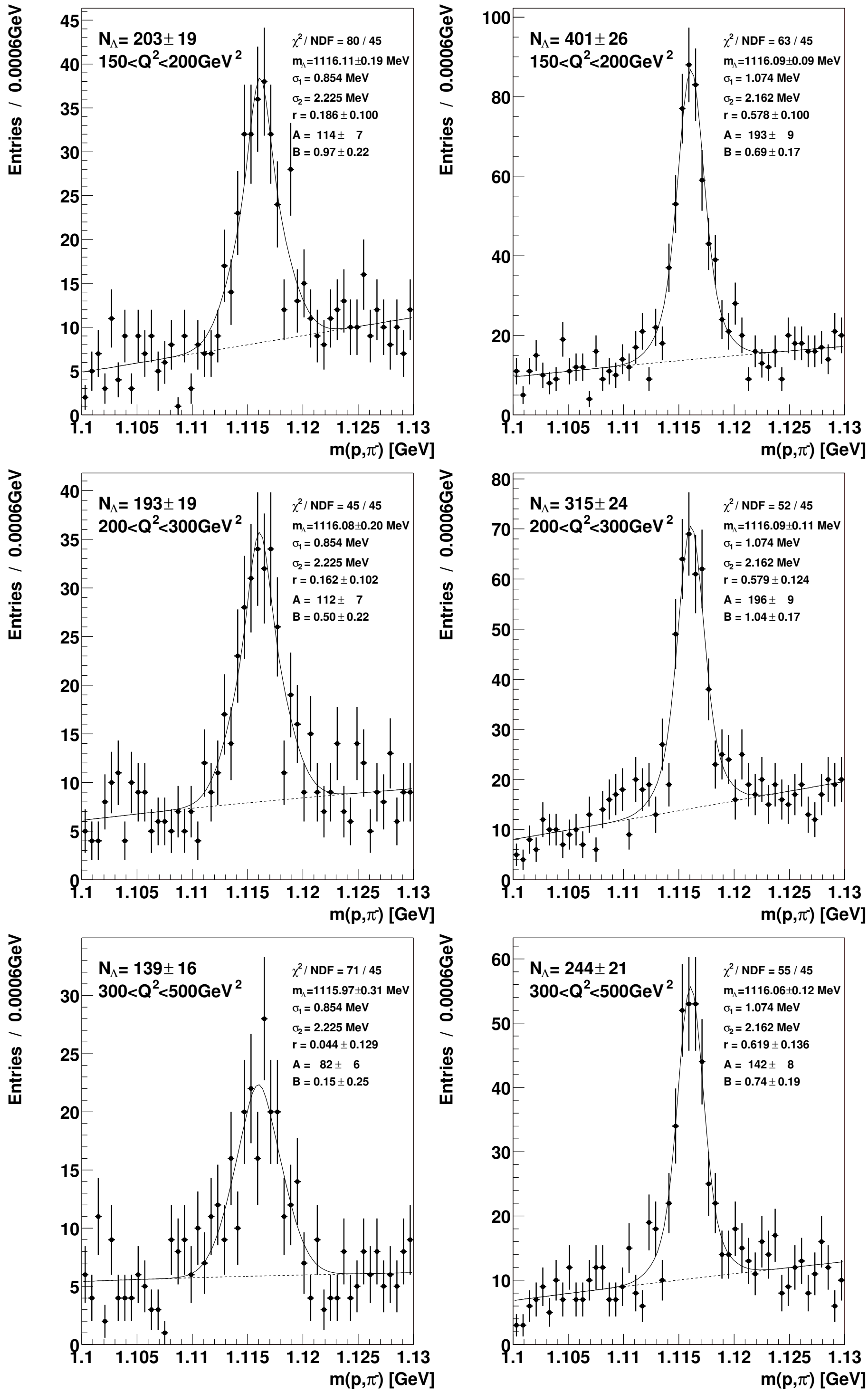

Figure B.10: Invariant mass $m(p, \pi^-)$ in bins of Q^2 for data (left) and ARIADNE MC (right) in the restricted kinematic region described in the text.

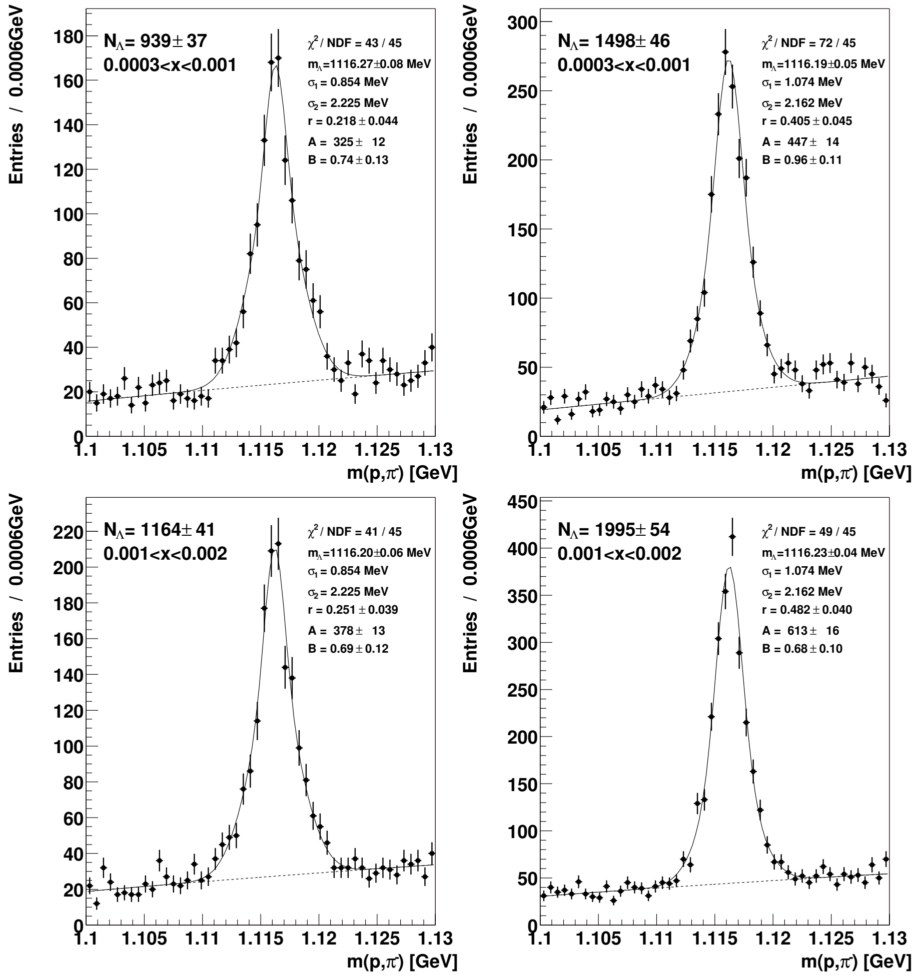

Figure B.11: Invariant mass $m(p, \pi^-)$ in bins of x for data (left) and ARIADNE MC (right) in the restricted kinematic region described in the text.

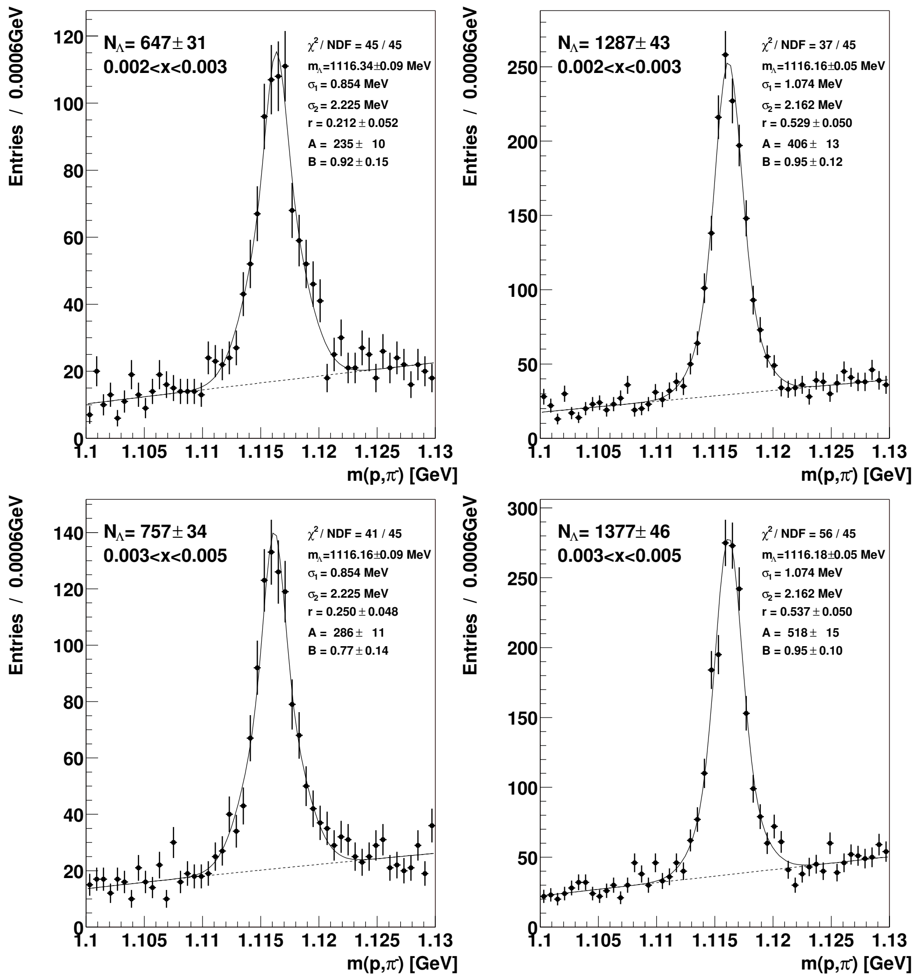

Figure B.12: Invariant mass $m(p, \pi^-)$ in bins of x for data (left) and ARIADNE MC (right) in the restricted kinematic region described in the text.

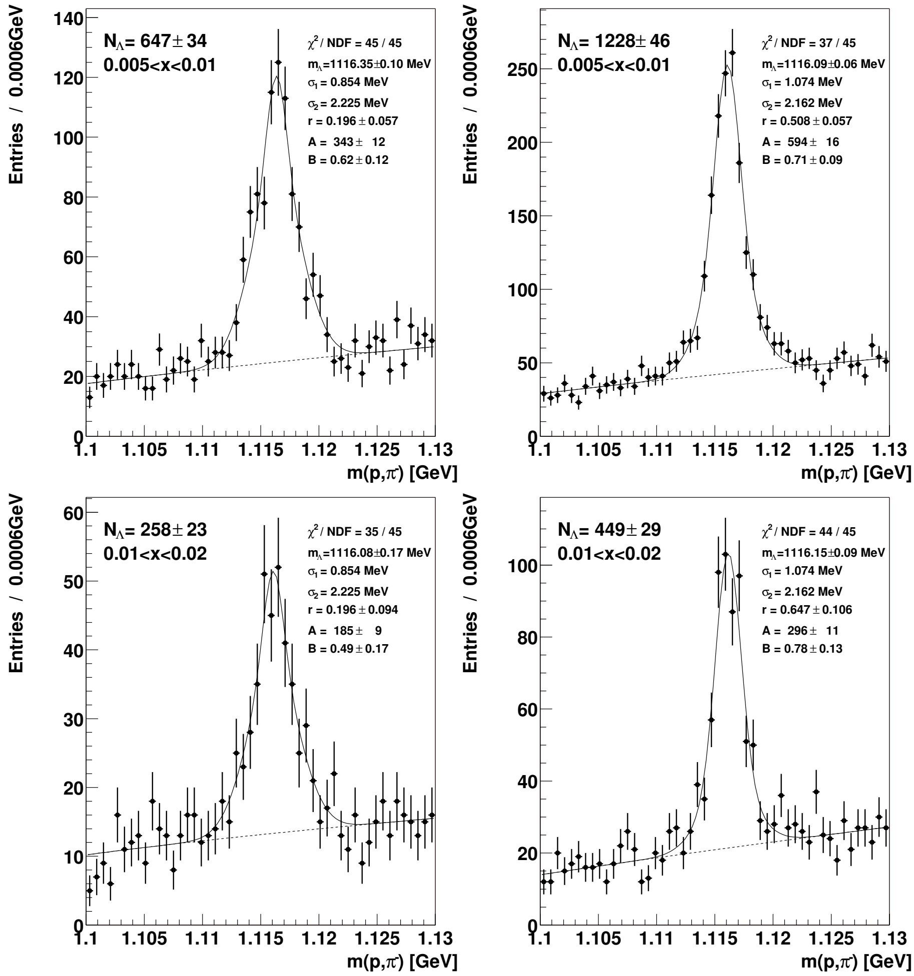

Figure B.13: Invariant mass $m(p, \pi^-)$ in bins of x for data (left) and ARIADNE MC (right) in the restricted kinematic region described in the text.

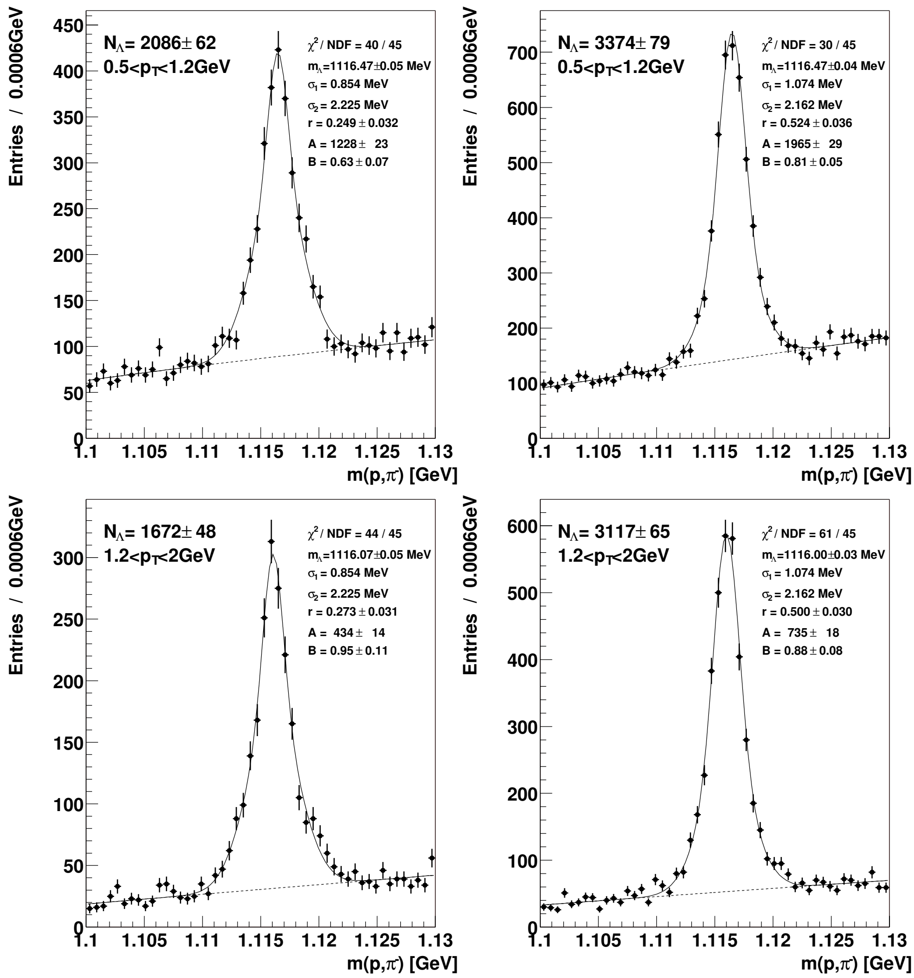

Figure B.14: Invariant mass $m(p, \pi^-)$ in bins of p_T for data (left) and ARIADNE MC (right) in the restricted kinematic region described in the text.

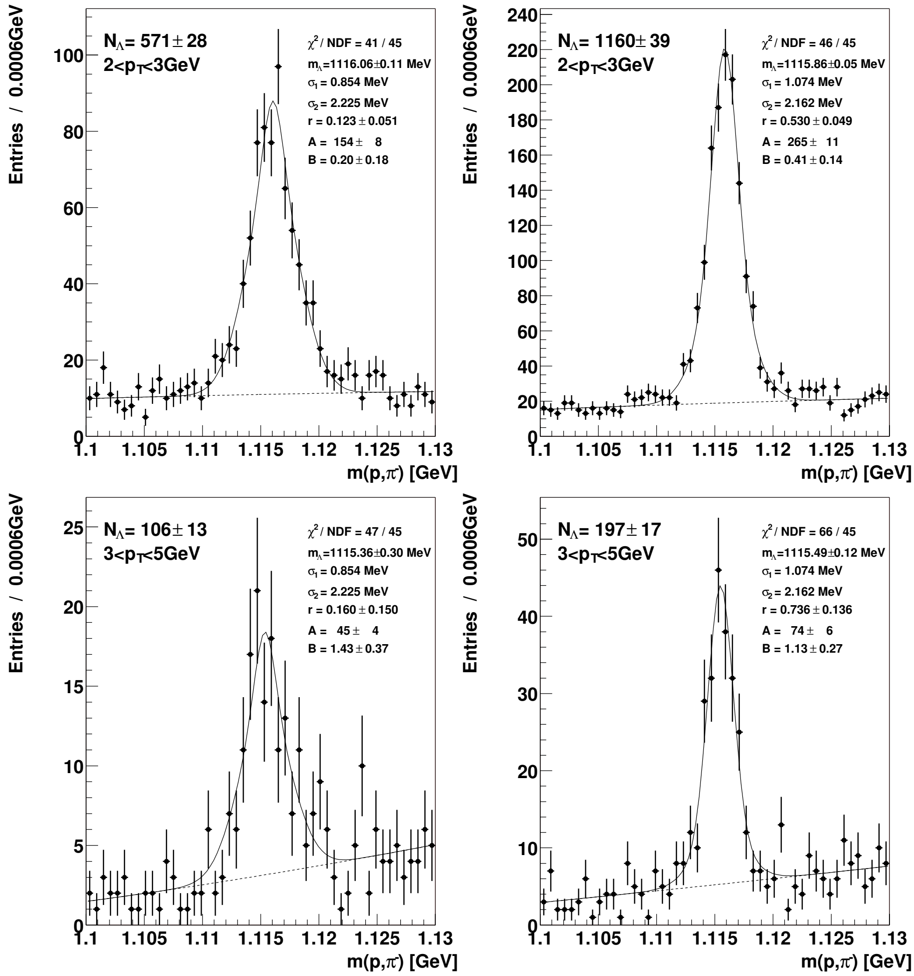

Figure B.15: Invariant mass $m(p, \pi^-)$ in bins of p_T for data (left) and ARIADNE MC (right) in the restricted kinematic region described in the text.

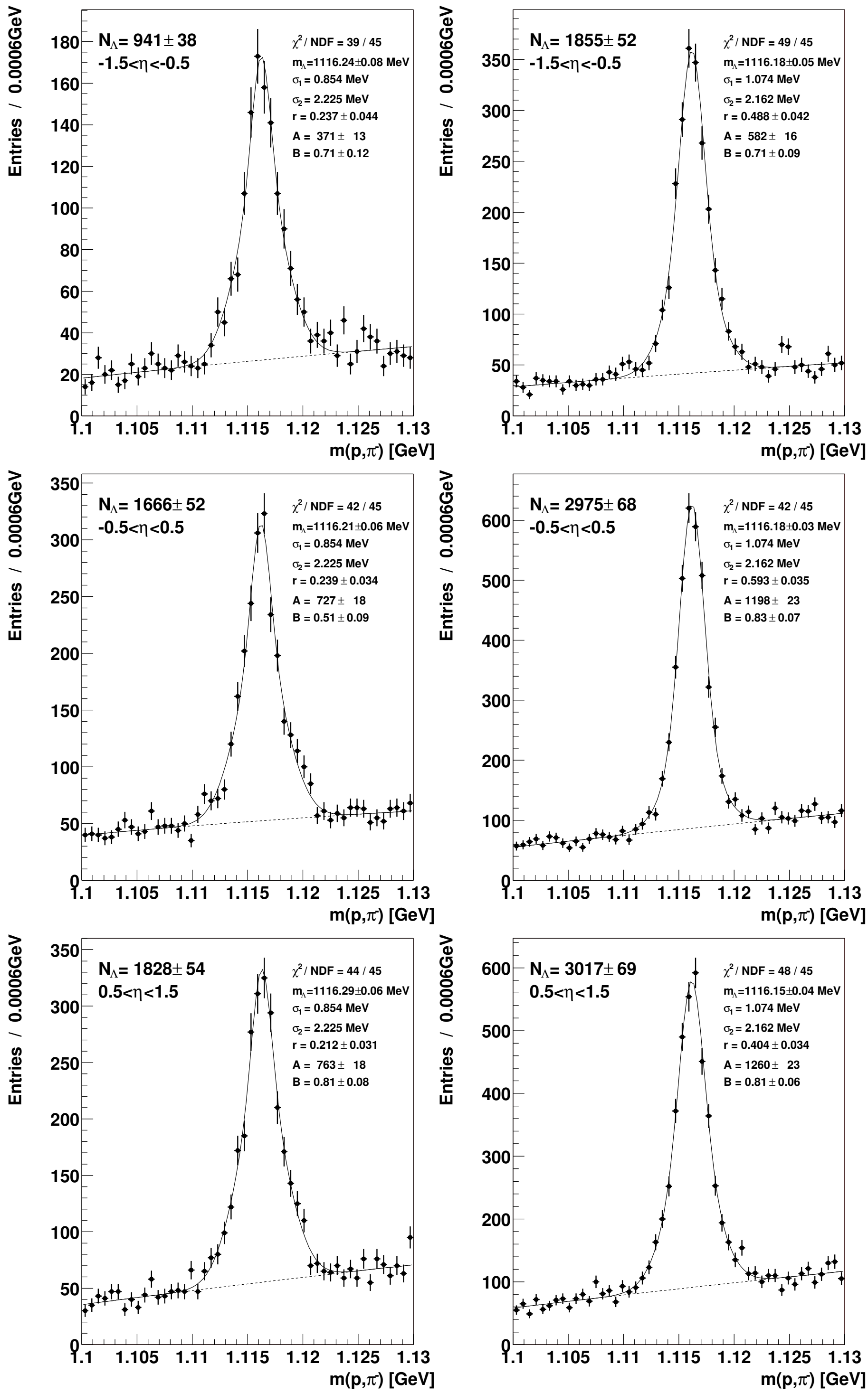

Figure B.16: Invariant mass $m(p, \pi^-)$ in bins of η for data (left) and ARIADNE MC (right) in the restricted kinematic region described in the text.

B.3 Mass distributions of $\bar{\Lambda}$ in bins of Q^2, x, $p_T(\bar{\Lambda})$ and $\eta(\bar{\Lambda})$

The invariant mass distributions $m(\bar{p}\pi^+)$ in bins of Q^2 (Figs. B.17–B.18), x (Figs. B.19–B.21), $p_T(\bar{\Lambda})$ (Figs. B.22–B.23) and $\eta(\bar{\Lambda})$ (Fig. B.24) are shown for data and ARIADNE MC. The number of $\bar{\Lambda}$ obtained from these invariant mass distribution are used to determine the differential cross section in bins of Q^2, x, $p_T(\bar{\Lambda})$ and $\eta(\bar{\Lambda})$. If the number of entries in the first four bins is below 48 a Maximum-Likelihood fit is performed on the data instead of an χ-fit. The widths of the two Gaussians which are used to parameterize the signal are fixed to the value determined by the fit to the total signal (Fig. 4.11).

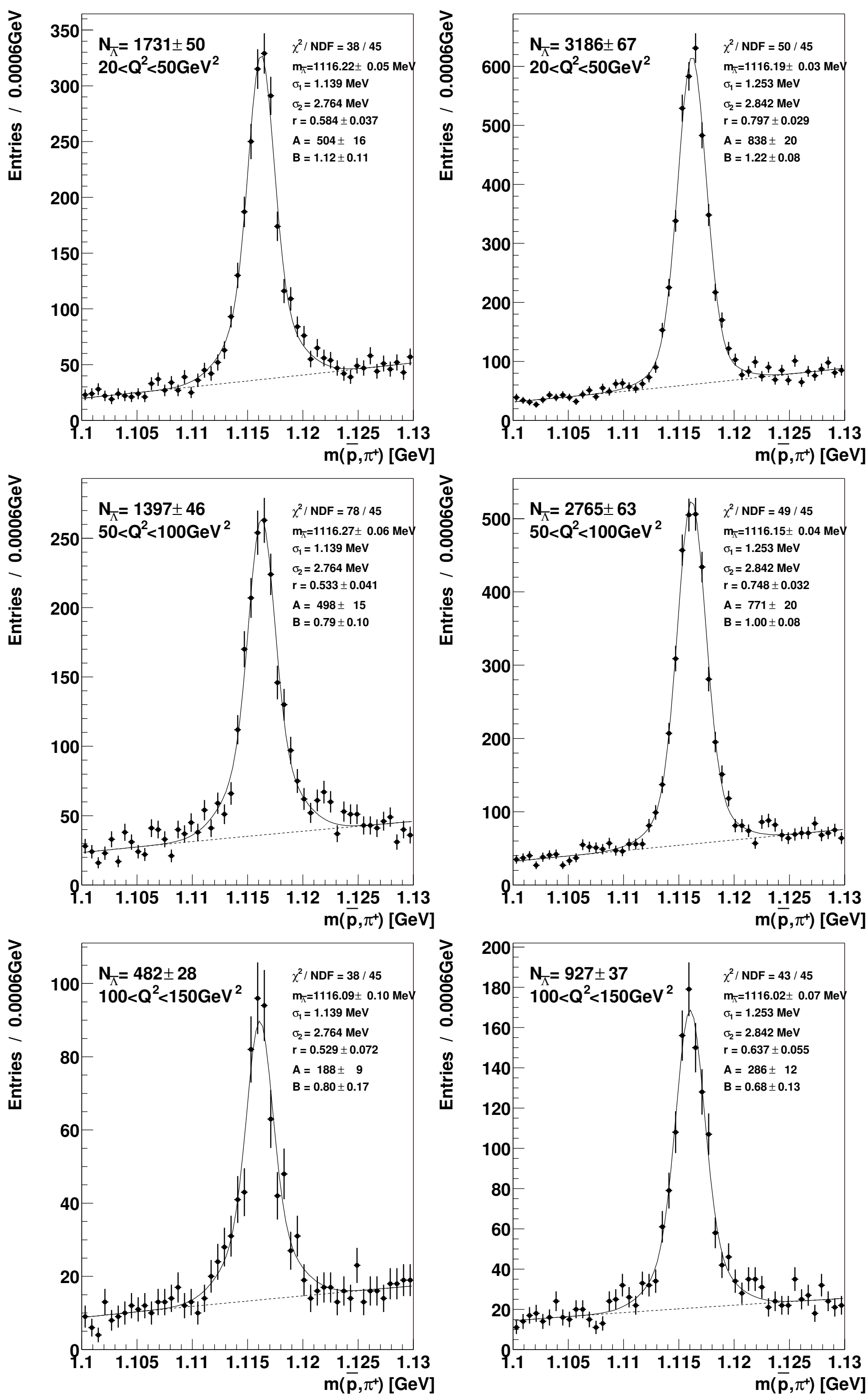

Figure B.17: Invariant mass $m(\bar{p}, \pi^+)$ in bins of Q^2 for data (left) and ARIADNE MC (right) in the restricted kinematic region described in the text.

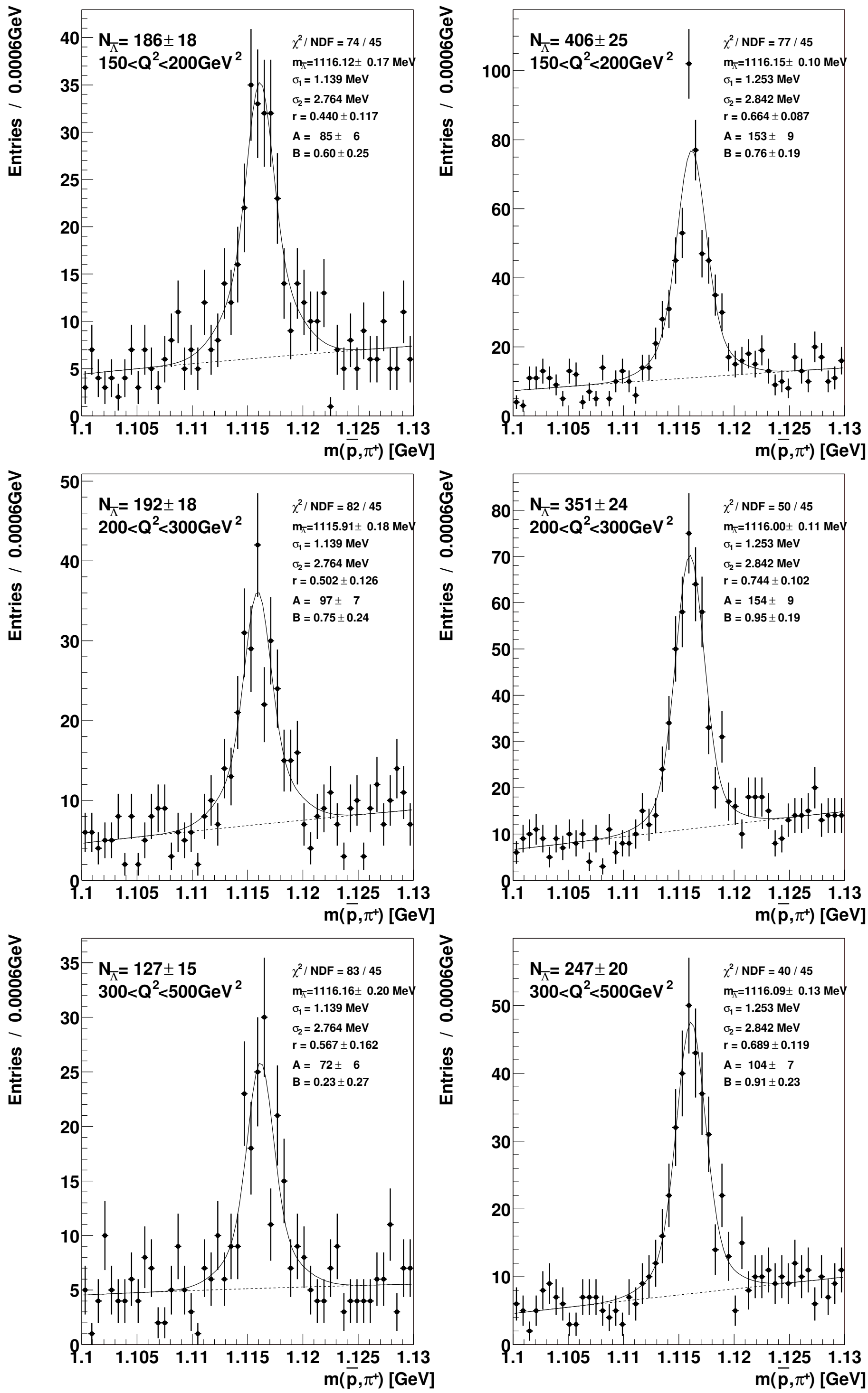

Figure B.18: Invariant mass $m(\bar{p}, \pi^+)$ in bins of Q^2 for data (left) and ARIADNE MC (right) in the restricted kinematic region described in the text.

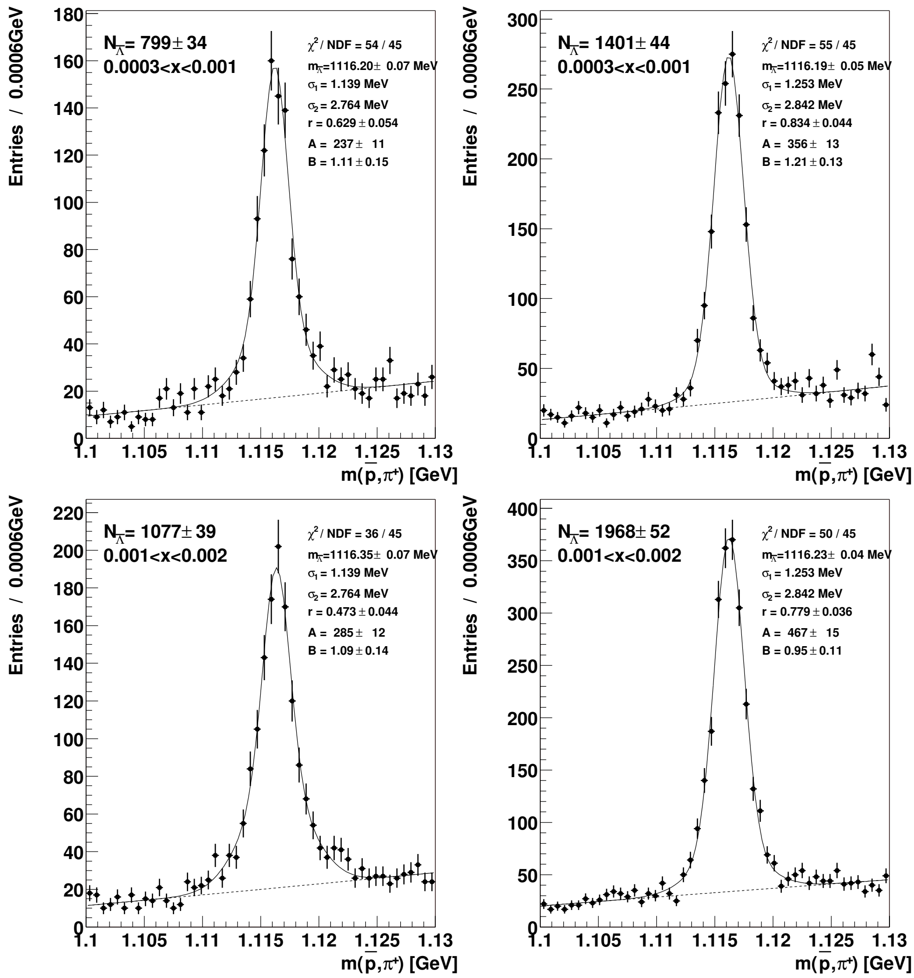

Figure B.19: Invariant mass $m(\bar{p}, \pi^+)$ in bins of x for data (left) and ARIADNE MC (right) in the restricted kinematic region described in the text.

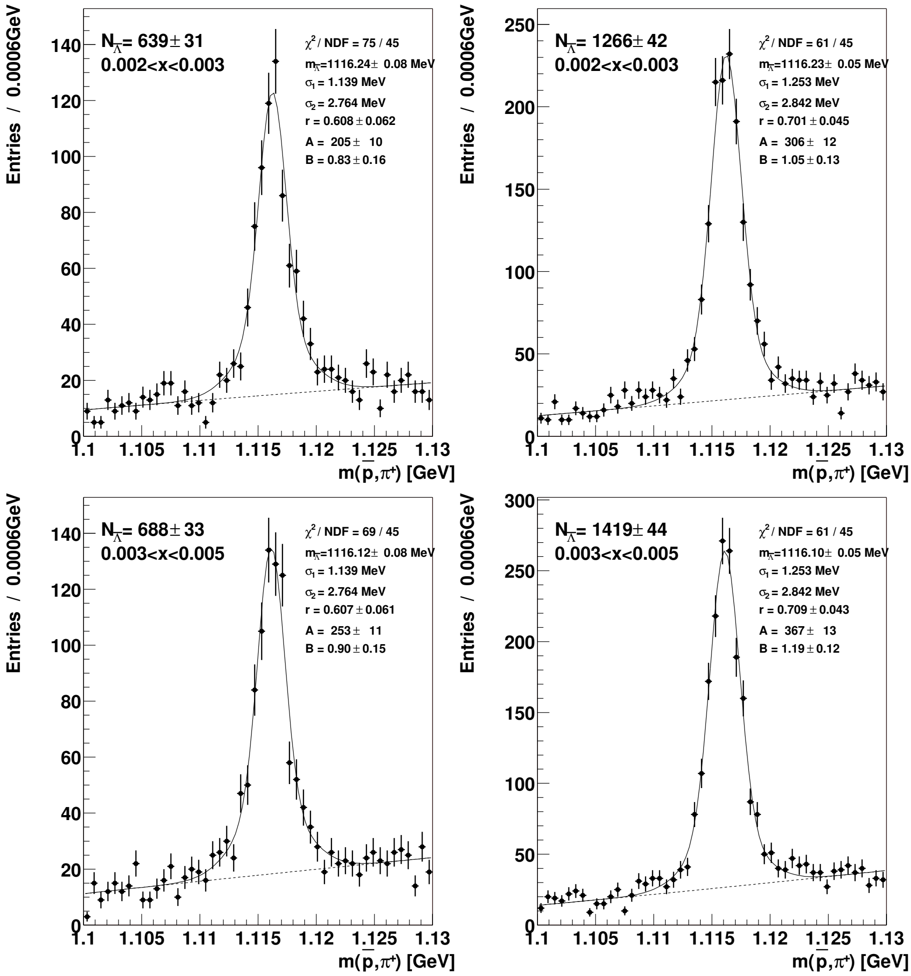

Figure B.20: Invariant mass $m(\bar{p}, \pi^+)$ in bins of x for data (left) and ARIADNE MC (right) in the restricted kinematic region described in the text.

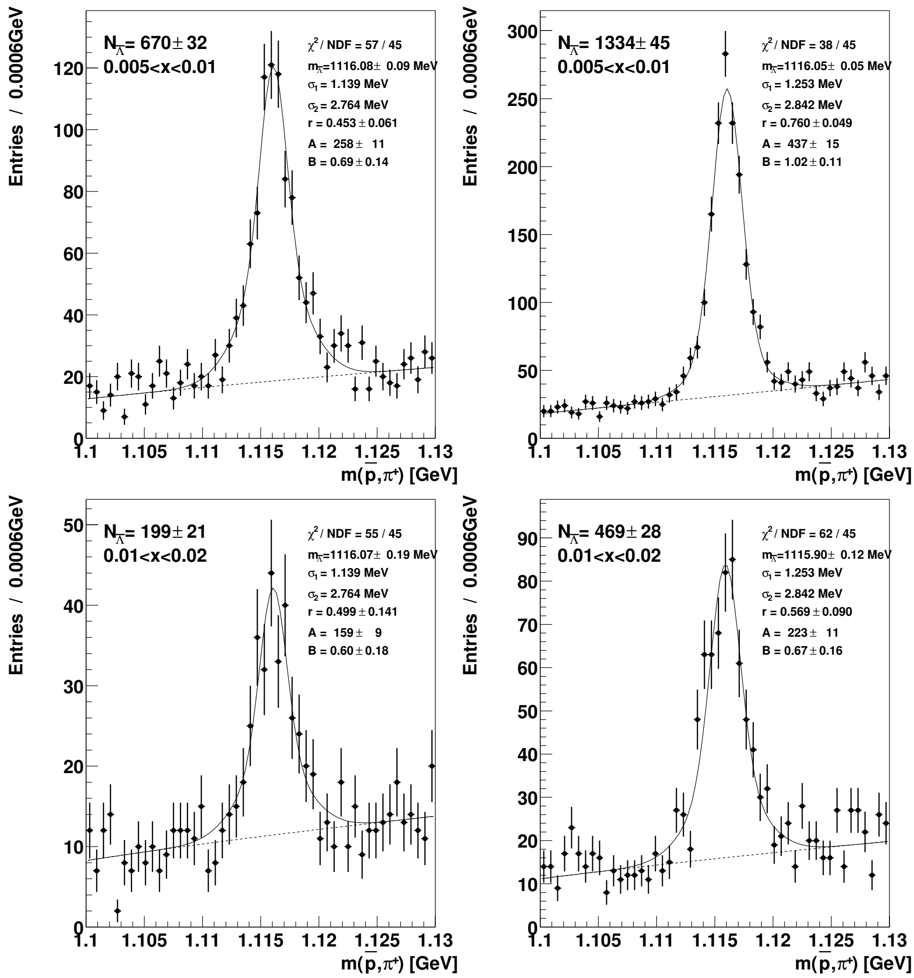

Figure B.21: Invariant mass $m(\bar{p}, \pi^+)$ in bins of x for data (left) and ARIADNE MC (right) in the restricted kinematic region described in the text.

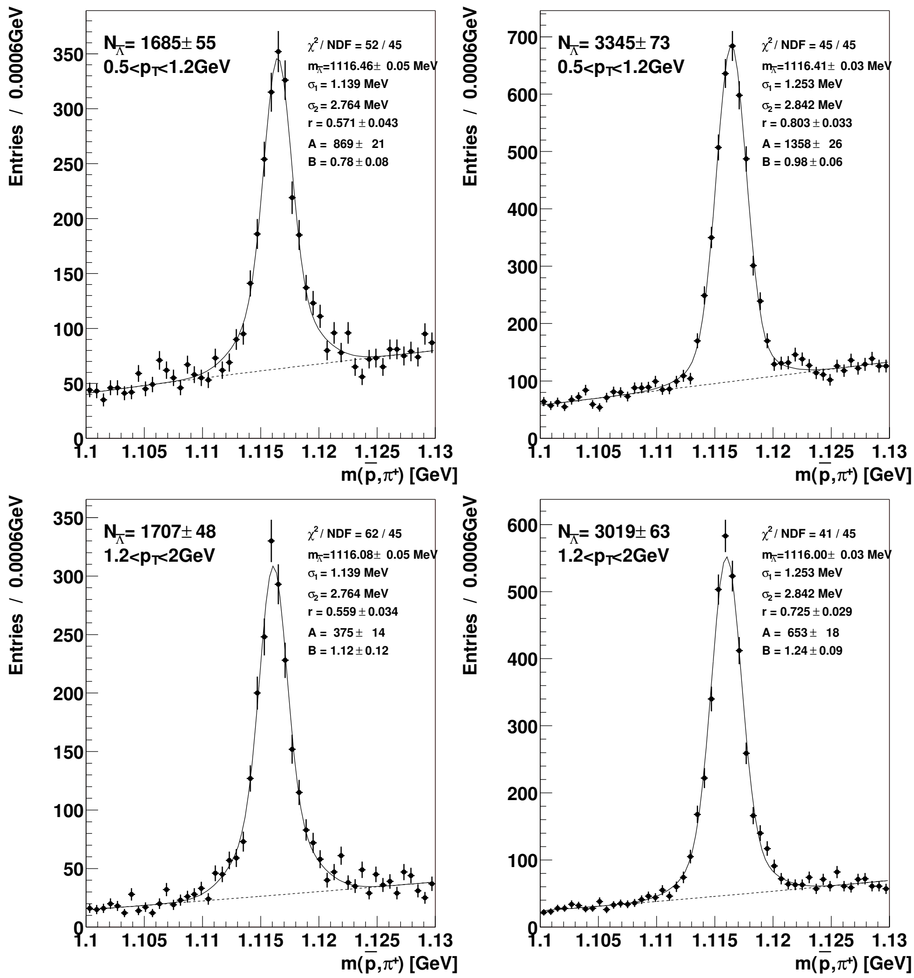

Figure B.22: Invariant mass $m(\bar{p}, \pi^+)$ in bins of p_T for data (left) and ARIADNE MC (right) in the restricted kinematic region described in the text.

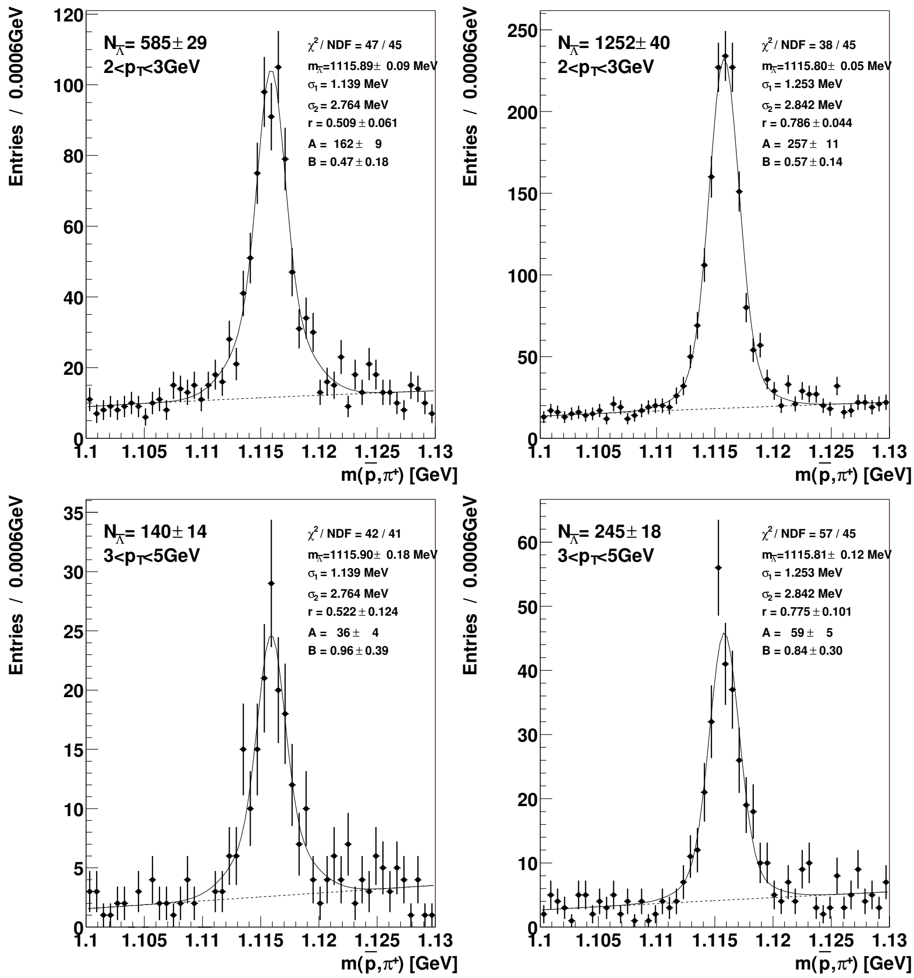

Figure B.23: Invariant mass $m(\bar{p}, \pi^+)$ in bins of p_T for data (left) and ARIADNE MC (right) in the restricted kinematic region described in the text.

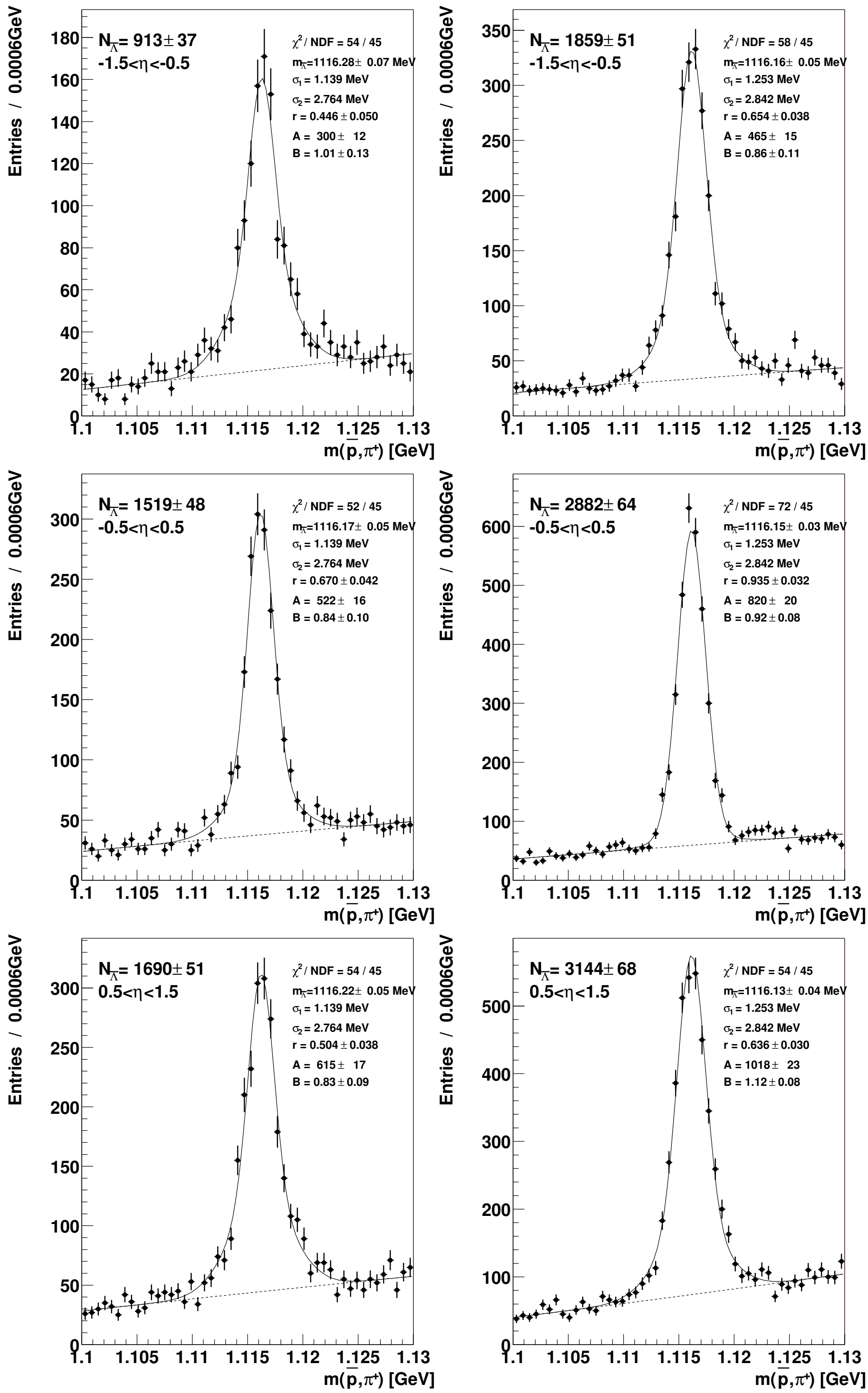

Figure B.24: Invariant mass $m(\bar{p}, \pi^+)$ in bins of η for data (left) and ARIADNE MC (right) in the restricted kinematic region described in the text.

B.4 Mass distributions of $\Lambda+\bar{\Lambda}$ in bins of Q^2, x, $p_T(\Lambda+\bar{\Lambda})$ and $\eta(\Lambda+\bar{\Lambda})$

The invariant mass distributions $m(p\pi)$ in bins of Q^2 (Figs. B.25–B.26), x (Figs. B.27–B.29), $p_T(\Lambda+\bar{\Lambda})$ (Figs. B.30–B.31) and $\eta(\Lambda+\bar{\Lambda})$ (Fig. B.32) are shown for data and ARIADNE MC. The number of $\Lambda+\bar{\Lambda}$ obtained from these invariant mass distribution are used to determine the differential cross section in bins of Q^2, x, $p_T(\Lambda+\bar{\Lambda})$ and $\eta(\Lambda+\bar{\Lambda})$. If the number of entries in the first four bins is below 48 a Maximum-Likelihood fit is performed on the data instead of an χ-fit. The widths of the two Gaussians which are used to parameterize the signal are fixed to the value determined by the fit to the total signal (Fig. 4.12).

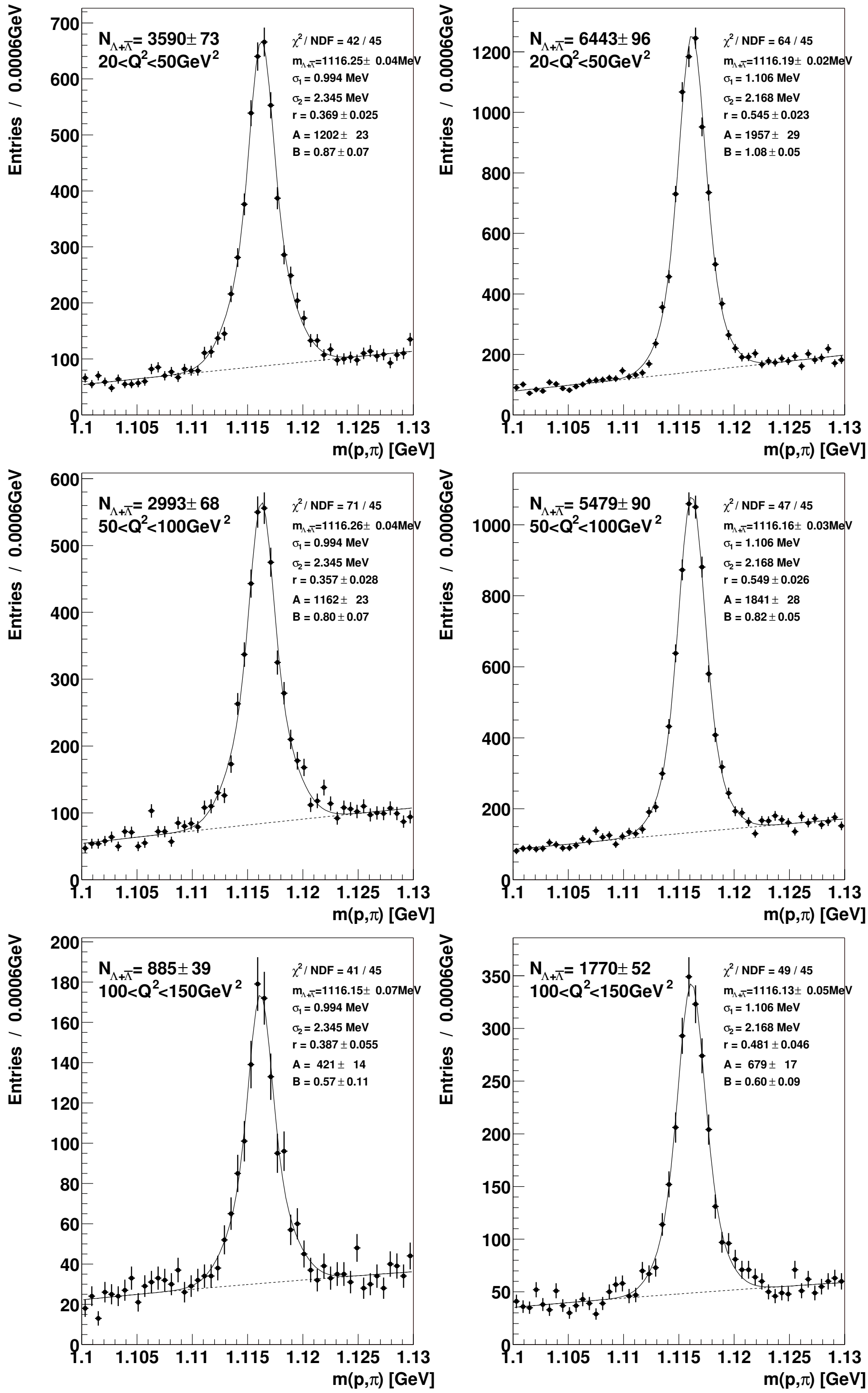

Figure B.25: Invariant mass $m(p, \pi)$ in bins of Q^2 for data (left) and ARIADNE MC (right) in the restricted kinematic region described in the text.

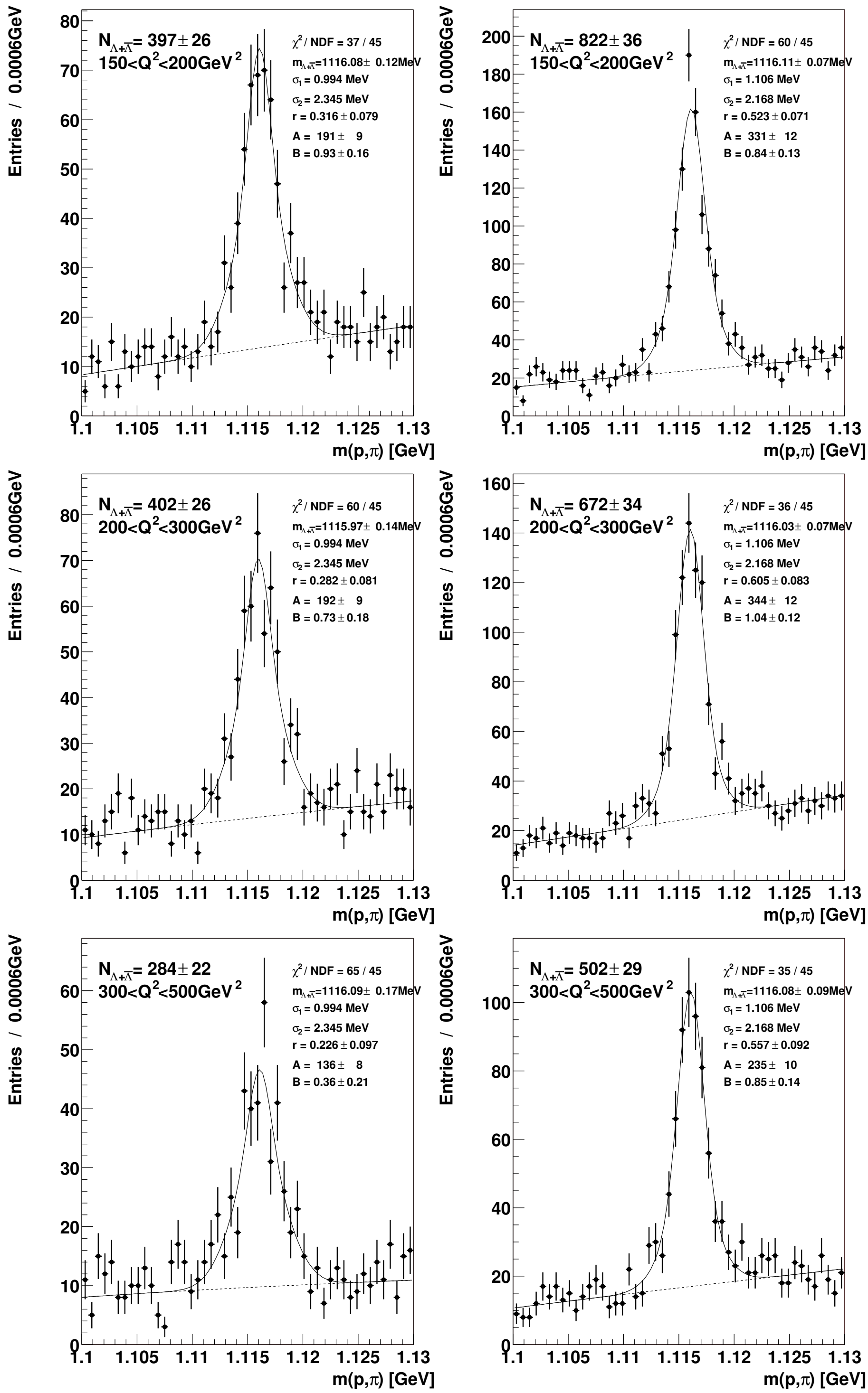

Figure B.26: Invariant mass $m(p, \pi)$ in bins of Q^2 for data (left) and ARIADNE MC (right) in the restricted kinematic region described in the text.

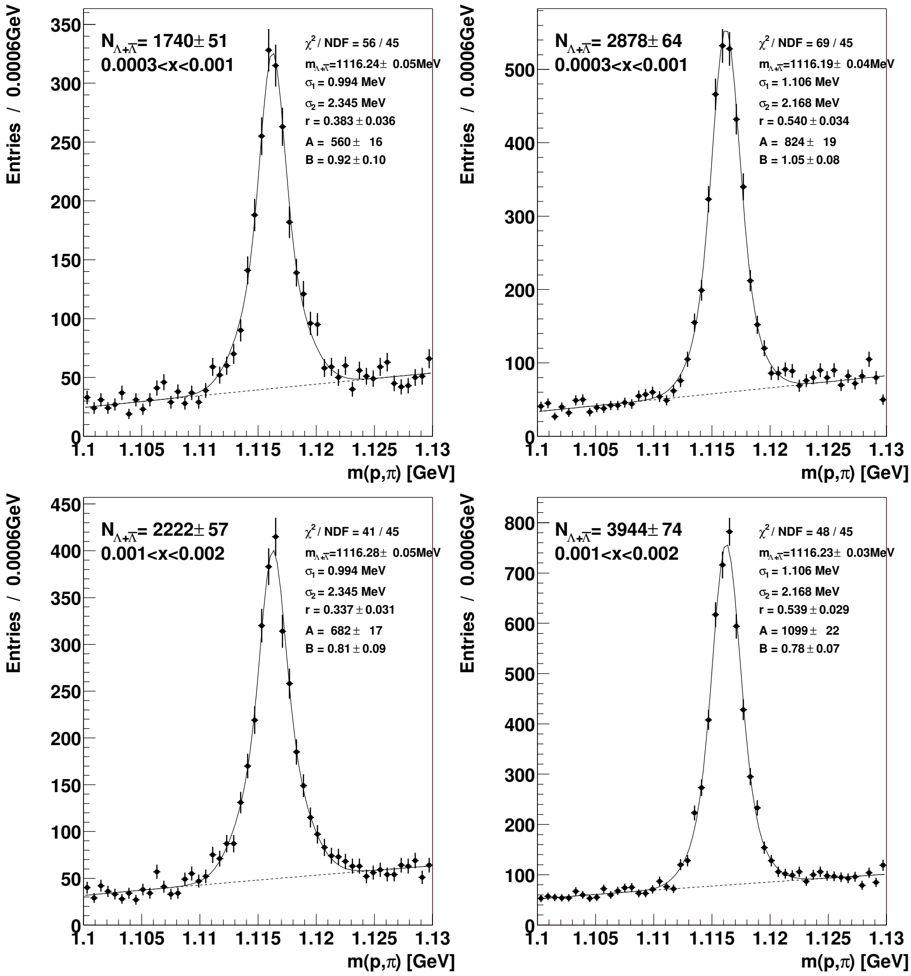

Figure B.27: Invariant mass $m(p, \pi)$ in bins of x for data (left) and ARIADNE MC (right) in the restricted kinematic region described in the text.

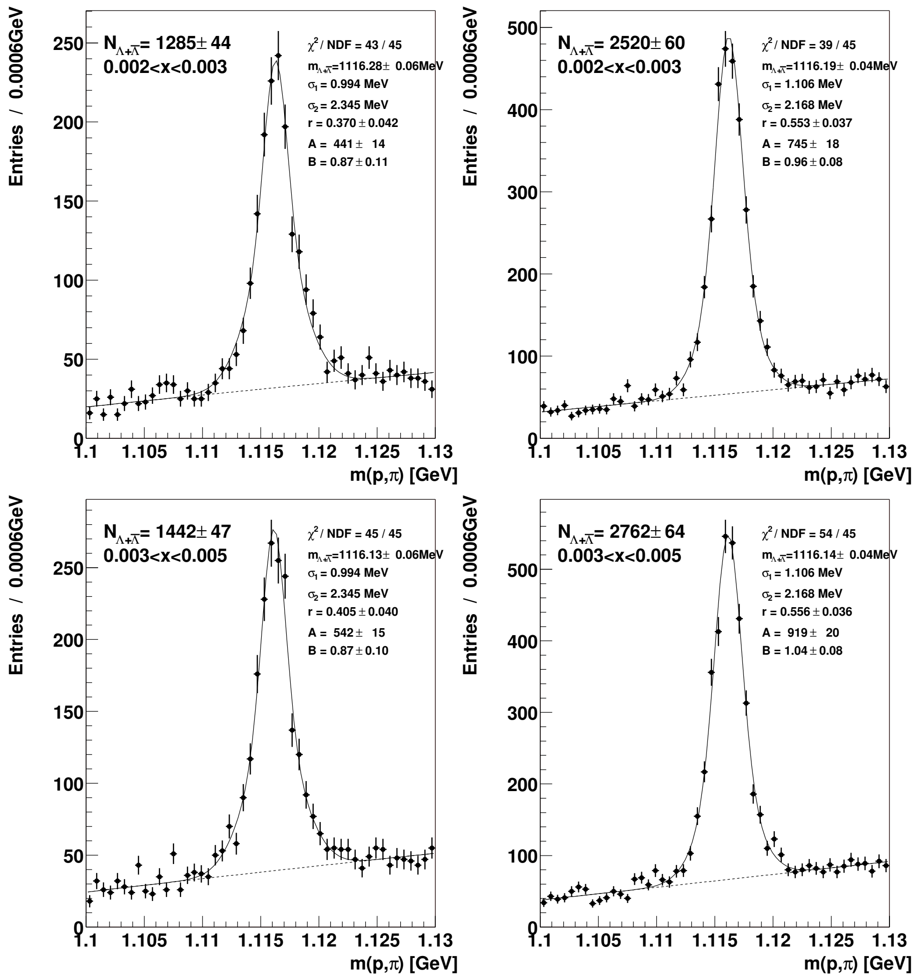

Figure B.28: Invariant mass $m(p, \pi)$ in bins of x for data (left) and ARIADNE MC (right) in the restricted kinematic region described in the text.

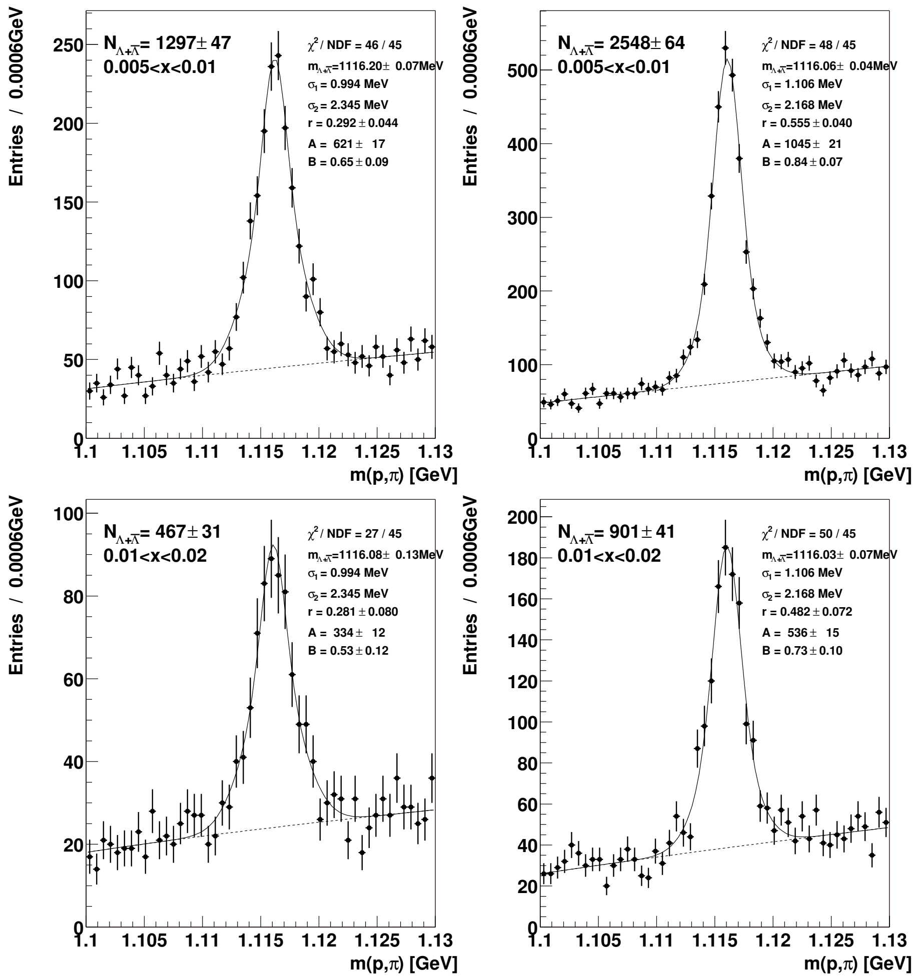

Figure B.29: Invariant mass $m(p, \pi)$ in bins of x for data (left) and ARIADNE MC (right) in the restricted kinematic region described in the text.

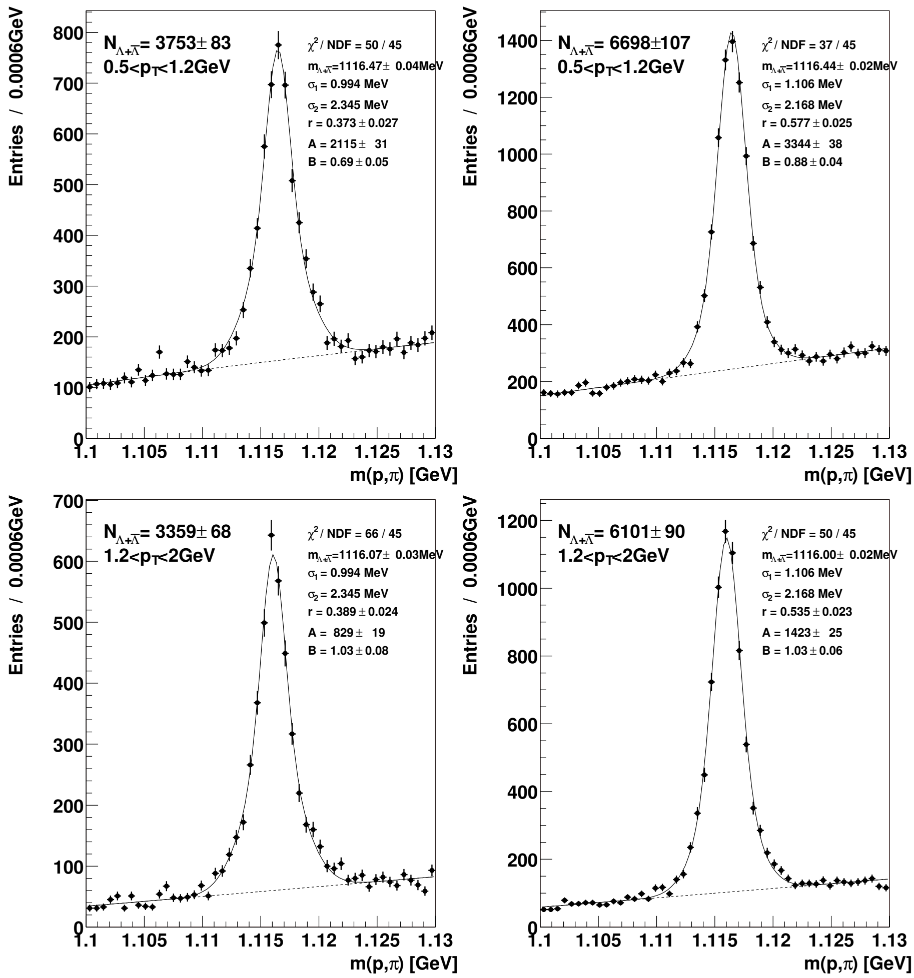

Figure B.30: Invariant mass $m(p, \pi)$ in bins of p_T for data (left) and ARIADNE MC (right) in the restricted kinematic region described in the text.

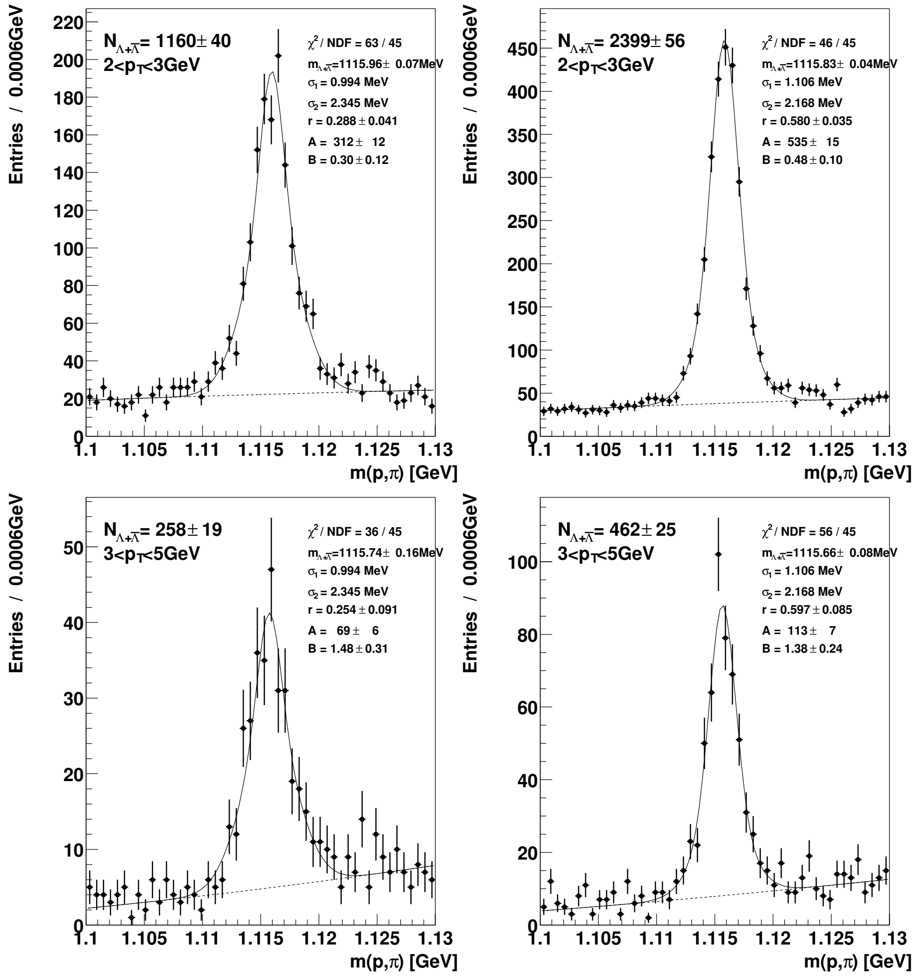

Figure B.31: Invariant mass $m(p, \pi)$ in bins of p_T for data (left) and ARIADNE MC (right) in the restricted kinematic region described in the text.

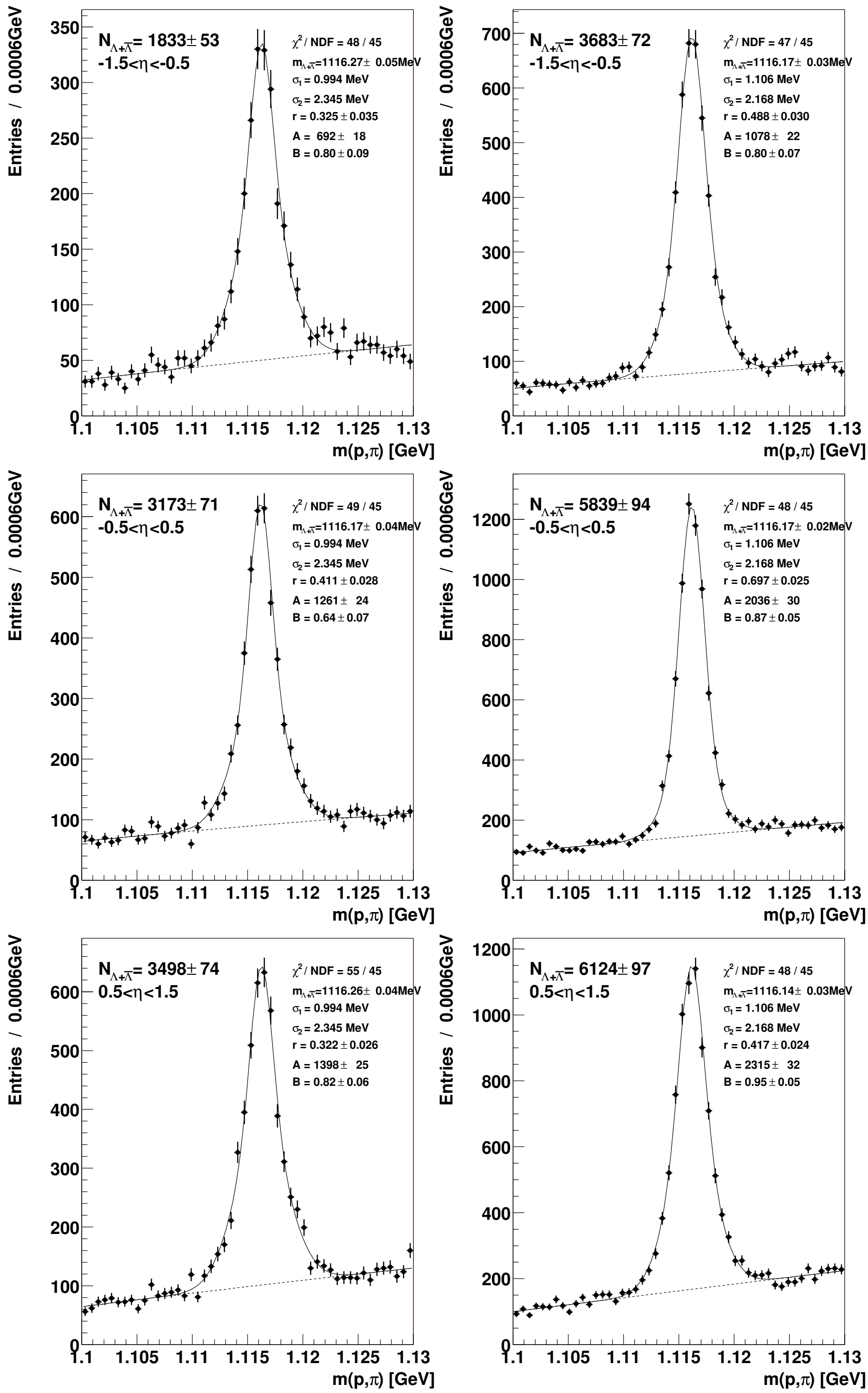

Figure B.32: Invariant mass $m(p, \pi)$ in bins of η for data (left) and ARIADNE MC (right) in the restricted kinematic region described in the text.

Bibliography

[1] H. Abramowicz, A. Caldwell, R. Sinkus. Neural network based electron identification in the ZEUS calorimeter. *Nucl. Instrum. Meth.*, **A365**:508–517, 1995.

[2] ALEPH Collaboration (D. Buskulic *et al.*). Inclusive production of neutral vector mesons in hadronic Z decays. *Z. Phys.*, **C69**:379–392, 1996.

[3] B. Andersson, G. Gustafson, G. Ingelman and T. Sjöstrand. Parton fragmentation and string dynamics. *Phys. Rep.*, **97**:31, 1983.

[4] B. Andersson, G. Gustavson, L. Lönnblad, U. Petterson. Coherence effects in deep inelastic scattering. *Z. Phys.*, **C43**:625–632, 1989.

[5] J. Andruszków *et al.* (ZEUS Luminosity Group). Luminosity Measurement in the ZEUS Experiment, DESY-Note 01-041, DESY, Hamburg, 2001.

[6] P.S. Bailey, B. Foster, G.P. Heath, *et al.* The design and perfomance of the ZEUS central tracking detector z-by-timing system. *Nucl. Instrum. Methods*, **A396**:320–349, 1997.

[7] U. Behrens *et al.* Quality control and calibration of the ZEUS forward and rear calorimeters with ^{60}Co sources. *Nucl. Instr. and Meth.*, pages 611–625, 1992.

[8] H. Bethe, W. Heitler. On the stopping of fast particles and on the creation of positive electrons. *Proc. Roy. Soc. Lond.*, **A146**:83–112, 1934.

[9] A. Blondel, F. Jacquet. *Proceedings of the Study of an ep Facility for Europe*, 1979. DESY-79-048.

[10] S. Chekanov, B. Levchenko, J. Repond. Inclusive $\phi(1020)$-meson production in neutral current deep inelastic scattering at HERA, Internal ZEUS-Note 01-047, DESY, Hamburg, 2001.

[11] ZEUS Collaboration. HERA Luminosity Upgrade, 1997.

[12] ZEUS Collaboration. The Upgraded Luminosity System for the ZEUS Experiment, 1999.

[13] G. Corcella *et al.* HERWIG 6.1 Release note. *CAVENDISH-HEP-99-17*, 1999. hep-ph/9912396.

[14] DELPHI Collaboration (P. Abreu *et al.*). Measurement of inclusive $K^{\star 0}(892)$, $\phi(1020)$ and $K_2^{\star 0}(1430)$ production in hadronic Z decays. *Z. Phys.*, **C73**:61–72, 1996.

[15] R.P. Feller. Private communication with Rainer Peter Feller, University of Hamburg, Inst. f. Exp., Luruper Chaussee 149, 22761 Hamburg.

[16] N. Gendner. Studies of $PbWO_4$ Crystals and Construction and Test of a Compact Crystal Calorimeter for ZEUS, PhD thesis, Hamburg, 2000.

[17] T. Gosau. Private communication with Tim Gosau, University of Hamburg, Inst. f. Exp., Luruper Chaussee 149, 22761 Hamburg.

[18] R. Graciani Diaz. A New W/Scintillator Electromagnetic Calorimeter for ZEUS. *Frascati Physics Series*, **XXI**:769–776, 2000.

[19] H1 Collaboration (C. Adloff *et al.*). Photoproduction of K^0 and Λ at HERA and a Comparision with Deep Inelastic Scattering. *Z. Phys.*, **C76**:213–221, 1997.

[20] H1 Collaboration (S. Aid *et al.*). Strangeness production in deep-inelastic positron-proton scattering at HERA. *Nucl. Phys.*, **B480**:3–34, 1996.

[21] R. Hall-Wilton, N. McCubbin, *et al.* The CTD tracking resolution, Internal ZEUS-Note 99-027, DESY, Hamburg, 1999.

[22] G.F. Hartner. VCTRAK briefing: Program and math., Internal ZEUS-Note 98-058, DESY, Hamburg, 1998.

[23] G.F. Hartner, Y. Iga, J.B. Lane, N.A. McCubbin. VCTRACK (3.07/04): Offline Output Information, Internal ZEUS-Note 97-064, DESY, Hamburg, 1997.

[24] H. Henschel, O. Köhn, H.U. Schmidt. Induced loss after pulsed and continuous irradiation of single mode and graded index fibres. *SPIE Vol. 992 Fiber Optics Reliability: Benign and Adverse Environments II*, pages 96–109, 1988.

[25] P. Söding I. Flegel. Das Supermikroskop HERA, Deutsches Elektronen-Synchrotron DESY in der Helmholtz-Gemeinschaft, Hamburg, 2002.

[26] C. Jordan. Private communication with Claudia Jordan, DESY, Notkestr. 85, 22607 Hamburg.

[27] N. Krumnack. Testbeam Experiments and Monte Carlo Simulation of the ZEUS 6m Tagger, Diploma thesis, Hamburg, 2001.

[28] Kuraray Co., Ltd. Scintillation Materials (Plastic Scintillating Fibers, SCSN Plastic Scintillators), sales brochure by Kuraray Co., Ltd., Methacrylic Resin Division, 8F, Maruzen Building, 3–10, 2-Chome, Nihonbashi, Chuo-ku, Tokyo, 103-0027, Japan.

[29] A. Kwiatkowski *et al.* HERACLES 4.5.2. *Comp. Phys. Comm.*, **69**:155, 1992.

[30] N. Latuske. Untersuchung von szintillierenden Fasern für ein Spaghetti-Kalorimeter auf ihre Strahlungshärte, Diploma thesis, Hamburg, 2001.

[31] L. Lönnblad. ARIADNE. *Comp. Phys. Comm.*, **71**:15, 1992.

[32] G. Marchesini *et al.* HERWIG: a monte carlo event generator for simulating hadron emission reactions with interfering gluons. *Comp. Phys. Comm.*, **67**:465, 1992.

[33] Particle Data Group (D.E. Groom *et al.)*. Review of particle physics. *Eur. Phys. J.*, **C15**:1, 2000. and 2001 partial update for edition 2002 (URL:`http://pdg.lbl.gov`).

[34] H. Prause. Private communication with Heinz Prause, University of Hamburg, Inst. f. Exp., Luruper Chaussee 149, 22761 Hamburg.

[35] H. Raach. Inclusive Jet Cross Sections in Neutral Current Deep Inelastic Scattering in the Breit Frame at ZEUS, PhD thesis, Freiburg, 2001.

[36] P. Schmüser. *Feynman-Graphen und Eichtheorien für Experimentalphysiker*. Springer, 1995.

[37] H. Spiesberger *et al.* `http://www.desy.de/~hspiesb/djangoh.html`.

[38] M.R. Sutton. Charm in Dijet Photoproduction at HERA, PhD thesis, University College London, 1998.

[39] N. Togo-Rosas. Pirvate communication with Noriko Togo-Rosas via e-mail sent by Hiroyuki Yonekura (Executive Vice President, Kuraray America, Inc.).

[40] P. Waloschek. HERA durchleuchtet das Proton. *Physik in unserer Zeit*, Nr. 6:263–271, 1992.

[41] W.S.C. Williams. *Nuclear and Particle Physics*. Oxford Science Publications, 1995.

[42] ZEUS Collaboratin (M. Derrick *et al.*). Comparison of energy flows in deep inelastic scattering events with and without a large rapidity gap. *Phys. Lett.*, **B338**:483–496, 1994.

[43] ZEUS Collaboration (J. Breitweg *et al.*). Charged particles and neutral kaons in photoproduced jets at HERA. *Eur. Phys. J.*, **C2**:77–93, 1998.

[44] ZEUS Collaboration (M. Derrick *et al.*). Neutral Strange Particle Production in Deep Inelastic Scattering at HERA. *Z. Phys.*, **C68**:29–42, 1995.

[45] ZEUS Collaboration (U. Holm (Ed.)). The ZEUS Detector : Status Report 1993, DESY, Hamburg, 1993.

[46] A. Ziegler. Private communication with Andy Ziegler, University of Hamburg, Inst. f. Exp., Luruper Chaussee 149, 22761 Hamburg.

[47] A. Ziegler. Measurement of inclusive Ξ^- and $\Sigma(1385)^\pm$ baryon production in neutral current deep inelastic scattering at HERA, PhD thesis, Hamburg, 2002.

[48] T. Zoufal. Beeinträchtigung der optischen Eigenschaften und Veränderung der Fluoreszenz von Kunstoffszintillatoren durch Röntgenstrahlung, PhD thesis, Hamburg, 2002.